

Quality Control of Micromegas Detectors for the  
ATLAS New Small Wheel Upgrade Project  
and  
Optimization of the Spatial Resolution of  
PoSSuMuS Detectors in two Dimensions



Dissertation der Fakultät für Physik  
der  
Ludwig-Maximilians-Universität München

vorgelegt von  
**Ralph Müller**  
geboren in München

München, den 12. Mai 2017



Erstgutachter: Prof. Dr. Otmar Biebel

Zweitgutachter: Prof. Dr. Wolfgang Dünneberger

Tag der mündlichen Prüfung: 22. Juni 2017



*The physicist Leo Szilard once announced to his friend Hans Bethe, that he was thinking of keeping a diary. "I don't intent to publish. I am merely going to record the facts for the information of God." "Don't you think God already knows the facts?" Bethe asks. "Yes," said Szilard. "He knows the facts, but He does not know this version of the facts."*

– Bill Bryson, *A Short History of Nearly Everything*



# Abstract

Micro Mesh Gaseous Structure Detectors (Micromegas) are planar gaseous tracking detectors for charged particles. This detector consists of three planar and parallel structures, a copper cathode, stainless steel micro-mesh and a segmented readout anode. Due to their high rate capability, their precise position reconstruction better than  $100 \mu m$  and the possibility to build them with a square meter size active area they will be part of the upgrade of the inner end cap of the ATLAS forward muon spectrometer. In Munich the  $2 m^2$  sized so called SM2 module is constructed and assembled. In order to provide the mentioned spatial resolution the requirements imposed on the detector components are high, like a planarity with a RMS of below  $30 \mu m$  over the full active area and a parallelism of the anode readout strips of better than  $20 \frac{\mu m}{m}$ .

This thesis covers the construction procedure of the SM2 modules to meet the requirements as well as a presentation of methods to perform quality control measurements of the mentioned requirements. The planarity is measured with a laser triangulation distance sensor. The topology measurement setup including this laser is better than  $10 \mu m$ . With this setup the planarity of the investigated module is up to  $14 \mu m$  over the full active area. These results show that the applied construction procedure can be used to build SM2 module according to the requirements.

It was shown, that studying Micromegas in the Cosmic Ray Facility (CRF) allows also for a measurement of the planarity of the detector and of the strip alignment. This study was performed using a  $1 m^2$  Micromegas, as long as no final assembled SM2 module exists. During series production of the SM2 modules it is planned to calibrate all detectors with the CRF.

In the second part a two dimensional position sensitive scintillating muon detector with silicon photomultiplier readout (PoSSuMuS) is studied with the aim of improving its spatial resolution to be better than  $10 mm$ . It is planned to upgrade the CRF with the implementation of a selection tool for high energetic muons. Such muons get less deflected by Coulomb interactions when passing matter. All measurements in the CRF are performed by comparing the track of a cosmic muon in the reference chambers to the tracklet in the detector under investigation. Those reference detectors of the CRF are Monitored Drift Tube (MDT) chambers consisting of aluminum tubes. The tracks of low energetic muons can get highly deflected when traversing those aluminum tubes as well as the Micromegas distorting the resolution of the CRF. Comparing the reference track to the position of the muon reconstructed with PoSSuMuS after traversing a layer of  $300 mm$  iron gives a way to determine the energy of the particle.

PoSSuMuS is a modular detector with each module consisting of two optical isolated trapezoidal scintillator rods with a silicon photomultiplier (SiPM) readout on both sides of the

rods. Scintillation light is gathered and by wavelength shifting fibers and guided to the ends of the rods. The first coordinate of PoSSuMuS along the rods is determined by the propagation time of the scintillation light towards both readouts. For the second coordinate perpendicular to the rods the light yield of both trapezoids is compared. The spatial resolution of the current design of PoSSuMuS is limited by the photon detection efficiency. A simulation of the setup showed, that by reducing the height of the trapezoid, optimizing the fiber position and increasing the fiber volume, the photon count per event can be drastically increased and with this also the spatial resolution.

In a test beam at CERN with 120  $GeV$  muons and Micromegas as reference detectors four trapezoidal geometries with a height of 50  $mm$  and length of 100  $mm$  and 300  $mm$  are investigated. The result for the best performing geometry allowed for 5  $mm$  spatial resolution from the relative light yield in the two trapezoidal scintillators and for 90  $mm$  spatial resolution from the difference in light propagation time. This is a result of an improved photon detection efficiency showing up to 150 photons in a SiPM per event. The aim of enhancing the light yield and improving the spatial resolution to below 10  $mm$  is reached.

# Kurzfassung

Micromegas sind planare Gasdetektoren zur Spurrekonstruktion geladener Teilchen. Ein solcher Detektor besteht aus drei planaren und parallelen Ebenen, einer Kupfer Kathode, einem rostfreien Edelstahl Mikrogitter und einer segmentierten Anode. Aufgrund ihrer Hochratenfähigkeit, ihrer präzisen Ortsrekonstruktion von besser als  $100 \mu\text{m}$  und der Möglichkeit sie mit Quadratmeter großen aktiven Flächen zu bauen wurden sie als Teil des Upgrades der inneren Endkappe des ATLAS Myonspektrometers ausgewählt. In München werden die  $2 \text{ m}^2$  großen sogenannten SM2-Module gebaut und montiert. Um die genannte Auflösung zu erreichen, ist die Einhaltung strenger Toleranzgrenzen für die einzelnen Detektorkomponenten notwendig. Diese sind etwa die Abweichung der Planarität der einzelnen Ebenen von maximal  $30 \mu\text{m}$  (mittlerer quadratischer Abstand der Messpunkte zum Mittelwert) und eine Parallelität der Auslestreifen der Anode von besser als  $20 \frac{\mu\text{m}}{\text{m}}$ .

In dieser Arbeit wird sowohl auf das Vorgehen beim Bau der SM2-Module, welches nötig ist um die gewünschte Maßhaltigkeit zu erreichen, als auch auf die Qualitätskontrolle der genannten Maße eingegangen. Die Messung der Planarität wird mithilfe eines Laser-Abstandssensors vorgenommen, der nach dem Prinzip der Triangulation funktioniert. Der Aufbau zur Oberflächenmessung, welcher diesen Sensor enthält, hat eine Genauigkeit von besser als  $10 \mu\text{m}$ . Die bisher gebauten Komponenten weisen eine Parallelität von  $14 \mu\text{m}$  auf ihrer gesamten aktiven Fläche auf. Damit ist gezeigt, dass das Vorgehen beim Bau der Detektoren Resultate liefert, die den Anforderungen genügen.

In früheren Studien wurde das Verhalten von Micromegas Detektoren mit kosmischen Myonen untersucht. Diese Messungen fanden im kosmischen Höhenstrahl-Messstand der LMU statt, in welcher die Spuren der Myonen mit Referenzkammern gemessen wurden, um sie anschließend mit der Vorhersage des Testdetektors zu vergleichen. Hierbei wurde herausgefunden, dass der Messstand sich auch dazu eignet, Verformungen der Ebenen eines Micromegas und die Ausrichtung der Auslestreifen zu vermessen. Bisher wurde nur ein  $1 \text{ m}^2$  großer Prototyp-Micromegas auf diese Weise vermessen, da bis jetzt keine funktionsfähigen SM2-Module montiert wurden. Für die Serienproduktion dieser Detektoren ist es vorgesehen, sie im Messstand zu untersuchen und zu kalibrieren.

Im zweiten Teil der Arbeit geht es um einen zweidimensional ortsauflösenden Szintillationsdetektor mit Silizium-Photomultiplier (SiPM) Auslese. Der Detektor trägt das Akronym PoSSuMuS. Ziel der Untersuchungen ist es, die Ortsauflösung dieses Detektors auf unter  $10 \text{ mm}$  zu verbessern. Mit einem solchen Detektor soll der Höhenstrahl-Messstand erweitert werden, um zukünftig eine Auswahl auf die Energie der einfallenden Myonen treffen zu können. Aufgrund von Coulomb-Wechselwirkungen werden niederenergetische Myonen beim Durchgang durch Materie leicht abgelenkt. Diese Kleinwinkelstreuung beeinflusst die Genauigkeit des Messstandes massiv, da dadurch die Referenzspur und die Micromegas-Spur

nicht mehr identisch sind. Vergleicht man nun die Referenzspur mit der Position des Myons hinter einer Schicht von  $300\text{ mm}$  dickem Eisen, hat man die Möglichkeit nur solche Teilchen auszuwählen, deren Abweichung von der Referenzspur einen bestimmten Wert nicht überschreitet. Dieser Wert ist abhängig von der Energie des Myons.

PoSSuMuS ist ein modulares Detektorsystem in dem jedes Modul selbst aus zwei voneinander optisch isolierten trapezförmigen Szintillatorstäben besteht. An den Enden der Stäbe befindet sich die SiPM-Auslese. Um das Licht zu sammeln und zur Auslese zu führen, werden wellenlängenschiebende Fasern entlang der Stäbe in den Szintillator eingeklebt. Die erste Koordinate von PoSSuMuS, entlang der Stäbe, wird durch Laufzeit des Szintillationslichtes zur Auslese bestimmt. Die dazu senkrechte Koordinate ist gegeben durch einen Vergleich der erzeugten Lichtmenge in beiden Szintillatoren. Die Auflösung dieses Detektors wird durch die begrenzte Lichtsammelleffizienz stark limitiert. Eine Simulation des Aufbaus zeigt jedoch, dass durch eine Reduzierung der Höhe des Trapezes (momentan  $90\text{ mm}$ ), eine Optimierung der Faserposition und eine Erhöhung des Faservolumens die Lichtausbeute drastisch verbessert werden kann.

Während einer Strahlzeit am CERN mit  $120\text{ GeV}$  Myonen und Micromegas Detektoren als Referenz werden vier neue Trapezgeometrien untersucht. Diese haben eine Höhe von nur  $50\text{ mm}$  und eine Länge von  $100\text{ mm}$  beziehungsweise  $300\text{ mm}$ . Das Ergebnis der besten Geometrie ergibt eine Auflösung von  $90\text{ mm}$  in Flugzeitrichtung und  $5\text{ mm}$  in der Lichtmengekoordinate. Diese Verbesserung ist ein Resultat der stark erhöhten Lichtsammelleistung von nun bis zu 150 Photonen in einem Myon-Ereignis. Damit kann gezeigt werden, dass die neue Geometrie sowohl die detektierte Lichtmenge erhöht, als auch die geforderte Auflösung von  $10\text{ mm}$  deutlich unterbietet.

# Contents

<b>1</b>	<b>Introduction</b>	<b>1</b>
<b>2</b>	<b>The LHC and the Atlas Detector</b>	<b>3</b>
<b>3</b>	<b>The Upgrade of the Inner Endcap of the Muon Spectrometer (Small Wheel) in ATLAS</b>	<b>5</b>
3.1	Motivation for the Upgrade . . . . .	5
3.2	Micromegas Detectors . . . . .	6
3.3	Design of the New Small Wheel . . . . .	9
3.4	Design and Construction of Micromegas for the New Small Wheel . . . . .	10
3.4.1	Idea of Using a Stiffback for Panel Construction . . . . .	13
3.4.2	Stiffback . . . . .	13
3.4.3	Gluing of SM2 Micromegas Panels . . . . .	16
<b>4</b>	<b>Setup for Topology Measurements at LMU</b>	<b>21</b>
4.1	Principle Idea of Fast and Precise Topology . . . . .	21
4.2	Tactile Distance Sensors . . . . .	23
4.3	Laser Distance Sensors . . . . .	25
<b>5</b>	<b>Topology Studies Using a Distance Sensor on a CMM</b>	<b>29</b>
5.1	Performance of the Setup . . . . .	29
5.2	Surface Study of the Granite Table . . . . .	35
5.3	Surface Study of Stiffback . . . . .	37
5.4	Surface Study of SM2 Panels . . . . .	43
5.5	Cosmic Ray Facility . . . . .	53
<b>6</b>	<b>PoSSuMuS - A Position Sensitive Scintillating Muon SiPM Detector</b>	<b>57</b>
6.1	Scintillating Materials . . . . .	57
6.2	Silicon Photomultipliers . . . . .	64
6.3	PoSSuMuS - The Detector Idea . . . . .	68
6.4	Limitation of the Design of Predecessor PoSSuMuS Versions . . . . .	71
6.4.1	Results for the Time of Flight Coordinate obtained with the First Prototype . . . . .	73
6.4.2	Results for the Light Yield Coordinate obtained with the Second Prototype . . . . .	76
6.5	Improved Position Sensitivity Using new Geometries . . . . .	80

<b>7</b>	<b>Testbeam with New Geometries at CERN</b>	<b>85</b>
7.1	Construction of new Geometries for Optimized PoSSuMuS . . . . .	85
7.2	Voltage Supply and Gain Stabilization . . . . .	89
7.3	Detector Telescope at CERN . . . . .	94
7.4	General Performance of the new PoSSuMuS . . . . .	99
7.5	Position Resolution in the Time of Propagation Coordinate . . . . .	106
7.5.1	How to get a Spatial Coordinate out of Timing Information . . . . .	106
7.5.2	Estimates about Achievable Spatial Resolution based on Light Propagation Time and Statistics Effects . . . . .	114
7.5.3	Achieved Timing Resolution with Different Techniques . . . . .	117
7.6	Position Resolution in the Light Yield Coordinate . . . . .	128
7.6.1	Technique to Combine all Readout Channels . . . . .	130
7.6.2	Achieved Resolution in Light Yield Direction . . . . .	131
<b>8</b>	<b>Conclusion and Outlook</b>	<b>139</b>
<b>Appendix A Investigation of Steel Tube and Hard Disk with Laser Distance Sensor</b>		<b>I</b>
<b>Appendix B Photos and Circuit Diagrams of SiPM Power Supply</b>		<b>III</b>
<b>Appendix C Spatial Resolution of the Time of Flight Coordinate for 100 mm long Geometries</b>		<b>XI</b>
<b>Appendix D Methods to Determine the Impact of the Landau Energy Loss</b>		<b>XIII</b>
<b>List of Abbreviations</b>		<b>XVII</b>
<b>Bibliography</b>		<b>XIX</b>

# 1 Introduction

This thesis deals with the quality control of large area Micro Mesh Gaseous Structure Detectors (Micromegas). Those are planar high precise particle tracking detectors with a high rate capability. Due to their good performance they will be installed in ATLAS, one of the four large particle detectors around the LHC beam line at CERN. In this upgrade the current detectors of the inner endcap of the ATLAS muon spectrometer, also called Small Wheel, will be renewed. With a diameter of  $\approx 14\text{ m}$  it is clear that the total active area of the New Small wheel will be very large. The new small wheel will consist of four types of Micromegas detectors differing in the geometrical shape, each having a size between  $2\text{ m}^2$  and  $3\text{ m}^2$ . At the LMU Munich the so called SM2 type of Micromegas having an active area of  $2\text{ m}^2$  is constructed for this upgrade.

The content of this thesis is divided in two parts. In the first part details of this upgrade are presented together with methods to construct sandwich panels for the Micromegas assembly. Afterwards, the focus turns to the quality control of those panels. One central issue of the panels is their planarity and homogeneity in thickness. Methods to determine both are presented together with results of the currently produced panels. The measurements are performed with a laser distance sensor. Such a device measures the distance to a point on the surface of interest with laser triangulation. It is moved with a Coordinate Measurement Machine (CMM) over the panels performing a topology scan of their surfaces. This enables us to check the quality of a panel directly after construction with a precision of better than  $10\text{ }\mu\text{m}$ . Up to now the final assembly to a working Micromegas has not been finished. After assembly, the detectors can be investigated in the Cosmic Ray Facility (CRF) belonging to LMU. The just mentioned quality control gives results of the raw panels, while using cosmic muons it is possible to determine the same values in a final assembled detector and to calibrate it.

Currently the CRF does not contain an energy selection tool for the cosmic muons. Important for the facility are muons traversing it on a straight line but the lower the energy of the muon, the more Coulomb interactions it will perform on its way. During such an interaction the muon gets deflected and does not follow the straight line anymore.

The second part of this thesis starting at chapter 6 deals with the improvement of a proof of concept study for an upgrade of the CRF called PoSSuMuS<sup>1</sup>. An additional fast tracking device should be implemented comparing the reference track of a cosmic muon determined by the CRF to its position after a  $300\text{ mm}$  thick iron absorber. Low energetic particles will undergo multiple Coulomb scatterings hence the position of such a muon after the absorber will differ by a few millimeter from the predicted position. The resolution of the current design of PoSSuMuS with up to  $13\text{ mm}$  should be improved to below  $10\text{ mm}$ . PoSSuMuS

---

<sup>1</sup>Position Sensitive Scintillating Muon detector with SiPM readout, PoSSuMuS. From Latin "we can".

---

is a modular two dimensional spatial resolving plastic scintillator. Each module consists of two trapezoidal shaped scintillator rods, read out on both ends with silicon photomultiplier (SiPM)s. Along the rods, defined to be the X coordinate of the detector, a spatial coordinate is reconstructed out of the time of flight of the scintillation photons towards both sides of the rods. Perpendicular to this the Y coordinate is reconstructed out of the different light yields detected in both rods according to their trapezoidal shape. Before presenting the improved detector a comprehension of the former prototypes is given in order to see the improvement in context of the original design. The focus to improve the design of PoSSuMuS is a reduced trapezoidal height. Four different geometries have been investigated in a beam time at CERN. A geometry is found with a resolution of  $3\text{ mm} - 5\text{ mm}$  in Y direction, which is the precision coordinate of PoSSuMuS. Also for the X direction a method to reconstruct a spatial coordinate is presented, providing a resolution of  $80\text{ mm}$  to  $90\text{ mm}$ .

## 2 The LHC and the Atlas Detector

The research site CERN in Geneva/Switzerland is one of the world's most important places for elementary particle physics research. The heart of the experimental facility is the Large Hadron Collider (LHC) with its four large particle detectors ATLAS, CMS, ALICE and LHCb. The LHC is a circular machine to accelerate and collide hadrons like protons or lead ions. The design center of mass energy for proton proton collisions is  $14 \text{ TeV}$ . This accelerator is housed in the  $27 \text{ km}$  circumference tunnel of the former LEP accelerator. The, by volume, largest detector around the LHC beam line is the ATLAS detector [ATLAS Collaboration, 2008]. It can be divided in a barrel region, detecting particles with a momentum dominantly pointing perpendicular to the beam axis and an endcap region for particles with a high momentum component in forward direction  $|\eta| > 1$ . A sketch of the entire detector system of ATLAS is shown in Figure 1, where all blue parts belong to the muon spectrometer.

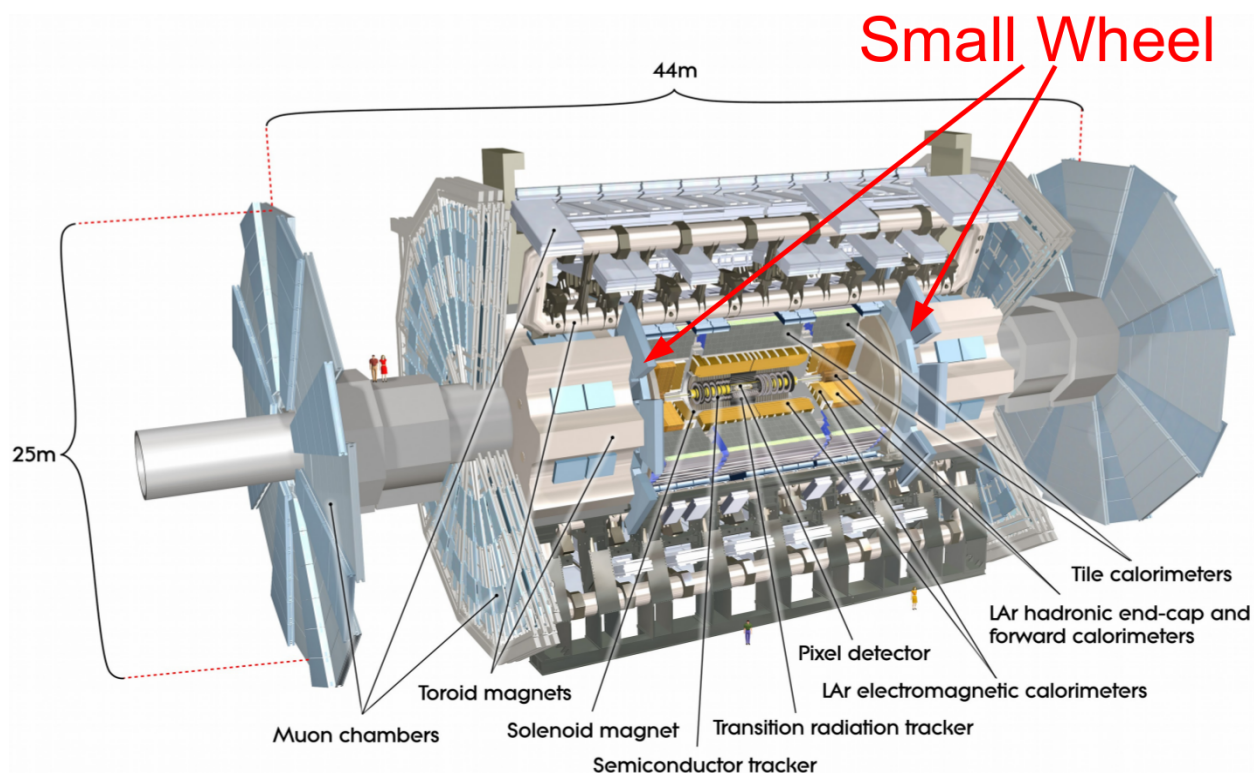


Figure 1: Sketch of the ATLAS detector. The inner endcap regions of the detector are named small wheel, hence the name of the upgrade project "New Small Wheel". Image taken from [Pequenao, 2008] and slightly modified.

The inner endcap layers of the ATLAS muon spectrometer, called small wheels, are located  $\approx 7.4 \text{ m}$  apart from the interaction point with a diameter of  $\approx 14 \text{ m}$ . The current detectors of the small wheel will be replaced during the second long shutdown period 2019/2020. One

---

reason for this upgrade is the upgrade of the LHC itself, providing more luminosity to the experiments. More details are described in section 3.1. The detector technologies used in the New Small Wheel (NSW) are small-strip Thin Gap Chambers (sTGC) and Micromegas, both high rate capable planar gaseous tracking detectors. Of course the new technologies should be at least as good as the old ones<sup>2</sup>. An example would be the momentum resolution of at least 15 % for 1  $TeV$  muon -  $p_T$ . With a diameter of  $\approx 14 m$  it is clear, that the single detectors forming the NSW will become large, while they still have to provide an extremely good spatial resolution below 100  $\mu m$  per detector layer, to provide the desired momentum resolution, [ATLAS MUON Collaboration, 2013]. The consequence for Micromegas, studied in this thesis, is that highly accurate planar surfaces with an active area of 2 – 3  $m^2$  have to be built. An arising question is, how to measure the planarity of the surfaces up to the desired precision of 80  $\mu m$  over the whole active area.

In the following the necessity of an upgrade of the small wheel is discussed, including design and technologies used.

---

<sup>2</sup>The currently used technologies are MDT detectors and Cathode Strip Chambers (CSC).

### 3 The Upgrade of the Inner Endcap of the Muon Spectrometer (Small Wheel) in ATLAS

The current time schedule for the LHC foresees an increase of the instantaneous luminosity to values above  $7 \cdot 10^{34} \text{cm}^{-2} \text{s}^{-1}$  in the so called High Luminosity LHC area. For this, also the experiments have to be improved, requiring the upgrade of the inner endcap of the ATLAS muon spectrometer, the New Small Wheel (NSW).

With the NSW all detectors of the current inner endcap stage will be replaced by sTGC and Micromegas. The main focus of the sTGC will be their trigger capabilities, while the Micromegas are mainly foreseen for offline precision tracking. For redundancy reasons both technologies should be able to fulfill the other task as well.

Starting with the motivation for a NSW, this thesis targets only on the Micromegas, especially the construction happening at LMU Munich.

#### 3.1 Motivation for the Upgrade

The main reason for this upgrade is to keep the possibility of a good muon reconstruction at full efficiency in the forward region without losing important physics. Looking at the current occupancy of the ATLAS Level-1 muon trigger, shown in Figure 2, it can be seen that the trigger rate for muons with a transverse momentum  $p_T > 10 \text{ GeV}$ , the histogram labeled with L1\_MU11, is significantly higher for  $|\eta| > 1^3$ .

The values for reconstructed muons with  $p_T > 10 \text{ GeV}$  give an essentially flat distribution over the whole detector, which means that most of the time a trigger from the forward region is recorded, it will not be reconstructed as a muon. Extrapolations show that the trigger rate will reach a level of  $60 \pm 11 \text{ kHz}$  for  $3 \cdot 10^{34} \text{cm}^{-2} \text{s}^{-1}$  with a momentum threshold  $p_T > 20 \text{ GeV}$  for muons, very close to the maximum bandwidth of the Level-1 trigger being  $100 \text{ kHz}$ . In the current design only the middle stage of the endcap muon spectrometer provides a Level-1 trigger. A sketch in Figure 3 shows possible events which are looking exactly as muons originating from the interaction point for the current design of trigger decision taking.

Since muons are particles easily distinguishable in a hadronic environment found in ATLAS, it is essential to be able to identify them as efficiently as possible to record as much interesting physics as possible. Setting the trigger threshold to a higher momentum value, a conceivable alternative to improving the detectors participating to the Level-1 trigger, would cause a significant cut into physics data. These data below the threshold would in this case be never recorded and are thus lost. A plot demonstrating this problem is shown in Figure 4.

---

<sup>3</sup> $|\eta| > 1$  is also referred to as the forward region of ATLAS

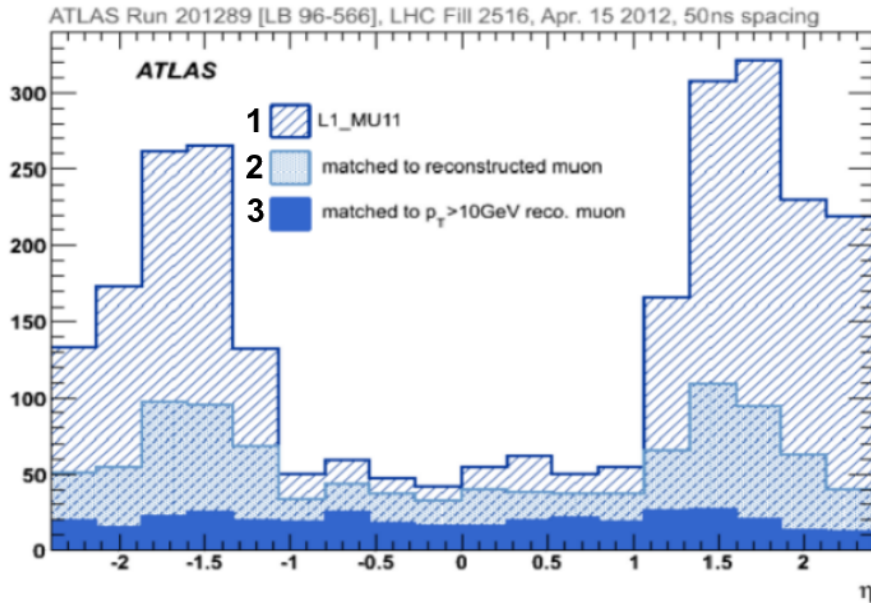


Figure 2: Trigger rate of L1\_MU11 trigger (muons with  $p_T > 10\text{GeV}$ ) as function of pseudo rapidity  $\eta$ . For  $|\eta| > 1$ , the forward region with muons hitting the endcaps, the rate increases significantly, dashed dark blue graph. After reconstruction of the real particle tracks a homogeneous distribution over the whole detector remains, solid dark blue graph. This means that most of the triggers from the endcap region do not correspond to real muons. Image taken from [ATLAS MUON Collaboration, 2013].

An increase of the threshold to, e.g.  $40\text{ GeV}$  significantly cuts into the Higgs signal. An upgrade of the small wheel is therefore the most reasonable way to cope with the bounding conditions during High Luminosity LHC. This will enable the small wheel to provide a spatial information at the Level-1 trigger stage as well, including the identification of tracks pointing towards the interaction point, [ATLAS MUON Collaboration, 2013].

### 3.2 Micromegas Detectors

Micro Mesh Gaseous Structure Detectors (Micromegas) have been introduced in 1996 by Y. Giomataris [Giomataris et al., 1996]. Their original concept has been improved with the goal to make them high rate capable, which is necessary in the ATLAS environment with a background hit rate of  $15 \frac{\text{kHz}}{\text{cm}^2}$  in the small wheel region. The technology using resistive strips is described in the following [Alexopoulos et al., 2011].

Micromegas are planar structures composed of three layers, a copper cathode, a stainless steel micro mesh and a micro structured anode plane for the readout. The volume between cathode and anode is filled with a gas mixture of  $\text{Ar}$  and  $\text{CO}_2$  in a volume ratio of  $93 : 7 \text{ vol}\%$ . The mesh separates this volume into a drift region, pointing towards the cathode, and an amplification region between anode and mesh. While the drift region has a height of typically

### 3 THE UPGRADE OF THE INNER ENDCAP OF THE MUON SPECTROMETER (SMALL WHEEL) IN ATLAS

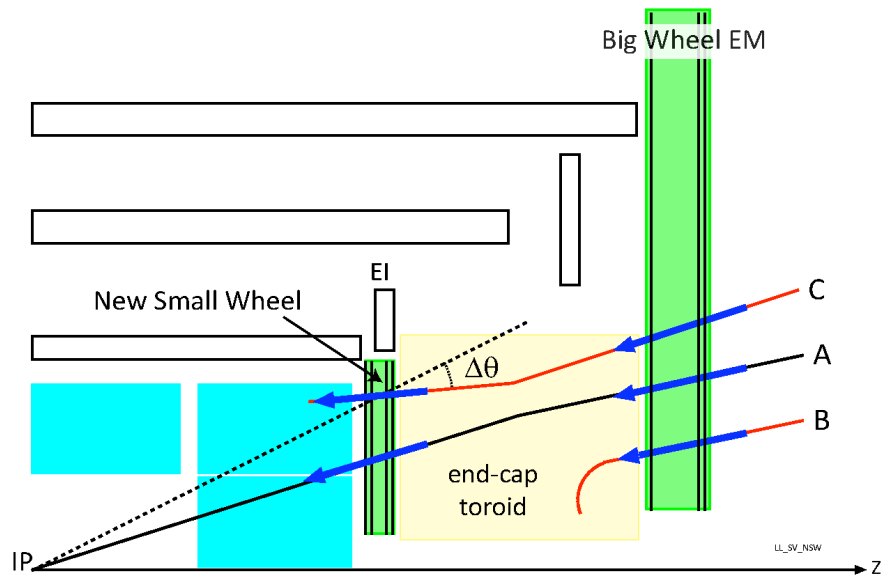
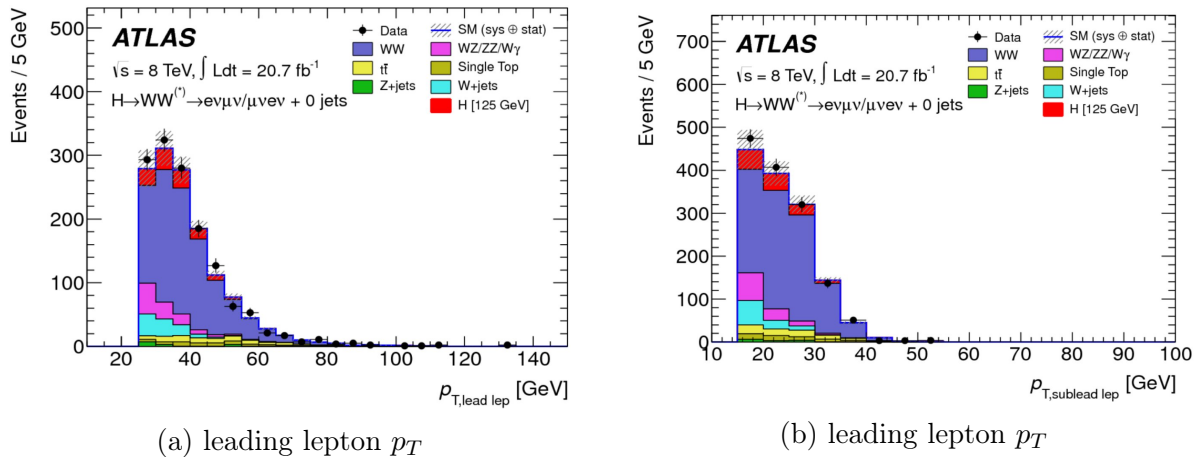


Figure 3: Sketch of the sideview of 1/4 of the ATLAS detector. Events A, B and C caused a trigger in the middle endcap (big wheel) due to a reconstructed track in this detector stage pointing towards the interaction point. This reconstruction happens at trigger level 1 and therefore only includes the information of the big wheel. If information of the small wheel can be included, event B - some particle coming from the beam pipe - or event C - a particle coming from a decay somewhere in the detector - can be rejected as being fake muon triggers already at the time of the Level 1 trigger decision. Image taken from [ATLAS MUON Collaboration, 2013].



(a) leading lepton  $p_T$

(b) leading lepton  $p_T$

Figure 4: Candidate events for the process  $H \rightarrow WW \rightarrow l\nu l\nu$ . 4a shows the distribution for the transverse momentum of the leading lepton and 4b gives the next-to-leading lepton. The Higgs signal is plotted in red. Image taken from [ATLAS MUON Collaboration, 2013].

5 mm the amplification region is with 0.128 mm much thinner. The mesh is supported at this small distance with pillars made out of soldering mask material, which is Pyralux<sup>®</sup> in the case for NSW. A sketch of a resistive strip Micromegas is shown in Figure 5.

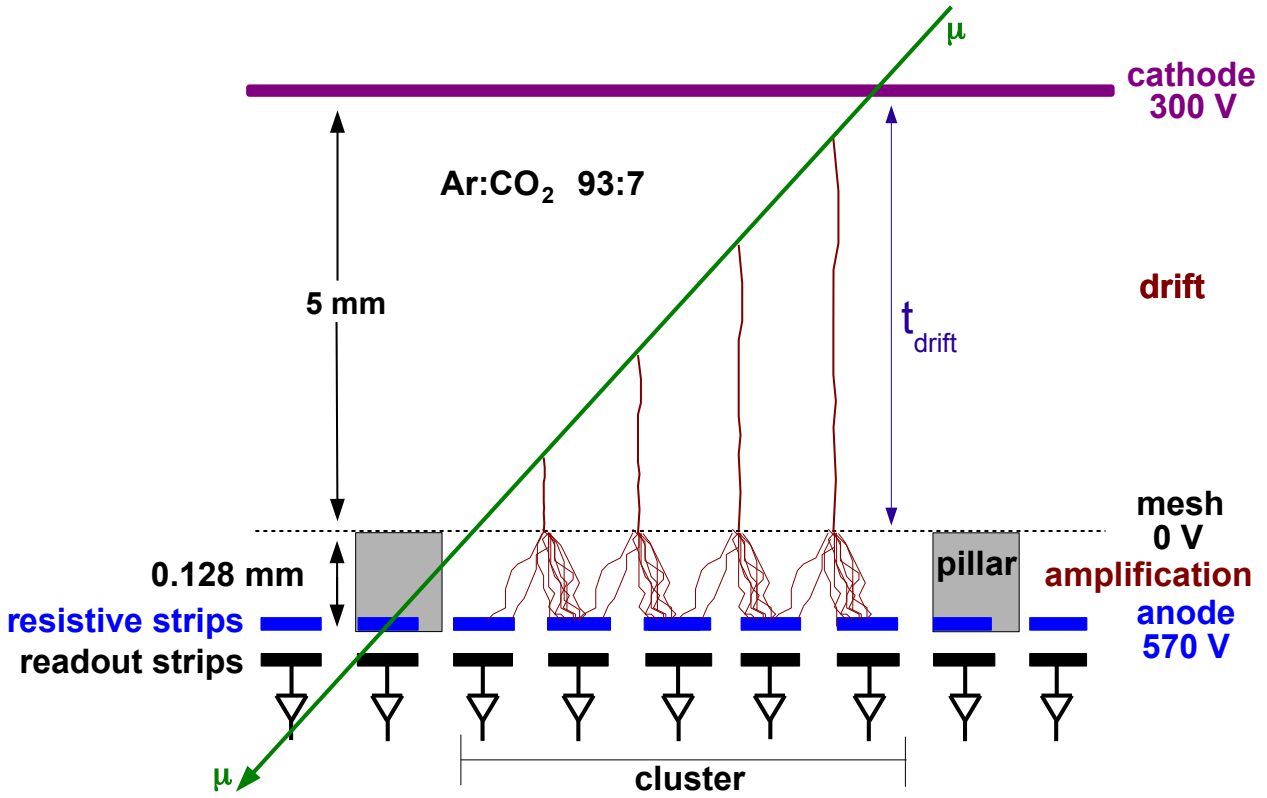


Figure 5: Sketch of a resistive strip Micromegas consisting of three parallel layers, the cathode, the stainless steel micro mesh and a segmented strip anode. The mesh is supported by insulating pillars with a height of  $128 \mu\text{m}$ . For the NSW Micromegas a gas mixture of *Ar* and *CO<sub>2</sub>* with a volume ratio of 93 : 7 vol% is used. A traversing muon ionizes the gas in the drift region between cathode and mesh. The electrons are pulled to the mesh due to an electrical field of  $E_{drift} \approx 600 \frac{\text{V}}{\text{cm}}$ . A much higher amplification field  $E_{amp} \approx 40 \frac{\text{kV}}{\text{cm}}$  pulls those electrons through the mesh and causes an electron avalanche in the amplification region between mesh and anode structure. This avalanche arrives at the resistive strip anode from which the charges couple capacitively to the copper readout strips. Image taken from [Lösel, 2017].

A muon traversing the Micromegas will ionize the gas atoms in the drift region. The electrical field of  $E_{drift} \approx 600 \frac{\text{V}}{\text{cm}}$  separates the electrons from the ions, letting the electrons drift towards the mesh. The combination of low drift field and much higher amplification field of  $E_{ampl} \approx 40 \frac{\text{kV}}{\text{cm}}$  below the mesh pulls the electrons through the mesh down to the anode strips. The electrons produce an avalanche in the amplification region. This charge signal, arriving on the resistive strips, is capacitively coupled to the copper readout strips.

For a highly precise position reconstruction it is mandatory to have parallel readout strips and planar surfaces to ensure a constant electric field in the detector. To better understand the procedure to construct such precise surfaces, the design of the NSW is explained beforehand.

### 3.3 Design of the New Small Wheel

The NSW is divided in alternating and slightly overlapping eight small and eight large sectors forming a wheel, shown in Figure 6. Also highlighted are the separations of each sector in radial direction into two modules, LM1/LM2 and SM1/SM2.

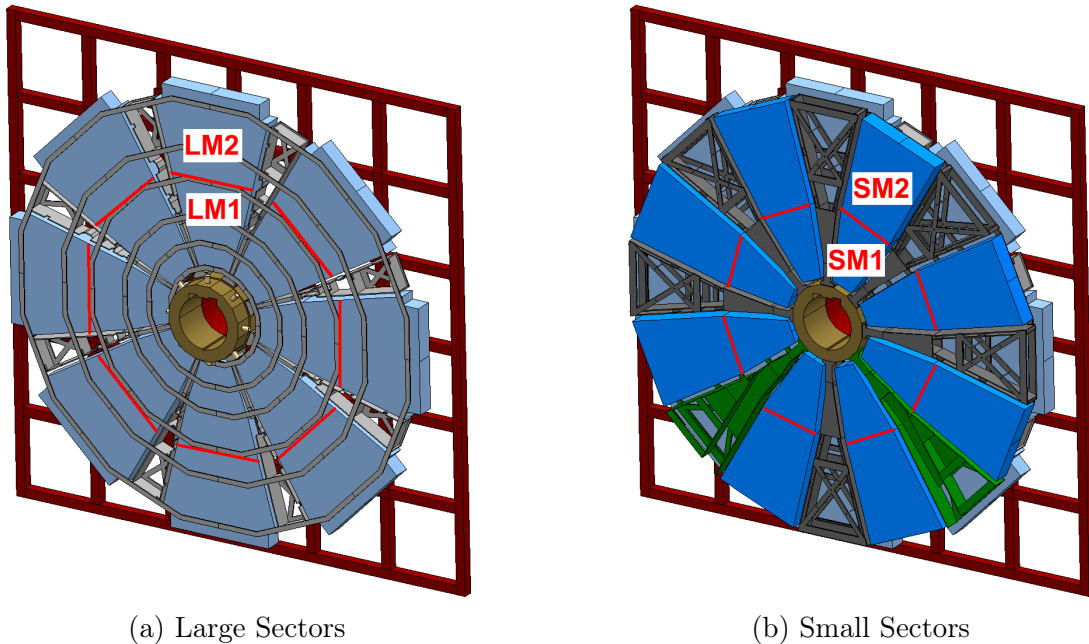


Figure 6: Layout of the large and small sectors of the New Small Wheel, having slight overlap. A separation in radial direction is also drawn resulting in four trapezoidal geometries called SM1 and SM2 for the small sectors and LM1 and LM2 for the large sector, [ATLAS MUON Collaboration, 2013].

Each module has a trapezoidal shape. A particle traversing such a sector will pass first four layers of sTGCs followed by eight layers of Micromegas and finally again four layers of sTGCs. Both detector types are constructed as quadruplets, hence two sTGC quadruplets sandwich two Micromegas quadruplets. This design is shown for both sectors in Figure 7. As mentioned earlier only the Micromegas quadruplets are described in section 3.4, since this is the technology studied in this thesis. The Micromegas quadruplet modules of the large sectors are called LM1 and LM2 (Large Micromegas 1/2), whereas the small modules are called SM1 and SM2 (Small Micromegas 1/2). The general layout of the quadruplet as well as its construction is similar for all four module types. The next chapters will only treat the SM2 module constructed in Munich.

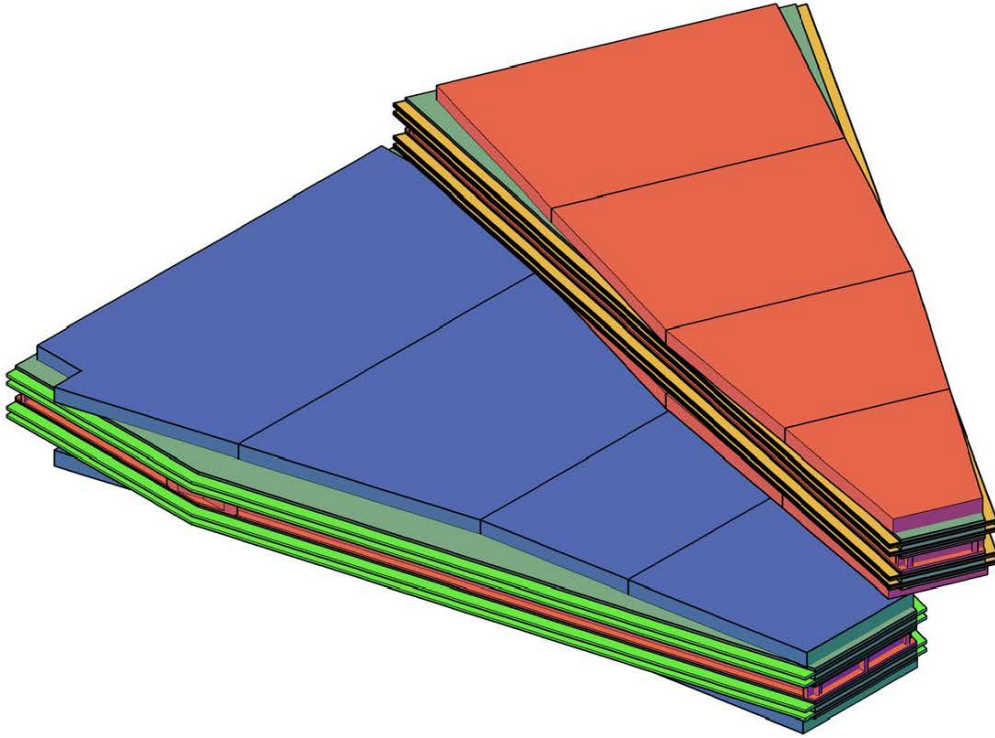


Figure 7: Sketch of sector configuration. Two Micromegas quadruplets (green and yellow) are sandwiched by sTGC quadruplets (red and blue). The small and large sectors are arranged such that they have a slight overlap. A particle therefore traverses at least 16 active detector layers, [ATLAS MUON Collaboration, 2013].

### 3.4 Design and Construction of Micromegas for the New Small Wheel

To construct the four gas volumes for a Micromegas quadruplet five light weight sandwich panels will be assembled. Such a panel consists of Printed Circuit Board (PCB) on both sides and has a core out of aluminum honeycomb. Each PCB can either have an active area for the drift cathode, or the anode readout strips. The two outer PCBs of a quadruplet will not belong to any active detector, hence they have just copper cladding as a passive shield<sup>4</sup>. The construction of such a panel will be described in section 3.4.3. For each module three different kinds of panels will be produced, distinguishable via the cladding of the PCB. A scheme of a cross section of a quadruplet is given in Figure 8.

Panel 1 and 5 only have the mentioned copper plane pointing outwards of the module. On the other side will be the layout for a cathode structure. Those panels are therefore called single drift panels. Panel 2 and 4 are double readout panels, since they embed the readout structure on their PCBs. In the center sits a double drift panel.

The dimensions of all four geometries are shown in Figure 9.

<sup>4</sup>For series production this copper layer is removed to reduce the weight of the NSW.

### 3 THE UPGRADE OF THE INNER ENDCAP OF THE MUON SPECTROMETER (SMALL WHEEL) IN ATLAS

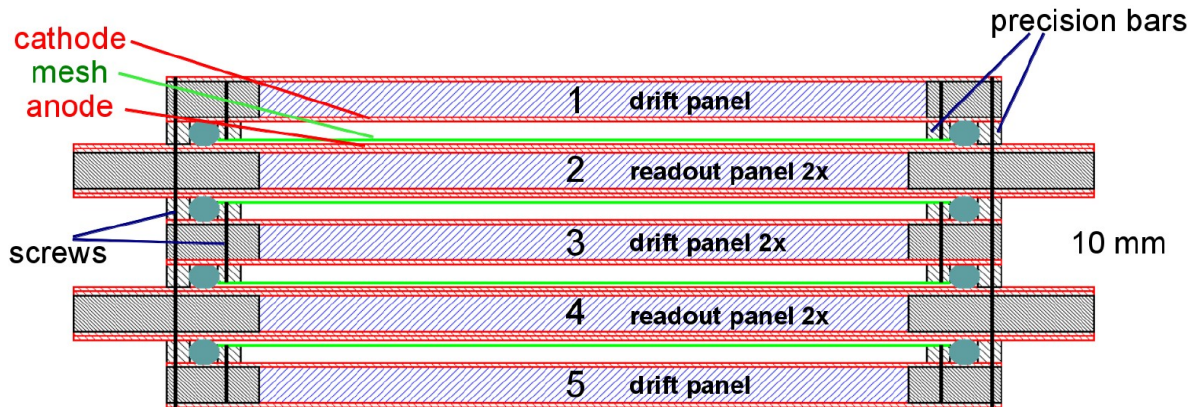


Figure 8: Sketch of a Micromegas quadruplet for NSW. Five sandwich panels are assembled to form the active volume of four Micromegas. Figure taken from [ATLAS MUON Collaboration, 2013].

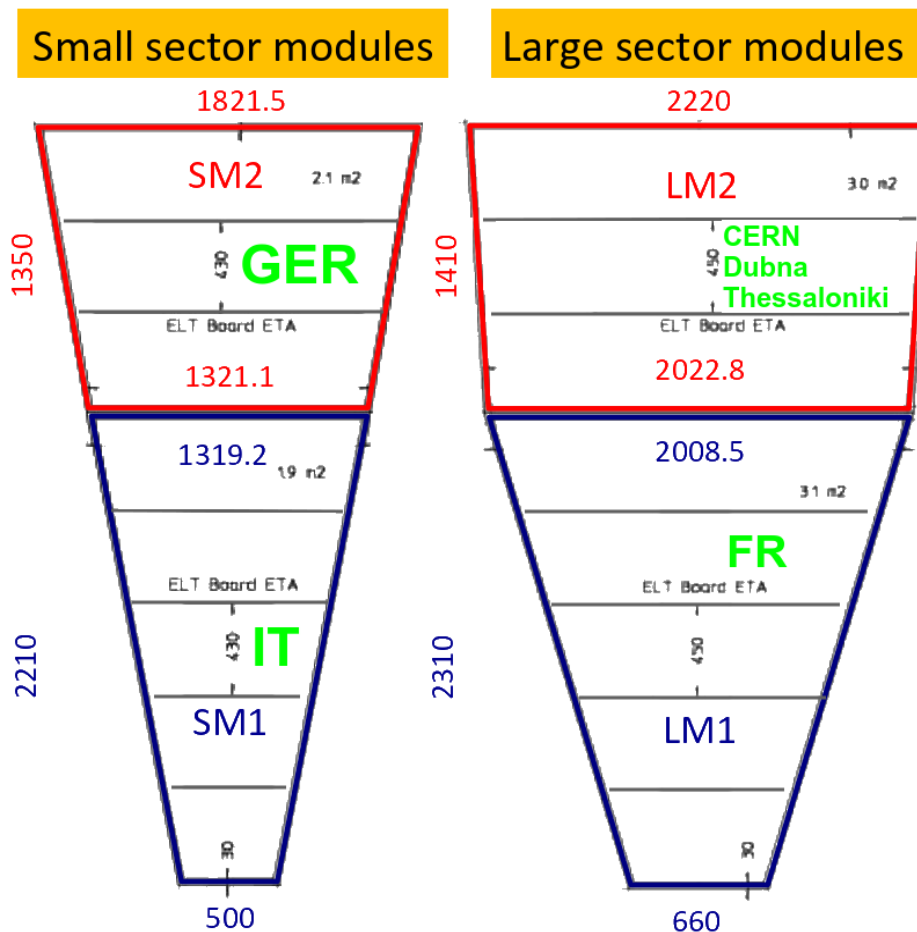


Figure 9: Dimensions of the Micromegas sectors. The horizontal lines indicate the boundary of the PCB sheets needed for one Micromegas layer. The SM1 and LM1 modules will consist of five PCB, whereas the SM2 and LM2 will be built of three PCBs. Figure taken from [ATLAS MUON Collaboration, 2013].

The horizontal lines in each module indicate that each layer cannot be made from one single PCB sheet due to size limitation of the PCB manufacturing. Thus in case of SM1 and LM1 five PCBs form the entire trapezoidal structure, while for SM2 and LM2 three boards are needed.

To the layout of a readout panel belong  $128 \mu m$  high pillars made out of coverlay as well. These pillars are located on top of the active area and ensure in a final assembly the correct distance between anode and mesh. The active area with the pillars is surrounded by a solid line of coverlay. The mesh, stretched with a tension of  $\approx 10 \frac{N}{cm}$ , will be glued to a mesh frame mounted on the drift rather than on the readout panel to allow easy access for cleaning of the narrow amplification gap. The area of the mesh slightly exceeds the area of the coverlay structure on the readout plane. Also mounted on the drift panel will be the gas gap frame, which ensures the correct distance of a readout and a drift panel. It has a height of  $5.20 \pm 0.03 mm^5$ , whereas the mesh frame has a height of just  $5.06 \pm 0.025 mm$ . When attaching drift and readout board, the mesh will be stretched over the solid coverlay line and lays perfectly on top of the pillars. The coverlay is the only contact between mesh and readout board. A scheme of this assembly is shown in Figure 10.

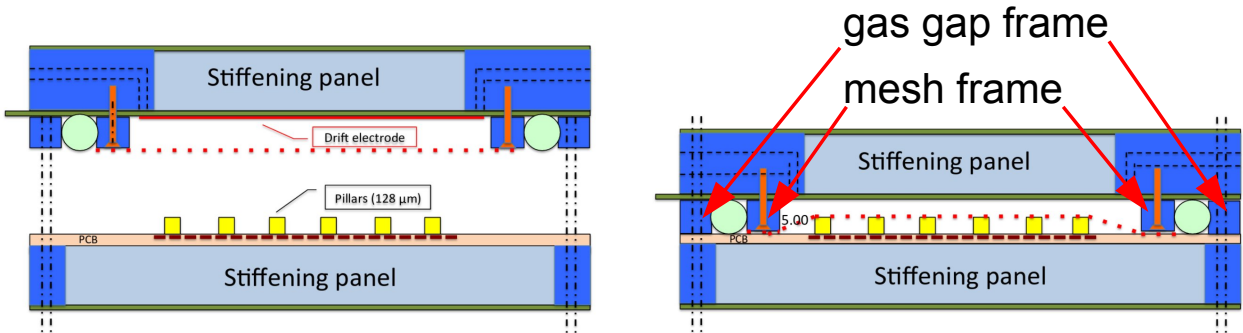


Figure 10: Scheme of Micromegas with sandwich panels in an open and closed stage, [ATLAS MUON Collaboration, 2013].

The highly sophisticated construction process described in the following chapters is mandatory, due to the high level of mechanical precision a quadruplet has to have in order to reach a momentum resolution better than 15 % for 1  $TeV$  muons. This requires, for example, a position resolution for each detector plane better 100  $\mu m$ . The whole set of tolerances is summarized in [Amelung et al., 2014] and [Bini et al., 2014]. Here just the strip non-parallelism limit of  $20 \frac{\mu m}{m}$  and the limit on the RMS of panel non-planarity of  $30 \frac{\mu m}{plane}$  whereas a plane for our module has a size of 2  $m^2$ , are mentioned.

<sup>5</sup>It is  $5.17 \pm 0.03 mm$  for the pre-series modules

#### 3.4.1 Idea of Using a Stiffback for Panel Construction

To reach these values two extremely planar surfaces are needed with an area larger than the size of a SM2 module. One is given by a  $1.7 \times 2.2 \text{ m}^2$  large granite table<sup>6</sup> with a planarity below  $6 \text{ }\mu\text{m}$ . The other will be a self made lightweight aluminum sandwich structure called stiffback, constructed similar to a Micromegas sandwich panel.

The idea is to suck two sets of PCBs to each of the mentioned surfaces in order to transfer their flatness to the boards. Gluing a light weight stiffening structure between the two PCB layers freezes this flatness.

The granite table has ten holes to apply the vacuum on its surface homogeneously. These holes are connected underneath the table to one vacuum pump. The stiffback will have a lot more holes connected to its inner volume formed by aluminum honeycomb. One valve at the side of the stiffback connects a second pump to its inner volume, evacuating the latter and sucking air through each of the holes on its surfaces. A micro perforation of the honeycomb allows for evacuation of the stiffbacks inner volume. Additional holes drilled through the entire honeycomb ensure a faster vacuum distribution and therefore a homogeneous air flow through the holes.

In the next chapters the construction of the stiffback will be explained followed by the gluing of a panel for the quadruplet.

#### 3.4.2 Stiffback

The procedure for the production of a stiffback is a two step gluing process. The idea is to suck an aluminum plate to the flat surface of the granite table, therefore copying its flatness to the plate and finally freeze this flatness by stiffening the plate before releasing the vacuum. In order to distribute the vacuum between the table and the aluminum homogeneously there are ten holes in the table and a  $0.180 \text{ mm}$  thin stainless steel mesh is placed between aluminum and granite. The borders are sealed with tape. Afterwards the plate is ground to ensure a good contact of the glue, which is distributed with a height of  $0.3 \text{ mm}$  over the plate, see Figure 11.

For the later handling of the stiffback it needs to be lightweight and has to have a possibility to mount handles at its side. An  $80 \text{ mm}$  high micro perforated aluminum honeycomb structures provides the desired stiffness combined with low weight [Pree, 2014]. The honeycomb is surrounded by an aluminum profile bar with a cross section of  $16 \times 80 \text{ mm}^2$ , see Figure 12. To ensure that the profile and the honeycomb are well glued to the aluminum plate, they have to be pressed towards the plate. This is done using the vacuum bag method. A frame with an elastic plastic foil is placed over the first side of the stiffback. By evacuating the volume between this frame and the granite table, the plastic foil presses the honeycomb

---

<sup>6</sup>The table was delivered by the company Oelze Aschaffenburg.

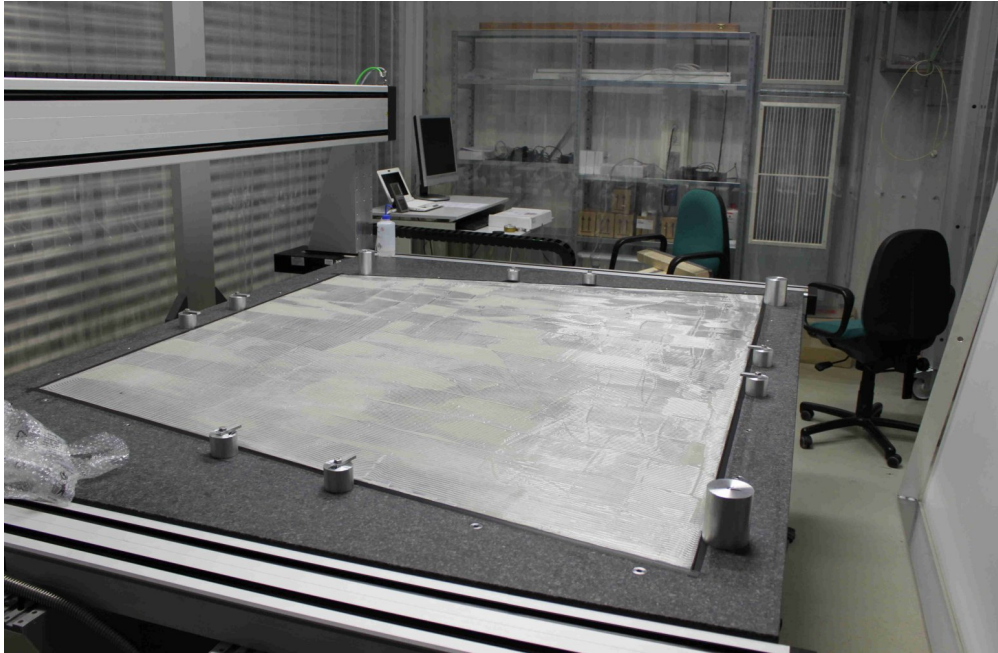


Figure 11: Preparation of first gluing step. After the aluminum plate is aligned using three high cylinders it is sucked to the flat granite table. Its face up surface is roughened and glue is dispensed on it with a height of  $0.3\text{ mm}$ .

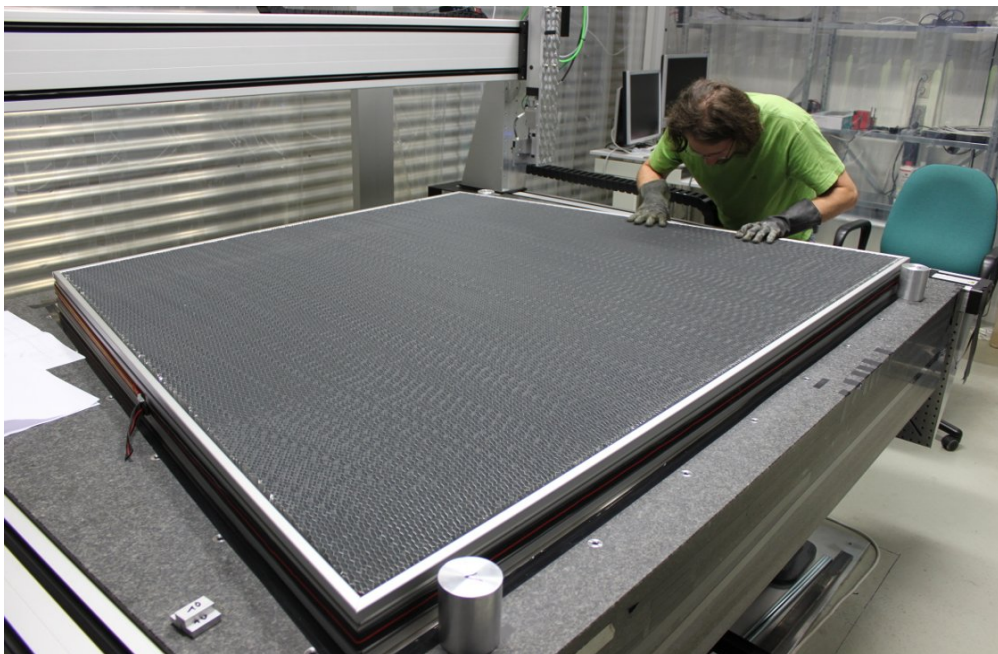


Figure 12: Placing the stiffening structure on the aluminum plate. One sheet of micro perforated aluminum honeycomb ( $8\text{ mm}$  cell size,  $80\text{ mm}$  high) is placed into the glue. For further stiffness and an easy handling of the final product a frame made of aluminum profiles ( $16\text{ mm}$  thick,  $80\text{ mm}$  high) surrounds the honeycomb.

### 3 THE UPGRADE OF THE INNER ENDCAP OF THE MUON SPECTROMETER (SMALL WHEEL) IN ATLAS

---

and the profiles into the glue. To protect the foil from the sharp edges of the honeycomb, a wooden plate is placed in between. The vacuum in the bag will be released after twelve hours of glue curing. Figure 13 shows the stiffback under the vacuum bag during gluing. Here the white area is the wooden plate having the same dimensions as the stiffback underneath.

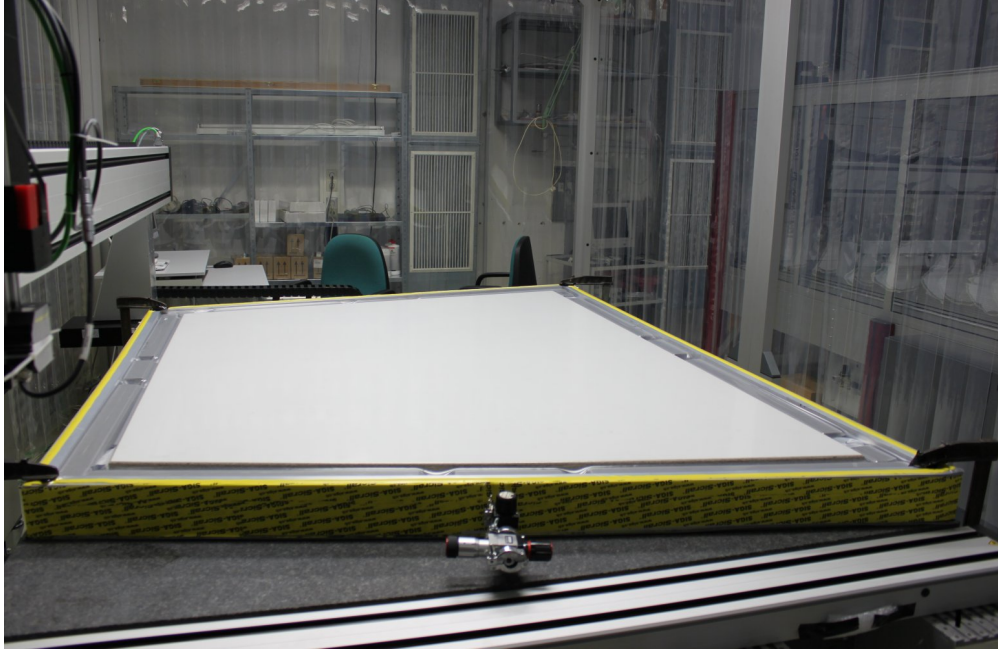


Figure 13: Vacuum bag method for the first step of stiffback gluing. During the curing of the glue the honeycomb and the frames are pressed into the glue using a vacuum bag technique. A frame with a tightly sealed plastic foil is placed over the stiffback. The volume inside this bag can be evacuated and therefore atmospheric air pressure is applied on top of the honeycomb. In order to protect the foil of the vacuum bag from the sharp edges of the honeycomb, a wooden plate separates both surfaces from each other.

For the second step the first half of the stiffback is removed and another sheet of aluminum is sucked to the table. Again the surface not facing the table is ground and glue is distributed. Afterwards the first half panel is placed upside down into the glue. Lead bricks press the structure into the glue, but in contrast to the vacuum bag the bricks are removed after 30 *min*. The first step ensures already a rather flat structure and the bricks should only provide a good connection before the glue cures. During curing the system should experience as few stress as possible in order not to freeze this stress, which would cause deformation after releasing the vacuum.

Compared to the panel gluing described in chapter 3.4.1, surfaces are only sucked to the granite table in case of stiffback construction, meaning that just one flat reference surface is used. This results in one perfectly flat surface, while the other side can be slightly deformed. In this case the following happens. Assume that the product of the first gluing step has not reached its full stiffness yet. Still the transfer of the granite table's flatness to the aluminum

plate worked, but it can still be deformed without much effort. Pressing this product to the second aluminum plate, which is sucked to the table, as well as internal stress in it, will deform the surface of the first gluing side slightly. But now a full sandwich panel is constructed with the desired stiffness, hence the second aluminum plate will have an extremely planar surface which can not be deformed easily. This side will be used for the panel construction, which will be shown next.

### 3.4.3 Gluing of SM2 Micromegas Panels

The concept of a lightweight sandwich structure is equal for Micromegas panels and the stiffback, hence the construction is very similar. Still there are two main differences compared to the stiffback construction. The first is the mentioned use of the stiffback for the second gluing step. As summarized in chapter 3.4.1, the second gluing side of the panel is sucked to the granite table, while the product of the first half panel is sucked to the stiffback, in order to ensure a good flatness on both sides, see Figure 14.

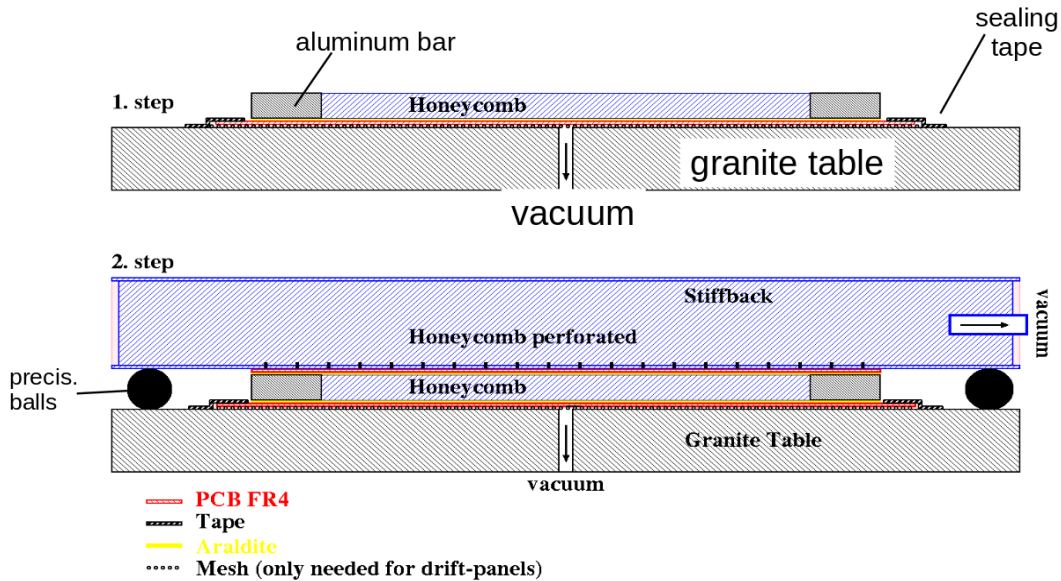


Figure 14: Scheme of two step gluing process of panels using a stiffback.

The other difference is the use of three boards forming each side of the sandwich structure, while for the stiffback one large aluminum plate is used on both sides of the sandwich. In order to have the strips on the readout panels parallel, these three boards need be aligned very precisely to each other as well as to the boards of the other side. A procedure to do the alignment is described in [Müller, 2015], while important steps are mentioned below. Two precise washers out of brass, one with a round hole and one with an elongated hole, are glued to the back side of each board. The position they are glued to is given by a crosshair on the front side of the PCB. This crosshair is created together with the strips during the

### 3 THE UPGRADE OF THE INNER ENDCAP OF THE MUON SPECTROMETER (SMALL WHEEL) IN ATLAS

---

photolithographical and etching process of the readout PCB, hence having a well defined position with respect to the readout strips on the PCB. All three boards are now placed on the granite table and are roughly aligned, which is sketched in Figure 15.

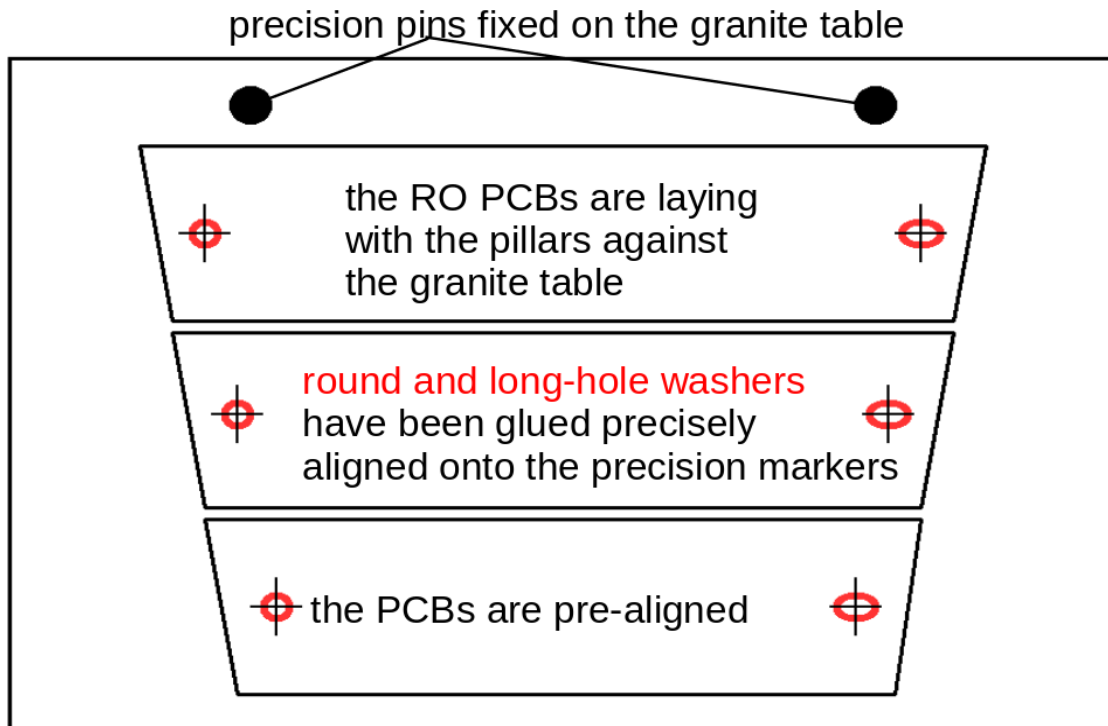


Figure 15: Scheme of readout board alignment. Round and elongated hole washers are glued precisely onto well defined positions on the boards. This gives a precise mechanical handling of the boards and thus a highly accurate positioning of the strips is possible.

A precise external alignment frame with six pins sticking out can now grab the six washers, aligning the three boards and therefore the strips on the other side as well. This frame has in addition one line-shaped and one V-shaped brass spacer. Two stainless steel precision cylinders mounted on an external reference frame which is fixed on the granite table, are the reference for the two spacers on the alignment frame. Touching both cylinders the alignment frame and with this also the three boards are positioned and vacuum can be applied to the boards. This fixes them on the table and the alignment frame can be removed. Two precision brass spacers are glued to the largest of the three boards, one having the form of a "V", while the other is straight as a line. Due to the line-shape this kind of spacer is called "L" shaped, see Figure 16.

During gluing each is touching one of the precision cylinders of the reference frame. They are pressed towards the steel pin mounted with a rectangular guiding. With both spacers a panel can be positioned with a high reproducibility on the same place as it was done with the alignment frame before. The precision pins are located axial symmetrically according

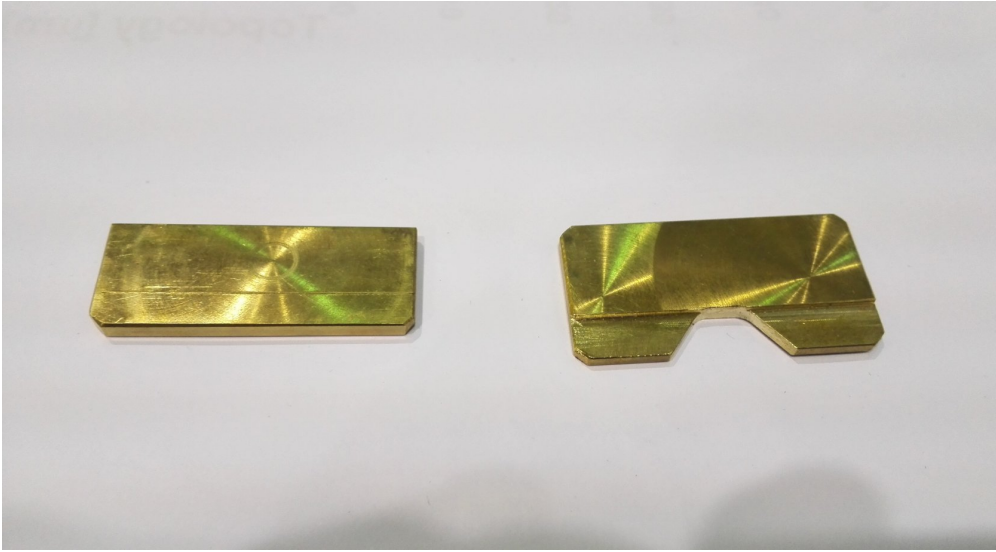


Figure 16: Line (L) and V shaped brass spacers for global positioning of the boards.

to the center of the trapezoid and a positioning upside down can be done with the same precision. A photograph showing the gluing of the spacers is given in Figure 17.

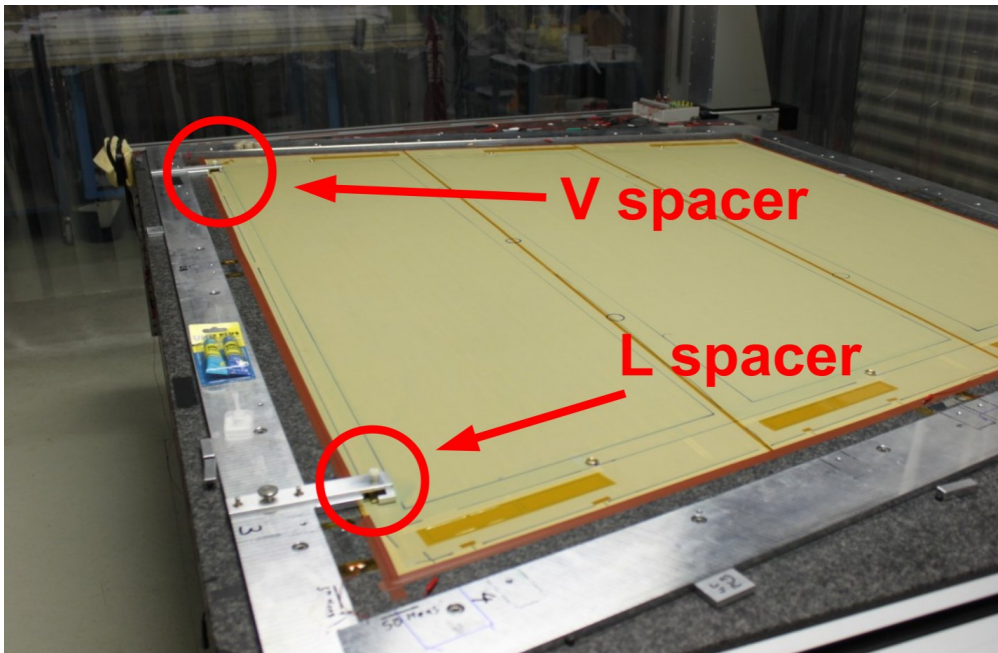


Figure 17: V and L spacer are glued to the largest board touching the same precision cylinders as the alignment frame before.

After the glue of the two spacers is cured the construction follows the steps for the stiffback's first side, distributing glue in a height of  $0.3\text{ mm}$  and placing frames and honeycomb on the boards. For this side also the vacuum bag technique is used.

For the alignment of the three PCBs of the second side, the same precision pins are used as

### 3 THE UPGRADE OF THE INNER ENDCAP OF THE MUON SPECTROMETER (SMALL WHEEL) IN ATLAS

---

before, to position everything exactly at the same place as the first side. The first half panel is sucked to the stiffback, as shown in Figure 18. Here the inner structure of a panel can also be seen which is slightly more complex than for the stiffback with just honeycomb and a frame. Details on this can be found in the Micromegas construction manual, [Jeanneau and Iodice, 2015] and in the technical design report of the NSW, [ATLAS MUON Collaboration, 2013]. The stiffback is now lowered onto the second set of PCBs which is already covered

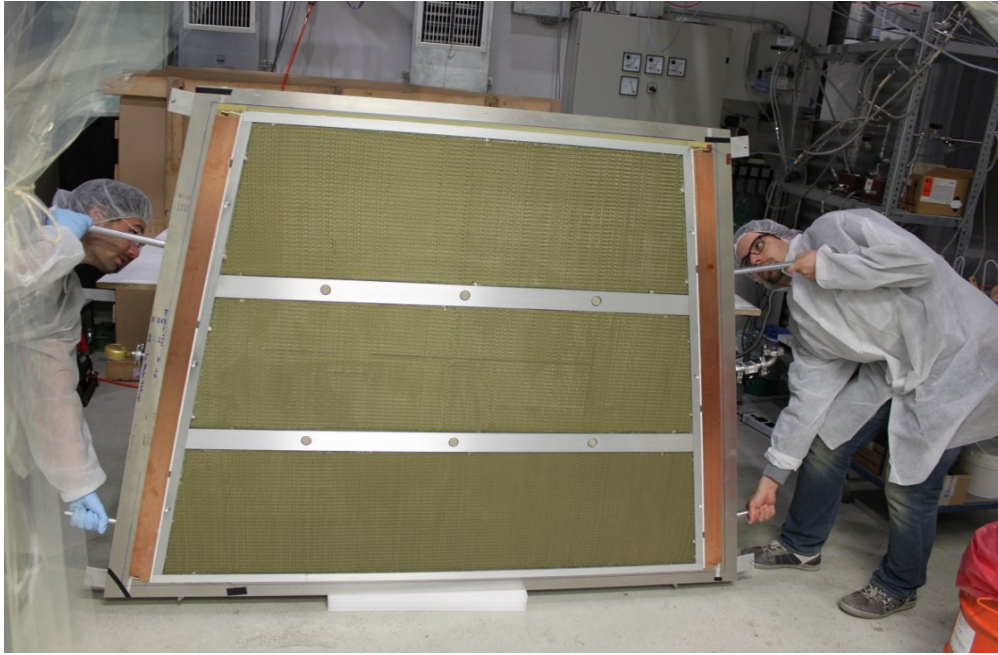


Figure 18: After the glue is cured the first side is released from the granite table and sucked to the stiffback.

with glue. Hereby and for the entire gluing the "V" and "L" shaped spacers are touching the pins on the outer frame to have the first and second set of PCB exactly aligned on top of each other. To ensure that top and bottom layer are precisely parallel and the panel has a well defined height, there are eight precision distance pieces between stiffback and granite table. They are located at the four corners and at the center of each edge of the trapezoid. The contact between stiffback and those eight distance pieces, as well as between "V" and "L" spacers to the pins is monitored using their Ohmic contact. For each of the ten contact areas a LED signals an electrical contact. In the beginning lead bricks right above the distance pieces press the stiffback downwards. After all LEDs start shining, the lead is removed and the glue can cure.

After a few test gluings of panels, with improving quality, it was realized, that the stiffback is not rigid enough and makes a sag of about  $0.15 \text{ mm}$  in the center, which is copied to the surface of the first gluing side of the panel, see figures 39 and 46. To compensate for this sag a bridge of aluminum profiles was constructed to pull the stiffback and therefore also

the first side of the panel upwards during the curing process of the glue. After lowering the half panel onto the second gluing side, the aluminum bridge is placed on the stiffback right above the positions of the distance pieces at the corner. An aluminum plate mounted in the center of this structure can now be attached to the stiffback using vacuum. This plate can be screwed upwards, and therefore compensates for the sag of the stiffback. This sag was determined to be  $0.150\text{ mm}$ , hence the plate has to be screwed upwards by  $0.150\text{ mm}$ , which is monitored with the tactile distance sensor Sylvac Dial Work [Sylvac, 2016]. Figure 19 shows an image of the correction tool on the stiffback during the curing process of the second panel production step.

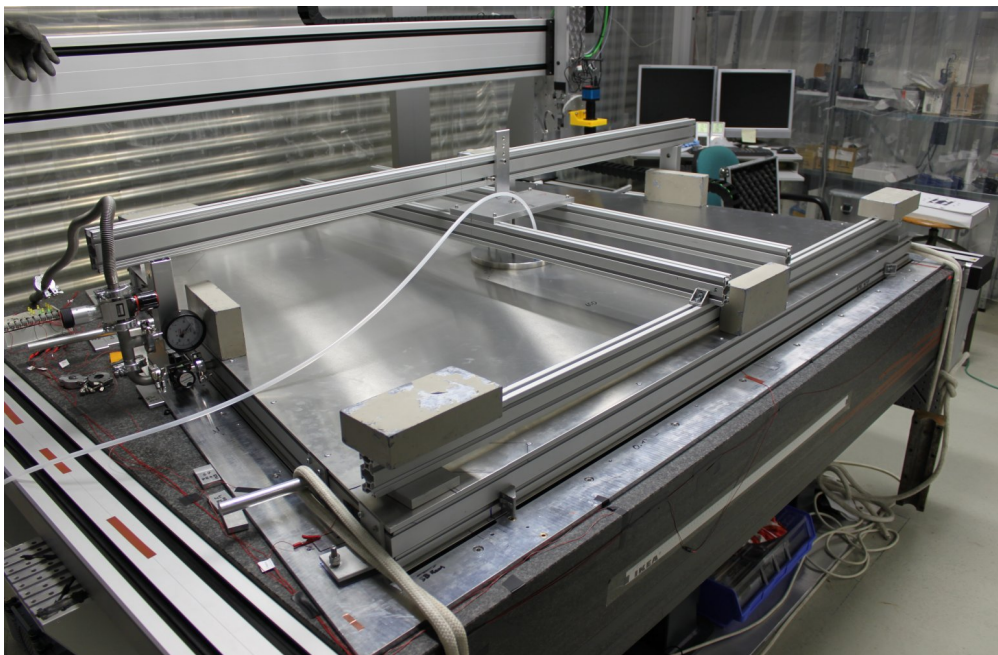


Figure 19: To compensate the sag of the stiffback a bridge of aluminum profiles lays on four of the eight contact points between stiffback and granite table. With this tool the center of the stiffback can be lifted and the height can be monitored. A LED board in the rear left indicates whether a contact between the eight distance pieces and the stiffback or the V and L spacer and the precision cylinder is given.

The next step would be a quality control of the produced panel including planarity measurements and control of the alignment results. The following chapter describes the techniques developed for fast and precise topological measurements of planar structures.

## 4 Setup for Topology Measurements at LMU

As discussed in chapter 3.4 a key feature of the Micromegas detectors for the NSW are the precise planar and parallel surfaces. After manufacturing the panels with great care, the quality of their surfaces needs to be controlled. This step is done with a Coordinate Measurement Machine (CMM). Using a CMM offers two ways to measure a surface:

The first possibility would be a tactile sensor which is moved to the object and then slightly touches it. This sensor gives a trigger to store the current coordinates of the machine. A highly accurate knowledge about the absolute position of the machine for every space point is mandatory. Such devices have the advantage that three-dimensional objects can be measured very well, but they are rather expensive given the size required for the NSW Micromegas.

A second approach uses the fact, that in the case of Micromegas only an extremely flat surface will be measured, where tiny deviations from planarity are of interest. A sensor which measures the distance to a certain object is moved by the CMM to the position where the measurement should be done and reads out the distance to the object and hence for a flat surface its local height. Moving in two dimensions over this  $2 - 3 \text{ m}^2$  sized surface and measuring its height at several thousand points provides a topology map of it. If the CMM moves perfectly parallel to this surface, small deviations in the height of the object can be measured, but since this is not the case the setup has to be calibrated against the flat reference surface of the granite table first. After calibration, this procedure allows for a high precision topology measurement of rather flat structures. Compared to the first method, this one is much cheaper, but is limited to a two dimensional scan of surfaces which is exactly the task for the quality control of the panels. A photograph of the machine mounted on the table is shown in Figure 20.

In this thesis only the second approach is discussed. Still in the collaboration building the SM2 module also a setup of the first type is in use, with which for example the alignment frame being a three dimensional object of interest had been measured. In the beginning of the study also test panels and stiffbacks have been investigated with both machines to get a feeling of the performance of the system in Munich.

In the next chapters the strategy, with which the machine and the sensors are calibrated is described, followed by the introduction of the two different types of such distance sensors available for this setup.

### 4.1 Principle Idea of Fast and Precise Topology

The setup in Munich contains a CMM which gets its position in space from an angle encoder for each axis, providing a precision of a few  $\mu\text{m}$ . But this accuracy assumes that the axis

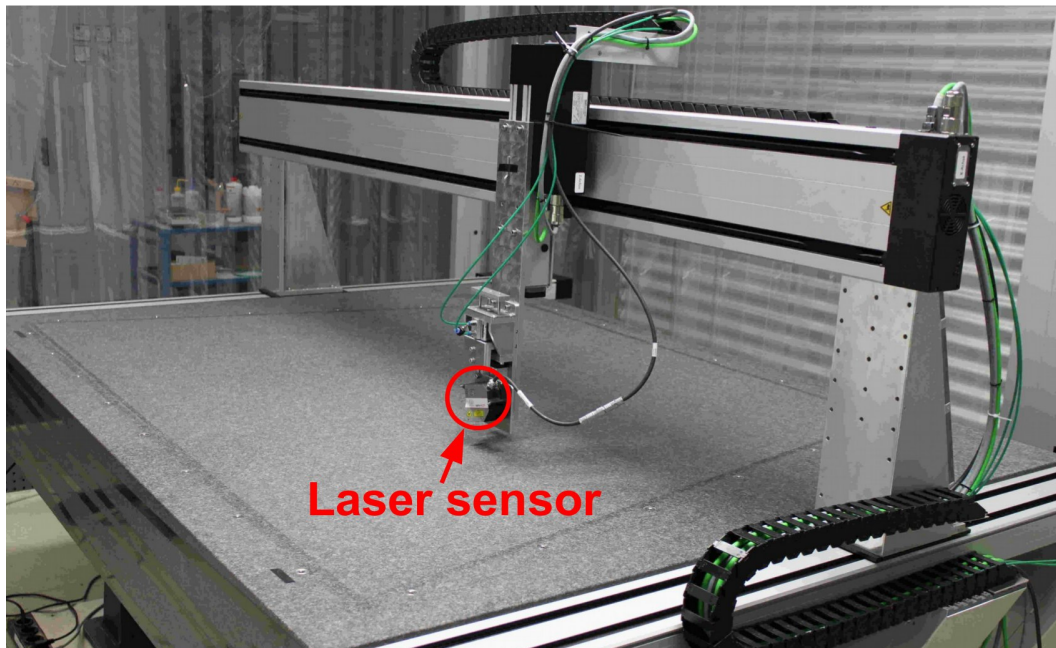


Figure 20: Photograph of the CMM system in Munich. A laser distance sensor is currently mounted.

moves on a perfectly straight line. Deviations from the position recorded by the encoders due to gravitational bending or misaligned guiding rails are not corrected or even realized by the machine itself. Those deviations have been determined to be up to  $0.5\text{ mm}$ , dominated by the gravitational sag of the  $2200\text{ mm}$  long crossbar. Still the reproducibility provided is much better, shown in chapter 5. The focus of the method, described in the following, lies on this high reproducibility of the machine.

The CMM is used as remote controllable translator. A sensor mounted to it is moved to the point where the distance should be measured. Performing lots of such single point measurements, the surface of an object of interest is scanned. For such a scan the value of the Z-coordinate is adjusted to a height suitable for the current sensor before starting the measurement and it must not be changed during the scan. In chapter 4.2 and 4.3 a definition of a suitable height is given for each type of sensor available. During the rest of the measurement, the CMM moves only in X and Y. A measurement with a large amount of data points, hence a small distance between those points in X and Y direction, is called a high granularity measurement.

Since sandwich panels for the Micromegas are built on a granite table large and precise enough for the construction, the quality control also takes place here. With its planarity of better  $6\text{ }\mu\text{m}$  the table is considered as perfectly flat, hence the mentioned deformations of the CMM are measured by scanning the tables surface, since all deviations from planarity must originate from the machine and not from the table. Each topology scan done with this

machine will include those deformations in addition to the non planarity of the measured object. Subtracting the granite measurement from all other scans eliminates the dependency of the CMM resulting in the true topology map of the surface measured.

To be more exact, only the effects on the Z-coordinate are eliminated, while displacements in the X-Y plane are remaining. But since only a high accuracy in Z-coordinate is required in this case, it does not matter if X or Y are displaced by a few tenth of a millimeter.

In principle each measurement consists of two sets of data. In a first scan the granite surface is measured, which is done with high granularity. What exactly "high" means is explained in a moment. The second set of data consists of the measured distances to the object of interest, which are called data points in the following. In the analysis of the topology of a certain object, the distance from a data point  $P_{test}$  to all reference data points  $P_{ref,i}$  in the X, Y plane is calculated for each data point. The reference point  $P_{ref, min}$  with the smallest distance to  $P_{test}$  will be used to calibrate the measured distance value at  $P_{test}$  according to:

$$Z_{true}(P_{test}) = Z(P_{ref, min}) - Z(P_{test}) \quad (4.1.1)$$

The smaller the distance between measurement and reference point is, the better will be the calibration of the CMM deformation. The ideal situation would be to measure the object's and the granite table's surface at exactly the same points. But since objects with different sizes and different granularities will be measured, this means that one would have to perform a reference measurement for almost every object of interest. In order to have just one reference, the granite table was scanned with high granularity resulting in a pitch of the reference data points of  $\approx 5 \text{ mm}$ , compared to the lower granularity of data points with up to  $20 \text{ mm}$  spacing.

## 4.2 Tactile Distance Sensors

The first sensor to be described is a classical tactile sensor. For the measurements done in Munich the Sylvac Dial [Sylvac, 2016] with a measurement range of  $12.5 \text{ mm}$  is used. A picture of this sensor in use is shown in Figure 21.

The sensor consists of a housing and a needle which can move just in the up-down direction. A spring inside the housing pushes the needle continuously downwards. The electronics inside the sensor measures how much the needle is pushed upwards with an accuracy of  $3 \mu\text{m}$ . In this setup the Sylvac sensor is mounted to a CMM with a pneumatic translator in between. The translator can move only parallel to the Z-coordinate of the CMM, which points perpendicular to the surfaces to be measured. It has two mechanically fixed end positions between which one can switch remotely.



Figure 21: Picture of a Sylvac dial mounted on an aluminum bridge to monitor the correction of the stiffback sag during panel gluing.

For a topology measurement of a panel, first the Z-coordinate of the machine is adjusted. On the one hand the sensor must not touch the panel at all, while the pneumatic translator is in its upper position. The lowering of the sensor towards the surface is done only with the pneumatic translator, until it reaches its lower position, which on the other hand means, that the Z-axis has to be close enough to the surface to enable a contact between needle and surface. After this adjustment the Z-coordinate must not be changed during a measurement. In a topology scan first the machine moves to a point where the distance should be measured with the translator in its upper position. After arriving at the desired position, the pneumatic translator moves slowly towards its lower fixation, the needle position is read out by the sensor and the data is stored in a table for later analysis. The translator now moves up again and the machine is ready to move to the next point on the surface.

Using such a device for topology scans has some advantages, e.g. its price is more than a factor of ten lower than for the laser distance sensors described in chapter 4.3, but more important is their reliable measurement value which will be described in chapter 5.2. Nonetheless they suffer in this setup of important disadvantages compared to the laser sensors. A surface scan takes about three times longer than the one with the laser, since for the latter the pneumatic translator is not used which saves time. Additionally, the panels consist of sensitive surfaces which may be damaged with a tactile sensor.

The next chapter will present the concept of laser triangulation giving an alternative to classical distance sensors.

### 4.3 Laser Distance Sensors

Laser triangulation is a modern development for distance sensors. Such devices do not touch the surfaces to be measured, which is of great importance for sensitive structures.

The principle of laser triangulation is shown in Figure 22.

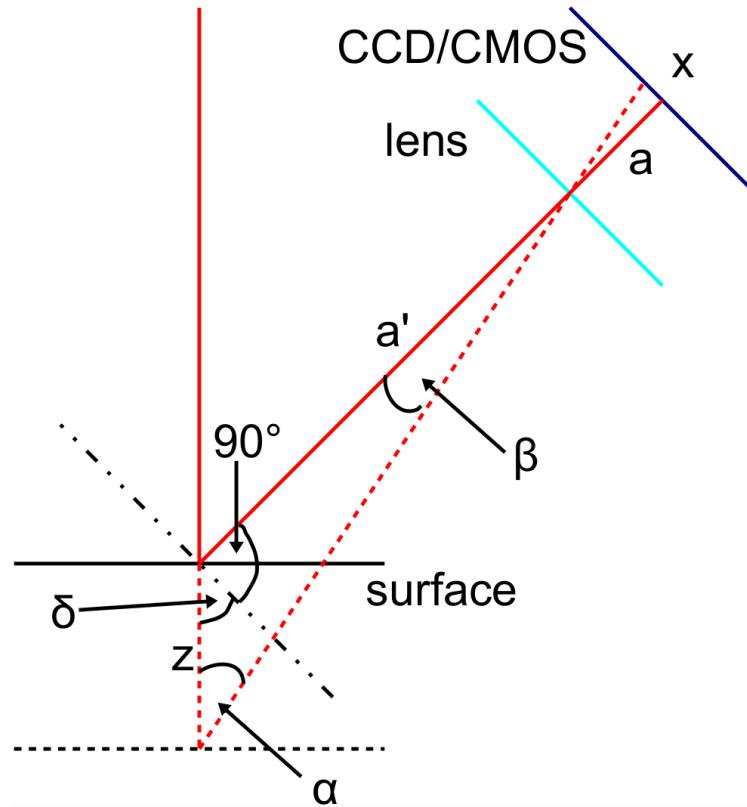


Figure 22: This picture shows a scheme of the triangulation method. A perpendicular laser beam is coming from the device and is reflected by a surface. The reflected light is focused on a position sensitive CCD or CMOS chip inside the sensor. If the measured surface is now on a different height, in this case lower, then the reflected laser light will be focused on a different point on the chip. The distance  $x$  between the points on the chip is now directly related to the change in height  $z$  of the surface.

Inside such a device a laser source emits its light perpendicular to the sensor. The beam from the sensor hits the surface to be measured and will be back reflected. A lens focuses the reflected beam on a certain point on a position sensitive CCD chip. For a surface at zero height, the length  $a'$  from the surface to the lens and  $a$ , the distance between the lens and chip, are known constants. Also the angle  $\delta$  between lens plane and the laser beam is known for this particular case, see Figure 22.

If the surface to be measured has a different height, which is shown with a black dashed line in Figure 22, the laser beam, red dashed line, will now be focused on a different position on the chip. It is now possible to find a relation between the new parameters in this setup and

the old ones in the case of a surface at zero height.

For example for the angle  $\alpha$  between the incident and reflected laser light the following relation holds:

$$\alpha = 90^\circ - \delta - \beta \quad (4.3.1)$$

This equation contains the angle  $\beta$  between the old and the new reflected beam. It can be related to the length  $x$  between old and new focus point on the chip. This distance is measured by the electronics in the sensor.

$$\tan \beta = \frac{x}{a} \quad (4.3.2)$$

Finally one can use the sine theorem to connect the height difference between old and new surface  $z$  to the other calculated parameters.

$$\frac{\sin \alpha}{a'} = \frac{\sin \beta}{z} \quad (4.3.3)$$

Using 4.3.1 and 4.3.2 to eliminate  $\alpha$  and  $\beta$  from equation 4.3.3 and applying some trigonometric identities, one obtains a formula which transforms the measured distance  $x$  on the chip to a height variation  $z$

$$z = \frac{a'}{\frac{a}{x} \cos \delta - \sin \delta} \quad (4.3.4)$$

A major problem with a laser based device is the possibility, that the laser penetrates the surface of the measured object. This happens if the surface is at least semi transparent, which is the case for the panels as well as for the granite table, since it has crystal enclosures, which are not opaque to the laser light. The light can then be reflected at a lower plane which gives a wrong distance. There are two possibilities to counteract this effect.

On the one hand some companies offer high precision devices with a blue laser beam in comparison to standard red lasers. Blue light has a shorter wavelength than red light, therefore it does not penetrate the surface as much before it is reflected.

The second method to reduce a surface penetration is to incline the sensor. In this case the light does not hit the surface to measure perpendicularly but under a certain angle. Hence the amount of specularly reflected light is increased, which happens dominantly at the surface itself.

The sensors available at LMU Munich are an opto NCDT 2300-20 and an opto NCDT 2300-2 BL by microEpsilon [MicroEpsilon, 2016]. Both are capable of inclined use, while the first one mentioned has a red laser (670 nm) and a height range of measurement of 20 mm and the second one uses a blue laser (405 nm) with 2 mm measurement range. Both sensors have a theoretical resolution of 0.3  $\mu$ m, but this value can not be reached using them with the CMM setup available in Munich. A picture of both sensors can be seen in Figure 23.

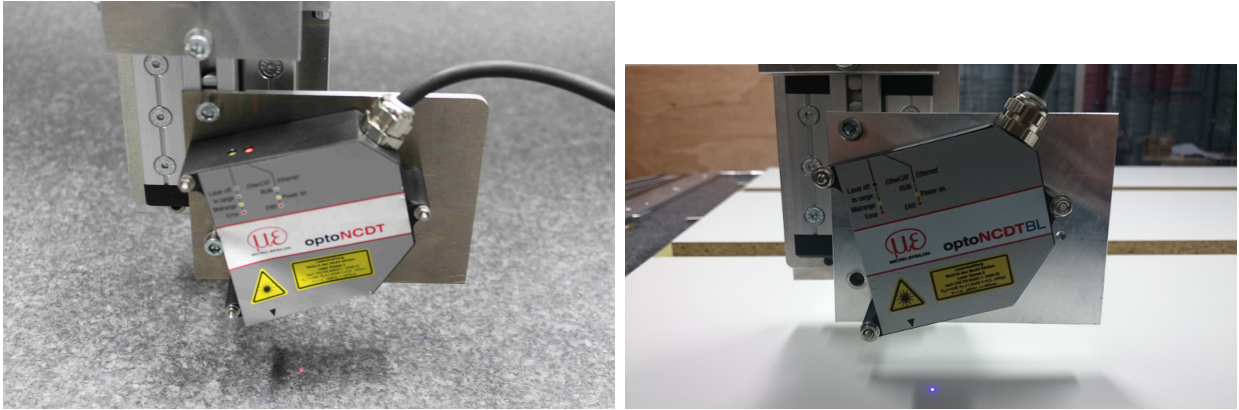


Figure 23: Two laser sensors from microEpsilon in use. Left: opto NCDT 2300-20, red laser beam ( $670\text{ nm}$ ),  $20\text{ mm}$  measurement range. Right: opto NCDT 2300-2BL, blue laser beam ( $405\text{ nm}$ ),  $2\text{ mm}$  measurement range.

Besides the wavelength of the laser also the measurement range is different. This value defines the distance in which the surface has to be for a valid measurement. Each laser has two LEDs on top. While the first one is just an indicator whether the device is ready to use, the second shows if the object has a proper distance. Therefore it can switch between three colors:

- **Red:** The object is either too close or too far away
- **Green:** The object is inside the measurement range
- **Orange:** The object is in the center of the measurement range

The laser of such a sensor is focused to the center of its measurement range, with the beam spot having its smallest diameter there. Since during the construction process and its pre-series also objects with a very fine structure are measured, a beam spot as small as possible is of high interest to investigate the smallest structures on those surfaces. Away from the focus point the beam spot increases and with this a larger area will be measured in one point and therefore this area gives just one distance value. This increases the chance to contaminate this measurement with structures of different height like pillars or scratches. The Z-coordinate of the CMM is adjusted such, that the surface to be measured stays as close to the focal point as possible during the scan to minimize the area of the beam spot. Also here this adjustment is done in advance of the scan and must not be changed until the measurement is finished. According to the data sheet, [MicroEpsilon, 2016], a resolution below  $1\text{ }\mu\text{m}$  is achievable, which is in our case not reachable, since the inaccuracies of the CMM sets a limit to a few micro meters.



## 5 Topology Studies Using a Distance Sensor on a CMM

During the construction process, the CMM will be used as tool for quality control measurements. Since this needs a high precise tooling, the performance of the CMM system needs to be demonstrated. For this, the granite table is studied, since its surface is needed as reference as described in chapter 4.1. After the reference measurements for the granite table have been performed, first some objects with known surfaces have been investigated followed by detailed studies of the stiffback and sandwich panels.

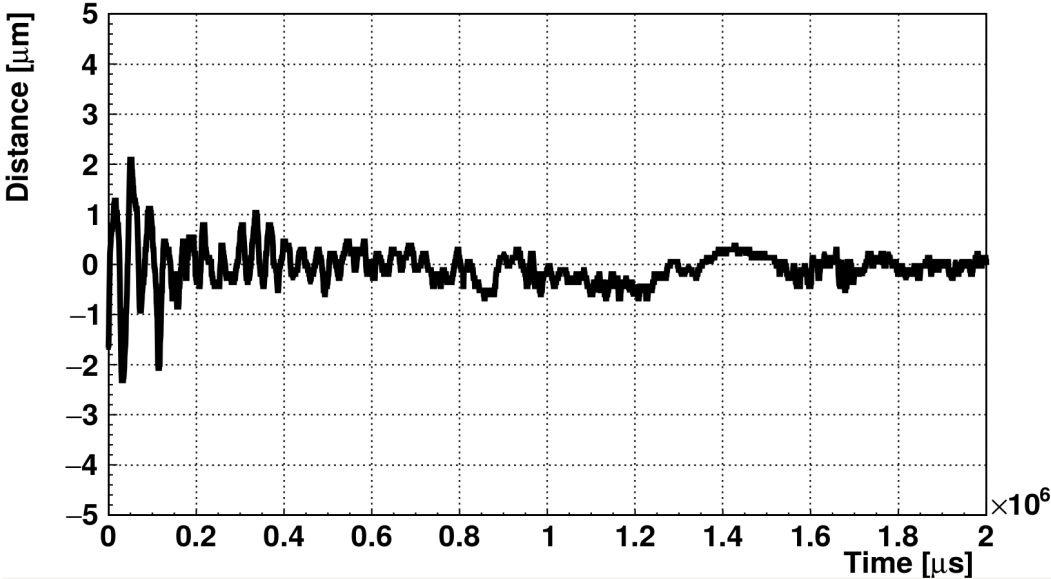
As mentioned, one reference measurement of the table with a point to point distance in X-Y plane of  $\approx 5 \text{ mm}$  is sufficient for all further topology scans of panels, as long as the setup remains unchanged and the granularity of such scans is more coarse than the reference measurement. In the next chapter the performance of the setup is investigated by scanning small pieces with a point spread of up to a few  $\mu\text{m}$ , thus special reference measurements with the same granularity are performed.

### 5.1 Performance of the Setup

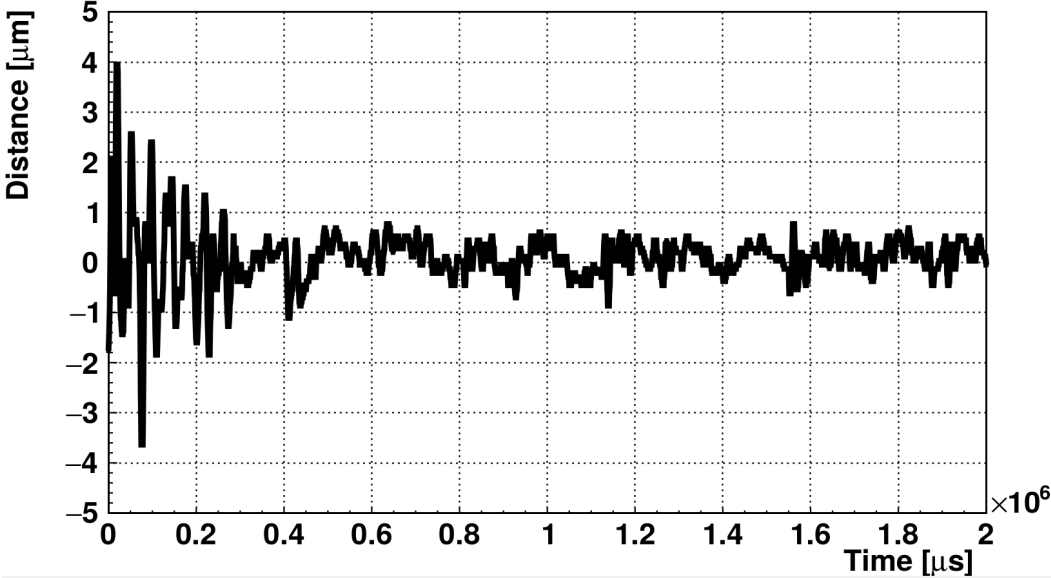
The measurement of a single point contains two stages, first the movement to this point, second the measurement of the distance. The movement speed of the CMM is adjustable, but not the acceleration. It is quite high, especially the deceleration of the machine, before a point is reached. This rather sudden stop brings the system into vibration and can result in an inaccuracy of the measurement, because the sensor is mounted on the long lever arm of the  $Z$  axis. Therefore it is mandatory to wait a certain amount of time after reaching the point to be measured, letting the vibration decay. The time for this decay is estimated by reading out the sensor continuously with a frequency of  $30 \text{ kHz}$ . The machine was moved with a speed of  $200 \frac{\text{mm}}{\text{s}}$  and then stopped, while the sensor readout started with the beginning of the movement of the CMM and stopped  $2 \text{ s}$  later, see Figure 24.

The measurement was performed once close to the fixation of the CMM to the granite table and once in the center of the table. The amplitude of the vibration is higher for the central measurement, since this region is far away from the CMM mounting, where the structure is more rigid. Also the decay happens with  $\approx 0.3 \text{ s}$  slightly more slowly in the center than at the border with  $\approx 0.2 \text{ s}$ . For further measurements the pause between arrival of the machine and start of the distance measurement is set to  $0.3 \text{ s}$  for the entire scan.

Before granite table, stiffback and panels can be investigated a feeling about the resolution achievable with the setup is given. For this objects of known topology are laid on the granite table: three aluminum profiles machined on a CNC milling machine in the mechanical workshop and an one Euro coin. Starting with the aluminum profiles, in Figure 25 the drawing can be seen according to which the aluminum is machined.



(a) border position



(b) middle position

Figure 24: Study of CMM vibration after abrupt stopping for a point close to the border of the granite table, where the machine is fixed, Figure 24a, and a point in the center region, Figure 24b. In the latter case the machine and hence the sensor itself is as far away from any fixed mounting point as possible. Therefore the vibration is more intense in this case, but both times after 0.3 s the vibration is over.

To improve the quality of the machining not one large tool was milled, but the three step profiles were produced independently, indicated by the red separation lines. The measurement with these profiles happened slightly different. The distance sensor normally waits until the CMM reached its destination and waits 0.3 s. In this scan a continuous measurement was

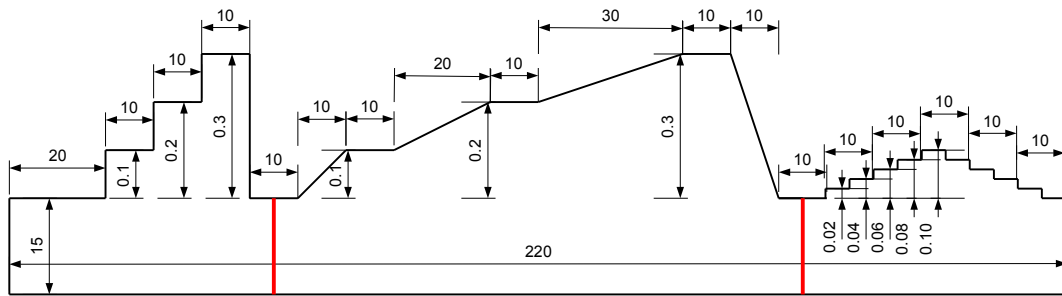


Figure 25: Drawing of an aluminum step profile. For increased precision this piece is split into three parts indicated by the red lines. Measuring such a piece should give a feeling about the resolution of the setup.

started, reading out the sensor with a  $5 \text{ kHz}$  rate. This happens while the CMM moves with a velocity of  $5 \frac{\text{mm}}{\text{s}}$  from start to end of the profile, meaning that every  $\mu\text{m}$  a distance measurement was performed. As a reference the same track was measured on the table. In contrast to the table, aluminum is much more reflective, resulting in mis-measurements when hitting little scratches or bulges, reflecting a significant amount of light to regions on the sensor CCD not correlated to the distance to the aluminum. Also the CCD can saturate due to the high amount of reflected light. Such effects have been studied by [Kolberg, 2016] and are briefly summarized in appendix A. For SM2 quality control the surfaces are not reflective enough that the CCD of the sensor saturates<sup>7</sup> and also scratches will not produce any systematic mis-measurements since they are very rare. What will result in sort of a mis-measurement are the pillar structures which will be hit accidentally in a surface scan. As shown later those structure are easily identified and distinguishable from the rest of the surface scan.

The measured profile of the first aluminum piece is shown in Figure 26.

The  $0.1 \text{ mm}$  high steps are perfectly visible and match exactly with the drawing. The broad structure on each step of about  $10 \mu\text{m}$  can have two reasons, first the machine is in movement during the measurement and second little scratches on the profile causing an irregular reflection of the beam. A measurement with the granite table will show that the difference from one point to the next, which are close together on a flat object, is in the order of  $5 \mu\text{m}$ , see chapter 5.2.

Inclined paths, as they are in the design of the second profile, are also well measurable surfaces for the setup, see Figure 27.

Again the height differences of  $0.1 \text{ mm}$  between the single plateaus pose no problem for the setup and also tracks with different inclinations are measured with the same accuracy as the plateaus. One point to mention is the fact that the start and end point of the measured tool does not lie on the same height, but have a difference of  $0.05 \text{ mm}$ , resulting in the fact

<sup>7</sup>Also the laser beam can be dimmed by adjusting the light intensity.

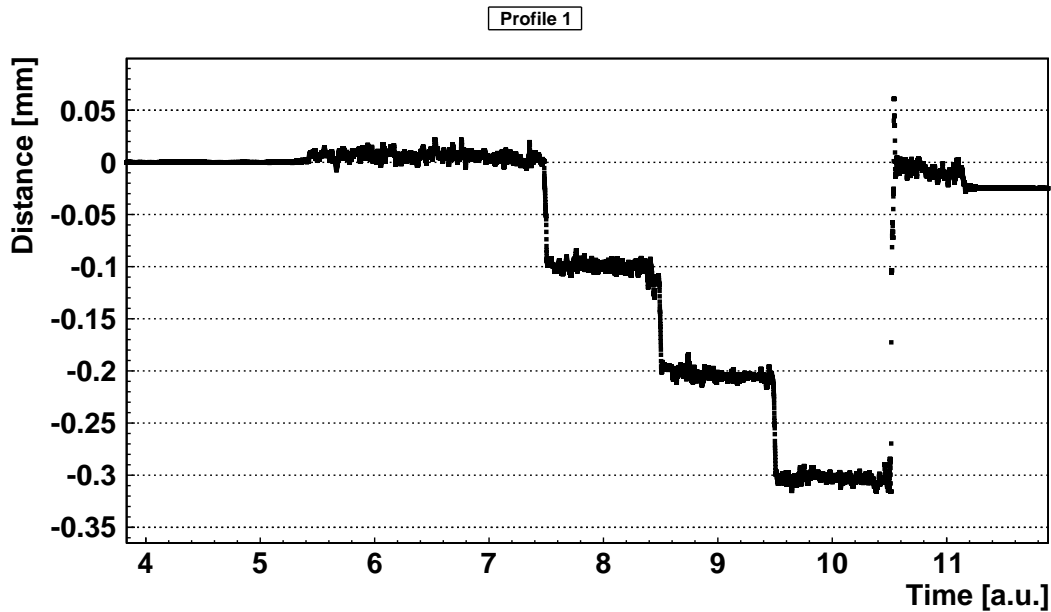


Figure 26: Height profile of the first aluminum piece. Steps of  $0.1\text{ mm}$  are clearly no problem for the setup.

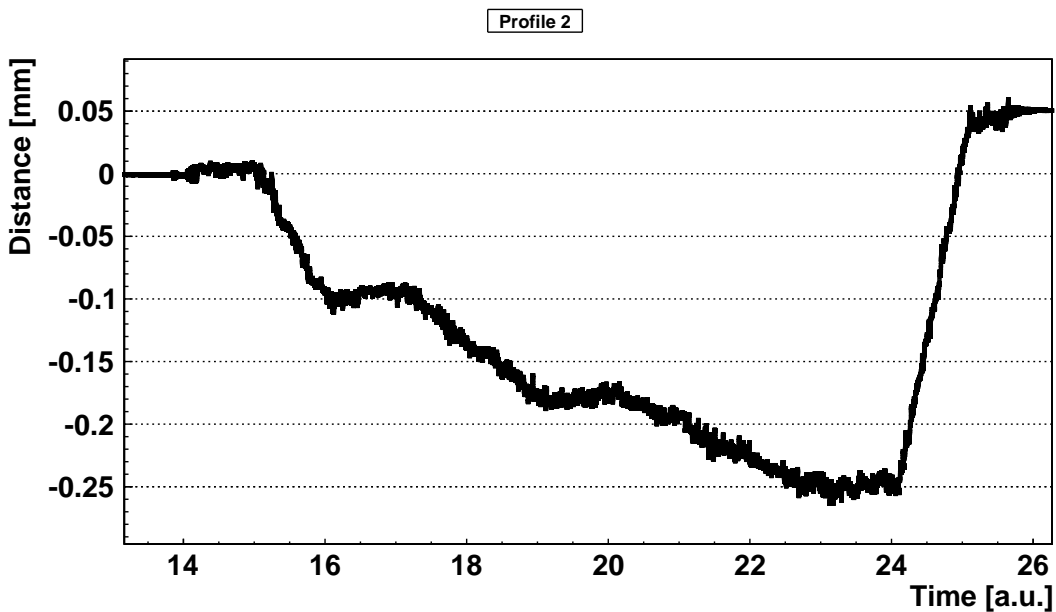


Figure 27: Height profile of the second aluminum piece. The height difference of the plateaus are identical to the first piece. This time including inclined steps. Also this works very well, besides the fact, that the end point lies  $0.05\text{ mm}$  above the starting point. This comes from a non parallelism of the tool and the CMM path.

that the height of the highest plateau is by  $0.05\text{ mm}$  too low. It can be explained by a non parallelism of the tool and the CMM path. Going to much smaller distances, i.e. the third profile, the results got slightly worse, see Figure 28.

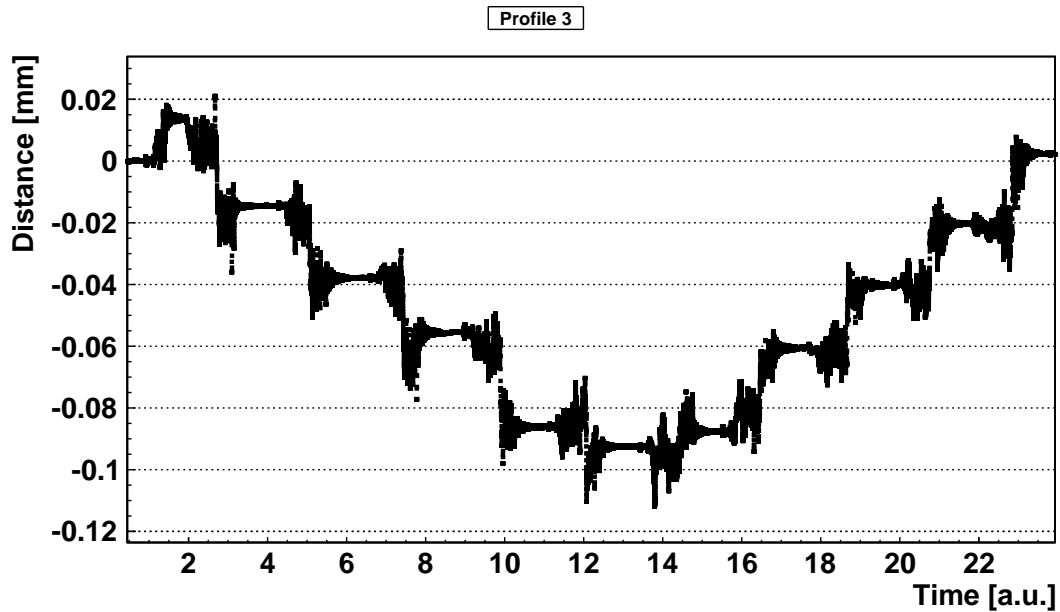


Figure 28: Height profile of the third aluminum piece. In this case the  $0.1\text{ mm}$  steps of the former profiles are subdivided in five equidistant parts of  $0.02\text{ mm}$ . For the beam spot being inside a single step, the results are still good. But two other effects are visible, the vibration at the edges as well as deviations from the drawing. With a mechanical caliper similar results to the laser distance sensor have been measured. It is assumed that this and the vibrations are coming from inaccurate milling.

Here the step size is just  $0.02\text{ mm}$ , which is in principle also clearly visible, but some extra distortions are very prominent as well. This effect at the border to the next step is assumed to originate from the machining of the profile. Also the height of the steps does not follow the drawing as for profile one and two. They had been remeasured with a micrometer screw showing that the dimensions of the drawing are not reached. This again proved that the setup is capable of measuring the tiny distances as necessary for the quality control.

Finally with the measurement of a 1 euro coin, shown in Figure 29, a topology with tiny and continuous height variations is investigated. The profile gives a nice 3D image of the coin, where all details are visible.

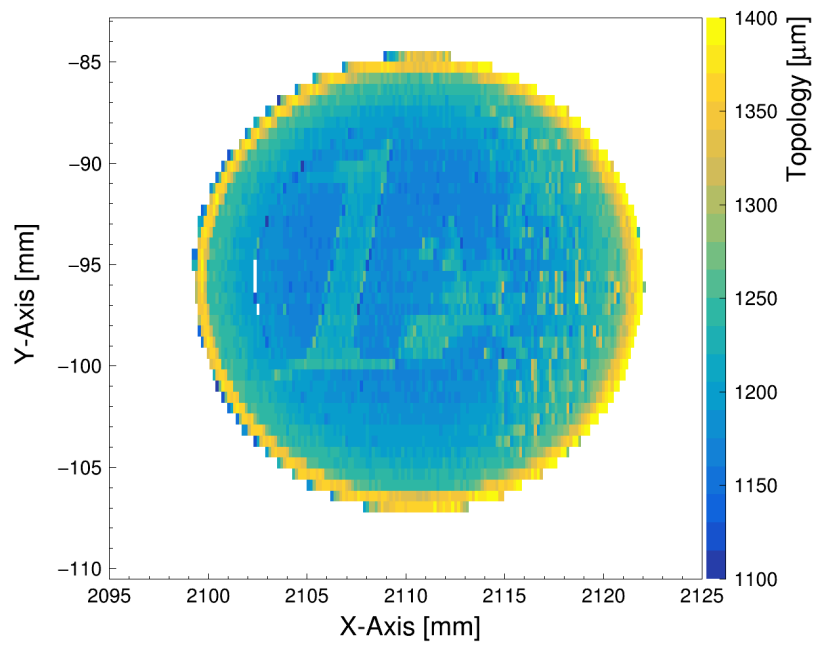


Figure 29: Scan of a one euro coin. Detailed structures with a height of  $< 50 \mu m$  are visible nicely.

## 5.2 Surface Study of the Granite Table

Granite is a heterogeneous material containing the semi transparent mineral quartz. Measuring the surface of such materials with laser distance sensors has the problem that the beam can penetrate the surface, hence the result gets shifted to lower values for the height like if one measures an elastic surface with a tactile sensor. The surface of the granite table is investigated with the tactile as well as with both laser sensors. Since on the one hand the table is extremely flat and on the other hand the distance between the data points is small, the impact of the deformations of CMM on such distances is negligible and one can compare the value measured by a sensor at a specific point with the mean of its neighboring points. What is meant by neighbors is depicted in Figure 30, where the red point is the current data point and the eight green points around are its neighbors.

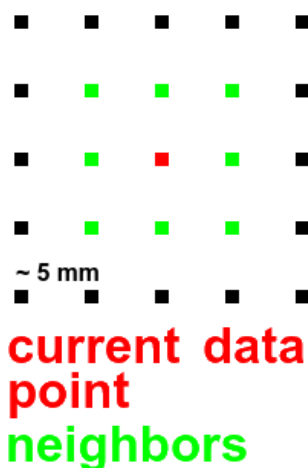


Figure 30: Definition of a neighborhood in a distance measurement with CMM. The measured points of a surface form a rectangular grid, hence each point, depicted in red, has up to eight neighbors drawn in green. If the point of current interest is at the border of the scan, not all of those neighboring points exist.

On this small scale the height measured for a point and its neighbors should be almost equal. But what was found is an asymmetric distribution for the laser sensors, whereas the tactile sensor gives a sharp peak with a width smaller than its own nominal resolution, see Figure 31.

The red distributions, corresponding to the red laser in its normal, diffuse reflecting mode (dashed line) and in its inclined, specular reflecting mode, show the broadest behavior in this study with an RMS of  $9.22 \mu\text{m}$  and  $8.63 \mu\text{m}$ , respectively. Compared to the blue distributions with an RMS of  $6.60 \mu\text{m}$  and  $4.46 \mu\text{m}$  it is obvious that the red light penetrates the surface of the table much more intense than the blue laser. It can also be seen that the right tails of the distributions are more prominent than the left ones. This means that

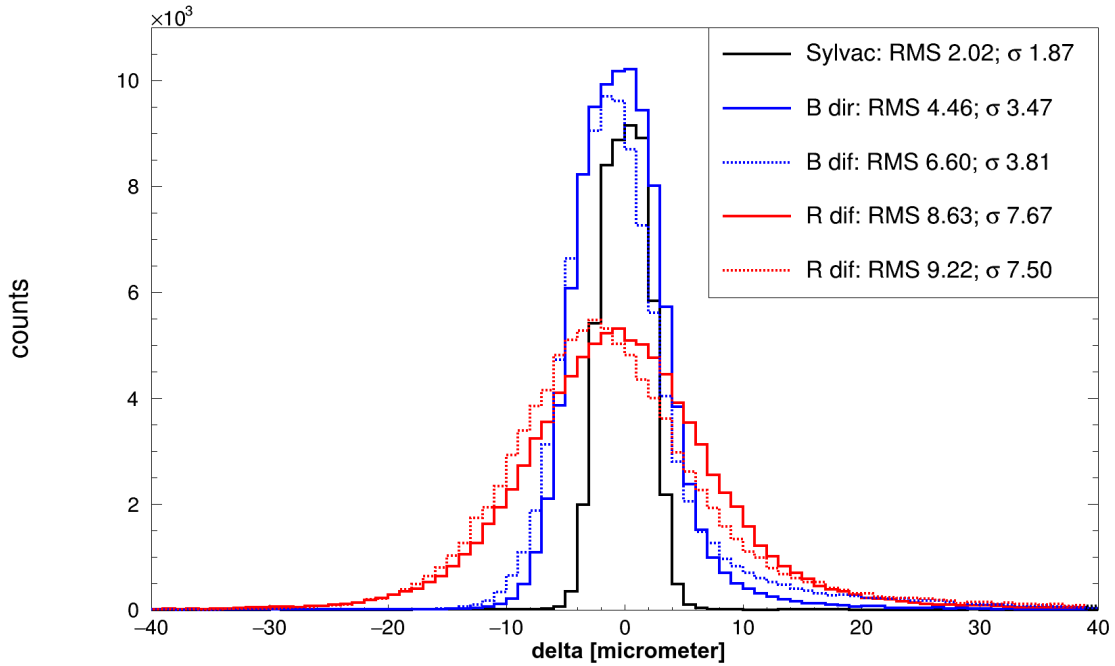


Figure 31: Comparison of measurement quality of tactile and laser sensors. Plotted are the difference of the measured distances of all data points compared their neighbors  $\delta = d_{mean\ neighbor} - d_{data\ point}$ . The red and blue lines give the distributions for the respective laser sensor, with the solid line representing a specular reflection measurement and the dashed lines the diffuse reflection of the beam. The black line is the result for the tactile sensor.

the mean of the neighbors is more often smaller than the distance measured for the point in the center as it happens the other way round, which is correct since single penetrations of light are suppressed when averaging over eight points. Also a slight improvement from normal to inclined mode is visible. Still the best result is given by the tactile sensor, but with the drawback that this measurement takes much longer than the laser scans and there is a possibility to harm sensitive surfaces. The number of points in the tactile measurement was therefore smaller than for the ones with laser. Since a fast and precise measurement technique is requested, the blue sensor in inclined mode is chosen to perform the topology measurements of the quality control.

The topology map of the table, shown in Figure 32 was measured with the blue sensor. Because the table is flat and this data is not corrected, the clear deviations from planarity are deformations of the CMM. Here a high value for  $Z$  means that the machine and the table are closer together and vice versa.

Besides the deviation on large scales two other features can be seen. First, a red spot at around  $(-1500 | -540)$ , is the result of a defect in the table. It is red in this plot, so it has a large  $Z$  value, in principle meaning, that it sticks out. In reality it is a dip deep enough, that its height is outside the  $2\text{ mm}$  measurement range of the sensor. In this case the sensor

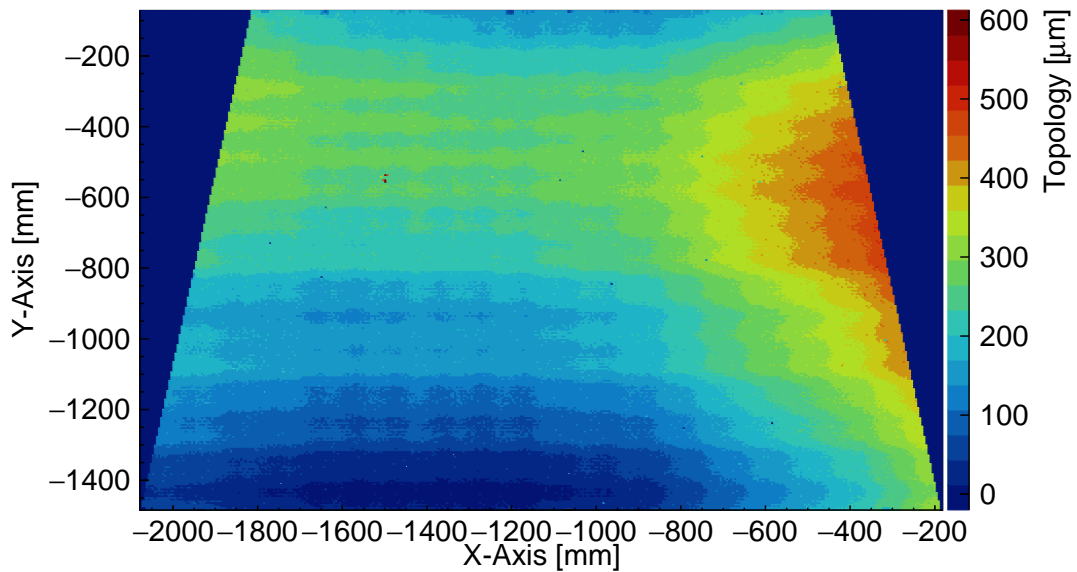


Figure 32: Topology measurement of the granite table. Since the table is flat, the variations of more than  $0.5\text{ mm}$  shown in this histogram are caused by the deformations of the CMM and its bending. These deformations are identical for any following measurements, hence they can be calibrated using this data as a reference.

gives an error value which corresponds to an extremely high value for the distance. Before going to series production the defect in the table needs to be repaired.

The second feature is a periodic structure, in  $X$  as well as in  $Y$  direction. In Figure 33 a slice through the topology plot 32 parallel to the  $Y$  axis is shown. On top of the global deformation of the machine a periodic function is modulated with a wavelength of almost exactly  $100\text{ mm}$ .

After a discussion with the company providing this CMM the cause for this periodic structure is understood as the mounting of the guide rail of the axis, which is done only every  $100\text{ mm}$  by a pair of screws, while it can sag in between.

Both, the global deformation of the CMM and the periodic structure are reproducible up to the  $8\text{ }\mu\text{m}$  level, measured with a laser sensor and up to  $\sigma = 2\text{ }\mu\text{m}$  measured with the tactile one.

### 5.3 Surface Study of Stiffback

The first flat sandwich objects, built on the granite table, are the stiffbacks. Actually there have been four of them built, with the fourth fulfilling all requirements best. None the less the first three have revealed problems and other issues, which lead to several improvements of the gluing process. Understanding all those problems, described in [Pre, 2014], e.g. necessary precautions for an improved stiffness, results finally in the stiffback used for production, which fulfills all requirements concerning stiffness and planarity.

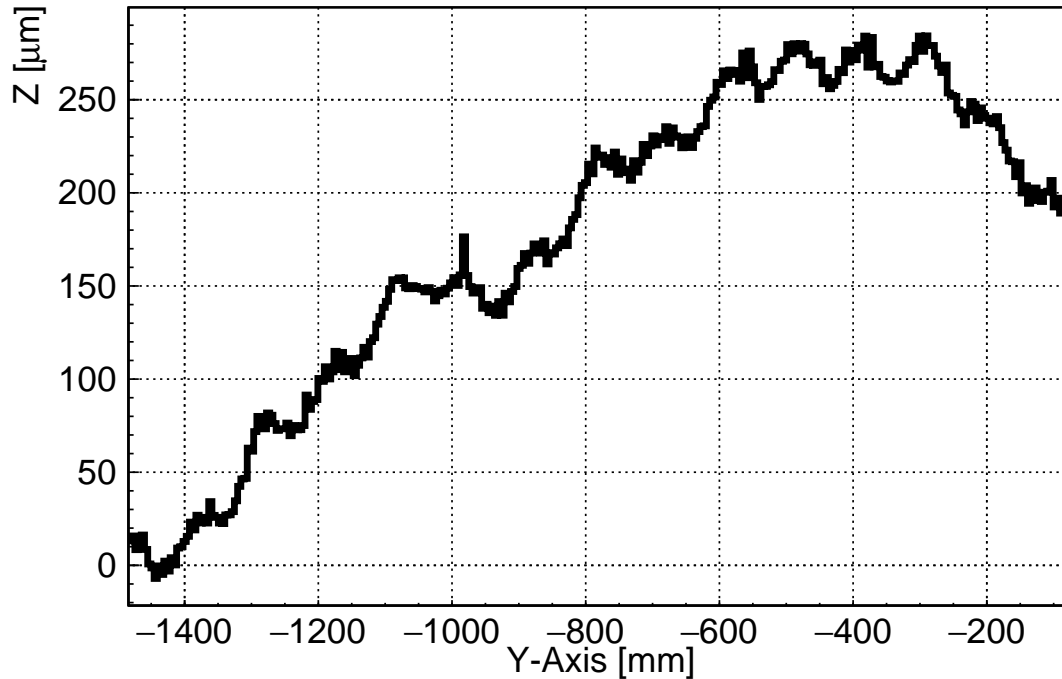


Figure 33: Slice in  $Y$  direction ( $X \approx -1200 \text{ mm}$ ) of the table topology. The periodic structure comes from the mounting of the guide rail of the  $Y$  axis of the CMM, which happens every  $100 \text{ mm}$

Measuring the topology of a stiffback provides some new features compared to a granite surface. In contrast to the table, the aluminum surface of the stiffback is non transparent and highly reflective. The good situation for the stiffback is, that it turned out to be extremely flat on small scales and has very little amount of scratches. Still the intensity of the laser has to be reduced, since the CCD saturates due to the high reflectivity. Figure 34 shows the topology of this stiffback measured with the red sensor. This sensor was chosen because the blue one was not yet available at this time.

This stiffback was made out of three pieces of honeycomb, causing the step in the upper part of the profile as well as the one in the center. The use of three pieces had two reasons. In first place the available honeycomb was not large enough, hence for the upper part an additional piece of honeycomb is used. Still for the larger part a single honeycomb sheet was available, but it was of poor quality, showing a bending of more than  $40 \text{ mm}$ . In order to have the honeycomb sticking to the aluminum plate during gluing it would have been necessary to apply a high force on the honeycomb, which results in a high internal stress introduced to the stiffback. Cutting the sheet into two parts before gluing reduced the bending of each sheet to less than  $20 \text{ mm}$  and therefore also reduced the stress the final stiffback would have. Despite the poor quality it was possible to produce a surface with a height difference of  $\Delta_{MinMax} = 0.5 \text{ mm}$ , which proves the feasibility of the construction method. Using better quality honeycomb and producing the stiffback from a single sheet will lead to highly precise

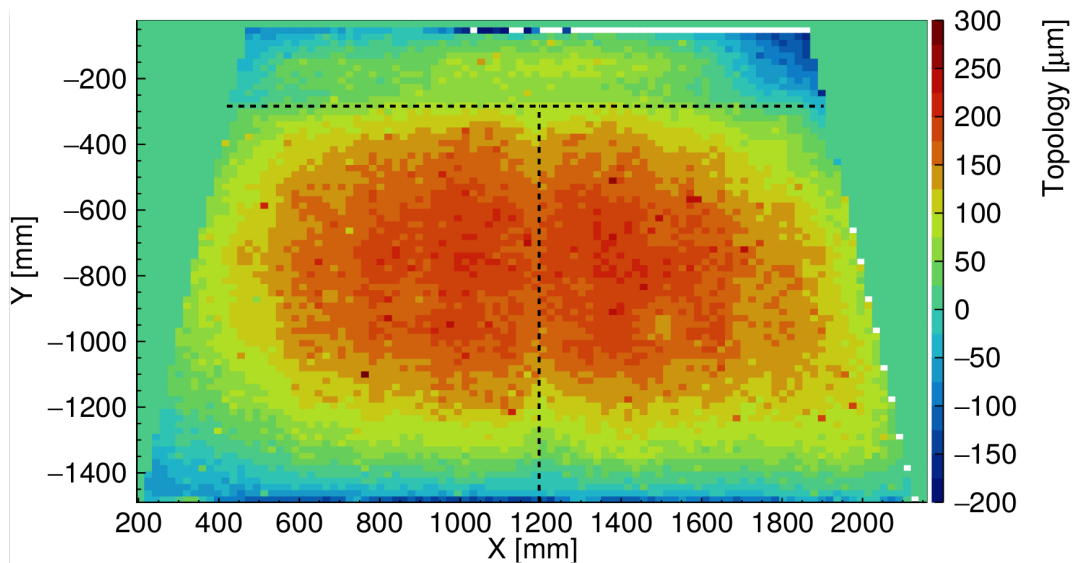


Figure 34: Topology map of the first stiffback. The use of three pieces of honeycomb are clearly visible with the result of a top, lower region, and a distinguishable left and right lower part. A black dashed line is drawn to better visualize the separation in three parts.

surfaces.

This stiffback was brought to the University of Freiburg to investigate it with their large CMM. The Freiburg CMM is a machine where a tactile sensor is moved carefully to the object to be measured and the three coordinates of the axis are read out when the sensor touches the object. It was proven to be extremely accurate during the production of MDT detectors for the ATLAS barrel muon spectrometer<sup>8</sup>. This now gives a method to compare the accuracy of the Munich CMM to a highly precise system. Subtracting both topology maps from each other gives the distribution plotted in Figure 35.

The result is on the first view not a perfect plane, as it should be if both measurements are equal. In the lower left and upper right corner the difference is slightly lower, than in a band going from the upper left to the lower right corner. This systematic behavior is not an effect of one of the machines, but of the stiffback itself due to a temperature difference in both air conditioned rooms of  $1^{\circ}\text{C}$  causing a global deformation due to thermal expansion of the aluminum. Another issue arises from the fact that the points measured are not perfectly overlapping, introducing the potential of another systematic error. But even neglecting the knowledge of the origin of those effects, the distribution of the difference of both machines has a width of  $\sigma_{Muc-Fr} = 14 \mu\text{m}$ , which is still well inside the acceptable range. For the final stiffback an RMS better than  $30 \mu\text{m}$  is requested, which will be measurable with this machine.

<sup>8</sup>The system is calibrated during an accurate measurement with a laser interferometer from the company Renishaw. Such a calibration includes a huge amount of measurements taking two months in total.

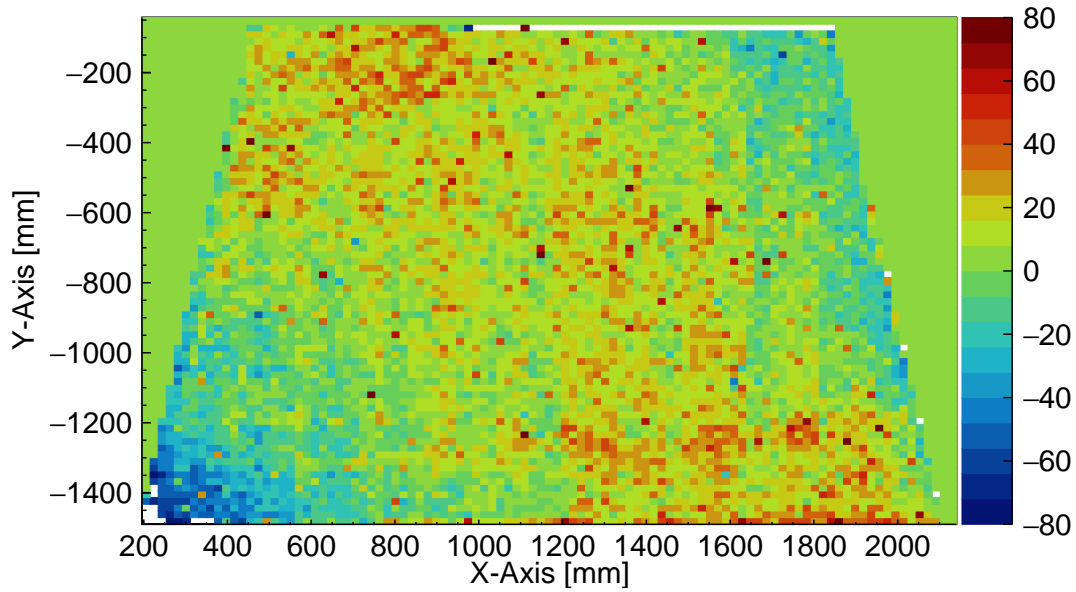


Figure 35: Deviation of Munich and Freiburgs CMM measured with the first stiffback. The visible band from top left to lower right is a temperature effect, since there is  $1^{\circ}\text{C}$  temperature difference in both rooms. Deviations on smaller scales are due to not perfectly overlapping measurement points of both scans.

Understanding and solving all problems occurred during gluing of the first three prototypes, the fourth one finally provides the best result well below what is requested by the NSW collaboration. The topology of the surface used for panel production is given in Figure 36.

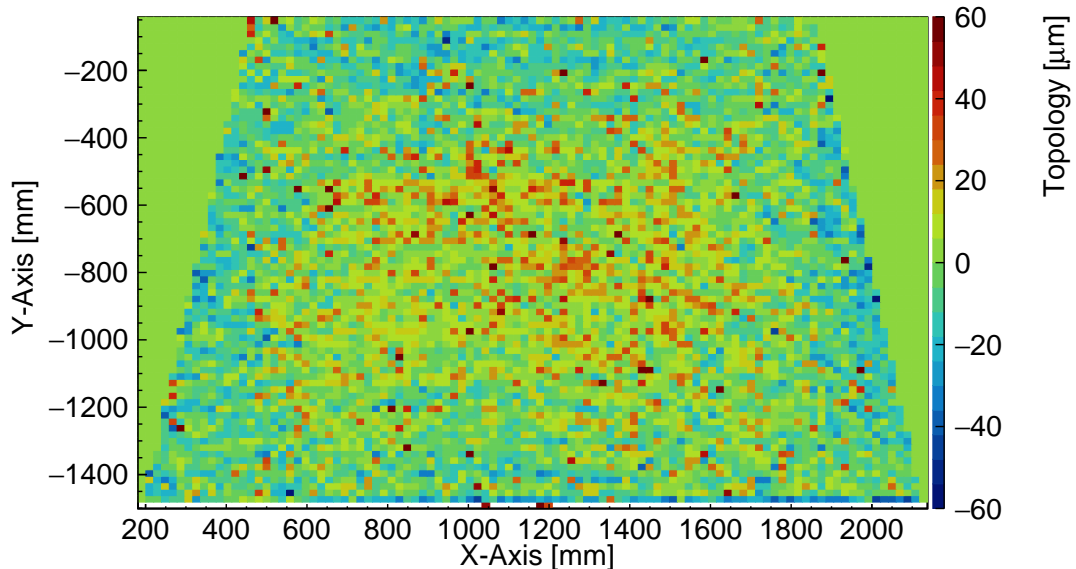


Figure 36: Topology of fourth stiffback. A tiny bump is visible in the central region, which originates from relaxation of internal stress.

The plotted range goes from  $-60\ \mu\text{m}$  to  $60\ \mu\text{m}$  showing a rather flat surface. From a look at

the distribution of the  $Z$  values, shown in Figure 37, it can be seen that almost all measured points are in a range from  $-40 \mu m$  to  $40 \mu m$  with an RMS of  $14.32 \mu m$ .

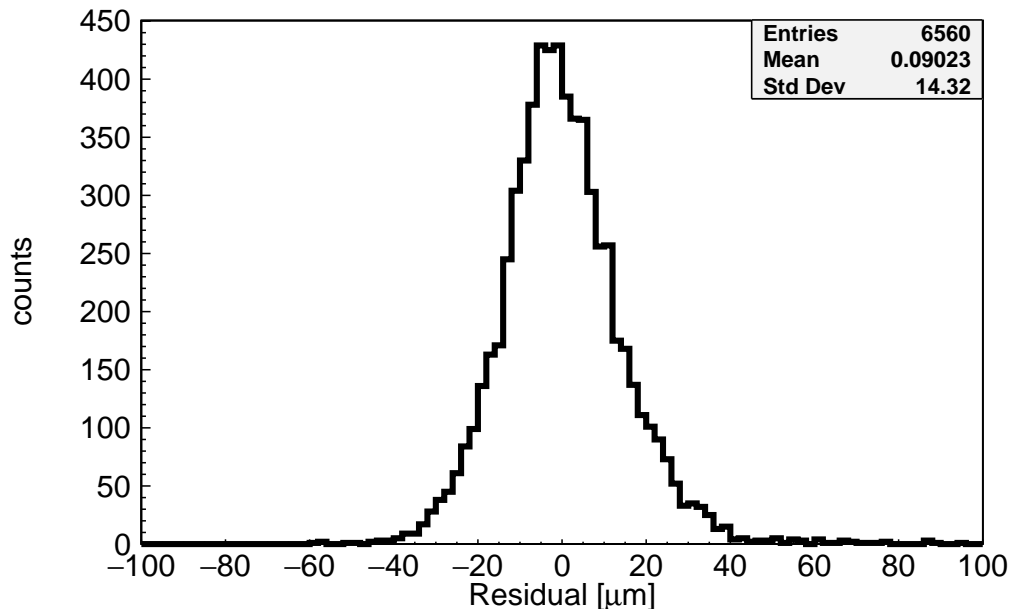


Figure 37: Height distribution of fourth stiffback. Since the range of almost all measured points varies from  $-40 \mu m$  to  $40 \mu m$  and it has an RMS of  $14.32 \mu m$ , it is the best stiffback produced and will be used for further construction.

Requested by the collaboration is  $\Delta_{MinMax} = 90 \mu m$  with an RMS of  $30 \mu m$ .

Another requirement of a good stiffback is that it does not deform under the evacuation during the panel gluing. To test this the topology of the stiffback was remeasured with vacuum inside, shown in Figure 38.

A deviation of both topologies of  $\sigma_{Vac-NoVac} = 5.2 \mu m$  is obtained, which is in the same order as the reproducibility of a granite table measurement, see chapter 5.2. Hence no deviation of this stiffback due to vacuum is observed.

The last requirement is the stiffbacks rigidity. To measure this in a situation as close to the panel gluing as possible the stiffback is laid on the table with its precise second gluing side pointing upwards. The stiffback is additionally supported in the center with a  $360 \mu m$  high aluminum piece, just thick enough that the stiffback still slightly touches the granite table at its corners. Since the first gluing side is slightly concave the height of the distance piece does not directly give a measure of the amplitude of the deformation. Still this setup simulates a sag of the stiffback during the panel gluing but without a panel attached. Again the surface was scanned and the difference between no support in the center and a support is plotted in Figure 39.

The histogram shows that this support results in a higher central region with an amplitude of  $130 \mu m$ , proving that the stiffback is not 100 % stiff. The negative of this plot can be

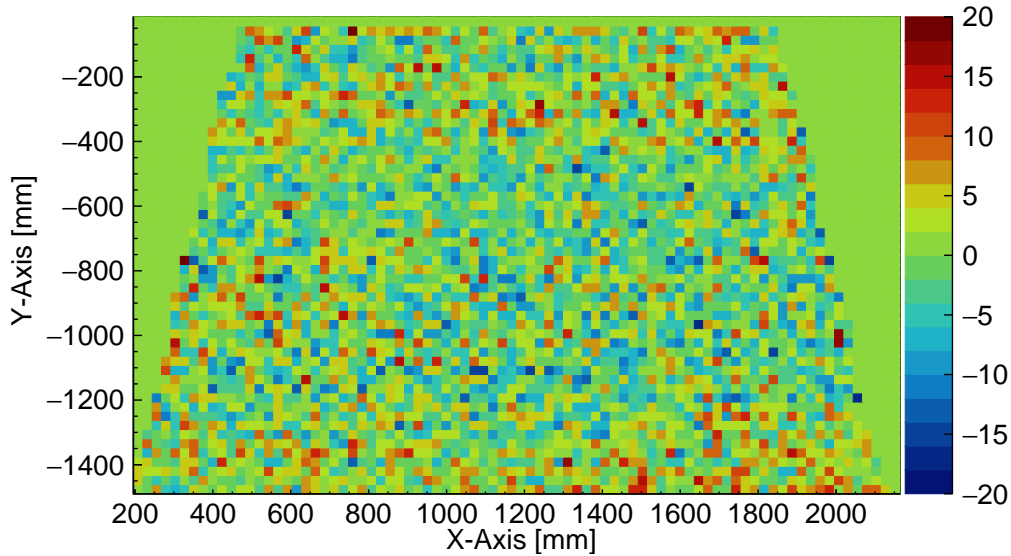


Figure 38: Difference between vacuum and no vacuum inside the third stiffback. During construction the stiffback will be evacuated, which must not deform the surface of the stiffback. This demonstrates as well that the stiffback was glued homogeneously.

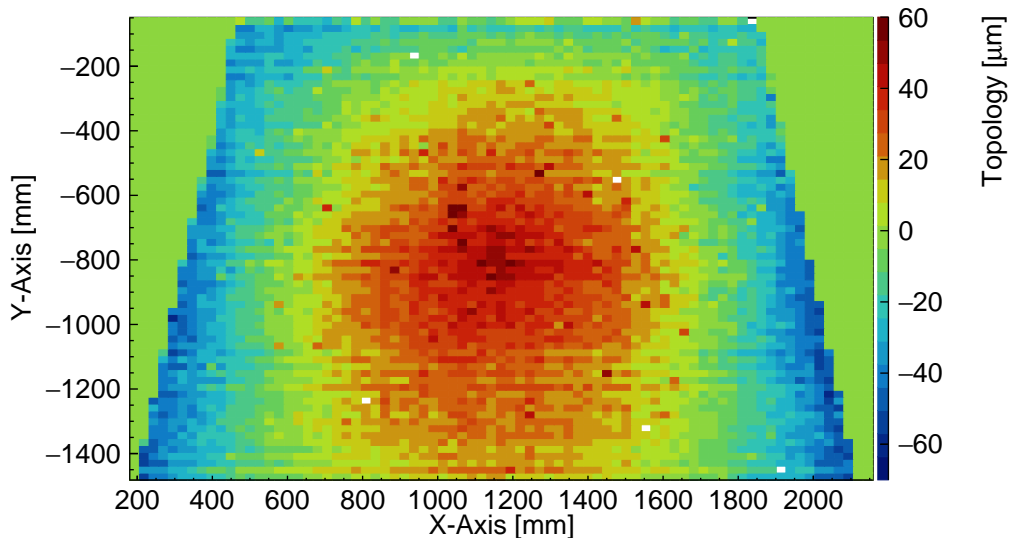


Figure 39: Hardware simulation of gravitational sag of the stiffback. A  $360 \mu\text{m}$  high distance piece between table and stiffback pushes the central part of the stiffback upwards. For this measurement, the good side of the stiffback points upwards. During panel construction such deformations occur as well, since the stiffback is supported only at its edges, when gluing the second half panel.

seen in the topology of the first panel gluing tests, discussed in chapter 5.4. Pulling up the center of the stiffback during panel production allows the production of flat panels.

Finally it can be concluded that the construction of a stiffback for NSW Micromegas production was successful. A light weight ( $25 \text{ kg}$ ) flat structure was build, which is rigid enough to be used in the production of sandwich panels with the desired quality.

## 5.4 Surface Study of SM2 Panels

Before discussing the actual products of the panel gluing, topology scans of intermediate steps are shown. As explained in chapter 3.4.3, the height of the glue is just  $0.3\text{ mm}$ . To ensure a proper gluing of all parts, it is necessary that all intermediate products itself are flat enough. Otherwise not or poorly glued spots are the consequence.

Starting with just the boards sucked to the table an extremely flat surface is expected. Figure 40 shows the topology of the three boards of a drift panel.

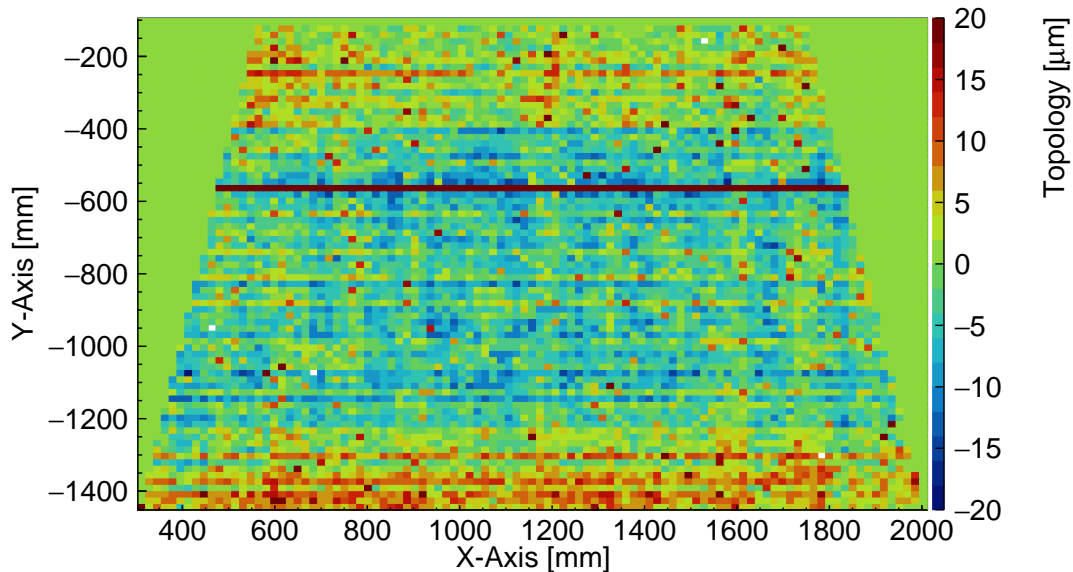


Figure 40: Quality of PCBs for outer panels. The central board is slightly thinner than the other two, but the gap of  $0.03\text{ mm}$  is easily filled by the  $0.3\text{ mm}$  high glue.

The dark red line in the upper part of this picture is a measurement of the sealing tape connecting the upper and the middle board. This tape was hit by accident, since the distance of two measurement points is  $15\text{ mm}$  in this case and the tape is just  $6\text{ mm}$  wide. That's why the tape connecting the middle and lower board is not visible. The height distribution of this measurement is plotted in Figure 41.

The entire distribution of the investigated boards has a range of  $\pm 20\text{ }\mu\text{m}$ , what is well below the specifications of  $\pm 50\text{ }\mu\text{m}$ , [Bini et al., 2014]. The little dents, visible in Figure 40 are easily filled with glue during production.

In contrast to such a drift PCB, the readout PCBs have a pillar structure on the side facing the granite table with a spacing of  $7\text{ mm}$ . A too high level of vacuum will press the board between those pillars towards the table, forming dents on the side where the glue will be distributed, and if the gluing works fine, the amplification region will have a height smaller than the one of the pillars causing lots of discharges or even shorts to the mesh. Applying a vacuum of only  $50\text{ mbar}$  reduced air pressure results in a topology shown in Figure 42.

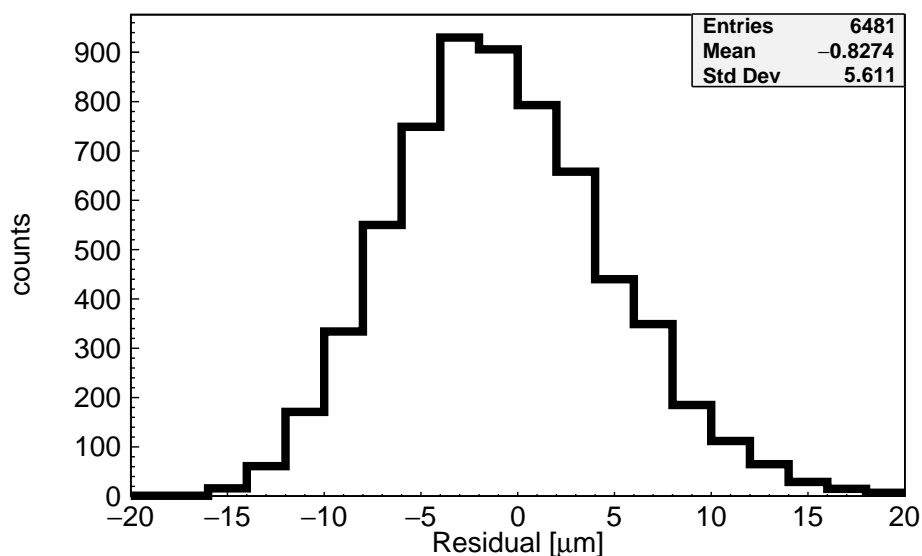


Figure 41: Thickness variation of PCBs for outer panels. An RMS of  $5.6 \mu\text{m}$  is measured, which is well satisfying the specifications of  $\pm 50 \mu\text{m}$ .

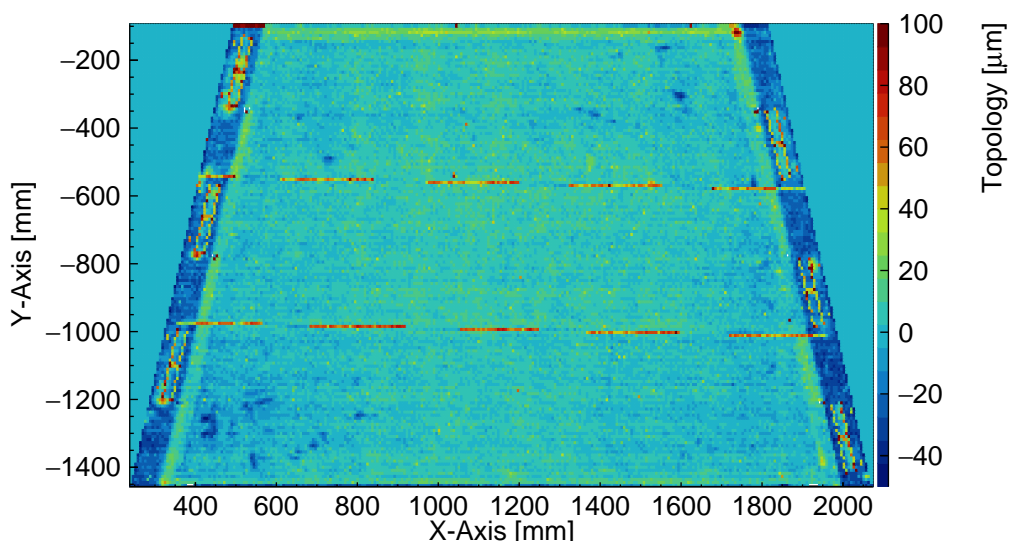


Figure 42: Quality of PCBs for readout panels. The slightly more complex structure of readout PCBs is visible, sucking them onto the table with the side to distribute glue on pointing up. The lower parts at the left and right side are regions with no resistive strips and no coverlay material, hence being slightly lower than the active area. The height difference measured here is only about  $30 \mu\text{m}$  and not the  $190 \mu\text{m}$  resulting from the total thickness of coverlay and resistive strip foil, since this area is additionally supported by a sheet of Mylar. This area also shows spots with dips resulting from either too low or even missing pillars.

Since the readout boards are more complex than the drift boards, more structures are visible in this plot. The blue parts at both sides of the trapezoid are the regions where the readout electronics will be placed in the final quadruplet. Here blank PCB material faces the granite table in contrast to the central region, where there are the copper readout strips,

the Kapton<sup>®</sup> foil with the resistive strips and the pillars in between. During gluing this area is supported by a 0.19 mm high Mylar<sup>®</sup> foil. Still this area is slightly lower than the active area by  $\approx 30 \mu m$ . Three slightly higher parts per side inside this electronics region are due to an extra layer of sealing tape. The PCB at these points will be removed before the assembly and to make this step more easy it is partially pre-cut and needs to be sealed during gluing.

Also visible are both sealing tapes connecting the three boards. The edges of the part facing the neighboring board are not parallel to the base line of the trapezoid, but have a tilt of  $1.5^\circ$  providing this step-like structure of the sealing tape. There will be two different types of readout panels produced, one with strips parallel to the base line, called  $\eta$ -panels and one with strips tilted by  $1.5^\circ$ , called stereo-panels. The first one will provide a precise  $\eta$  coordinate of the traversing muon, while the stereo boards provides an additional coarse position in  $\phi$  direction.

But the most interesting feature visible are the blue spots inside the active area representing a lower altitude. The only reason why such regions can occur are too small or missing pillars. After releasing the vacuum and turning the boards around for further inspection, it turns out that pillars were missing at those extended spots. This is in clear contradiction to the acceptance requirements for readout boards imposed on the manufacturer, where it is stated that if one pillar is missing, all neighboring pillars have to be present. For module zero production a 120  $\mu m$  high double layer of Kapton<sup>®</sup> tape replaces the missing pillars. Since this problem happened on almost every board, a new pillar design is used for the series production introducing long pillars with a larger area attached to the readout board and strongly increased adhesive force. This additionally makes a visual inspection of missing pillars much easier and on a first look the new boards have no more missing pillars at all.

But this topology also shows a problem concerning the quality requirements. Just looking at the height distribution, shown in Figure 43, is in principle enough to get a value for the  $\Delta_{min-max} = 100 \mu m$  as well as for the  $RMS = 12.52 \mu m$ . Both values would be fine, if this would be the topology of a panel. But due to local defects, as missing pillars not detected at the given measurement periodicity, the panel would have to fail in the quality check. It is therefore necessary to find a compromise between a long lasting high granularity measurement, which reveals in the topology map local defects, as too small pillars, and a fast measurement, which is needed since there is only one granite table for production and measurement. Depending on the workload a distance between measurement points of 15 – 20 mm is chosen, resulting in  $\approx 7000$  measurement points taking about 1.5 h.

To get used to the entire gluing process and iterate over some weaknesses in the original construction plan, it was planned to build some panels with bare PCB material. In this step also other honeycomb suppliers and different honeycombs were tested, than the one used for series production. The quality of the honeycomb is therefore also very interesting.

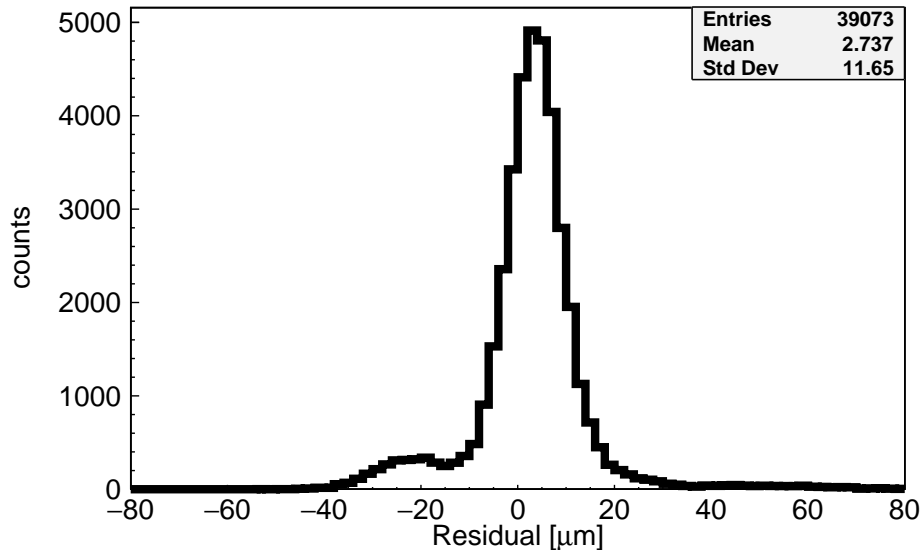


Figure 43: Thickness variation of PCBs for readout panels. This plot shows two prominent peaks, the smaller one at around  $-30 \mu m$  is given by the region for electronics and the central one gives the active area. The entire height variation is at around  $100 \mu m$ , which also can easily be filled with glue.

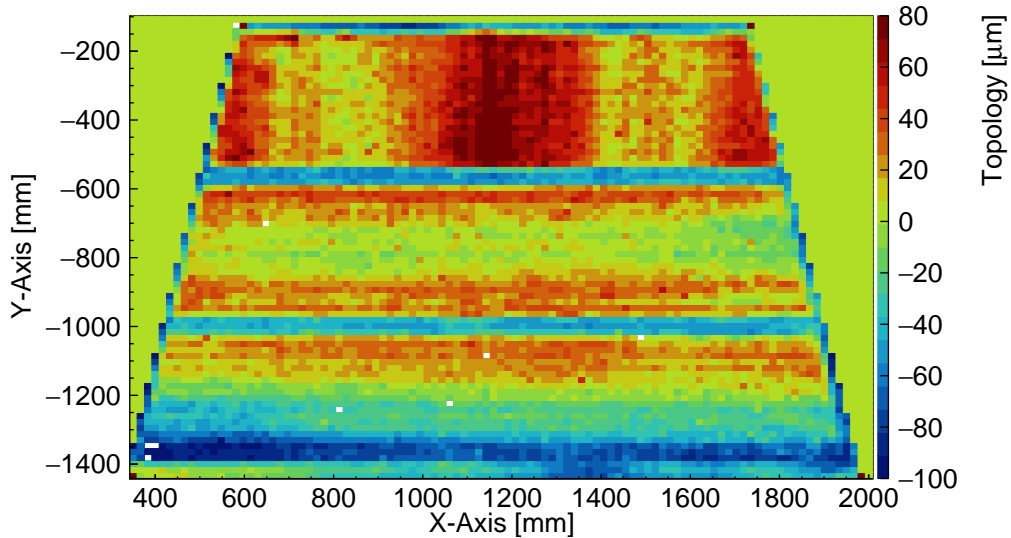


Figure 44: Quality of aluminum bars and honeycomb for internal structure of a test half panel. Both were sucked with the vacuum bag technique to the panel. The honeycomb shows a wavy structure and is higher than the bars. Grinding this structure made the gluing possible.

A convenient way to measure the thickness of the honeycomb is to bring the needle of the tactile sensor, mounted on a broad plate, into the cells. The needle will touch the surface below the honeycomb, while the mounting plate lies flat on top of it. With this method the height variation can be measured at several points which is done for a quality control of the honeycomb. A more elegant method, which can also be done after gluing of the first half

panel, uses the CMM. A  $1\text{ mm}$  thin aluminum plate with the dimensions of the trapezoid is laid on top of the first half panel and is pressed to it with the vacuum bag technique. The laser sensor can now measure the distance to the plate which follows the honeycomb surface structure. As mentioned, this can be done before and even after gluing providing a much more detailed height profile of the honeycomb than measuring it just at a few points, but again this blocks the table for construction. Still for the test panels this was done and the result is shown in Figure 44.

Visible are the three honeycomb sheets separated by aluminum bars, similar to the photograph of Figure 18. In the honeycomb region, a wavy structure is measured, which is oriented from left to right for the two lower sheets and from top to bottom for the upper sheet. All three parts were cut from one larger sheet, but the upper part was cut perpendicular to the two lower ones, which explains the fact that the wavy structure is perpendicular. For the production of the honeycomb sheets of aluminum are glued together at regular points and afterwards cut to the desired height and then pulled out like an accordion, forming an extended sheet with regular hexagonal cells. If the cut to the correct height before the extrusion is not precise enough, this structure is seen in the extrusion as well and it is this effect what is observed as wavy structure.

In addition also the internal aluminum bars are visible in this plot due to their lower height compared to the honeycomb. Figure 45 shows that this surface has a  $\Delta_{min-max} \approx 0.2\text{ mm}$ .

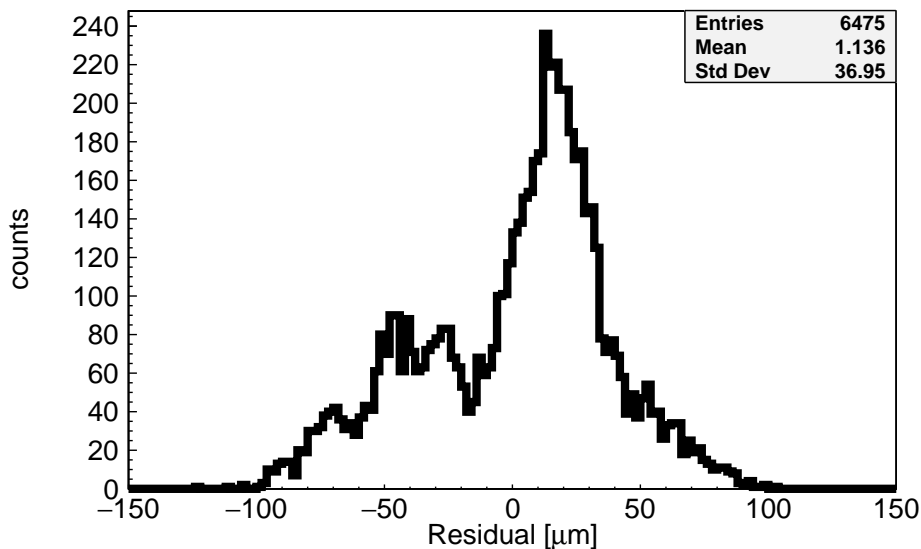


Figure 45: Thickness variation of aluminum bars and honeycomb for the internal structure of panels. The range of this distribution is around  $200\ \mu\text{m}$  and in this situation it was doubted, that a proper gluing will be possible hence the structures have been ground before gluing. For series production honeycomb and bars of higher quality are going to be used.

This enormous amplitude encouraged us to grind the honeycomb to improve the chance of a homogeneous gluing of the second side. Such problems did not occur during the gluing of

panels for real Micromegas panels, since the material used there meets the quality requirements much better.

The gluing process continuously evolved during construction of four test panels. Within the topology of the fourth test panel the sag of the stiffback mentioned in chapter 3.4.3 is clearly visible, see Figure 46.

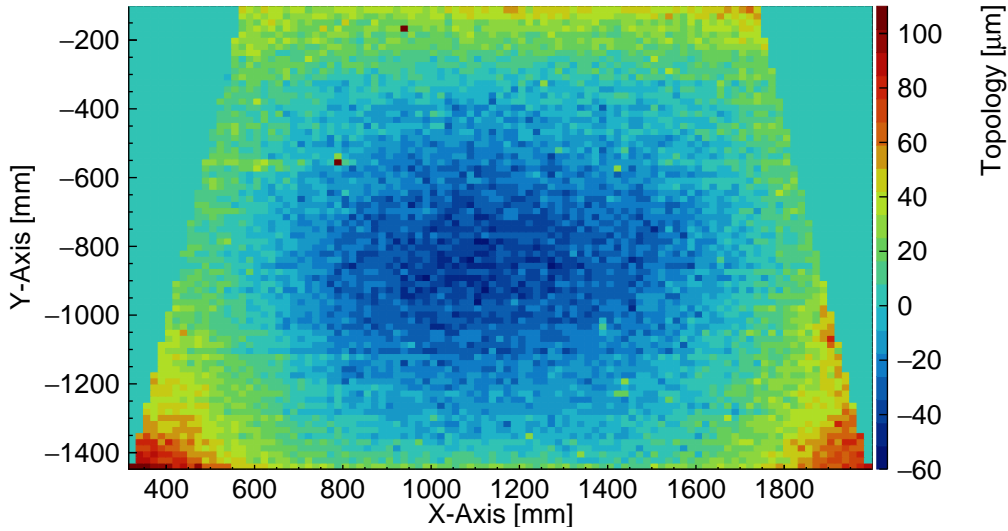


Figure 46: Topology of the fourth test panel. A dip covering the entire panel is measured, resulting from gravitational sag of the stiffback during gluing.

It has a dip in the center with an amplitude of  $\Delta_{min-max} \approx 150 \mu m$ . This value is by  $20 \mu m$  larger than the  $130 \mu m$  of the stiffback with the support in the center, see chapter 3.4.2. This is explained by the first half panel hanging as additional payload on the stiffback causing a more extreme bending. For the future panel construction the stiffback correction tool is used and the upward pull is iterated starting with  $150 \mu m$ .

The distribution of height values, Figure 47, gives an RMS of  $23.9 \mu m$  for this panel which would be sufficient for a final sandwich panel, but the hope is that even better panels can be produced using the correction tool.

Since the real bending of the stiffback is not measurable, the correct upwards pull can only be determined by controlling the gluing result and continuously adjusting it. The first two drift panels, built in Munich, were constructed using the correction tool, both showing a slight overcompensation of the sag. For the first panel the height of the resulting bump is  $\approx 50 \mu m$ . In the iteration of the second drift panel the produced bump is only at a level of  $\approx 30 \mu m$ , see Figure 48.

This overcompensation shows on the one hand that a correction for the sag, visible in the test panels, works, and on the other hand a converging iteration to tune the panels to the desired quality is possible. The figures of merit for this panel, shown in Figure 49, are a  $\Delta_{min-max} \approx 80 \mu m$  and an RMS of  $18.6 \mu m$ , which is a clear improvement to the non com-

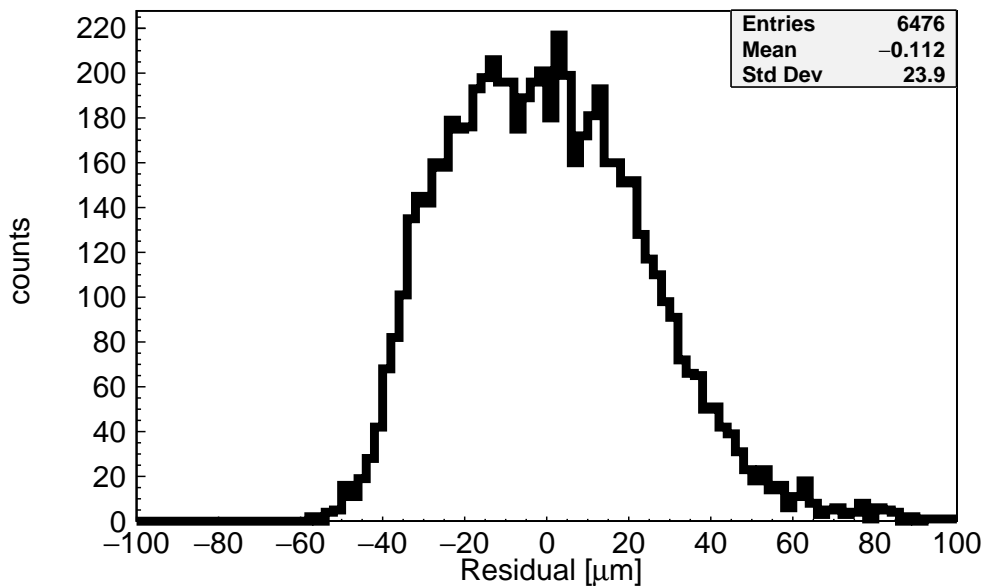


Figure 47: Thickness variation of the fourth test panel. Even with an RMS of  $23.9 \mu m$ , well satisfying the criteria to be under  $30 \mu m$ , it is considered that a better panel can easily be constructed by pulling up the stiffback in the center during gluing.

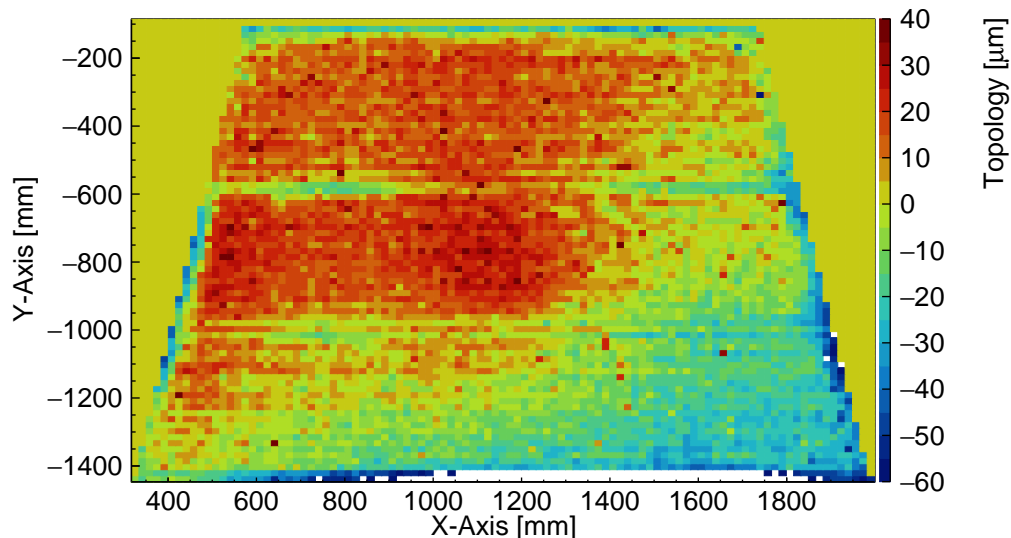


Figure 48: Topology of the second drift panel, produced with stiffback correction. The former dip is now gone, but due to a slight overcompensation a bump was produced. Still the thickness variation goes down from  $150 \mu m$  for the fourth test panel to  $80 \mu m$  for this drift panel.

pensated panels and well matching the specifications.

In a next step the first readout panels for SM2 have been produced. As discussed above, the layout of the PCBs for those panels is more complicated than for test and drift panels. Hence also the topology scan of those panels shows the same features of the PCB layout as the scan of just the backside of the panels sucked to the granite table of Figure 42. The scan

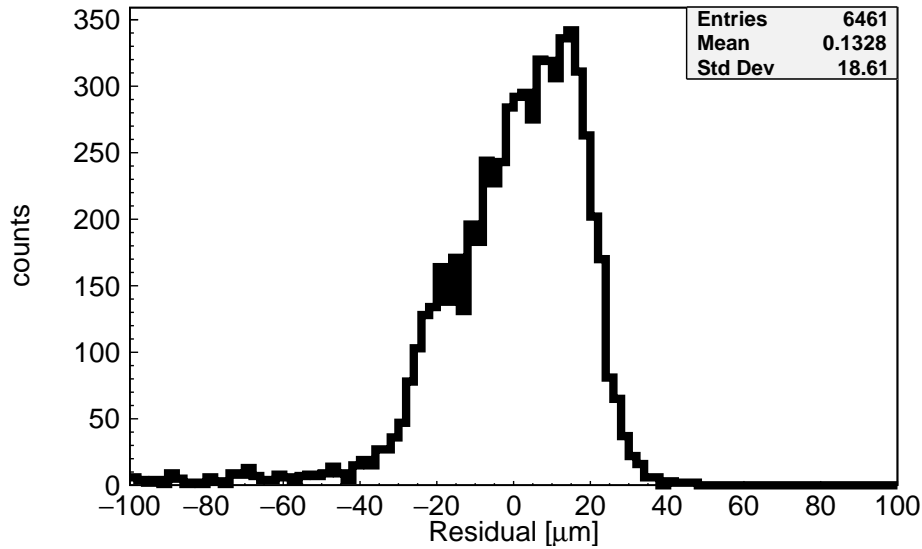


Figure 49: Thickness variation of the second drift panel. With a  $\Delta_{min-max} \approx 80 \mu m$  and an RMS of  $18.6 \mu m$ , this panel is almost a factor of two better than the test panel, proving the successful use of the stiffback correction.

of the first readout panel is plotted in Figure 50.

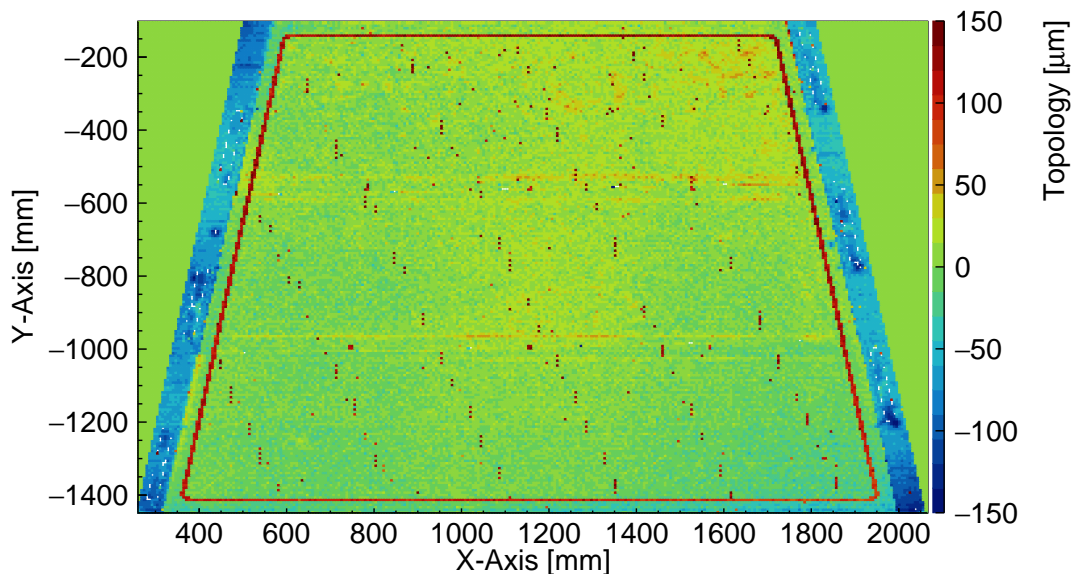


Figure 50: Topology of the first readout panel. Like before different height levels for different regions on the measured surface are visible - the part for the electronics, the active area, and the coverlay parts.

To make all structures visible in this plot, a range of  $300 \mu m$  is chosen. The three layers - bare PCB, readout structure and coverlay - are clearly distinguishable from each other, which can also be seen nicely in Figure 51.

The first peak in this distribution corresponds to the area where the electronics will be

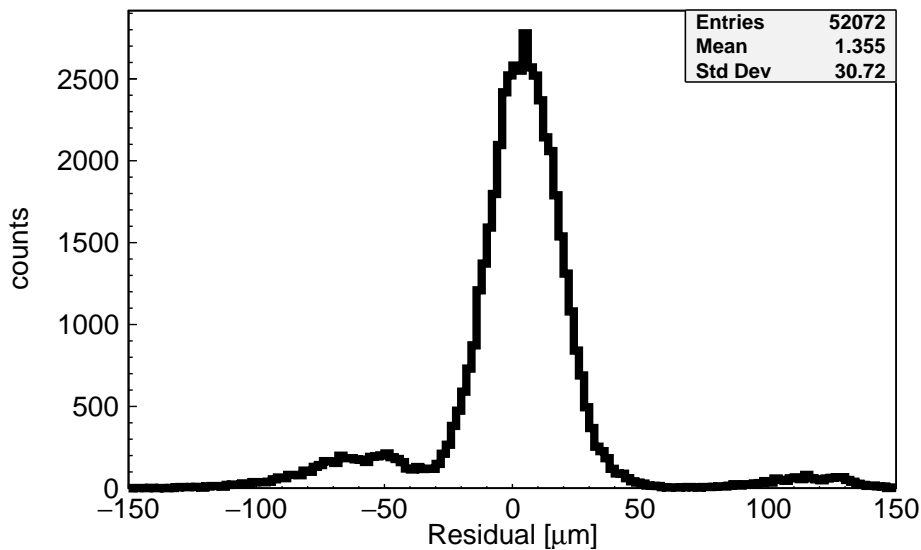


Figure 51: Thickness variation of the first readout panel. The three regions visible in the topology map of this panel can be clearly distinguished in this histogram. The left peak belongs to the electronic part, the central one represents points in the active area, where no coverlay has been hit and the last peak results from the accidentally hit coverlay parts. The most interesting central peak has an RMS of  $13.8 \mu m$ , being the best result produced so far. Also nice to see is the fact that the peak of the coverlay peaks at  $\approx 130 \mu m$  above the central peak, giving the correct height for the pillars.

placed, while the third peak originates from the coverlay. In the latter also the height of the pillars can be seen, which peaks at  $\approx 130 \mu m$ , the correct height of the coverlay material. The points measured here are either the coverlay line around the active area or pillars hits by accident. Since this pillar structure sits on top of the active area, its height distribution is a convolution of the coverlay height and the distribution of heights of the active area. Most interesting is the result of the active area, represented by the large central peak. It has an RMS of only  $13.84 \mu m$ , which is satisfying the requirements by more than a factor of two. In a state of an assembled detector position dependent efficiencies can be measured which would reveal inhomogeneities of the pillar height much better than by measuring their height with the laser distance sensor, where a pillar is only hit accidentally [Lösel, 2017]. Another important issue to mention is that all topology plots of panels shown up to now are in a state where they have been sucked to the granite table. Releasing the vacuum allows the panel to deform under its internal stress. A lot of specifications of parts for a sandwich panel like bending of aluminum profiles and honeycomb aim to reduce such internal stress, still it can not be fully avoided. Figure 52 shows the difference between vacuum and no vacuum for readout panel two.

The vacuum plot has an RMS of  $14.38 \mu m$ . Still the difference to no vacuum applied is clearly visible, with its distribution having an RMS of  $15.94 \mu m$ .

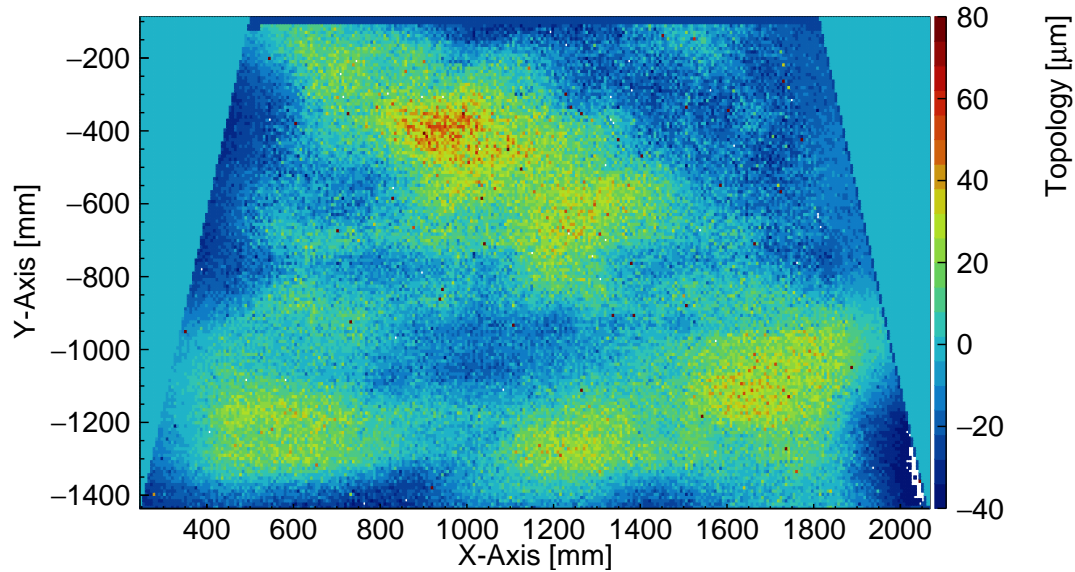


Figure 52: Difference between applied and not applied vacuum during a topology scan of the second readout panel. The picture shows some deformation due to internal stress. Calibration measurements with an assembled detector will show, if these deviations will produce problems during operation.

For the quality data base both sides of the panel have to be measured with and without vacuum. On the one hand in a final assembly the panel is not sucked to any stiff and flat structure. On the other hand the assembly itself connects five panels and this not only around the trapezoidal structure, but also at 6-8 points inside the active area. Finally the quadruplet is mounted to a rigid spacer frame. Additionally there will be an overpressure inside the Micromegas mostly deforming the outer drift panels by pressing them outwards. Therefore, before the quadruplet is assembled, it can not be stated how the panels will behave and what flatness can finally be reached. A way to measure the topology after assembly was introduced by Philipp Lösel [Lösel, 2017] using the CRF in Garching near Munich. The concept will be described shortly in chapter 5.5.

To use a common scheme, the method with vacuum is up to now the most convenient way to classify the panels right after construction, since it provides at least the thickness variation of the panels. If the investigations of quadruplets in the CRF show further issues they will be taken into account in the measurement with the laser distance sensor.

Summarizing the knowledge learned from the measurements with the CMM it has to be stated that it is possible to build lightweight sandwich structures well within the desired specifications. The CMM and the distance sensor have been taken successfully into operation providing results with an accuracy below  $10 \mu\text{m}$ .

## 5.5 Cosmic Ray Facility

The Cosmic Ray Facility (CRF) in Garching was originally designed for the calibration of MDT chambers for the ATLAS detector. A photograph is shown in Figure 53.



Figure 53: Photograph of the Cosmic Ray Facility (CRF) of LMU Munich.

In the space between upper and lower reference chamber the MDT chamber under test was inserted. On this picture a  $1\text{ m}^2$  Micromegas is installed between the reference MDTs on the left side of the system. A scheme describing the CRF is shown in Figure 54.

A cosmic muon penetrating the CRF causes a trigger, when the scintillators of the upper and lower hodoscope layer detect a signal. Two precise MDT chambers<sup>9</sup>, sandwiching the device under test, which will be now a Micromegas quadruplet, provide a reference tracking information. This track is compared to the reconstructed track of the quadruplet to study its behavior like detection efficiency or pulse height distribution. Tests with a  $1\text{ m}^2$  Micromegas showed, that it is possible to investigate the topology, the efficiency and the alignment of the strips of a Micromegas with cosmic muons, [Lösel, 2017]. Such calibration studies are shown in figures 55 and 56, giving the strip alignment and the topology, respectively. This detector consists of two PCBs and its construction happened without the precise alignment scheme for readout boards. A slight shift ( $100\text{ }\mu\text{m}$ ) and tilt ( $350\text{ }\frac{\mu\text{m}}{\text{m}}$ ) of both boards was measured with the CRF. Also the deformation was investigated, resulting in a blow up of  $1.6\text{ mm}$ . The value measured is the height of the central part of the chamber which is half its thickness deformation.

The same tests will be performed in the future with the SM2 modules built in Munich, also providing information about the topology of each layer. With this the results of the CMM

<sup>9</sup>It was measured by a computer tomographic scan.

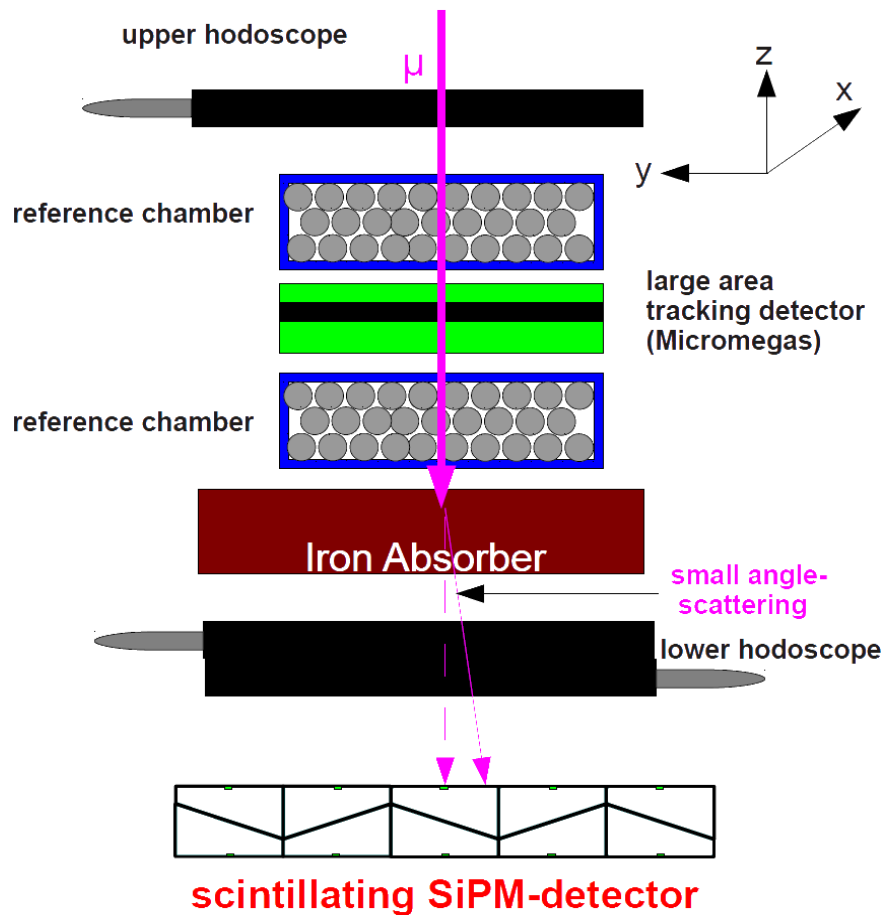


Figure 54: Scheme of the CRF. Two MDT reference chambers provide a tracking information of a traversing muon, which is compared to the position reconstructed by the detector under test. A trigger hodoscope starts the readout of the facility. Measuring the deflection of the muon track after a  $300\text{ mm}$  thick iron absorber by a third position sensitive detector provides a possibility to cut on low energetic cosmic rays. Those muons suffer from multiple Coulomb scattering and, thus, their track will not be perfectly straight when going through the setup. However, the lack of straightness blurs the effects from the test detector's potential distortions, [Ruschke, 2014].

should be verified and the position of the strips in the four layers of the detectors will be calibrated.

Since there is no energy selection tool installed in the CRF at the moment all muons causing a trigger are used for calibrating the SM2 modules. But muons can perform small angle scattering on their way through the CRF, which especially for low energetic muons results in large deflection angles, worsening the track reconstruction of the MDTs. A way to cut on the energy of the muons is to measure their deflection angle after traversing a  $300\text{ mm}$  thick iron absorber. This should in future be done with a position sensitive scintillation detector which compares the predicted track of the MDTs with its own reconstructed muon position. If the

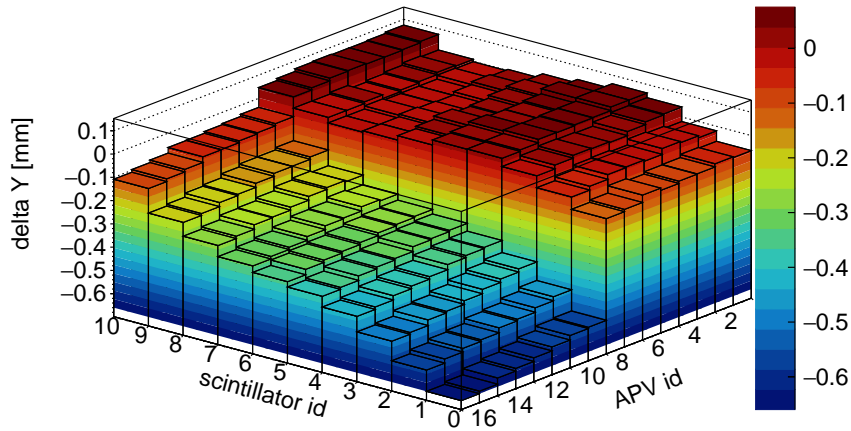


Figure 55: Mis-alignment of the L1 chamber readout boards. The PCBs show a shift of  $100 \mu\text{m}$  and a tilt of  $350 \frac{\mu\text{m}}{\text{m}}$ , which results from the fact that no alignment tooling was used during construction, [Lösel, 2017].

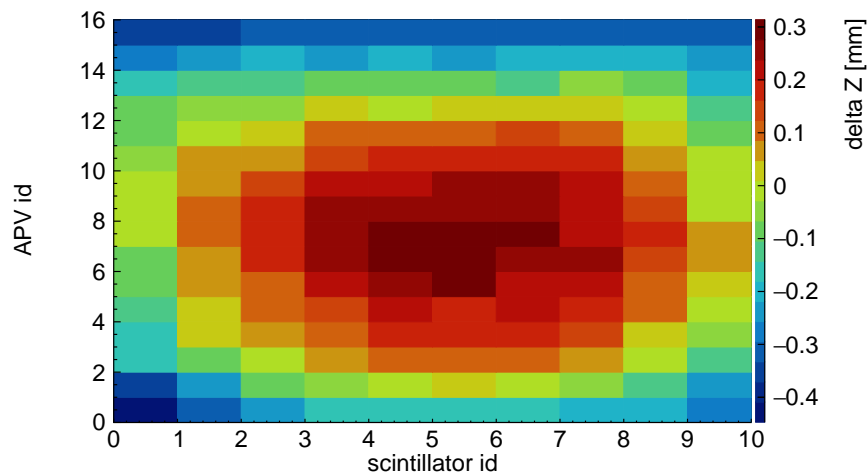


Figure 56: Blow up of the L1 chamber. Due to  $8 \text{ mbar}$  overpressure in the chamber it blows up similar to an air balloon. The values plotted here correspond to the center of the gas gap, which corresponds to half of the detectors deformation. Therefore a blow up of  $1.6 \text{ mm}$  is observed, [Lösel, 2017].

distance is too large this device can provide a veto for such a muon with a large scattering angle. In Table 1, taken from [Müller, 2013], Gaussian widths of the distribution of small angle Coulomb scattering are shown for eight relevant muon energies when traversing the setup of the CRF.

In order to reject muons with too low energy, the resolution of the detector should be at least as good as the width of the angular distribution of the deflected muons. In this table it can be seen that with a resolution better than  $10 \text{ mm}$  already a good variety of rejection

---

$E_\mu$ [GeV]	< 1	1	2	3	4	5	6	> 6
$y$ [mm]	> 100	60	30	20	20	10	10	< 10

Table 1: Gaussian width of scatter for six muon energies, taken from [Müller, 2013].

levels can be achieved.

In the second part of the thesis a proof of concept study for such a detector is presented.

## 6 PoSSuMuS - A Position Sensitive Scintillating Muon SiPM Detector

PoSSuMuS is a scintillation detector providing two dimensional spatial resolution due to its trapezoidal shape. In this chapter first the basics about scintillation and important information concerning a silicon photomultiplier (SiPM) are discussed, followed by the concept of PoSSuMuS. Finally the results of first prototypes and the achieved spatial resolution are presented.

### 6.1 Scintillating Materials

Before actually introducing the physics of scintillation, basic principles of the energy loss of particles in matter are discussed. The energy loss is described by the Bethe - Bloch formula, [PDG, 2012], plotted in Figure 57 for muons in copper.

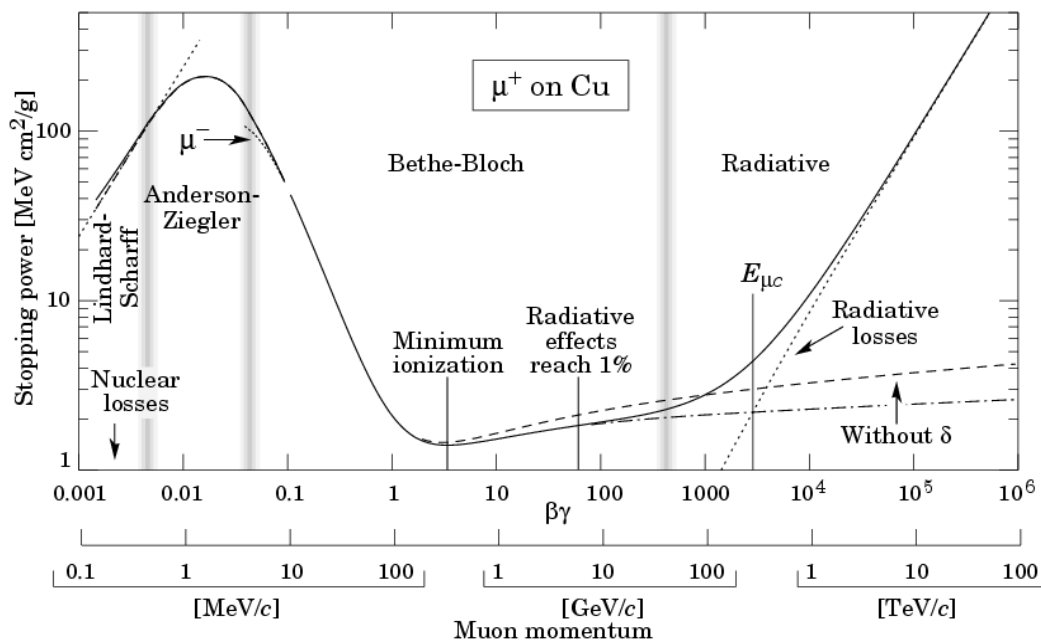


Figure 57: Energy loss of a muon traversing copper according to Bethe-Bloch, [PDG, 2012].

This distribution describes the mean energy loss of particles. Important for the later introduced detector concept is an energy loss, which is small compared to the particle's energy and therefore in a very good approximation constant for traversing a piece of plastic of up to 100 mm thickness. The particle momenta, discussed in this thesis, reach from a few GeV for cosmic muons up to  $\approx 100$  GeV for particles in a test beam at CERN<sup>10</sup>. When the ionization

<sup>10</sup>In a test beam 2012 120 GeV pions have been used, while 2016 muons coming from the decay of 120 GeV pions are used. According to [PDG, 2012] the difference in energy loss for muons and pions with an approximately equal energy is small.

power for a cosmic muon lies in the minimum of the Bethe-Bloch formula, such a particle is called minimum ionizing particle (MIP), which is the case for cosmic muons. The particles in the test beam lose only about a factor of two more energy and an approximately constant energy loss can be assumed for both types. But even if this is the case for the mean energy loss, the momentary energy loss of a single particle follows a Landau distribution [Landau, 1944]. This distribution has a steep rising edge and a slower falling edge, meaning that the mean energy loss is higher than the most probable one and even higher losses can occur up to a kinetically given maximum. A measurement of the deposited energy of cosmic muons in PoSSuMuS is shown in Figure 58, including a fit of a Landau function to the data.

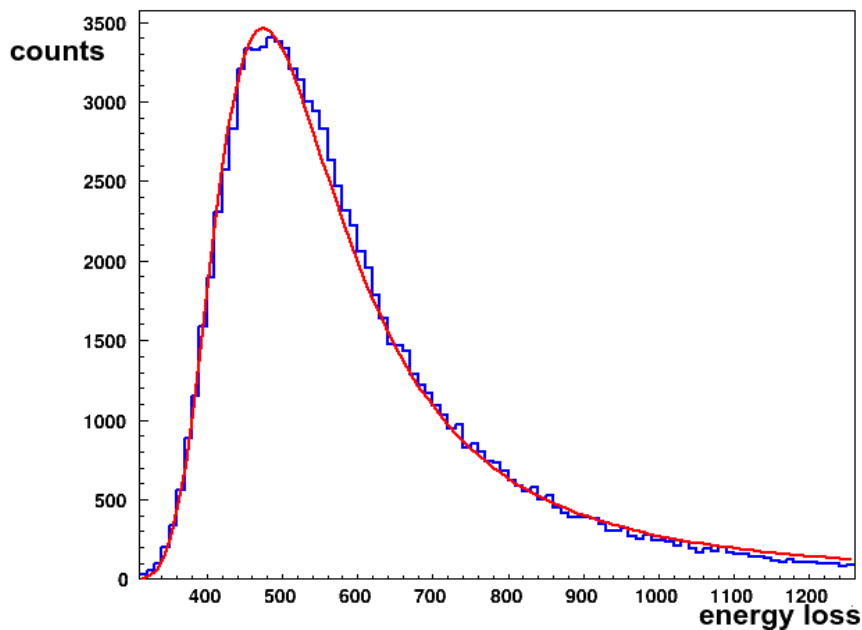


Figure 58: Landau distributed energy loss measured with cosmic muons in PoSSuMuS. Figure taken from [Müller, 2013].

A special form of energy loss for charged particles is a scintillating process. A scintillation material has to provide an electron structure which can be excited easily by a traversing particle. In the de-excitation process scintillation light is emitted via two processes, shown in Figure 59.

The ground state of the molecule is called  $S_0$  which is a singlet state. A traversing particle can excite this molecule in its higher singlet and triplet states like  $S^{**}$  or  $T^{**}$ . Via internal degradation, which happens either without light emission or with low energetic photon emission, the molecule undergoes a deexcitation to its first excited singlet or triplet state,  $S^*$  or  $T_0$ , respectively, depending on its initial excitation. The decay from  $S^*$  to  $S_0$  is called fluorescence and happens via emission of light. While this process is with up to  $10^{-8}$  s very fast, [Leo, 1994], the direct decay from  $T_0$  to  $S_0$  is forbidden by multipole selection rules. It

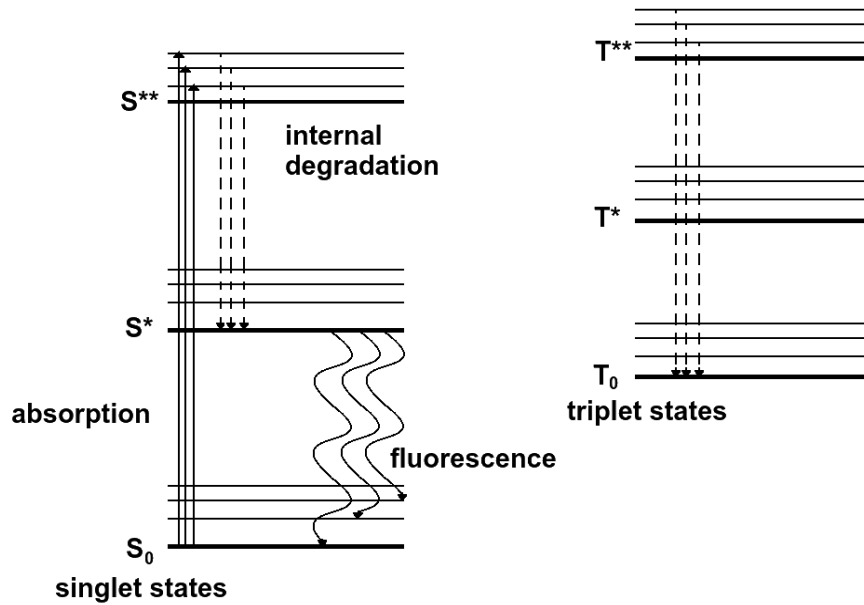


Figure 59: Energy levels of scintillation. The transition from a highly excited state down to the lowest excited singlet or triplet state happens via internal degradation, which is either a non radiative process or a process with emission of low energetic photons. The transition from the lowest excited level to the ground singlet state is a fast process and accompanied by emission of a photon typically in the upper range of the visible spectrum, called fluorescence. In contrast to this the transition of a triplet state to the singlet ground state is called phosphorescence and takes much longer, because it is forbidden according to selection rules for dipole transitions. So the process has to happen by an interaction with another triplet state of an excited molecule, [Leo, 1994].

happens in reality with a second molecule via



The  $S^*$  produced this way can now emit a photon to decay to the ground state. This process is called phosphorescence. A theoretical decay involving both processes is plotted in Figure 60.

The material used for PoSSuMuS is the plastic scintillator BC 400, [Saint Gobain, 2011a], consisting of the scintillation material polyvinyltoluene, shown in Figure 61.

For this material it turns out, that the phosphorescence is negligible and the fluorescence is so fast, that even the rise time of the signal plays a role. The entire process can be described as a Gaussian function multiplied by an exponential function, [Bengtson and Moszyński, 1974]:

$$N(t) = N_0 \cdot f(\sigma, t) \exp\left(-\frac{t}{\tau}\right) \quad (6.1.2)$$

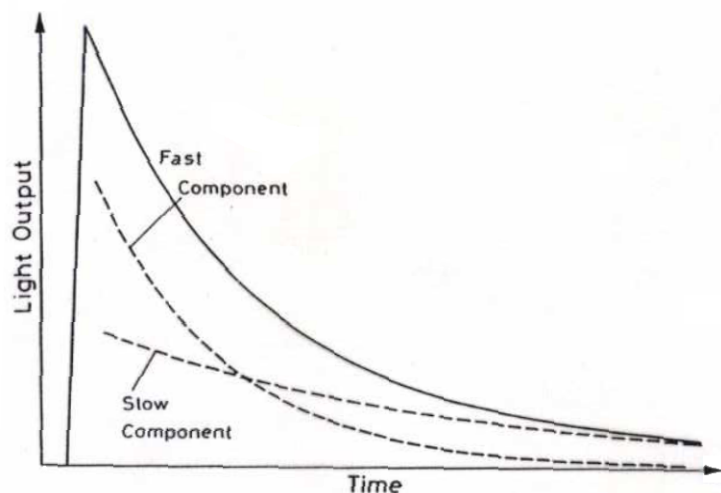


Figure 60: Light emission of a scintillator divided in fast component (fluorescence) and slow component (phosphorescence), [Leo, 1994].

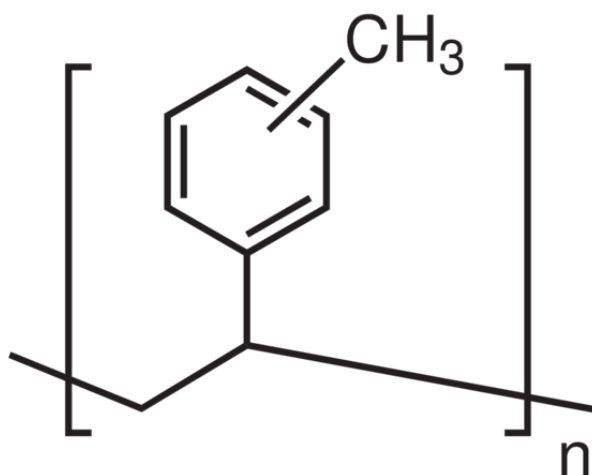


Figure 61: One repetition unit of polyvinyltoluene, [Sigma-Aldrich, 2013].

with the two time constants  $\sigma = 0.7 \text{ ns}$  and  $\tau = 2.4 \text{ ns}$ , [Leo, 1994].

Since a material emitting a certain wavelength will also absorb this wavelength very well, a bare scintillator would be opaque to its own light. By adding additional materials which shift the wavelength of the scintillation light from UV to blue this problem can be solved. The wavelength shifting is based on the Franck-Condon principle, shown in Figure 62.

Following this principle a decay happens dominantly to a state where both initial and final wave functions of a molecule have the highest overlap. If during excitation the wave function gets not just an energy shift but also a spatial shift as due to vibrations, a decay into the ground state, hence a re-emission of a photon with exactly the same wavelength, is not the

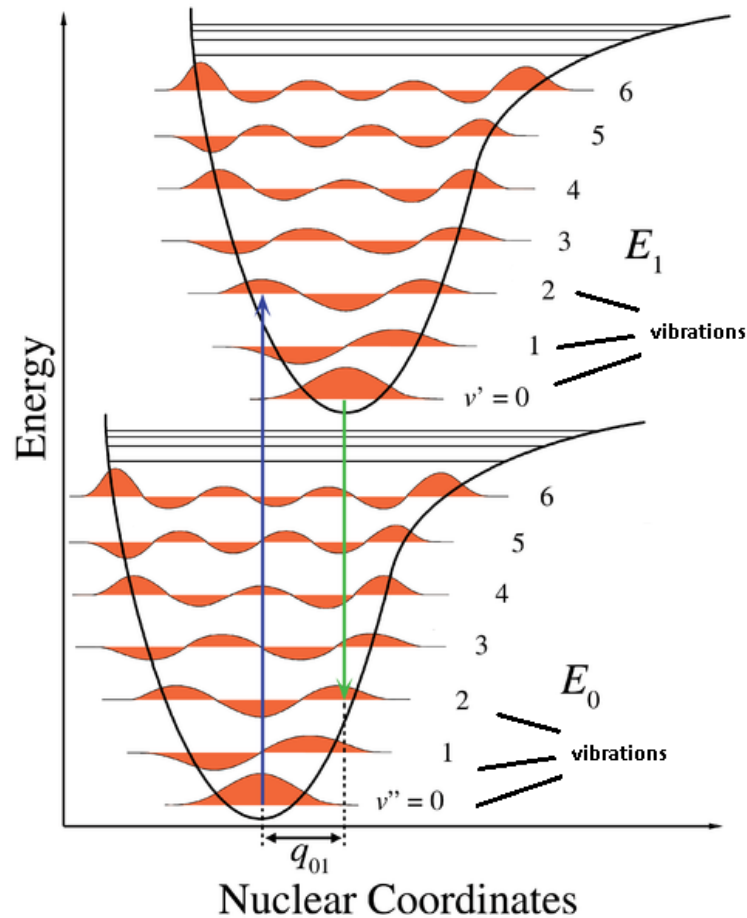


Figure 62: Wavelength shifting explained with the Franck-Condon principle. The latter says, that a decay of an excited state has the highest probability for a transition into a state where initial and final wave function have the highest overlap. If the molecule gets a spatial shift during excitation a decay into the ground state is not the most probable process any more. The emitted photon has a longer wavelength than the initial photon. The picture is taken from [Wikimedia Commons, 2007].

most probable one anymore. Any other decay will result in a photon with a longer wavelength compared to the incoming photon, [Meschede, 2015]. In the case of the scintillator this is done in several steps of wavelength shifting because in a single process the amount of the shift is limited but the photon detector has a certain optimal wavelength, and to reach this, several steps are required, see Figure 63.

Also the light guiding fibers used here perform a wavelength shifting. A normal light guide has a higher refractive index than its environment. Light coupled frontally into the fiber can be guided using total reflection. But if the coupling happens from the side, as it is the case for PoSSuMuS, a guiding is no longer possible because the entering photon breaks already at this stage the condition for total reflection and this condition cannot be reached anymore. Hence light coming from the side will leave the fiber just at the opposite of its entrance.

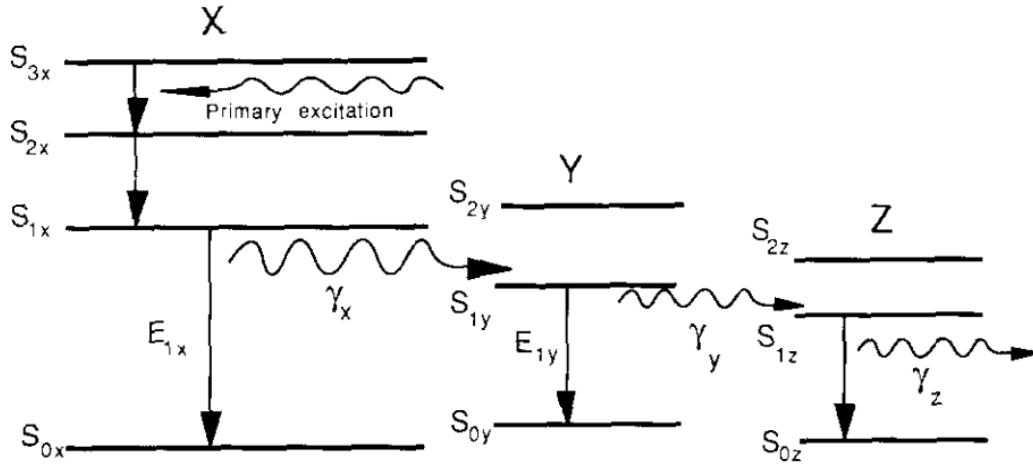


Figure 63: To make a scintillator transparent, wavelength shifting molecules, so called fluors, are added to the scintillator. A cascade of wavelength shifting processes transforms the initial UV scintillation light towards the visible range, [White, 1988].

Using the process of wavelength shifting has the advantage that the incoming photon is absorbed and a new photon is emitted in a direction which is independent of the former direction. A certain amount of light will therefore fulfill the condition of total reflection and is guided towards the end of the fiber. The solid angle for which this condition holds can be calculated from the refraction index of the fiber core of  $n_{core} = 1.60$  and of the fiber cladding  $n_{clad} = 1.49$ . First one obtains the total reflection angle  $\vartheta_{tot}$  using Snell's law

$$\vartheta_{tot} = \arcsin \frac{n_{clad}}{n_{core}} = \arcsin \frac{1.49}{1.6} = 1.198 \quad (6.1.3)$$

This angle inserted into the formula for the solid angle gives:

$$2 \cdot \int_0^{2\pi} d\varphi \int_0^{\frac{\pi}{2} - \vartheta_{tot}} d\vartheta \sin \vartheta = 2 \cdot \int_0^{2\pi} d\varphi \int_0^{\frac{\pi}{2} - 1.198} d\vartheta \sin \vartheta = 0.8632 \quad (6.1.4)$$

This calculation uses the symmetry of the photon emission, hence the total solid angle, for which the condition of total reflection is fulfilled, is calculated doubling the one for a single direction. Dividing this result by the entire solid angle  $4 \cdot \pi$ , one gets the percentage of photons guided via total reflection, which is in this case only 6.9 % of all shifted photons. A sketch of this is shown in Figure 64.

A direct consequence of this way of coupling light into a fiber is that every little bending of the fiber reduces the amount of light which can be guided. In common light guiding applications, the light is coupled perpendicularly into the front of the fiber, hence up to a certain bending radius the condition for total reflection still holds. In this case using a

## 6 POSSUMUS - A POSITION SENSITIVE SCINTILLATING MUON SIPM DETECTOR

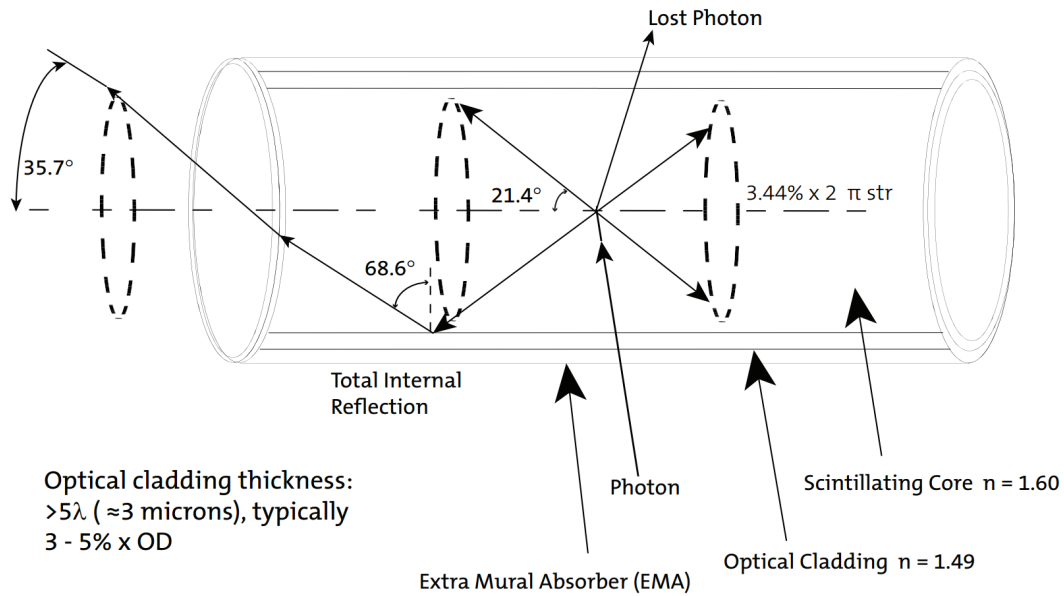


Figure 64: Scheme of a wavelength shifting fiber. A photon enters the fiber and gets absorbed, exciting a molecule of the fiber. If the emission of a photon happens with an angle smaller than  $21.4^\circ$  it can be guided to the end of the fiber. All other photons leave the fiber and are lost, [Saint Gobain, 2011b].

wavelength shifting fiber to couple photons from the side most of the light is already guided under the maximum angle. This light would immediately be lost due to fiber bending and it should be avoided, since already 93 % of the incoming light is lost.

The path of the wavelength shifted photons was simulated by [Kröger, 2014], using the simulation toolkit Geant4, [GEANT4-Collaboration, 2017]. It was shown that most of the photons are guided along the edge of the fibers. This has also an impact at the point of exit of the guided photons which is shown in Figure 65.

This histogram shows the end of a fiber with a diameter of  $1.5 \text{ mm}$ . The amount of photons exiting the fiber is with  $\approx 8000$  per bin in the edge region much higher than the central bins with just 4500 in this simulation.

In a next step the photons have to be detected, which in this case is done using SiPMs.

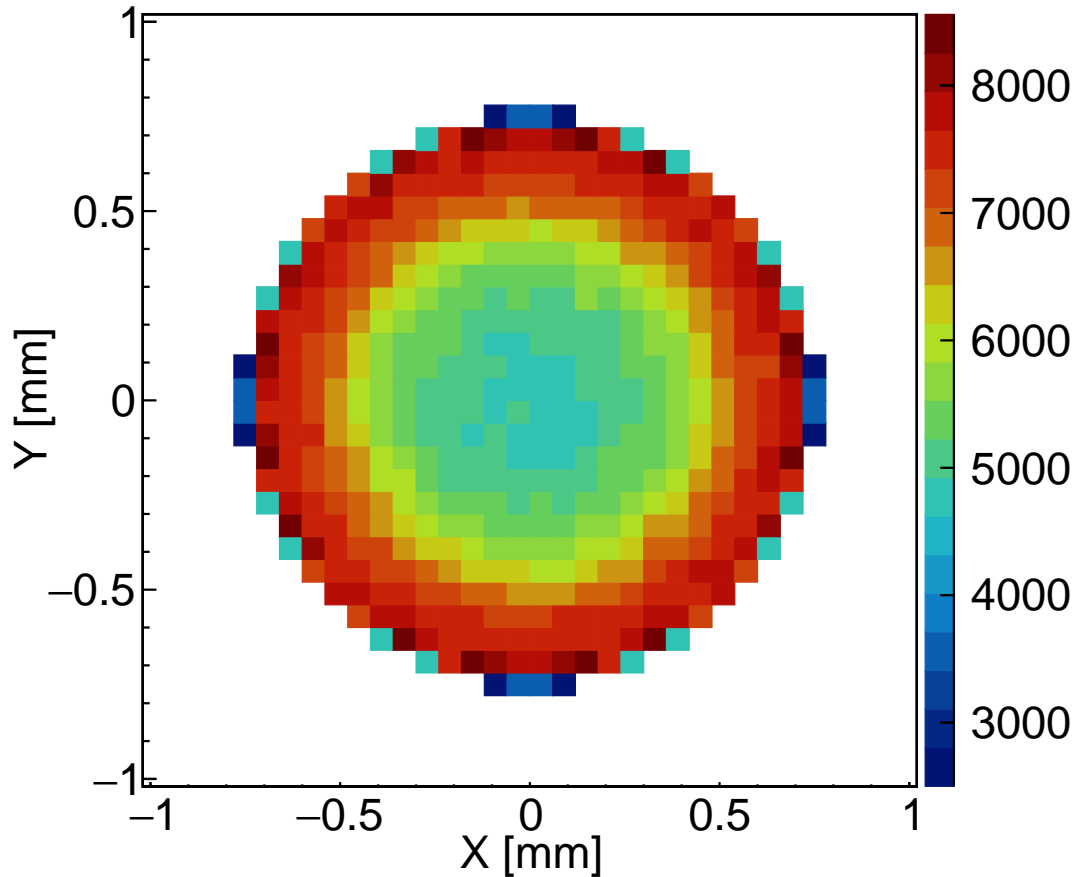


Figure 65: Simulation of light output of a round fiber. It can be seen that most of the photons are emitted close to the border of the fiber, [Kröger, 2014].

## 6.2 Silicon Photomultipliers

All information about semiconductor devices being summarized in the following is taken from [Leo, 1994]. A silicon photomultiplier (SiPM) is a substitute for a photomultiplier tube on semiconductor basis. It is a matrix of light sensitive avalanche photo diodes (APD) connected in parallel. Like in a diode the junction of the p- and n-type layer forms a depletion region, where the electrons from the n-type layer combines with the holes from the p-type layer, leaving themselves holes behind. The p-doped side close to the junction therefore gets negatively charged and vice versa, while no free charge carriers are available anymore in this region. This process creates a stationary electrical field, stopping further charge carrier diffusion at a certain threshold. Applying a voltage to the diode, such that the minus pole is connected to the n-type layer and the plus pole to the p-type, the diode is conductive, while it is blocking in the reverse biased direction. Operating a diode in reverse biased mode increases the depletion region. Increasing this bias voltage ( $V_{bias}$ ) prevents general charge flow, only a tunneling of electrons and holes through the band gap is allowed, which means a movement of charge through a charge carrier depleted region. Above a certain threshold

## 6 POSSUMUS - A POSITION SENSITIVE SCINTILLATING MUON SIPM DETECTOR

---

for  $V_{bias}$ , called breakdown voltage ( $V_{BD}$ ), the charge gets during this spatial movement enough energy to produce secondary electron hole pairs due to collisions with the lattice. These additional electrons and holes are accelerated themselves by  $V_{bias}$ , producing further electron hole pairs. Hence, one tunneling electron can trigger a self sustaining avalanche of charges. This way of operating a diode is called Geiger mode. To stop this avalanche in a SiPM a resistor is connected to the diode in series. The avalanche current in the diode causes a voltage drop at the resistor, thus reducing the voltage at the diode below  $V_{BD}$  and quenching the avalanche. Since the tunneling is a process not including any external light source it is called dark current. SiPMs are designed such that interacting photons are triggering an avalanche. But an avalanche can also be triggered by dark current events. The combination of several avalanche photo diodes and quenching resistors, called pixels, connected in parallel, as it is the case for a SiPM, is shown in Figure 66 as an equivalent circuit diagram.

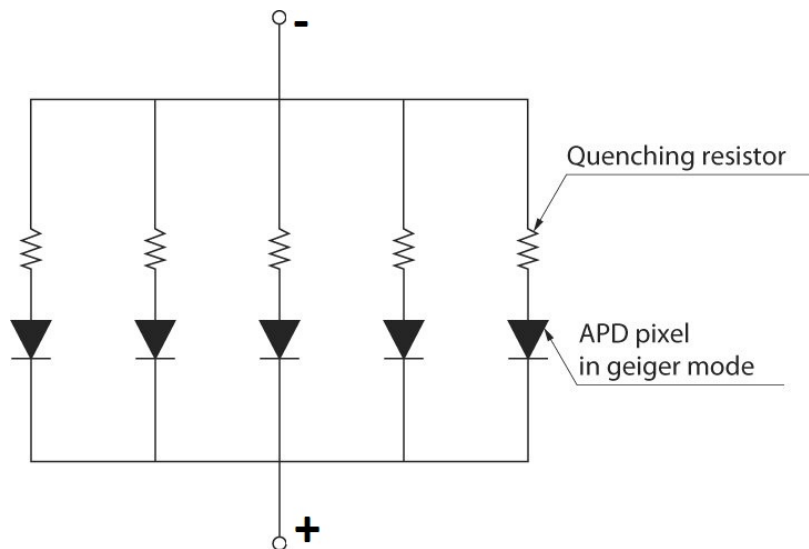


Figure 66: Equivalent circuit diagram of a SiPM. Each combination of a diode and a resistor is a pixel of the SiPM, [Hamamatsu Electronics, 2008]

The difference of  $V_{bias}$  and  $V_{BD}$  is defined as over voltage ( $V_{over}$ )

$$V_{over} = V_{bias} - V_{BD} \quad (6.2.1)$$

which is typically in the order of a few volts.  $V_{over}$  gives a measure of the kinetic energy the charges get on their way through the diode. A higher kinetic energy lowers the mean free path of the charge before an ionizing collision with another atom, hence more secondary charge carriers are produced. This so called gain is not depending on the number of photons hitting a pixel, since it is operated in Geiger mode. The amount of photons reaching a SiPM in each event can only be determined by assuming that each photon hits a cell which is not

hit by any other photon in this event. Then the pulse height is directly proportional to the number of incident photons. For a low photon count, given for example by a dark current event, the different numbers of simultaneously firing pixels are easily distinguishable, see Figure 67.

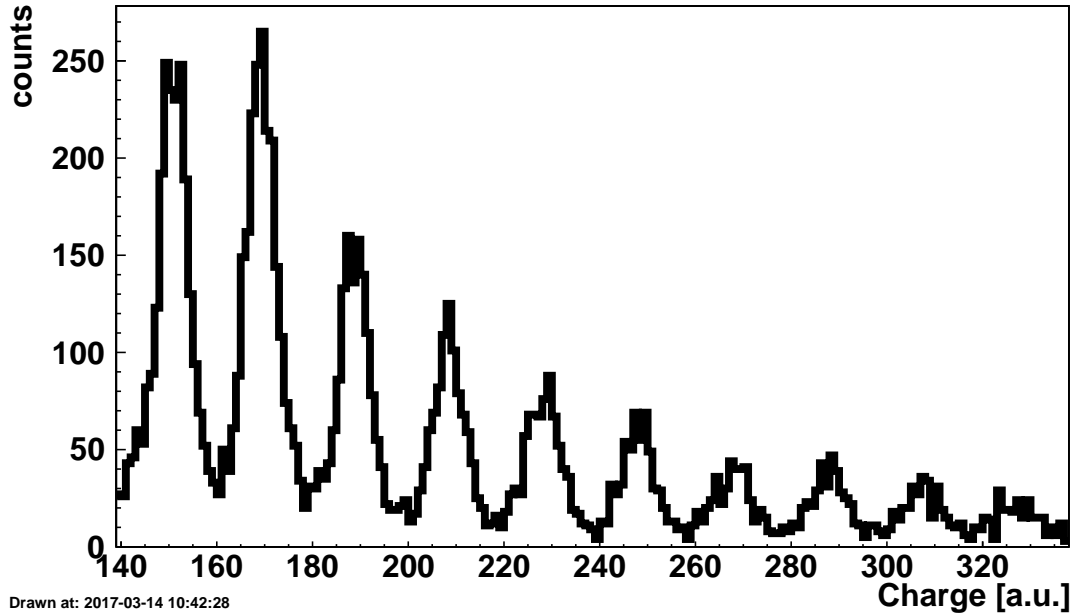


Figure 67: Spectrum of dark current detected in a SiPM. Each peak corresponds to a certain amount of fired pixels.

Each peak in this plot of a dark current measurement with 20000 events corresponds to a certain number of fired pixels. The leftmost peak corresponds to events with three fired pixels. The peaks for events with one or two fired pixels are not shown since the pulse height of such events is below the discriminator threshold<sup>11</sup>. Such a nice picture, where the individual firing pixels are clearly distinguishable, is not possible to obtain for a larger amount of incoming photons, since the pixels do not provide an avalanche with an identical amplitude, hence the picture will be washed out. The difference between two neighboring peaks is the gain and is only depending on  $V_{over}$ . A drawback of SiPMs is their high sensitivity to temperature. The actual breakdown voltage has a temperature coefficient of  $60 \frac{mV}{K}$ , [Hamamatsu Electronics, 2008]. Providing a constant bias voltage and having a temperature depending breakdown voltage,  $V_{over}$  and therefore the gain is varying with temperature. This can be compensated in a real muon measurement by adjusting  $V_{bias}$  according to temperature changes and determining the gain as the mean distance between adjacent peaks in a timely close dark current measurement which is used in the analysis to scale the data to constant gain. A more detailed explanation of this calibration process is given in chapter 7.2.

For the experiment to be conducted, it is important to know how many photons in average

<sup>11</sup>The discriminator is part of the readout chain explained in chapter 7.3.

## 6 POSSUMUS - A POSITION SENSITIVE SCINTILLATING MUON SIPM DETECTOR

---

are expected per event. A smaller pixel size and therefore a larger amount of pixels per SiPM is necessary if the photon density becomes high, because a double hit of a pixel directly means the loss of a photon. But going to a larger amount of pixels, also the inefficient area of the SiPM is enlarged, e.g. due to optical and electrical insulation between adjacent pixels which does not shrink with the pixel size. This means for a photon density expected to be low, the dead area should be small, hence a larger pixel size is requested. For the investigation of a new geometry for PoSSuMuS, discussed in chapter 7, the S12572-100C SiPMs from Hamamatsu, [Hamamatsu, 2015], are used. The 100 in the name means that this device has a pixel size of  $100 \times 100 \mu\text{m}^2$ , hence this SiPM has an active area of  $3 \times 3 \text{mm}^2$  with 900 pixels in total. A photograph of it is shown in Figure 68.

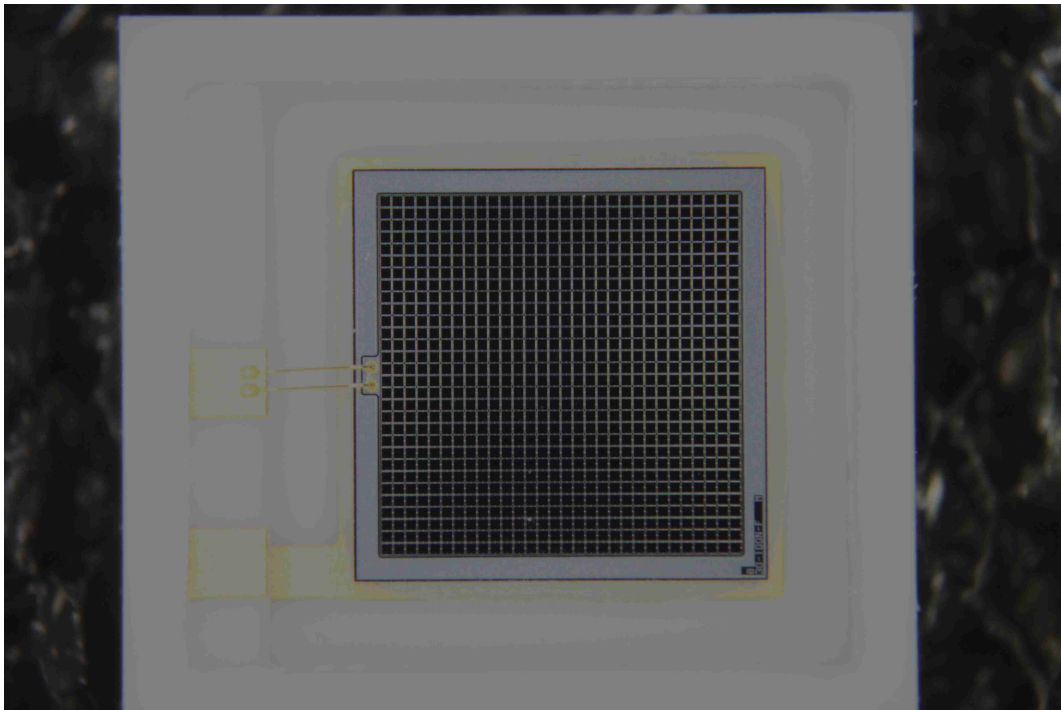


Figure 68: Photograph of a SiPM with  $3 \times 3 \text{mm}^2$  active area. The pixel size is  $100 \times 100 \mu\text{m}^2$ , hence 900 pixels are visible.

In the discussion it will become clear that a photon count in the order of up to 150 firing pixels per event is recorded by each SiPM, being rather low compared to the 900 cells of the SiPM, hence the large pixels. But, as shown in Figure 65, the light arriving at the device is not distributed homogeneously over its active area. It is therefore reasonable to investigate also SiPMs with smaller pixels in future setups.

### 6.3 PoSSuMuS - The Detector Idea

The amount of light produced by a muon traversing a scintillator is depending on its energy, the scintillation material, the landau distributed energy loss and the path length in the scintillator. The last point is the crucial one for PoSSuMuS, having a varying thickness, hence a determination of the light yield gives a measure on the distance the muon traveled in PoSSuMuS. Since it is known where the scintillator has a certain thickness the position of the muon impact can be reconstructed out of the light yield. A sketch of this detector is shown in Figure 69.

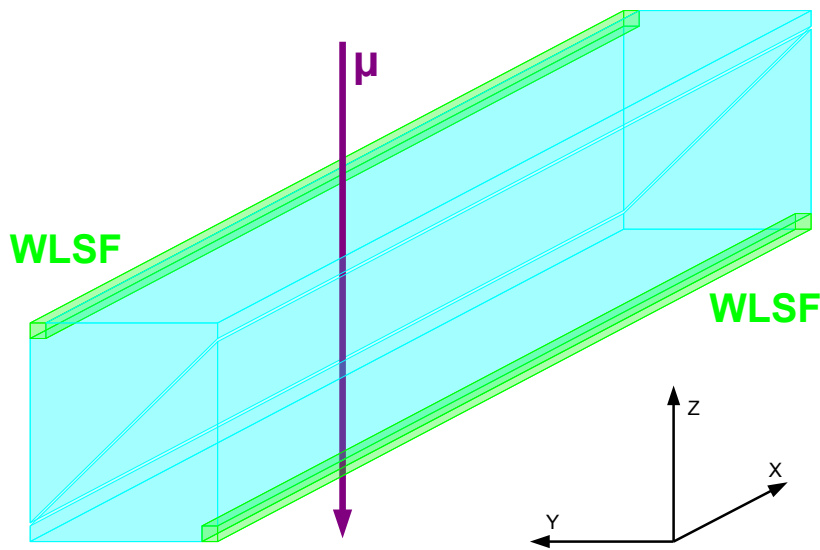


Figure 69: Scheme of a PoSSuMuS detector. It is formed by two trapezoidal scintillator rods, each optically isolated from the other. A charged particle like a muon passing the detector produces scintillation light which is collected by the wave length shifting fibers (WLSF) and is guided to their ends, where SiPMs are located to detect the light and convert it into an electrical signal. If the muon is closer to the fiber of, for example, the upper trapezoid, it traverses a longer path in this scintillator and a shorter path in the lower one. Thus a higher signal is measured in the upper wavelength shifting fiber (WLSF), a lower signal in the lower WLSF. By reading out the time it takes the light to propagate to the left and to the right end of the fiber and by comparing the amount of light produced in the upper and lower scintillator, a X and a Y coordinate can be obtained, respectively.

Two trapezoidal shaped scintillators are forming one module of PoSSuMuS. Both halves are optically isolated from each other. The cover material for this isolation is discussed later on, since it has a great influence on the performance of the detector. The light produced in both halves is collected by a wavelength shifting fiber and guided to the SiPM readout. A two dimensional spatial resolution is achieved by reading out the arrival time and the amount of light detected by the SiPMs. The time of flight coordinate is defined to be the X-coordinate while the light yield direction is called Y-coordinate.

### **The X-coordinate:**

On each end of a wavelength shifting fiber a SiPM is mounted. During readout the time of arrival of the photons at the SiPM is measured. A comparison between the arrival time at the left and at the right SiPM gives a measurement of the path length of the photon towards the readout. This difference in time can be converted to a spatial position of the muon.

Statistically it is possible, that, e.g., the muon traverses the detector close to the left SiPM, but the photons perform a lot of reflections before they hit the left end of the scintillator and fewer reflections towards the right end, which leads to wrong reconstruction of the muon position. Therefore a good reconstruction requires a good light yield to increase the amount of photons performing less reflections before being detected.

### **The Y-coordinate:**

Since the energy of the muon and the scintillator material are identical for both halves, only the path length and the energy loss differs when it comes to measuring the amount of light produced in both trapezoids. If the path length in the first trapezoid is shorter, then it will be longer in the second one and vice versa. Neglecting the Landau energy loss for the moment, this means that the particle produced less light in the first half and more light in the second half, and this dependency is linear for incidents of muons perpendicular to the X-Y scintillator plane. Therefore a position in this coordinate is given by the ratio of the produced light in both scintillators. In this case three effects influence the resolution:

- The first one is the energy loss following a Landau distribution. For example, it is possible, that in the half with less path the muon undergoes a lot of central impacts, hence producing a lot of light compared to the long path in the other half, shifting the reconstructed position towards the center of PoSSuMuS, or even to the other side. It is, more extremely, also possible to reach a light ratio which could mathematically not be obtained with the used geometry. The reconstructed point will be outside the scintillators. One either has to live with this problem or one tries to find a fiber position on the trapezoid where the amount of arriving photons is independent of the path length. In such a case only the Landau distributed energy loss is responsible for detecting different light yields. Out of this fiber the current energy loss can be extracted and used further to eliminate this dependency in the position sensitive fiber. Such a position could exist on the thin base of PoSSuMuS, where the geometrical dependency is canceled with the impact distance dependency.
- The amount of light arriving at the fiber is dependent of the distance between the place of photon creation and the fiber, [Müller, 2013]. The closer both points are, the more light is collected. In Figure 70 this behavior is shown schematically. For a fiber position at the broad end of the trapezoid this gives a monotonously growing light intensity when getting closer to the fiber. On the one hand a larger

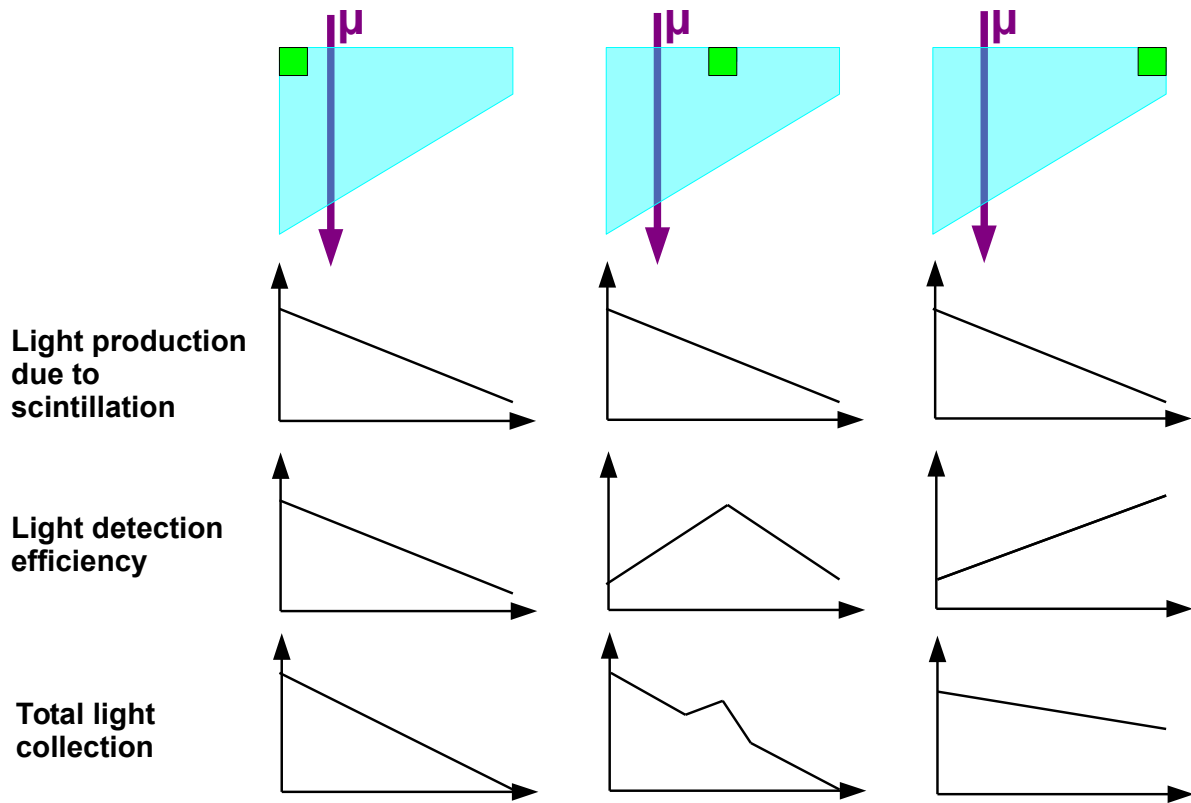


Figure 70: Scheme of light detection efficiency for different fiber positions. The total light collection of a fiber depends on the light production and the detection efficiency, which is higher the closer the muon impact happens to the readout fiber. For a fiber on the thick base of the trapezoid both the light production and the detection efficiency goes down for decreasing scintillator thickness, adding up to a steeply decreasing function. In contrast to this for a fiber at the thin base the detection efficiency increases, because the impact happens closer to the fiber. This ends up in a less steep functionality which can even be flat or has a changed sign. In case of a fiber being positioned not at the edge, the detection efficiency is not monotonous and the curve for the total light collection will have a peak at the position of the fiber.

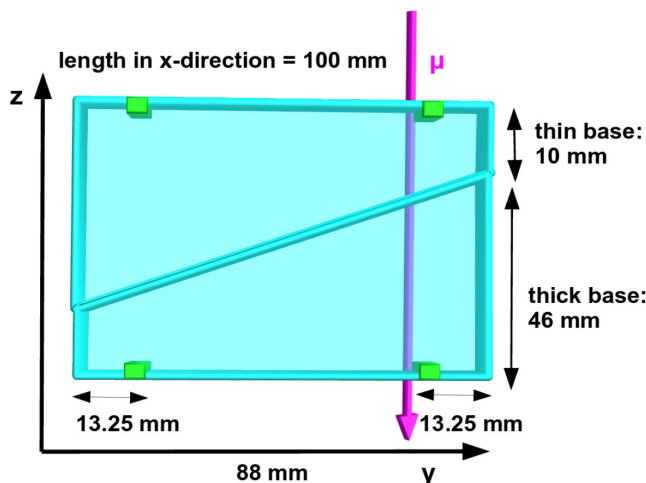
path of the muon, hence a passage closer to the just mentioned fiber, results in more photons created and on the other hand being closer to the fiber additionally increases the detection efficiency. If the fiber is located at the thin side, still more light is produced if the muon is farer away from the fiber, but the detection efficiency goes down. This gives rise to the assumption, that it could be possible to find a position insensitive place for the fiber and therefore a possibility to correct for the Landau distributed energy loss. A fiber somewhere between both edges shows a non monotonous light yield, since the path length is a linear function of  $Y$ , while the distance to the fiber has a turning point, see Figure 70.

- Similar to the X-coordinate the third influence is given by the total amount of detected light. If the detection efficiency is high, the loss of single photons due to absorption does not change the total light yield that much. Hence the shift of the reconstructed position due to local inefficiencies becomes more and more negligible for higher light yields.

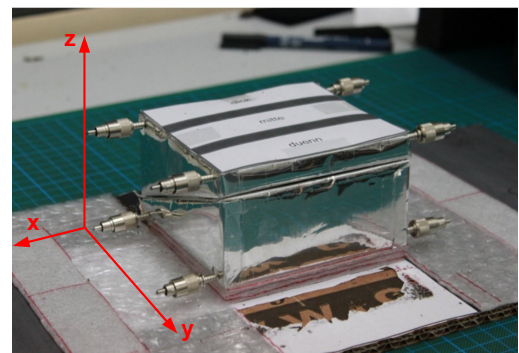
Since the timings will show a much broader distribution, see chapter 7.5.2, than the light yield, the Y coordinate will be the more precise one. In the next chapter the present status of PoSSuMuS is summarized motivating the applied changes to this concept.

### 6.4 Limitation of the Design of Predecessor PoSSuMuS Versions

Up to now there are two predecessor designs of PoSSuMuS with noteworthy results having the same trapezoidal cross section. The major change in geometry is an improved fiber position for the second prototype, [Ruschke, 2014]. The dimensions and a photograph of the prototype with optimized fiber positions is shown in Figure 71.



(a) Schematic drawing of PoSSuMuS Geometry



(b) Photograph of second prototype

Figure 71: Figure 71a shows a drawing of the second prototype. The dimensions of the trapezoid are identical for the first and second one, just the fiber positions and the length differ, with the latter being 300 mm for the first and 100 mm for the second detector. In Figure 71b a photograph of this prototype is shown. One can see the connectors of the fibers positioned right after the scintillator, [Ruschke, 2014].

The scintillation material used, BC400 [Saint Gobain, 2011a], comes from the OPAL experiment, a former detector at the LEP accelerator at CERN. The scintillator rods had a rectangular cross section of  $\approx 50 \times 90 \text{ mm}^2$  and a length of 2.5 m. Out of those rods trapezoidal geometries have been milled which, as a first try, should produce low waste but still a significant difference of thin and thick base. Therefore a length of 45 mm and 10 mm was

chosen for the thick and thin base, respectively, with a height of 88 *mm*, see Figure 71a. While the mechanical workshop can produce trapezoids with lengths up to 300 *mm*, also length of only 100 *mm*, have been investigated, because they are easier to handle.

For the collection of scintillation light, wavelength shifting fibers BCF92 [Saint Gobain, 2011b], have been glued into grooves milled in these trapezoids. While for the first prototype five grooves have been distributed homogeneously on the top side, the second version only had two grooves, one close to the thick and one close to the thin base, as shown in Figure 71. This optimization was done due to the non monotonous light collection of the fibers described in chapter 6.3. Since there is only one fiber per groove, it is possible to use common connectors of fiber optics to connect the wavelength shifter to the SiPM. As wrapping material for the scintillators bare aluminum foil was used for the first prototype, while for the second prototype three layers of a diffuse reflective cover, namely Tyvek, [DuPont, 2012], were chosen, which provided a higher light yield. To further isolate each scintillator half, a final layer of aluminum was stretched around it.

As these two predecessor versions of PoSSuMuS, the first and second prototype, are the basis for the final setup, I recollect first the important results from [Müller, 2013] and [Ruschke, 2014]. The first prototype was up to now the only PoSSuMuS device with a length of 300 *mm* and hence the one where it makes sense to study the time of flight coordinate. Results of this X coordinate are summarized from [Müller, 2013] in chapter 6.4.1. Due to several improvements concerning the light yield, the second prototype has a significantly higher spatial resolution in the Y coordinate, taken from [Ruschke, 2014], shortly presented in chapter 6.4.2.

#### 6.4.1 Results for the Time of Flight Coordinate obtained with the First Prototype

The first prototype, with a length of 300 *mm*, was investigated in detail with a 120 *GeV* pion beam at CERN. This beam hits the detector perpendicularly and the readout was triggered by two crossing scintillators with a cross section of  $\approx 5 \times 5 \text{ mm}^2$ . Since this is the first PoSSuMuS, it was of interest to investigate it in greater detail, hence one also wanted to see the pulse shape and used for this task a flash analog-to-digital converter (FADC)<sup>12</sup>, sampling the pulse in steps of 0.5 *ns*. Three locations of irradiation along the two directions have been studied, which is sketched in Figure 72.

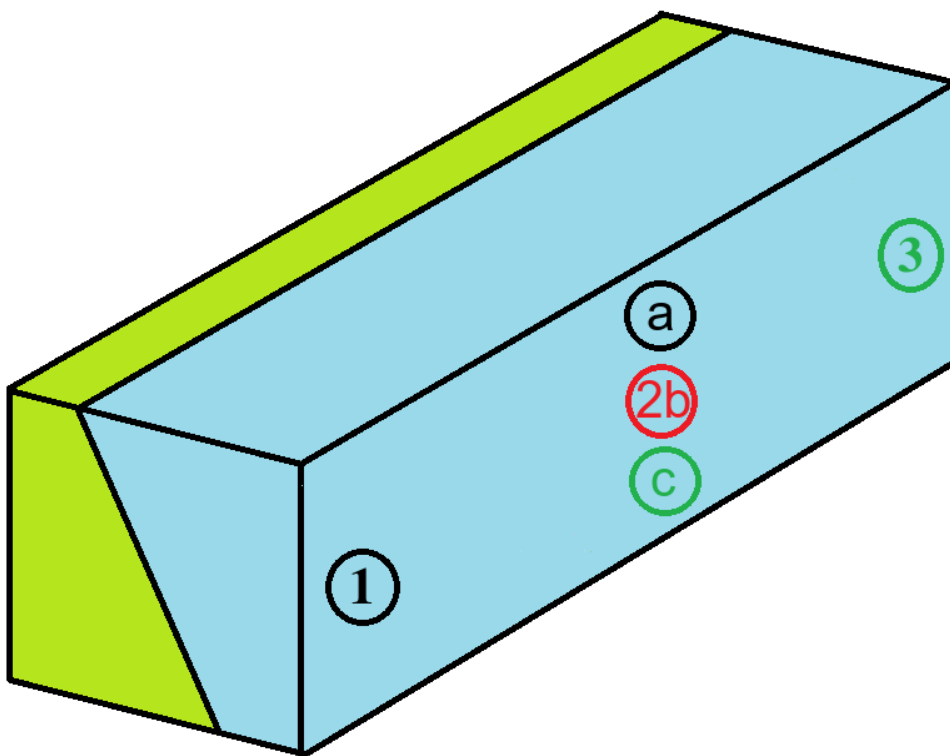


Figure 72: Scheme of the first CERN Prototype. In this thesis only the trigger positions 1 2 and 3 are discussed. They are formed by two crossing scintillators forming a cross section of  $\approx 9 \times 9 \text{ mm}^2$ . The exact coordinates of this trigger cross is given in Table 2. [Müller, 2013].

As best timing information a certain threshold was defined for each channel and the first bin in the FADC pulse shape above it was chosen as timing. Performing instead a fit to the signal gave broader distributions, [Müller, 2013]. A consequence of this is, that reconstructing the timing just one bin wrong gives a result which is off by 100 *mm*. This timing is converted

---

<sup>12</sup>V 1729, [CAEN, 2011]

into a spatial coordinate using

$$x = \frac{1}{2} \cdot (t_{left} - t_{right}) \cdot \frac{c}{n} \quad (6.4.1)$$

with the refraction index of the scintillator  $n$ . The timings  $t_{left}$  and  $t_{right}$  are the measured arrival times of the signal on the left and right side of PoSSuMuS. With the center of the detector being in the origin, the relevant trigger positions for the timing study are 1, 2 and 3, located at  $-110 \text{ mm}$ ,  $0 \text{ mm}$  and  $+120 \text{ mm}$ , respectively<sup>13</sup>. The distributions of all three positions is shown in Figure 73.

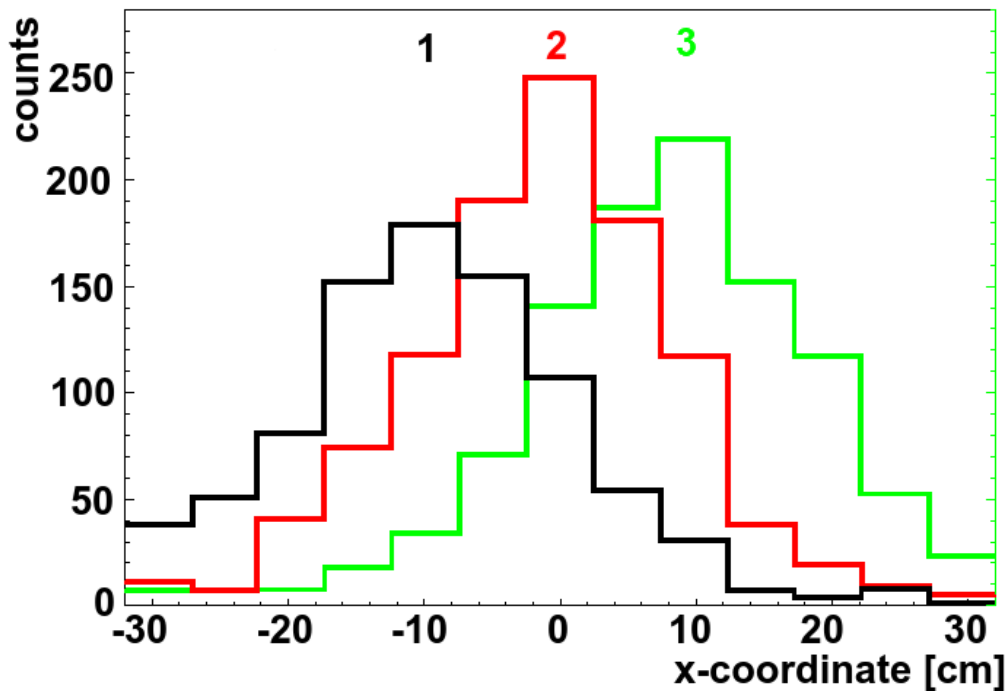


Figure 73: Timing result of the first prototype. The peaks are a bit too close to the center, see Table 2, but still a clear position sensitivity is noticeable, [Müller, 2013].

Fitting a Gaussian to all three distributions gives the value shown in Table 2.

	true	measured
$X_1 [mm]$	-110	$-95 \pm 99$
$X_2 [mm]$	0	$-10 \pm 92$
$X_3 [mm]$	+120	$86 \pm 100$

Table 2: Result of the first PoSSuMuS prototype’s X-coordinate investigated at CERN, [Müller, 2013]. The measured values are a bit too small, but the true result is inside the measured errors.

<sup>13</sup>The asymmetry of the three positions is resulting from mounting issues of the triggers.

Compared to the position, where the trigger has been placed, the measured values are slightly too small and an offset of 10 *mm* is given. These results will later serve as a reference measurement and are therefore now re-calculated to the correct values. The offset can originate from just a tiny difference in between the two FADC channels of both SiPMs. Subtracting this offset gives Table 3.

	true	measured offset subtracted
$X_1$ [ <i>mm</i> ]	-110	$-85 \pm 99$
$X_2$ [ <i>mm</i> ]	0	$0 \pm 92$
$X_3$ [ <i>mm</i> ]	+120	$+96 \pm 100$

Table 3: Offset corrected results for reconstructed X-coordinate

One can now calculate the factor that quantifies the offset of the results with respect to the true position. For  $X_2$  to  $X_1$  it is  $\frac{110}{85} = 1.29$ , while for  $X_2$  to  $X_3$  it is  $\frac{120}{96} = 1.25$ . With an average factor of 1.27 the results given in Table 3 can be rescaled and they are shown in Table 4.

	true	measured rescaled
$X_1$ [ <i>mm</i> ]	-110	$-108 \pm 126$
$X_2$ [ <i>mm</i> ]	0	$0 \pm 117$
$X_3$ [ <i>mm</i> ]	+120	$+122 \pm 127$

Table 4: Calibrated results for reconstructed X-coordinate. With the values for the peaks now being very close to the real positions, the errors on the reconstructed positions are trustworthy.

The peaks of the distributions can be reconstructed up to a few *mm* correctly, even the case of non symmetric trigger position was obtained well from the data. Still the distributions with up to 127 *mm* are rather broad. As mentioned, the main problem in this setup was the low light yield and the coarse sampling frequency of the FADC. With the FADC basically replaceable by a much more time resolving time-to-digital converter (TDC), the focus was primarily on optimizing the light collection efficiency of PoSSuMuS, which has especially a very high impact on the precision coordinate described below. After this is achieved, one can return again to the photon time of flight and see how this evolved, see chapter 7.5.3.

### 6.4.2 Results for the Light Yield Coordinate obtained with the Second Prototype

The optimizations done for the second prototype, described in great detail in [Ruschke, 2014], include the following steps:

1. Using only fibers at position sensitive places, see chapter 6.3.
2. Using thicker fibers. At CERN 1 *mm* diameter fibers have been used, while now they have a diameter of 1.5 *mm*, which increases the light collection area and lowers the risk of fiber breaking.
3. Reducing the length of the fiber outside the trapezoid. In contrast to common wave guides, the coupling of the scintillation light into the fiber happens not along its axis but due to the Frank-Condon-Principle, discussed in chapter 6.1. Little bending of the fiber immediately results in light loss. An extreme bending was a problem with high impact for the first prototype.
4. Using diffuse reflective cover. A trapezoidal geometry is not an ideal light guide. In a good guiding system the photons fulfill the requirement of total reflection during the entire guiding length. If this requirement is not fulfilled, a photon will leave the detector and is reflected at the wrapping and such a surface transition increases the chance of absorption. In a trapezoidal shape the probability of two consecutive total reflections is rather low compared to, for example, a round fiber. A diffuse reflecting material can optimize this behavior by reflecting the photon in a random direction compared to the well defined direction of specular reflective cover. This improves the chance to have a total reflection at the next surface and hence the angular acceptance of the detector.

A photograph of the second prototype is shown in Figure 71b and a scheme of the trigger setup can be seen in Figure 74. For this study cosmic muons are used.

It is a 100 *mm* long PoSSuMuS with two single fibers, one close to the thick base and one close to the thin base, for each trapezoid. The fibers are read out on both sides and the over voltage of all eight SiPMs is controlled independently and automatically by a voltage control system designed and developed by [Grossmann, 2014]<sup>14</sup>. Six trigger scintillators are placed around PoSSuMuS, three below and three above it. They have with 100 *mm* the same length as the trapezoids and are 25 *mm* wide each. A trigger is produced, if one scintillator from above and one from below detect a muon at the same time. In the following only vertical tracks are investigated, see Figure 74. A first look at the light yield per channel,

---

<sup>14</sup>This system was slightly optimized and is used in this form in the setup for this thesis, it will therefore be explained in chapter 7.3.

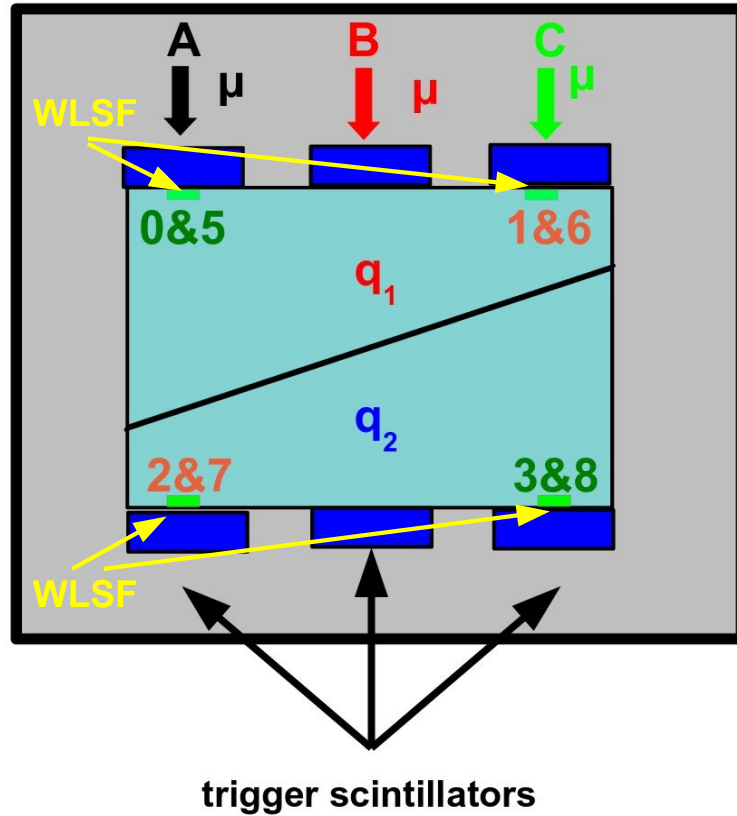


Figure 74: Scheme of the setup for the second prototype using cosmic muons. Each of the four wavelength shifting fibers (WLSF) are read out on both sides with the labeling of the channels given in the figure. A trigger is formed if one trigger scintillator from above PoSSuMuS and one from below detect a muon simultaneously. With  $100\text{ mm}$  these trigger scintillators have the same length as the detector, their width is  $25\text{ mm}$ . The amount of produced light in the upper and lower half is called  $q_1$  and  $q_2$ , respectively, [Ruschke, 2014].

plotted in Figure 75, shows that the number of photons has been improved from  $< 10 \frac{\text{photons}}{\text{event}}$  to  $\approx 30 \frac{\text{photons}}{\text{event}}$ .

Combining the signal of the two SiPMs at each end of one fiber up to 60 photons are collected, e.g. channel 0 and 5 for track (a), which is about a factor of four more than what has been collected by the CERN prototype. It is also clearly visible, that there are fibers detecting approximately the same amount of light, no matter where the muon traversed, i.e. channel 1, 2, 6 and 7 in Figure 75, while there are others with clear spatial dependency of the light yield, i.e. channel 0,3,5 and 8 in Figure 75. The position sensitive fibers are the ones close to the thick base. For the following only the position sensitive fibers are studied.

Calculating the ratio of the light produced in the upper part and the total amount of light gives a measure on the position resolution.

$$y \propto \frac{q_1}{q_1 \cdot q_2} \quad (6.4.2)$$

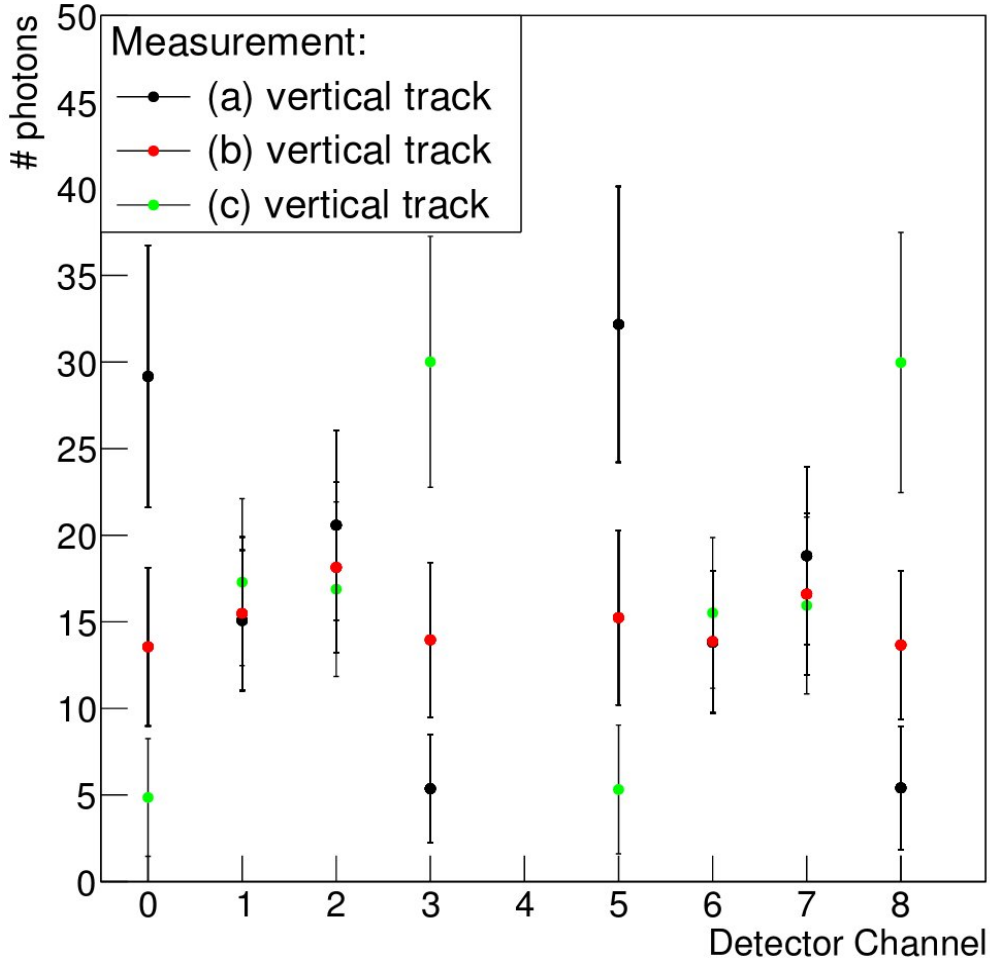


Figure 75: Light yield per channel of the second prototype. Having SiPMs with up to  $\approx 35 \frac{\text{photons}}{\text{event}}$  means an improvement of the light yield by a factor four in comparison to the first prototype. The photon count for channels at the thin side, 1, 2, 6 and 7, is approximately independent of the path length a muon has in the detector. Still the SiPMs on the long base show a nice position dependent photon collection, [Ruschke, 2014].

Following equation 6.4.2 the Y positions are plotted for the three trigger combinations in Figure 76.

It is immediately clear that the resolution in Y is much better than for the X-coordinate, if one compares Figure 76 with Figure 73. The peaks in this case are separated much clearer. The position resolution achieved in this direction is summarized in Table 5.

Depending on the position of the muon a resolution up to 8.6 mm is achievable, which is an improvement of almost a factor of two compared to the Y resolution of the first prototype, [Ruschke, 2014].

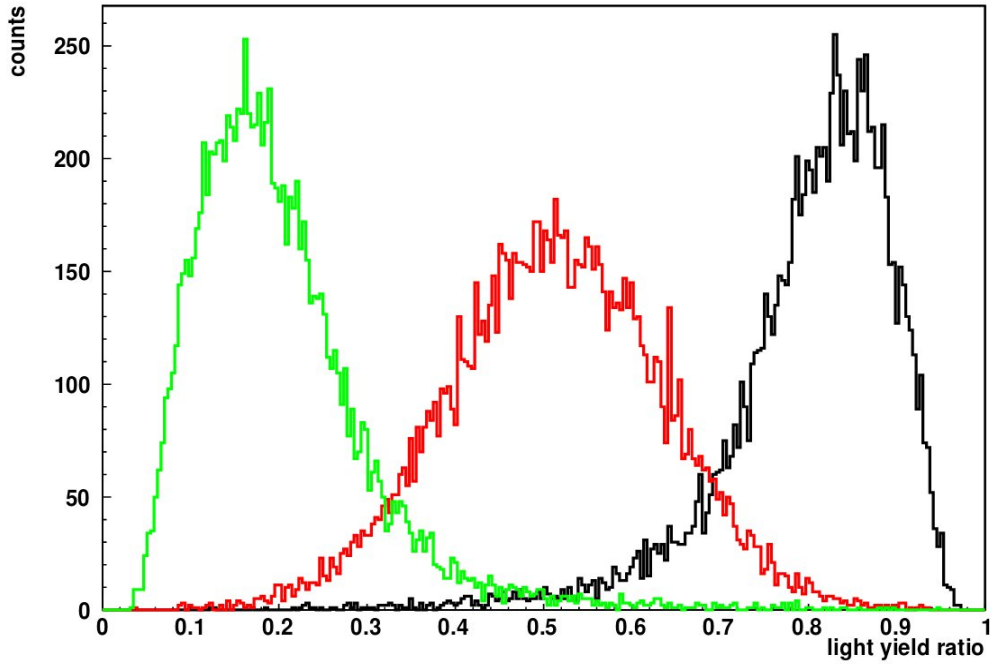


Figure 76: Light yield ratio result of second prototype detector. Three clearly distinguishable distributions can be seen. The peaks are at the positions  $Y_a = 0.85$ ;  $Y_b = 0.51$  and  $Y_c = 0.16$  with standard deviations  $\sigma_a = 0.09$ ;  $\sigma_b = 0.12$  and  $\sigma_c = 0.08$ . Calculating a spatial resolution out of the standard deviations gives  $\Delta_a = 9.7 \text{ mm}$ ;  $\Delta_b = 13 \text{ mm}$  and  $\Delta_c = 8.6 \text{ mm}$ , [Ruschke, 2014].

	ratio	std. dev.	resolution [mm]
$Y_a$	0.85	0.09	9.7
$Y_b$	0.51	0.12	13
$Y_c$	0.16	0.08	8.6

Table 5: Result of the PoSSuMuS Y-coordinate investigated in [Ruschke, 2014]. The spatial resolution is better for muons traversing at the edges.

## 6.5 Improved Position Sensitivity Using new Geometries

After the analysis of the test beam in autumn 2012 at CERN, it was clear that the light yield needed to be improved. To study possible solutions for this problem a program was written, simulating the production and propagation of photons in a trapezoidal rod due to scintillation, [Müller, 2013].

Since the simulation was written shortly after the investigation of the CERN prototype, the geometry of this prototype was used as a starting point. A sketch of such a simulation is shown in Figure 77.

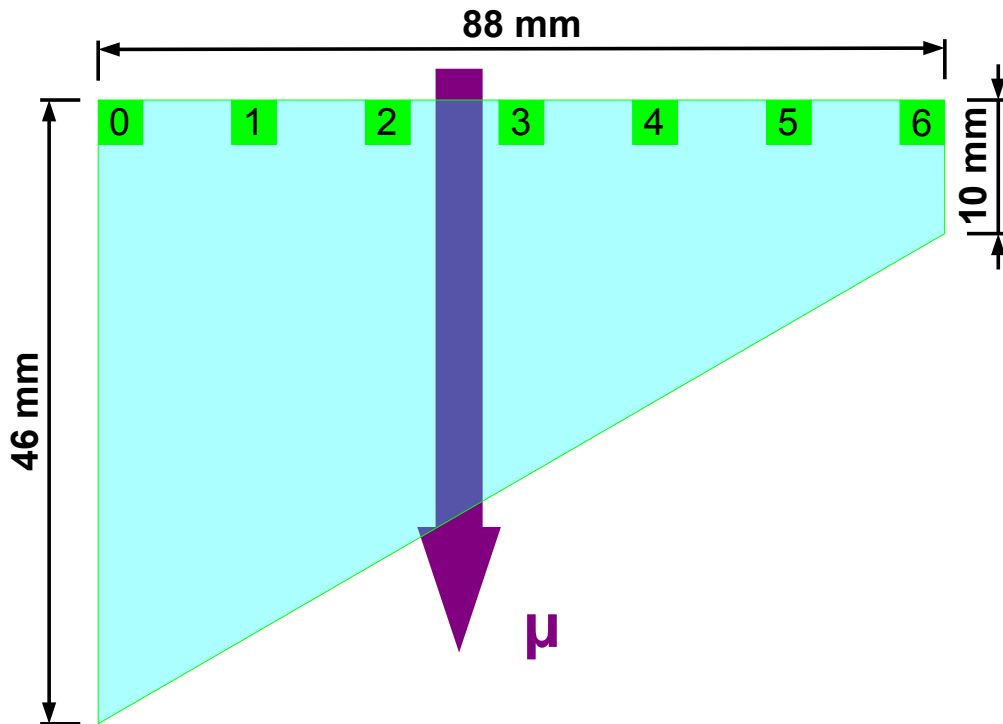


Figure 77: Sketch of trapezoidal geometry and fiber position (green) in simulation. A  $5 \times 5 \text{ mm}^2$  source (purple) was moved from left to right in 17 steps of  $5 \text{ mm}$  pitch.

Additionally to the fibers 1 to 5, as defined in Figure 77 copied from the prototype layout, also fibers 0 and 6 are introduced to investigate the position resolution depending on the fiber position. Moving a  $5 \times 5 \text{ mm}^2$  source (purple in fig. 77) in  $5 \text{ mm}$  steps from left to right results in 17 continuous muon track volumes. This simulation performs no wavelength shifting, it just counts the number of photons arriving at a groove per event, while considering the photon attenuation by absorption in the scintillator rod. A switch between diffuse and specular reflective cover material is possible showing that more photons reach a groove for a diffuse cover. In chapter 6.3 the dependency of the light yield from the distance between source and fiber was discussed. This result was also observed in this simulation, strongly suggesting only to use fiber positions 0 and 6. For the second prototype

## 6 POSSUMUS - A POSITION SENSITIVE SCINTILLATING MUON SIPM DETECTOR

---

a groove not exactly at the border was chosen, due to an easier handling of the detector. The suggestion to use diffuse reflective cover and to investigate new fiber positions are two results of this simulation already applied to the second prototype detector and successfully increasing the light yield by a factor of up to four. In the following the investigation of new trapezoidal heights is shortly summarized. For the study with lower trapezoidal heights the simulated trapezoid has only grooves at position 0 and 1, since these are the only two, which are not cut away for any investigated height. Still groove 1 is neglected in this summary, since groove 0 gave the better results, [Müller, 2013].

There will be one minor drawback of this height reduction, namely a higher ratio of readout channels per active area. Therefore one has to investigate a good compromise between a good position resolution and a high coverage of the detector with less channels.

A systematic lowering of the height can be done in two ways.

- Starting with the CERN geometry one can leave the dimensions of the two parallel base lines constant just reducing the height. This gives a compression of the trapezoid, shown in Figure 78.

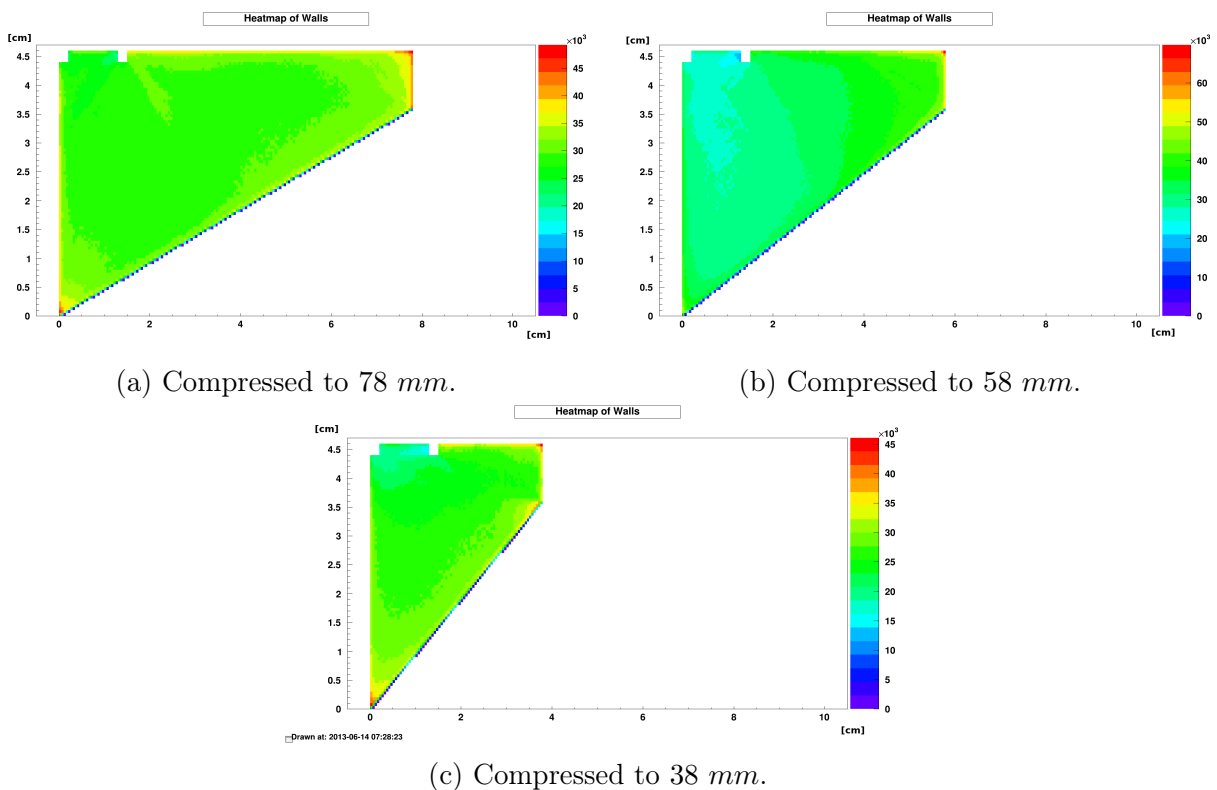


Figure 78: Simulation of compressed geometries. The length of the thin base was kept constant, while the height of the trapezoid was shrunk. The pictures show hit maps indicating the amount of photons hitting the side of the trapezoid, [Müller, 2013].



## 6 POSSUMUS - A POSITION SENSITIVE SCINTILLATING MUON SIPM DETECTOR

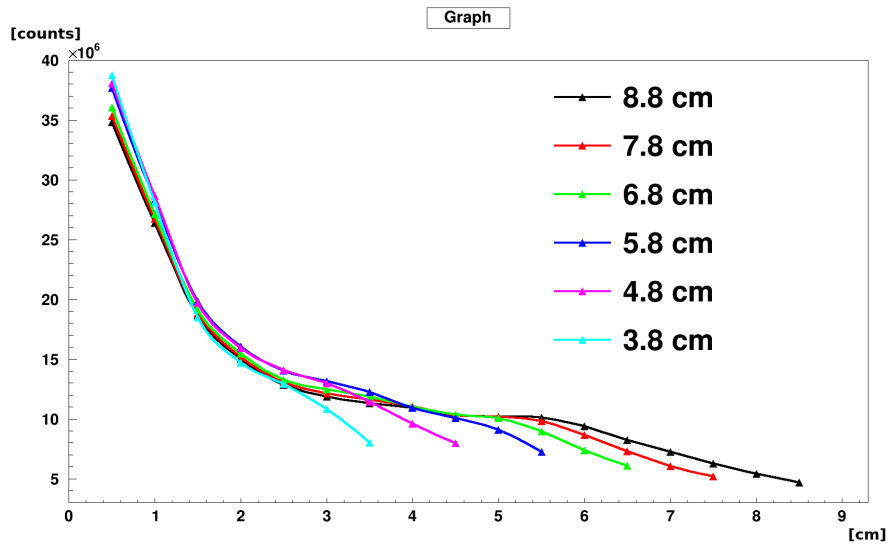


Figure 80: Result of compression study. The curves show the amount of photons reaching fiber 0 as a function of the source position for all six trapezoidal heights, [Müller, 2013].

flattens out in the center ( $25\text{ mm} - 55\text{ mm}$ ). The rest of the scintillator gives again a fall off, but by far not that steep than the one in the beginning. This behavior will result in a quite bad position resolution for the central region of PoSSuMuS using those dimensions. A more compressed version of this detector eliminates this flat region and a steep decreasing of the photon count from the beginning to the end of the detector can be achieved.

The initial situation for the *cut* study, plotted in Figure 81, is identical to the *compressed* geometries.

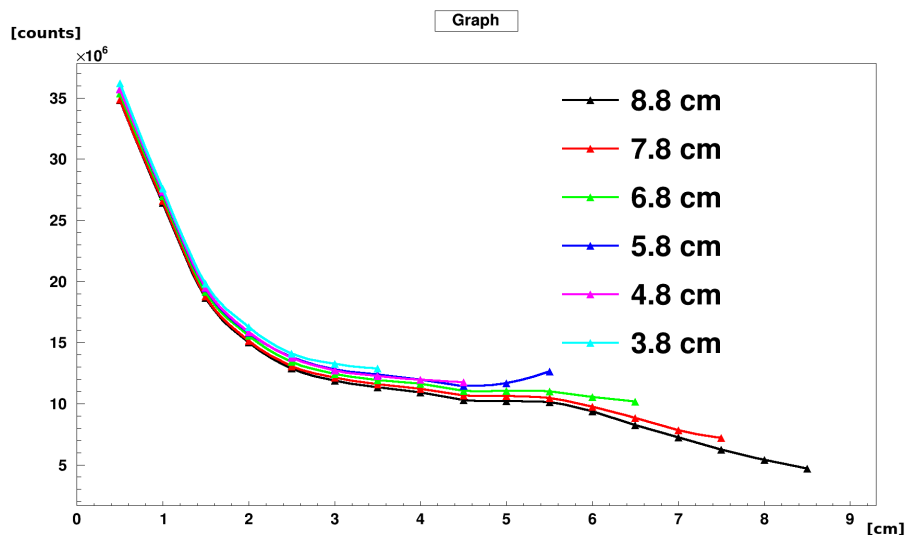


Figure 81: Result of cut study. Again the total number of collected photons for channel 0 is shown as a function of the position of the source. [Müller, 2013].

In this case, going to geometries with a lower height does not eliminate this constant light yield in the center but the slope is literally cut. Due to the smaller geometry the photon count is slightly increased. In contrast to the *compressed* situation all source positions give a higher light yield when comparing a certain geometry with any other having a larger height. Since a PoSSuMuS always consists of two trapezoids, even the regions of a rather flat slope, e.g.  $25\text{ mm} - 45\text{ mm}$  for the pink curve in Figure 81, could possibly result in a suitable spatial resolution, since the other half will have its part with the steep slope just at this position.

The simulation shows that a fiber at the thick side will have a monotonous slope proportional to the amount of detected photons. The question is now what argument has to be considered more:

- A steep position dependent light yield as for the *compressed* geometry. This will be the optimal situation, if the light yield for a muon traversing close to the thin base is still high enough for good statistics.
- If this is not the case, than one can hope that the rather constant slope in the end of a *cut* geometry can be compensated with the steep slope of the second trapezoid.

## 7 Testbeam with New Geometries at CERN

Summarizing all informations from the first two prototypes and the simulations suggest the following features of a new geometry:

1. Increased fiber diameter,
2. Small length of the fiber outside the scintillator before coupling to the SiPM,
3. Fiber position at the thick base for a good spatial resolution,
4. Fiber position at the thin base for correction of the Landau distributed energy loss,
5. Wrapping the trapezoids in a diffuse reflective cover like Tyvec,
6. Geometry with lower height

The next chapter describes the realization of issue 1-5 for the new design. The different geometries studied are introduced later in chapter 7.3 in the context of the detector setup at CERN.

### 7.1 Construction of new Geometries for Optimized PoSSuMuS

Taking all mentioned possibilities to improve the detector concept into account, the PoSSuMuS design discussed in this thesis is shown in Figure 82.

As mentioned the fiber positions are now in the corners of the thick and thin base of the trapezoid. But more important than the position are the fibers themselves. Four of them, each with a diameter  $\varnothing = 1.5 \text{ mm}$ , fill a quadratic shape perfectly fitting the  $3 \times 3 \text{ mm}^2$  active area of the SiPMs used. This increases the area to collect and convert the scintillation photons. It has two direct consequences compared to the old design.

- First, gluing has to be divided into two steps to obtain a proper result. In the first step packages of four fibers are glued using plastic profiles, see Figure 83. The used forms have always the same length as the scintillator to which the fiber package will be glued later on.

The forms need to be stable and the glue should not stick to them. The two materials teflon and poly-ethylene are used and both show a similar behavior. For gluing, the profiles are arranged such that a simultaneously gluing of two packages is possible as sketched in Figure 83a, but yet without the fibers inside. The fibers are guided into the vertically fixed forms from top to bottom, while continuously glue<sup>15</sup> is filled into the

---

<sup>15</sup>BC - 600, [Saint Gobain, 2012]

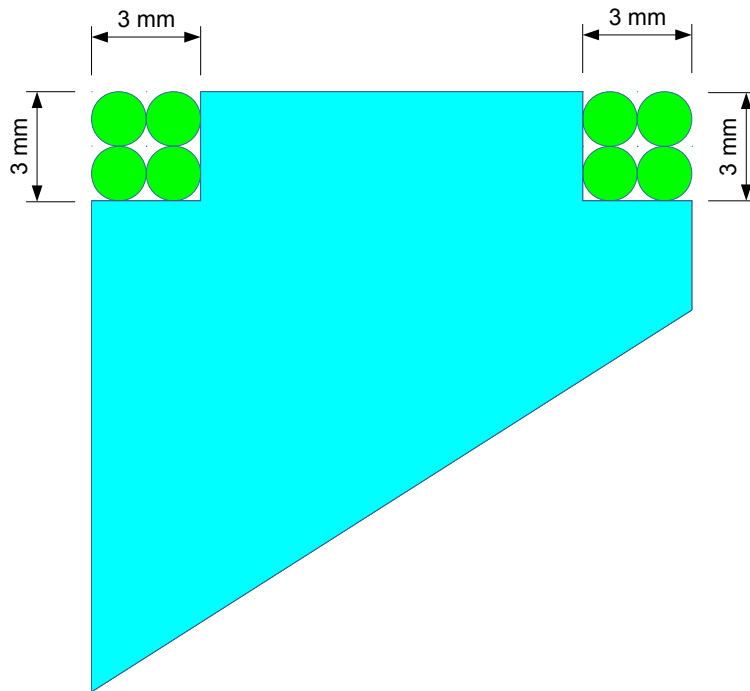
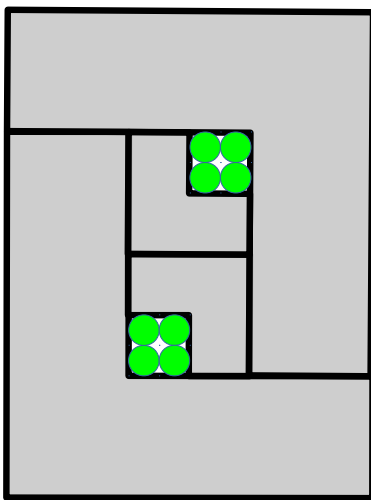


Figure 82: Sketch of new PoSSuMuS design. The trapezoidal height was shortened and a package of four fibers with a diameter  $\varnothing = 1.5 \text{ mm}$  is used. The fibers are now also located at the edges of the scintillator.



(a) Sketch of gluing profiles



(b) Photograph of 300 mm profiles

Figure 83: Positioning the fibers at the edges of the trapezoid and using four of them makes it necessary to join them to a package before gluing them onto the scintillator. Therefore profiles made of teflon (front in Figure 83b) and poly-ethylene (rear in Figure 83b) are used. They are designed to allow a production of two packages at the same time.

form together with the fibers. This provides a homogeneous glue distribution with very little amount of air bubbles. A reservoir with glue is finally placed on top, to provide

a continuously glue rinsing downwards until it becomes very sticky, which takes less than an hour. After that no glue will pass the forms and it takes another twelve hours until the glue is finally hardened. A Photograph of this is shown in Figure 84.

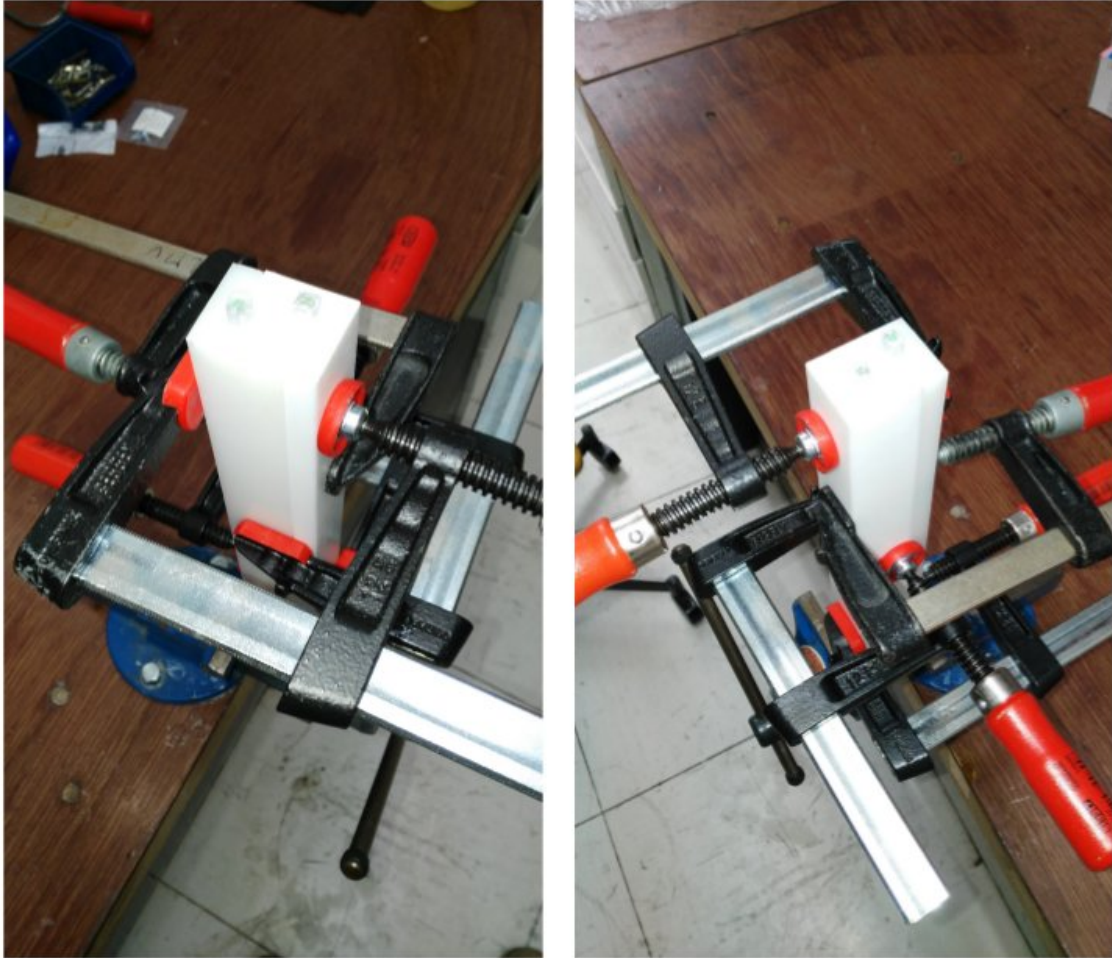


Figure 84: Gluing of two fiber packages. The profiles are mounted vertically and are pressed together at several points in order to have just the  $3 \times 3 \text{ mm}^2$  area for the fibers.

- The little pieces of aluminum which can be seen in Figure 84 on top of the white forms and with the fiber package inside, are part of the new self made connection system to the SiPMs, described later in this chapter. They are glued to both ends of the fibers while they are formed to a package. Standard connectors for fiber optics are designed for single fiber connection only and therefore do not fit to these fiber packages.

After the glue has hardened and the forms are removed from the package, the fiber ends sticking out of the aluminum connectors are polished to form a flat surface together with the aluminum. There might also be remnants of the glue sticking to the package's quadratic shape which are pulled by capillary force into the very narrow gaps of the forms. They have

to be removed carefully before proceeding.

The fiber package now has to be glued to the grooves of the scintillator. The distance between the two aluminum pieces is just exactly the length of the trapezoid, hence along this direction no movement during gluing can happen. Therefore one only has to dispense glue into the groove and press the package towards it. This is done using cling film<sup>16</sup>, which proves to be totally non-adhesive to the glue. It can be stretched around the trapezoid and thus homogeneously press the fiber to the scintillator.

The trapezoid can now be wrapped with a suitable cover material and is then ready to use. As such material a triple layer of Tyvek covered by aluminum has been used. During the beam time the cover was switched to bare aluminum foil to investigate the new design also with specular reflecting cover.

A scheme showing the connection of the fiber package to the SiPM is drawn in Figure 85.

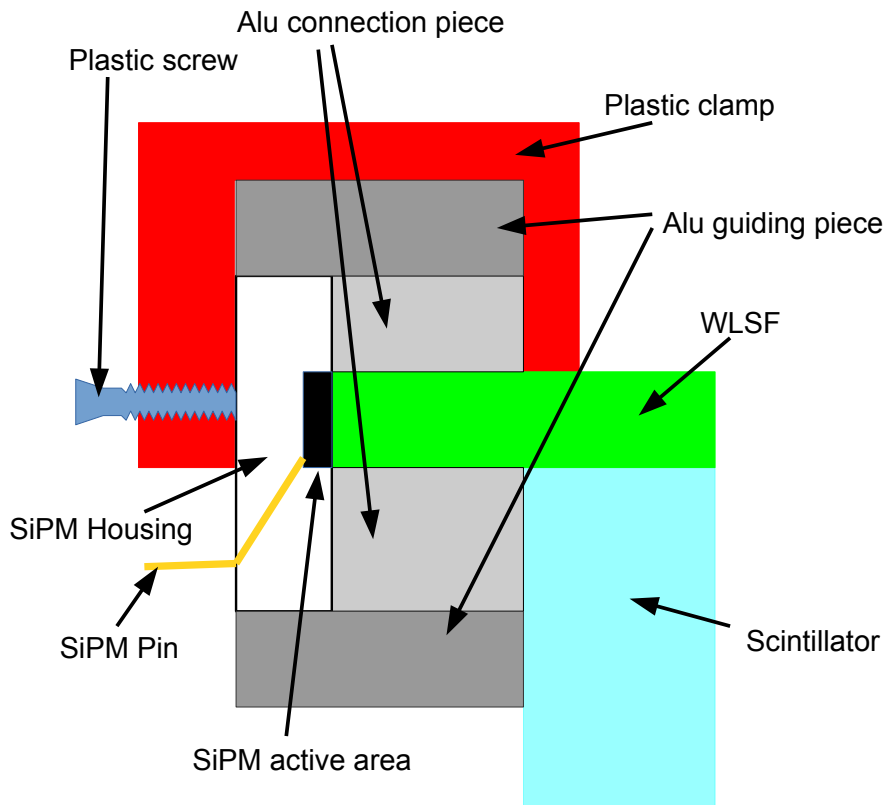


Figure 85: Scheme for the connection of fiber and SiPM. The cross section of the aluminum connection piece glued to the system during production of the fiber package is identical to the cross section of the housing of the SiPM. A second aluminum guiding piece around SiPM and connector assures a correct alignment of fiber and active area of the readout. A plastic clamp fix the setup with a plastic screw.

The aluminum connection pieces already glued to the fibers have the same cross section as

<sup>16</sup>Cling film from the company **alio** was used which is made out of poly-ethylene.

the housing of the used SiPM and the fibers are located inside this connector at the same position as the active area of the SiPM inside its housing. A second piece of aluminum guides both, the SiPM and the connector, perfectly on top of each other, and by this the four fibers are aligned to the active area of the SiPM. A plastic clamp manufactured by a 3D printer is used to press both surfaces towards each other with a plastic screw and therefore fixing the system.

The next chapter discusses the electronics used to power and readout the SiPMs

## 7.2 Voltage Supply and Gain Stabilization

For this test beam not only the geometries of PoSSuMuS have been improved, but also the readout electronics, including the voltage supply, have been revised. In the old layout each SiPM had its own amplification board schematically drawn in figure 86.

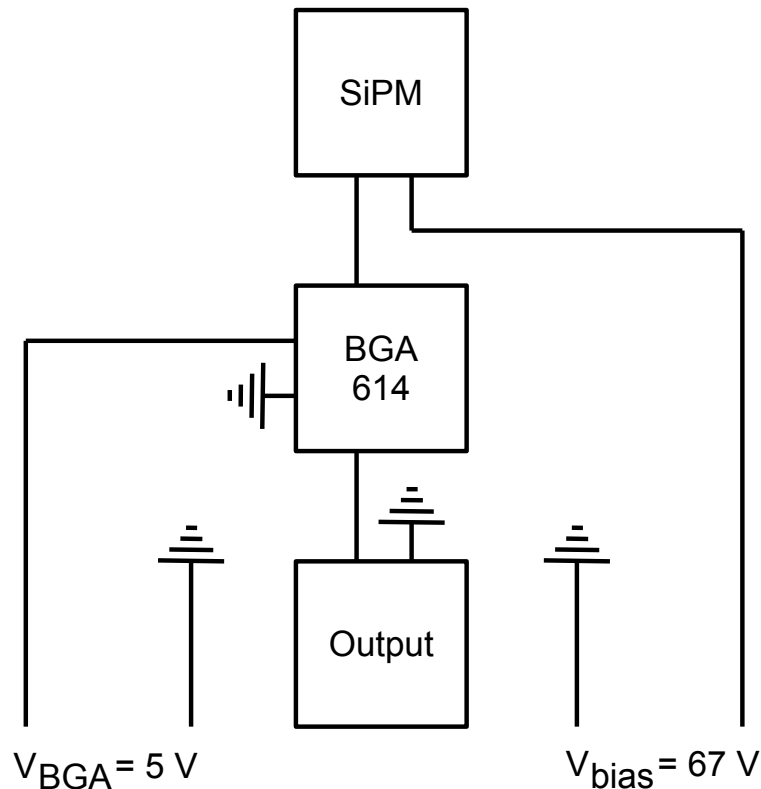


Figure 86: Scheme of old SiPM amplification board. The bias voltage for the SiPM is adjusted according to its breakdown voltage. A breakdown of the SiPM is recognized by the BGA 614, amplifying this signal and passing it to the output of the board.

These boards consisted of the SiPM, a connection to the  $\approx 67\text{ V}$  power supply of the SiPM, a BGA 614 pre-amplifier [Infineon, 2011], a connection to its  $5\text{ V}$  power supply and a data cable for readout. The bias voltage is chosen according to the breakdown voltage of the SiPM. A breakdown of the latter is recognized by the BGA 614, amplifying the signal and

passing it to the output of the board. Since the SiPM is directly soldered to the board, it has to be inside the light tight box together with the PoSSuMuS detector, and therefore each channel requires three cables to go inside the box. An additional temperature sensor for each channel measures every five minutes the temperature of the SiPM. The  $\approx 67\text{ V}$  comes from a programmable voltage divider for each channel separately, adjusting the voltage according to the measured temperature of the SiPM. This online gain adjustment was developed by [Grossmann, 2014].

In the new design always four SiPMs are soldered to an Ethernet cable. For those channels only this single cable has to be guided into the box, while all further electronics happens outside gathered on a single board for in total eight SiPMs, hence two Ethernet cables per board. Such a card performs the online gain stabilization compensating temperature fluctuations and the amplification for each channel individually using exactly the same scheme as in the former design but now concentrated on a single board. The heart of this system is now a crate which houses one card with an arduino and has the space to further plug in up to seven amplification boards for the SiPMs. Circuit diagrams and photographs of the electronics are provided in appendix B. Utilizing the  $I^2C$  bus protocol, the arduino can control each voltage divider on the amplification cards plugged into the crate independently. A scheme illustrating the power supply is shown in figure 87.

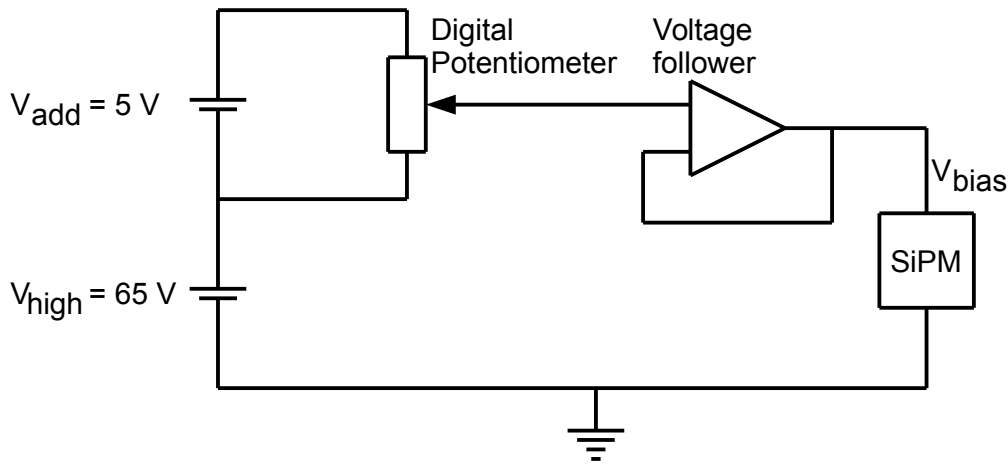


Figure 87: Scheme of remote controllable power supply for a SiPM. Two power supplies are providing a stable voltage of  $V_{high} = 65\text{ V}$  and  $V_{add} = 5\text{ V}$  with  $V_{add}$  sitting on top of  $V_{high}$ . With a remote controllable potentiometer a voltage  $65\text{ V} \leq V_{bias} \leq 70\text{ V}$  can be adjusted. A voltage follower ensures that the potentiometer is not loaded.

In the setup two power supplies deliver stable voltages of  $V_{high} = 65\text{ V}$  and  $V_{add} = 5\text{ V}$ <sup>17</sup> with  $V_{add}$  sitting on top of  $V_{high}$ . Using the digital potentiometer AD5263, [ANALOG DEVICES, 2012], a voltage  $65\text{ V} \leq V_{bias} \leq 70\text{ V}$  can be adjusted. The controlling of the voltage divider

<sup>17</sup>For  $V_{high}$  a Keithley 6517B is used, [Keithley, 2016a], and for  $V_{add}$  a Keithley 2400, [Keithley, 2016b].

is done with a galvanically insulated arduino with the  $I^2C$  bus protocol optically coupled to the potentiometer. Since these potentiometers should not be used as a voltage source, a voltage follower is used to ensure that the potentiometer is not loaded. The arduino card has four connectors:

1. A USB connector to control the arduino
2. A 5 V voltage connection for the BGA614 on the voltage divider cards
3. A connection for  $V_{high}$
4. A connection for  $V_{add}$

All three voltage connectors are guided to the backplane of the crate, where the voltages are distributed in parallel to all connected amplification cards. On each card, there are two voltage dividers, providing four channels each. As mentioned, only the additional 5 V are adjusted with this divider and added to the high voltage, which is common for all channels. At the CERN test beam a high voltage of 63 V is set with an external power supply and therefore the bias voltage of each SiPM can be adjusted between 63 V and 68 V. Finally the SiPM signal gets amplified and each channel can be plugged separately to the readout chain, explained in chapter 7.3, which is not a part of the just mentioned electronics.

Since the experimental hall at CERN is huge and it was winter time, it was supposed that the temperature does not change rapidly and moreover stays rather constant. Therefore only one temperature sensor was used, which was mounted outside of the light tight aluminum box of PoSSuMuS, in order to drill less holes into the box reducing the probability to get light into the box. The temperature measured with this sensor during 20 days of data taking is shown in figure 88.

This setup is used for an online gain stabilization by measuring every five minutes a temperature value and adjusting all SiPMs using the temperature coefficient  $60 \frac{mV}{K}$ , [Hamamatsu, 2015]. In addition to this, in the analysis an offline gain correction is applied to reconstruct the data with a constant gain. For this first the gain has to be determined. This is done using two features of SiPM's, which are in principle drawbacks of this technology, the dark current and the crosstalk, explained in chapter 6.2. If a dark current event happens in a single cell, it is likely to induce a second avalanche in a neighboring pixel, and so on, each with continuously reduced probability. By measuring such dark currents one is in the situation of very few cells firing. The readout is capable of resolving small numbers of fired pixels, while a large amount of pixels get smeared out due to slightly different pulse heights for each pixel. In this setup a small number of firing pixel in the order of 1 – 10 is observed only in dark current measurements in contrast to at least 40 for muon events. The result for a dark current measurement is shown in figure 67, which was performed using a charge-to-digital

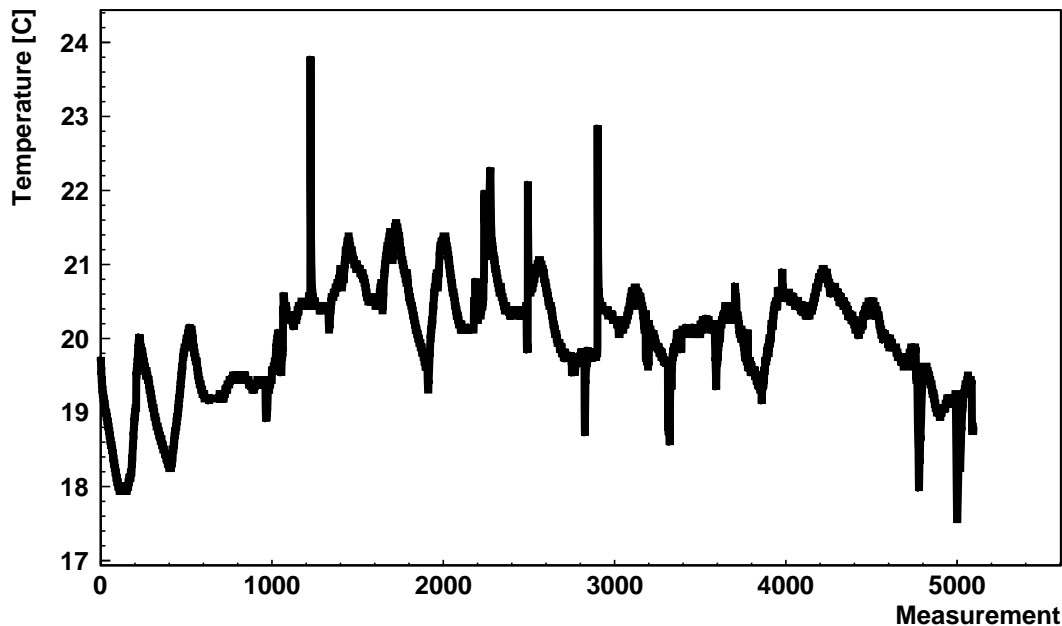


Figure 88: Temperature variation during test beam 2016 at CERN. A temperature measurement was done every five minutes, resulting in  $\approx 5000$  temperature measurements during 20 days of data taking. Taken from [Kulosik, 2017]

converter (QDC) to digitize the SiPM signal. This device will be explained in more detail in chapter 7.3.

On the X-axis, the unit is QDC charge count. The QDC digitizes the charge arriving at its input, while the digitization units are these QDC charge counts. This picture shows clearly distinguishable peaks, corresponding to the amount of simultaneously firing pixels. The gain of the SiPM is defined as the mean distance between the neighboring peaks, having the dimension QDC-charge-counts per firing pixel. Therefore dividing the number of QDC charge counts for a muon event by the gain results in a value for the amount of incident photons. Another effect of the QDC is that it always has a certain offset, meaning that even a background signal at its input produces a certain amount of QDC charge counts. This offset is always identical for each input channel individually, as long as nothing changes in the setup, like the time the QDC collects the data of an event. Combining the information of the gain and the offset one can calculate the amount of light produced out of the number of responding QDC channels:

$$\#Photons = \frac{\#QDC\ channels - offset}{gain} \quad (7.2.1)$$

A minor problem is now that the gain can change slightly even using the voltage divider to stabilize it. To compensate this, a muon measurement run is sandwiched by two runs of dark current measurements. The time for a muon run is adjusted such that it does not

exceed 30 *min*, by finishing this run after  $N_\mu$  events. In the mean time, the temperature and hence the gain is assumed to change linearly. By determining the gain before and after the muon measurement, the amount of measured photons for the  $i^{\text{th}}$  event can be calculated by slightly improving equation 7.2.1 using a linear interpolation between both gain values:

$$\#Photons(i) = \frac{\#QDC\ channels(i) - offset}{gain_{before} - i \cdot \frac{gain_{after} - gain_{before}}{N_\mu - 1}} \quad (7.2.2)$$

The setup used at CERN (described in chapter 7.3) is designed for an automatized switching between both measurements. Therefore every muon measurement has a gain measurement in advance and afterwards to calculate the number of detected photons using the correct gain. The number  $N_\mu$  was not always the same, but it was chosen such that a measurement took at maximum 30 *min* if there have not been any problems with the beam. If everything worked fine 50000 events took  $\approx 10$  *min*.

Figure 89 shows the distribution of gains for a run with a certain geometry, for channel six.

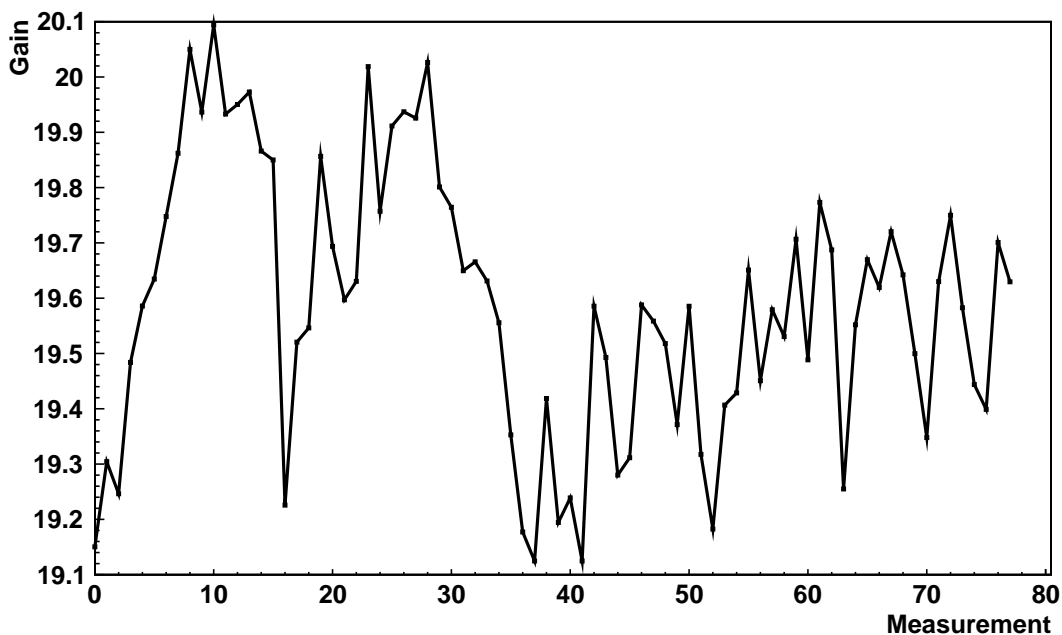


Figure 89: Gain variation during a run with 80 dark current measurements. The value varies about 5 % in total but adjacent measurement points are much closer together. Taken from [Kulosik, 2017]

It can be seen that the total variation is in the order of  $\pm 2.5$  %, while the variation of two adjacent points is much less. In comparison to the distribution of measured temperatures, the X-axis is not equidistant in time, due to the mentioned variety of  $N_\mu$  and longer periods with no beam.

### 7.3 Detector Telescope at CERN

To investigate the new geometries, trapezoidal rods in four different angular cuttings and two different lengths have been brought to a test beam at the CERN H8 beam line. The muon beam had an energy of  $E_\mu \approx 120 \text{ GeV}$  and a diameter of  $r_\mu \gtrsim 200 \text{ mm}$ .

Besides the new geometries also a new scheme for the reference system is used, see Figure 90.

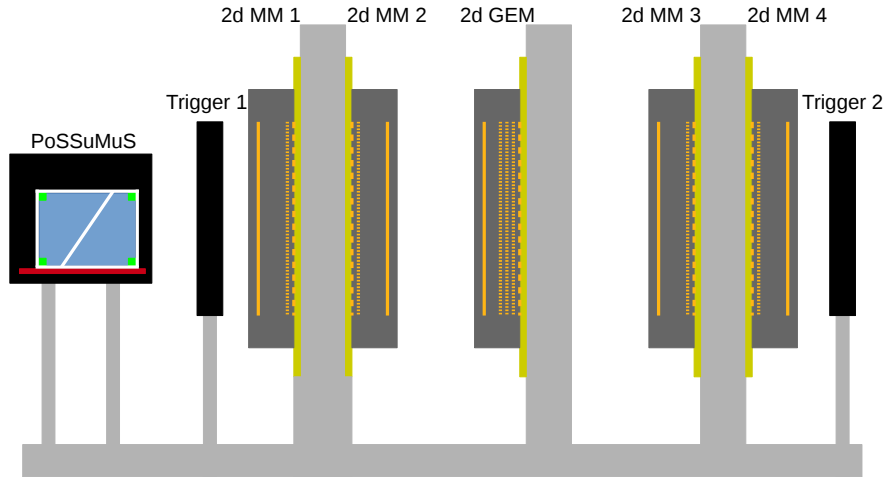


Figure 90: Scheme of the telescope used at CERN. Two 2D Micromegas doublets provide a reference track for PoSSuMuS and a 2D GEM detector, also investigated in this setup. The readout was triggered by two  $9 \times 10 \text{ cm}^2$  scintillators.

Reference tracks were defined by two 2D Micromegas doublets. In this test beam a 2D GEM detector is investigated by Bernhard Flierl. Since this detector needs a reference with a precision better than  $0.1 \text{ mm}$  it was sandwiched by the Micromegas, [Flierl, 2018], while the PoSSuMuS was mounted outside due to a lack of space and lower required resolution of  $\approx 1 \text{ mm}$ . A slightly more detailed view of PoSSuMuS is shown in Figure 91, providing the labeling of the SiPM channels as well.

For the connection of the SiPMs to the voltage divider cards the channels 0-3 and 4-7 are connected to one ethernet cable each. Five PoSSuMuS with different trapezoidal shapes have been investigated at this test beam. The different values of  $a, b, c, d$  and  $\alpha$  have been summarized in Table 6

Tests with the  $d = 100 \text{ mm}$  long geometry aimed on studies concerning the light yield of the geometry. Since a diffuse reflective cover material gave a higher light yield in former studies, these geometries have been investigated only with a diffuse reflective covering, which is Tyvek<sup>®</sup>. It was also suspected, that this cover results in a worse timing resolution and therefore the long geometry,  $d = 300 \text{ mm}$ , was covered once in Tyvek<sup>®</sup> and once in aluminum, to compare the resolutions. Unfortunately the aluminum wrapping happened rather at the end of the test beam, where there had been several problems with the accelerator, hence the

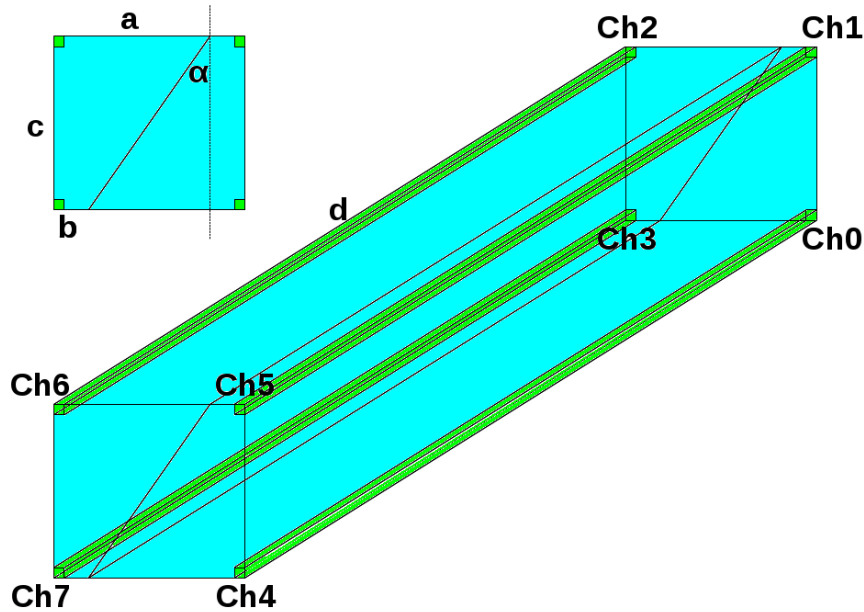


Figure 91: PoSSuMuS used at CERN. The sketch in the upper left corner is a cross section through the detector with a beam coming from the left. Here also the relevant dimensions of the trapezoid,  $a, b, c, \alpha$  are labeled. The other picture shows a 3D impression of PoSSuMuS with a length  $d$ , also defining the position of the eight readout channels.

$a$ [mm]	$b$ [mm]	$c$ [mm]	$d$ [mm]	$\alpha$
45	9.81	50	100	$35^\circ$
45	16.13	50	100	$30^\circ$
45	26.80	50	100	$20^\circ$
45	36.18	50	100	$10^\circ$
45	16.13	50	300	$30^\circ$

Table 6: Dimensions of the PoSSuMuS geometries used at CERN.

amount of collected statistics is very low. As a consequence not the entire detector could be investigated.

For the eight SiPM channels only one voltage divider card, see section 7.2, is needed. All four channels of one side, Ch0-Ch3 and Ch4-Ch7, are soldered to an Ethernet cable, which is plugged into the voltage divider card, performing the online gain stabilization and amplification. This signal is further plugged into the readout chain. It is designed to perform automatized alternating gain and muon measurements, and to be able to synchronize PoSSuMuS and reference track data, which are acquired on different data acquisition (DAQ) systems with different data streams. The logic behind the switching between the trigger sources of the two measurement modes is sketched in Figure 92.

The two sources for the trigger pulse are the trigger scintillators for the muon measurements and the SiPMs for the dark current measurements. All ten channels are plugged into a pro-

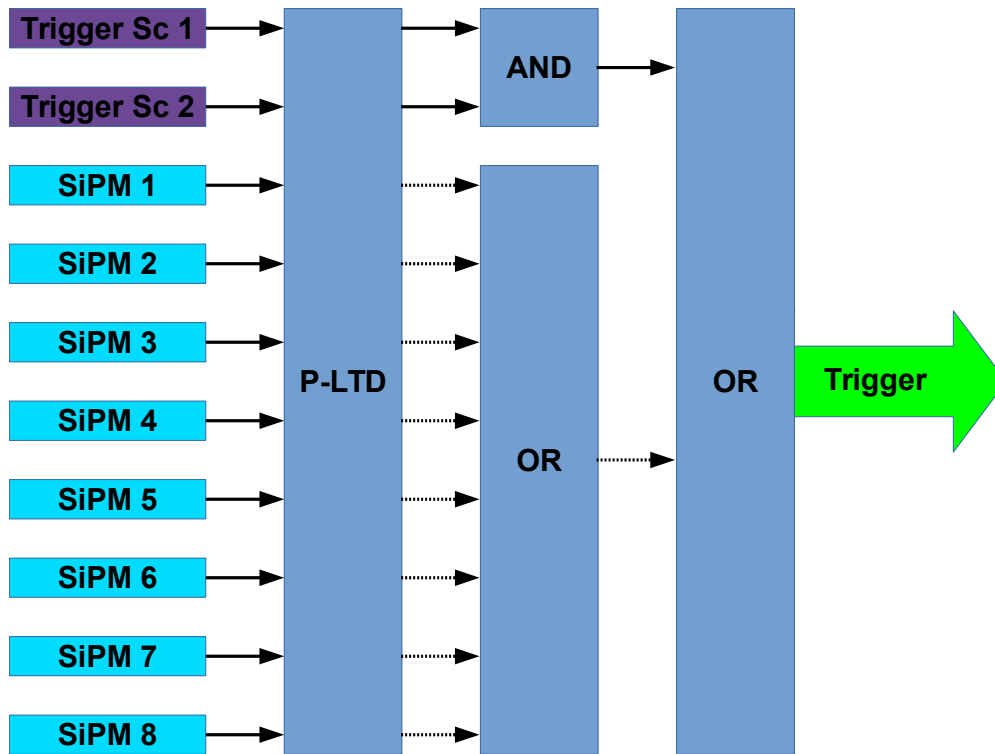


Figure 92: Measurement mode switching logic. It is done by selecting the source of the trigger with a programmable low threshold discriminator (P-LTD). This device can be remotely controlled to enable and disable channels and to set one common threshold to all enabled channels. The signal from the two trigger scintillators (magenta) and the eight SiPMs are connected to this P-LTD. For a muon measurement the SiPMs are disabled and the threshold for the scintillators is set to  $15\text{ mV}$ . To force a coincidence signal both pulses are plugged to an AND unit. In case of a dark current measurement the scintillators are disabled, while enabling the SiPMs in pairs of two, hence four dark current measurements are performed to have the gain spectrum for all eight channels. A threshold of  $6\text{ mV}$  is set by the discriminator. This time the output of the P-LTD is plugged to an OR unit since it does not matter which channel provided the pulse. The final trigger pulse (green) is formed by a second OR unit combining the AND output with the output of the first OR unit.

programmable low threshold discriminator (P-LTD)<sup>18</sup> capable of enabling and disabling single output channels and setting one common threshold value for all enabled outputs. During a muon measurement the signals from the two trigger scintillators produce the trigger pulse. Therefore the threshold of the P-LTD is set to  $15\text{ mV}$  for the trigger channels while disabling all SiPM channels. The output for these two channels is plugged to an AND-logic<sup>19</sup>, to require a coincident muon signal. For dark rate measurements the P-LTD disables the signal coming from the trigger scintillators and enables the eight SiPM channels consecutively in pairs of two with a very low threshold of  $6\text{ mV}$ . Therefore the low intensity dark rate events

<sup>18</sup>V814N [CAEN, 2010b]

<sup>19</sup>N113 [CAEN, 1991]



first they have to be copied. This is done plugging the output of the voltage divider cards to a Fan in - Fan out (FiFo)<sup>26</sup>, which creates three identical analog copies of this signal. The first output of the FiFo is used for trigger purposes, while the second output of the FiFo is delayed by a delay unit<sup>27</sup> before passing it to the QDC. This delay is necessary because the trigger processing takes longer than the direct signal propagation to the digitizers, but it needs to arrive, e.g., at the QDC at least 15 ns in advance of the data signal. During the gate pulse duration of the second timing unit, the QDC integrates the charge arriving at its input channels. In order to accumulate only the signal corresponding to the current trigger the delay is adjusted so that the gate pulse starts the required 15 ns before and ends  $\approx 25$  ns after the signal pulse started. During the 25 ns just the maximum of this pulse is recorded while the rest of the pulse is rejected. It turned out that this adjustment gives the clearest signal, because the chance to accumulate additional after-pulses, reflections in the cable or other events not directly related to the produced scintillation light, is highly suppressed.

To get a timing information of the muon signal the SiPM signal from the third output of the FiFo is converted to a NIM pulse via a low threshold discriminator (LTD)<sup>28</sup>. The pulse goes into a TDC which is operated in "common stop" mode with a time resolution of 35 ps. This means that a pulse from a signal channel generates a start signal in the TDC and the time is digitized in steps of 35 ps, which is the highest resolution this device can provide, until the stop signal for all channels arrives. After the data from the QDC, TDC and TTCvi is successfully acquired by a computer, a reset pulse is sent to the first timing unit via an In/Out register<sup>29</sup>. The infinite pulse is reset and a new trigger can be processed.

The last part of the data acquisition concerns the muon reference track. This is provided by reading the data of the Micromegas via the scalable readout system (SRS), [Zibell, 2014]. Since it is necessary to synchronize later the data streams of PoSSuMuS and Micromegas, a TTCvi is used for trigger numbering. For the PoSSuMuS part the internal counter of the TTCvi is read out for each event in the same cycle as the QDC and TDC, which is incremented for each trigger pulse. For the SRS part it passes the trigger pulse to the scalable readout unit (SRU), which is part of the SRS setup. Due to this trigger the SRU requests data from all plugged in front end concentrator cards (FEC)s<sup>30</sup>, and pipes this data and its own internal event ID to another data acquisition PC. It was proven that the TTCvi and the SRU always show the same event counter, hence in the later analysis one only has to match events with equal numbers. The readout of the Micromegas is done using APV25 chips<sup>31</sup> connected to the FECs. During the test beam period the first Micromegas doublet showed

<sup>26</sup>N625 [CAEN, 2006a]

<sup>27</sup>N108A [CAEN, 2003]

<sup>28</sup>N845 [CAEN, 2011]

<sup>29</sup>V977 [CAEN, 2004]

<sup>30</sup>In this setup two FECs are used

<sup>31</sup>A readout chip originally designed for CMS detector, [Jones et al., 1999].

some problems, but the reference information of just one Micromegas is sufficient to analyze the data of PoSSuMuS. Micromegas 3 was used for this purpose.

The entire test beam targets on the investigation of the new geometries with perpendicular incident muons and therefore only such measurements have been performed. Still in a future study also the behavior under inclined tracks need to be studied, like it was done by [Ruschke, 2014] for the old geometry. In the next chapters the results from this beam time are discussed showing an increased resolution due to the new geometries.

## 7.4 General Performance of the new PoSSuMuS

In this chapter general characteristics of the setup are explained. The first issue to discuss is the hit distribution of muons in the detector. As an example for this a plot with the 100 mm long 30° geometry is shown in Figure 94.

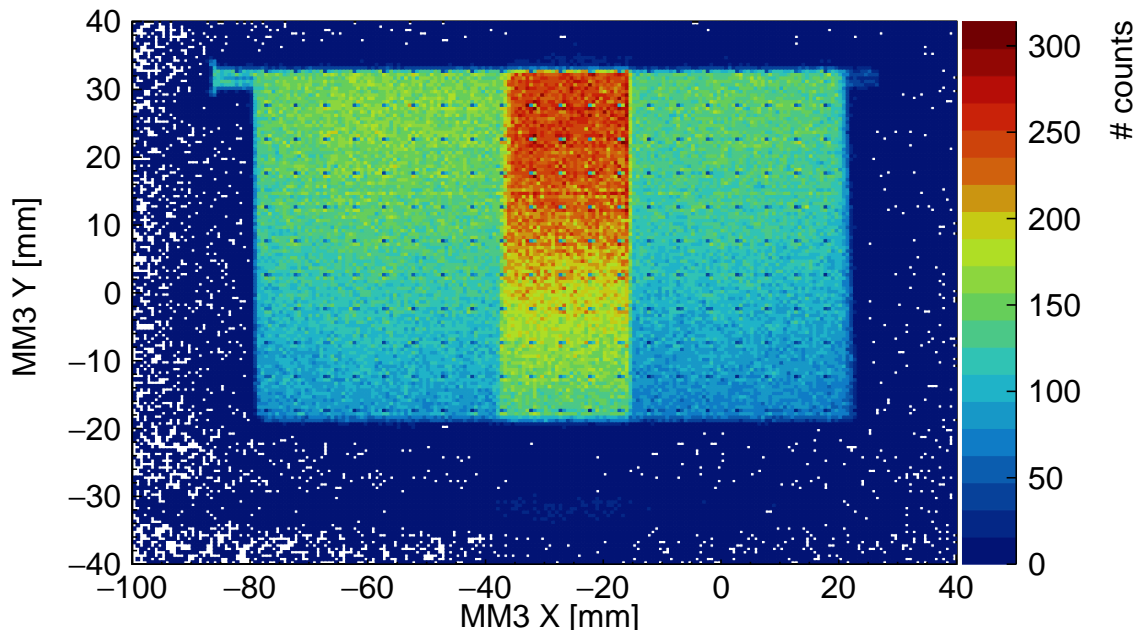


Figure 94: Hit distribution for 100 mm long 30° geometry. Since this PoSSuMuS is larger than the trigger and reference area it is investigated in two runs. After finishing the first run the detector is moved by 60 mm resulting in a 20 mm broad overlap visible as the red to green band in the center. The fact that the detector was hit more often in the upper part results from the fact that whole setup was a bit too deep with respect to the beam center.

Looping over all events belonging to this geometry it is requested, that channel one<sup>32</sup> has detected at least 15 photons and that Micromegas 3 recorded a muon track in order to fill the X and Y coordinate of the reference into this histogram. The data of this geometry

<sup>32</sup>Looking along the beam axis channel one is the SiPM mounted on the top left position (thin base) of the rear half of PoSSuMuS, see Figure 91

is recorded in two runs, since the total active area of PoSSuMuS is larger than the one of the trigger and reference system. For the next run, PoSSuMuS is shifted by 60 *mm* to the right. This shift results in an overlap of the investigated area visible as the red to green band in the center of Figure 94. As mentioned before, in the analysis it is assumed that the PoSSuMuS stays spatially constant while the reference system together with the beam shifts. Therefore for each run the beam is in X direction always centered to the investigated area, which appears in the hit distribution as an extended or moving beam along X. While the alignment of the whole system according to the X position of the beam was done well, the telescope is positioned in Y direction slightly too low, visible as an increase of the hit level from about 100 detected muons for low Y values to almost 200 muons for high Y values in each bin in the non overlapping part of histogram 94. Since for this purpose the alignment was sufficient and another group investigating new electronics for an upgrade of ATLAS also used our triggers, it was decided not to disturb their settings and hence not to further optimize the height of the telescope.

The pillar structure, supporting the mesh against the anode strips, is responsible for the inefficient area on the Micromegas. This inefficiency is shown by the rectangular pattern of blue dots inside the PoSSuMuS area.

Also interesting to observe is the scintillation of the fiber package. Clearly distinguishable from the surroundings are those parts of the package sticking out of the detector on the left and right side. In this direction also the substructure of the package can be resolved because the requirement of at least 15 photons is fulfilled more frequently where the beam penetrates two consecutive fibers along their centers compared to positions where the fibers touch each other in Y direction since there is less material. The fibers have a diameter of 1.5 *mm* each and since this structure is resolvable, it is assumed that using just one reference Micromegas is sufficient to investigate PoSSuMuS with a reference resolution of  $\approx 1$  *mm*.

The last important point to discuss concerning the hit distribution is the region outside of the PoSSuMuS detector, but where the threshold of 15 photons measured in channel zero is still fulfilled. In the following such an event is called mis-measurement. This can have three reasons

- The first one is an accidental coincidence with a dark current event. This should have a very small impact in this figure since a dark rate event with 15 responding pixels is by itself very unlikely with a rate between 10 *Hz* and 100 *Hz* depending on the gain and recording this event in the coincidence time window given by the gate pulse of 25 *ns* length suppresses the probability even more.
- The second one results from secondary particles due to atomic or nuclear reactions of a muon with the material outside of the PoSSuMuS scintillators. In such events a muon traversing the light tight box without hitting PoSSuMuS for example knocks out

electrons of the box material (aluminum), which then can enter the scintillator and produce light. A good candidate is here especially the plate of the dark box in front of the scintillator, since this case allows for a momentum component of the produced secondary particles along the muon momentum.

Similar reactions happen in the housing of the SiPM. In Figure 94 SiPM one located in the upper left is studied. Only the housing of this channel is visible in this picture, hence a reaction with the housing obviously results directly in a response of the SiPM without performing a scintillation first, otherwise the other SiPM housings should be visible as well.

- The last possibility is a deflected muon or a wrongly reconstructed reference track. In both cases the muon originally traverses the scintillator, producing light which is detected by the SiPM, but the reference position determined by the Micromegas does not correspond to this passage.

The last two points are those which are responsible for most of such mis-measurements as recorded in Figure 94. But as shown in this histogram, the number of such events where there is no scintillator in the path of the track is small compared to the number of events inside the active detector area. Using an entire telescope as reference system the impact from wrongly deflected muons can be further suppressed, but as mentioned this was not possible in this test beam time. Since the number of detected events outside PoSSuMuS is small, and also structures like the fibers are resolvable, the existence of such mis-measurements can be neglected in the further analysis.

In the analysis two similar histograms to Figure 94, one filled with the average number of collected photons in each bin and one filled with the standard deviation from this average number is created. The one for the photon count is shown in Figure 95 again for channel one and the 100 *mm* long 30° geometry.

Following the discussion of the secondary particles it can be seen that the surroundings of PoSSuMuS is rather bright in the few cases of such events and the distribution of charge is homogeneous. Besides the front of the light tight box, where such secondaries can be produced, also the spacers maintaining a 10 *mm* distance between PoSSuMuS and the bottom of the box as well as this bottom plate itself are within the range of the triggers. Both mentioned structures are clearly visible below PoSSuMuS.

Looking at the light yield distribution inside PoSSuMuS it can be seen that the distribution ranges from about 60 photons to about 100. In general more photons are detected for lower *Y* values. Channel one is located in the second trapezoidal half being thicker at lower *Y* values, hence producing there more light. It is also observed that the light yield goes up for muon tracks close to channel one - the readout channel currently discussed, a behavior already discussed in chapter 6.4.2. Important to notice is the improvement of the light yield

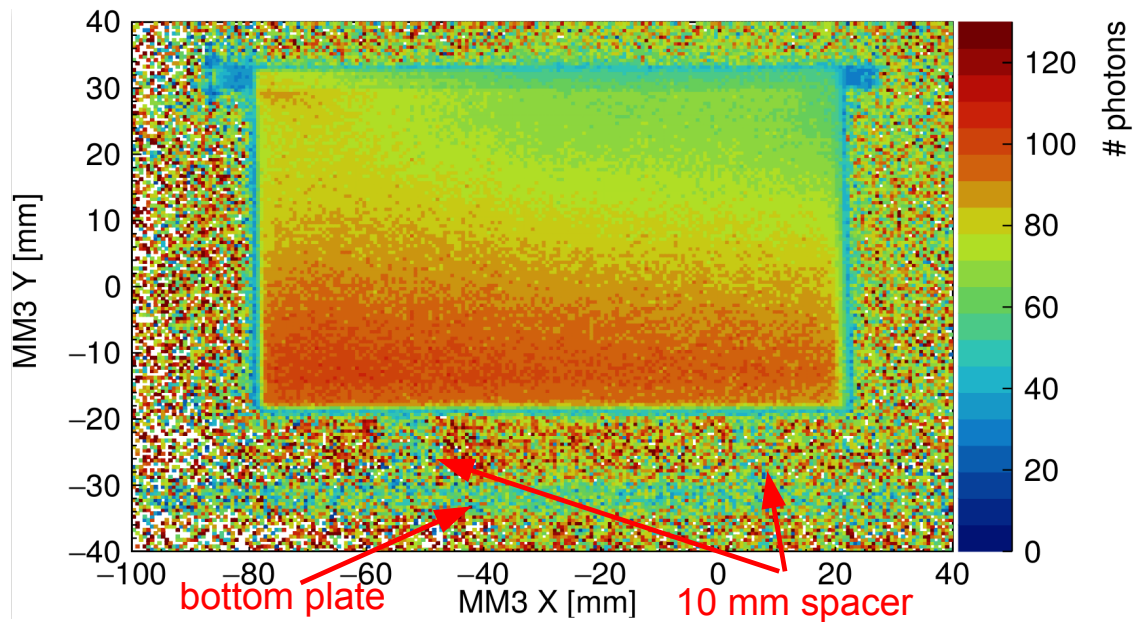


Figure 95: Average light yield distribution of channel one of PoSSuMuS. The background events show a homogeneous light distribution and a rather high light yield coming from very low statistics per bin to average over it. Also visible here are the spacers maintaining a  $10\text{ mm}$  distance between PoSSuMuS and the bottom of the box as well as this bottom plate itself. With a slightly higher statistics the average results in a slightly lower light yield compared to the rest of the background events. The charge distribution inside the PoSSuMuS detector shows an increase of light for lower  $Y$  values which corresponds to a longer path of the muon in this scintillator half. Also an increase of the light yield towards the actual readout channel is observed.

compared to the former prototypes. In Figure 75 the number of photons detected in an event with the second PoSSuMuS prototype with a muon close to the fiber at the thin base was  $\approx 15$ <sup>33</sup>, while it is now at least  $\approx 60$ <sup>34</sup> which is an increase of a factor of four.

Compared to the height of the thin base of the trapezoid for this geometry with  $\approx 16\text{ mm}$  the groove height of  $3\text{ mm}$  reduces the thickness of the detector material by 19%. This is a large reduction also visible in the charge distribution plot (Figure 95) for  $30\text{ mm} < Y < 33\text{ mm}$ . On the thick side the step in scintillator thickness, from  $\approx 45\text{ mm}$  to  $\approx 42\text{ mm}$  of about 7% is not observable in the charge distribution.

In the later discussion about position resolution always the sum of two SiPMs attached to the same fiber is used. A histogram showing this light yield distribution for the same fiber and the same geometry as discussed before<sup>35</sup> is plotted in Figure 96.

<sup>33</sup>In this picture the readout channels of the thin base are 1, 2, 6 and 7. A value of  $\approx 15$  photons is measured by all those channels rather position independent.

<sup>34</sup>Channel one is in this case located at the upper thin base fiber showing values of at least 60 photons for muons close to this fiber.

<sup>35</sup>Channel one and channel five of the  $100\text{ mm}$  long  $30^\circ$  geometry

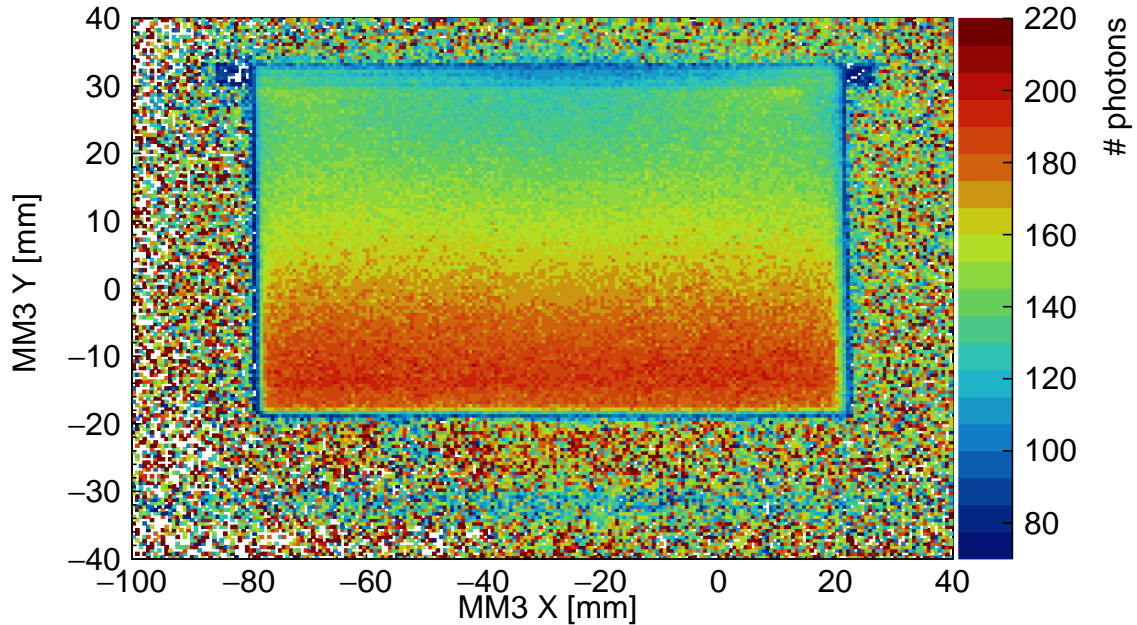


Figure 96: Light yield distribution for the sum of the detected photons of two SiPMs sitting opposite to each other at the same fiber. The plotted sum is obtained from channel one and channel five.

Compared to the case where just one end of the fiber is read out (Figure 95) the light yield distribution for a double sided readout is much more homogeneous. Still a slight enhancement of the collected light close to the ends of the fiber is expected and observed. The impact of those inhomogeneities on the spatial resolution will be discussed in chapter 7.6. In the following the light yield for the different fibers is presented. As shown in Figure 96 the light yield is rather constant in X direction. The light yield quoted is the average photon count in two  $1 \times 1 \text{ mm}^2$  sized areas. The position of those areas and the labeling of the fibers are sketched in Figure 97.

The areas are located in the center of PoSSuMuS in X direction with one being close to the lower edge of PoSSuMuS and the other close to the upper edge. Studying one particular fiber the average photon count in one of these areas can be interpreted as the maximum photon count, while the value in the other area is the minimum photon count. It is observed that with just one exception the area closer to the thin base of the current PoSSuMuS half gives the lowest light yield and vice versa. The one exception is the  $100 \text{ mm}$  long  $10^\circ$  geometry and both fibers of the thin base. For this particular case the thickness of the thin base is large enough that despite the fact that a muon travels through less material when traversing the scintillator at the thin side still more light arrives at the fibers close to such an impact position compared to a path with more material but larger distance between impact and readout. Labeling the four fibers of each geometry according to their readout channels, the light yield of all investigated trapezoids is summarized in Table 7.

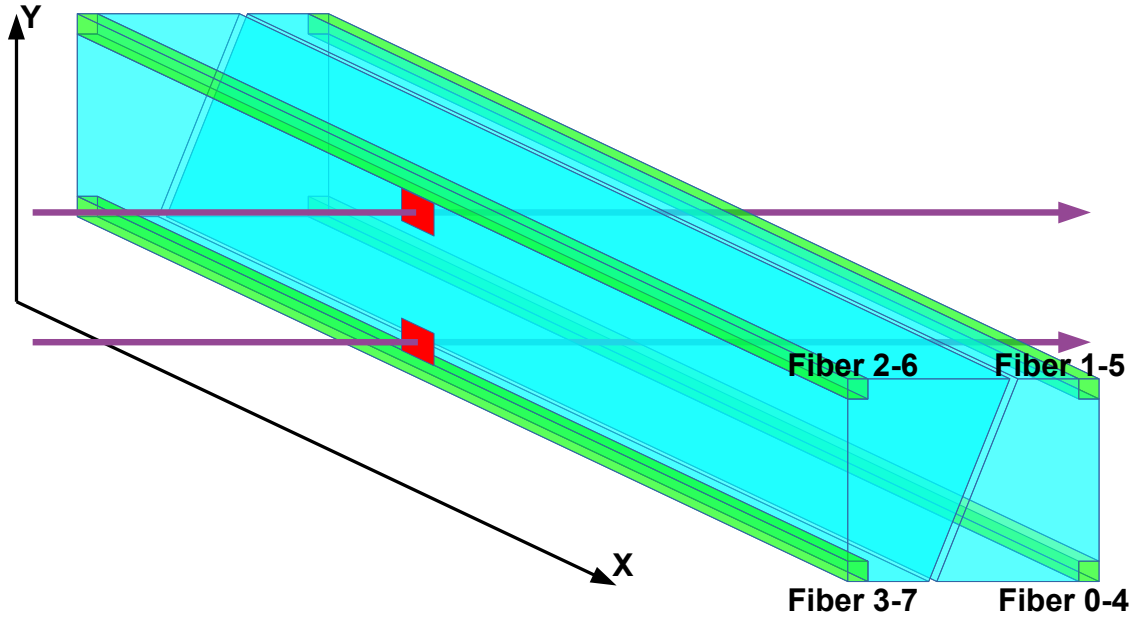


Figure 97: Scheme for the evaluation of the light yield. For each of the four fibers the average photon count in the two red areas is taken. According to Figure 96 these two values can be interpreted as maximum and minimum light yield the fiber detects.

	fiber 0-4	fiber 1-5
100 mm; 35° Tyvek	$87 \pm 36 - 247 \pm 36$	$127 \pm 44 - 225 \pm 45$
100 mm; 30° Tyvek	$119 \pm 43 - 269 \pm 39$	$131 \pm 42 - 188 \pm 42$
100 mm; 20° Tyvek	$146 \pm 42 - 252 \pm 46$	$156 \pm 42 - 173 \pm 44$
100 mm; 10° Tyvek	$138 \pm 38 - 194 \pm 34$	$122 \pm 36 - 136 \pm 37$
300 mm; 30° Tyvek	$81 \pm 40 - 173 \pm 40$	$106 \pm 43 - 149 \pm 41$
300 mm; 30° Aluminum	$64 \pm 24 - 120 \pm 41$	$86 \pm 30 - 109 \pm 38$

	fiber 2-6	fiber 3-7
100 mm; 35° Tyvek	$78 \pm 30 - 244 \pm 36$	$113 \pm 36 - 205 \pm 40$
100 mm; 30° Tyvek	$79 \pm 27 - 191 \pm 36$	$114 \pm 34 - 189 \pm 38$
100 mm; 20° Tyvek	$153 \pm 40 - 251 \pm 34$	$199 \pm 42 - 228 \pm 40$
100 mm; 10° Tyvek	$193 \pm 36 - 261 \pm 33$	$236 \pm 38 - 242 \pm 39$
300 mm; 30° Tyvek	$59 \pm 30 - 111 \pm 33$	$103 \pm 34 - 138 \pm 38$
300 mm; 30° Aluminum	$62 \pm 30 - 98 \pm 23$	$85 \pm 35 - 120 \pm 29$

Table 7: Light yield of the new geometries. The first number in each row is the length of the trapezoid. The given values are average number of photons recorded in a central position along the rod and once close to the thin and once close to the thick base. Lower values are always measured close to the thin base and vice versa for the high value, except for the fibers at the thin base investigating the 100 mm, 10° geometry, where it is the other way round. The errors given are the standard deviations derived from the light yield distribution.

The values given in this table are taken from the respective plots similar to Figure 96. The absolute minimum and maximum photon count measured for each geometry is always lower respectively higher compared to the value in the chosen area, but within the given error band. The latter gives a feeling about the variation of the energy loss in each event.

With a light yield of up to 300 photons<sup>36</sup> the primary goal of finding a geometry with an increased detection efficiency of scintillation photons is reached by using a shorter trapezoidal height. A statement about the best performing geometry will follow in chapter 7.6.2.

The observed higher value for the minimal photon count of fibers at the thin base compared to fibers at the thick base<sup>37</sup> in Table 7 is again explained by the shorter distance from impact to the readout. The minimum is always reached at positions where the trapezoid is thin, still the light yield is increased by reading such events close to the impact. An identical argumentation can be made for the higher maximum light yield of fibers at the thick base. Since the minimal values in Table 7 are observed always at the thin base, an increase of the length of this base, i.e. going to smaller inclination angles, should also increase those minimal values. For fiber 0-4 and 1-5 this behavior is observed for all 100 *mm* long geometries besides the case of the 100 *mm* long 30° geometry. But even here the results are within the error bands. A reason for this different behavior of this scintillator is given by an increased amount of air enclosures in the fiber package as well as in the junction of package and scintillator. Additionally the surface of this scintillator showed cracks, which are responsible for a higher photon absorption.

Another non intuitive result is a general increase of the maximum light yield for both fibers of the first scintillator (fiber 2-6 and 3-7)<sup>38</sup> when going to smaller inclination angles, while those values tend to decrease for both fibers of the second scintillator. The observation resulting from the second trapezoid is more intuitive. The possible path length of a photon is increased for decreasing trapezoidal inclination angles and therefore the chance of the photon to be absorbed before reaching the fiber increases. In addition to that the trapezoidal geometries should act like a cat eye, reflecting photons predominantly towards the thick side and this effect should increase with a steeper inclination. The only reasonable explanation for this behavior is a not well reproducible coupling of the SiPM to the fiber and of the fiber to the scintillator. It is therefore necessary to develop a better technique to glue the fibers to the scintillator in order to achieve a more reproducible result with less air enclosures and a better polishing procedure of the fiber ends. The latter is done in industry via a diamond milling tool, while here common grinding papers have been used. If such a milling is feasible in our case needs to be further investigated.

---

<sup>36</sup>This value is the maximum average photon count for of fiber 0-4 for the 100 *mm*, 30° geometry.

<sup>37</sup>E.g.  $127 \pm 44$  photons are measured for the 100 *mm* long 35° geometry at fiber 1-5 (thin base), while only  $87 \pm 36$  photons are counted with the same detector at fiber 0-4 (thick base).

<sup>38</sup>An exception here is the first scintillator in the 10° geometry, which has again a surface with more cracks compared to other scintillator halves.

Due to a limited beam time only the  $30^\circ$  geometry of the 300 mm long PoSSuMuS could be investigated. Covered in the same material, Tyvek, the longer trapezoid generally shows a lower light yield, which can be explained by the absorption length of the fiber and the scintillator. The company claims for both values  $> 3500$  mm, [Saint Gobain, 2011b], and  $\approx 1600$  mm, [Saint Gobain, 2011a], respectively. A comparison of a simulation and a measurement with this scintillator material suggests a much lower mean free path of  $\approx 700$  mm, [Müller, 2013], which is explained by aging effects of the material. In addition to this also minor cracks due to milling at the borders of the scintillators can absorb light. Therefore the slight decrease of the light yield for longer PoSSuMuS seems reasonable. For a use in the CRF as  $\approx 4000$  mm long versions, this decreasing can in the worst case result in almost no photon detection efficiency in the center of PoSSuMuS. It is advisable to use new scintillation material for such an application. Another result which could have been reproduced with the new geometries is the increased light yield of Tyvek compared to aluminum. All fiber combinations in the case of Tyvek wrapping show a higher light yield.

After finishing the discussion about the general performance of the detector, the next two chapters deal with the achieved spatial resolution in both directions of PoSSuMuS.

## 7.5 Position Resolution in the Time of Propagation Coordinate

Starting with the X-coordinate the reconstruction method of this spatial information from the timing information is described, followed by calculations concerning the achievable resolution. One of the key aspects here is to determine how long the light, triggering the TDC, has traveled from the place of creation to the readout. Here various possibilities can occur all disturbing the resolution. Each light trajectory can be separated into a part inside the scintillator volume and another part inside the wavelength shifting fiber. In Figure 98 three possible ways the light can travel are shown for each volume.

As an example one combination for a light trajectory is shown in the lowest sketch of Figure 98. It is very long, hence a reconstruction to a spatial coordinate can even lead to a position outside PoSSuMuS. It is therefore necessary to find a method with a high discrimination power for long trajectories, hence to find the timing value most suitable for reconstruction of a spatial coordinate. In the last part of this chapter different definitions achieving such a timing value and their resulting spatial resolutions are discussed.

### 7.5.1 How to get a Spatial Coordinate out of Timing Information

This chapter deals with methods to reconstruct a spatial information from a timing signal. Already in the former chapters, dealing with the first prototypes a reconstruction method was described representing the general idea. A reference system defines the spatial coordinate system of the setup and the timing information is scaled by a certain factor so that the

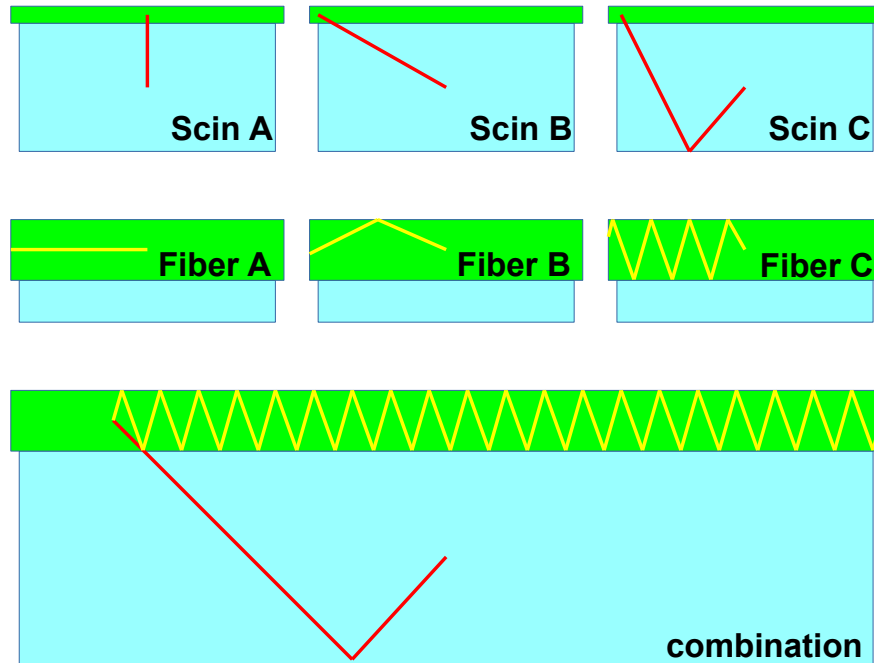


Figure 98: Possible pathways the light takes to the readout. The path of the light can be separated into the path in the scintillator (red) and the path inside the fiber (yellow). Three different scenarios for the light inside the scintillator and inside the fiber are shown with increased length from case A to case C. In the lowest scheme an example for a possible combination is shown, which results in a very long propagation time of flight.

data fit into this system. The factor itself can be interpreted as the effective speed of light with which a scintillation photons travels to the readout. It takes into account several issues like reflections, meaning that a photon does not take the direct path to the readout, or the wavelength shifting process, which has a decay time of  $2.7 \text{ ns}$ , [Saint Gobain, 2011b]. It is calculated simply by comparing the value of the timing signal with the spatial coordinate of the muon, defined by the reference system. The width of the resulting distributions is defined to be the spatial resolution.

Since for the new geometries also a much finer reference system is chosen, the method to determine the effective speed of light is done on a finer grid. For the following explanations the  $300 \text{ mm}$  long  $30^\circ$  geometry wrapped in Tyvek serves as example. As method to determine the timing just the time difference, given by the TDC, of both SiPMs connected to fiber 1-5 is used. Figure 99 shows the distribution of this timing inside PoSSuMuS.

This histogram shows an average of the recorded timing in each bin, obtained similar to the charge average histograms in chapter 7.4. The condition to fill this histogram is a signal in both TDC channels. It can be seen that the timing decreases from left to right. The barely visible effect of a Y dependence of the timing is neglected for the moment. It will be considered later in this chapter for a fiber where this effect is more prominent. Considering

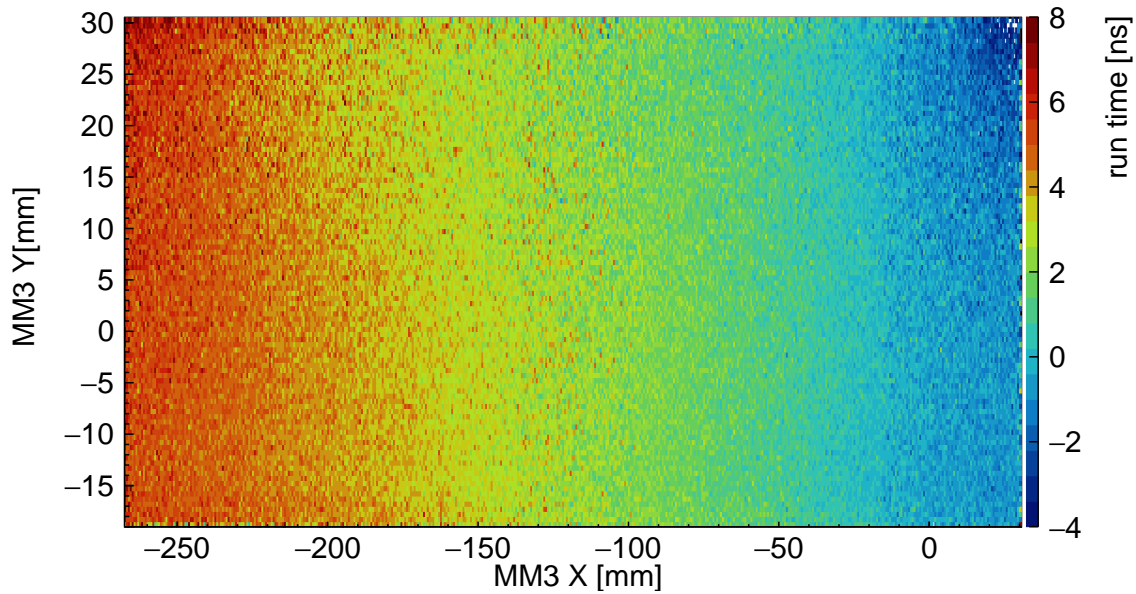


Figure 99: Timing distribution of the 300 *mm* long 30° geometry wrapped in Tyvek for fiber 1-5. Calculating the difference of the timing of the TDC signals for both SiPMs connected to this fiber defines the timing.

the timing to be independent of Y Figure 100 shows the distribution of the timings for each bin in X direction, hence a projection of the timings of Figure 99 onto the X axis.

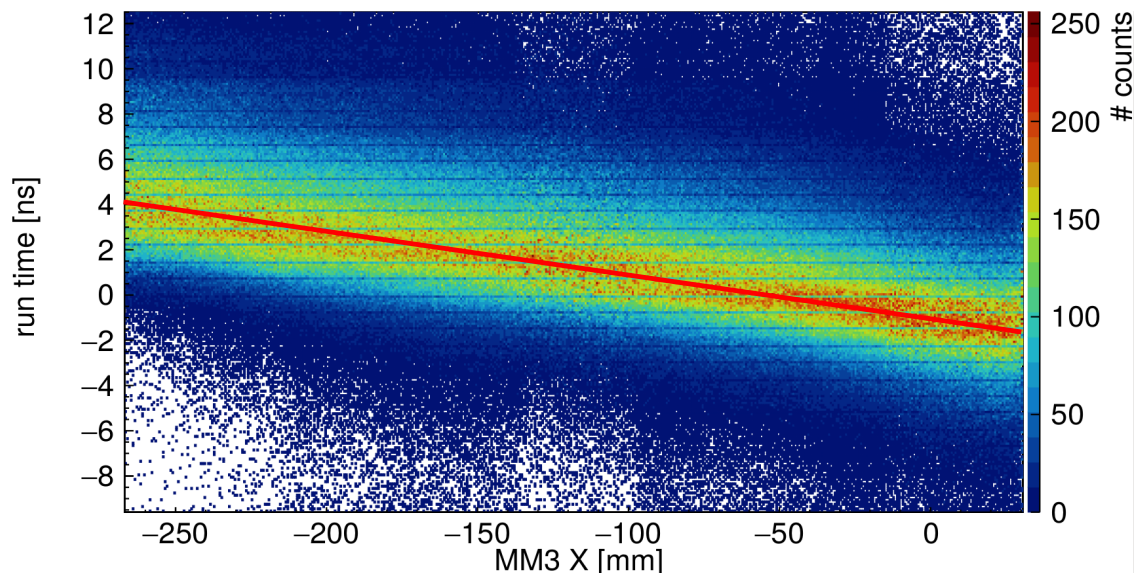


Figure 100: Distribution of propagation time difference along the X direction for the 300 *mm* long 30° geometry wrapped in Tyvek for fiber 1-5.

Again a monotonous decrease in timing is observed, but this time also the fluctuations of the measured propagation time difference are shown. The horizontal lines visible in this histogram originate from the digitization steps introduced by the TDC and a too fine binning

of the plot. From this histogram the effective speed of light is determined for this setup. For this purpose the propagation time distribution of each slice along X is fitted with a Gaussian function, resulting in two new histograms<sup>39</sup>. The first one gives the mean of the Gaussian along X. It is fitted with a straight line, with the slope of this linear function being the inverse of the effective speed of light this system provides. The other histogram is given by the width of each Gaussian along X. Up to now this width is measured in *ns*, but dividing it by the slope of the linear fit done before, the width is given in units of *mm*, see Figure 101.

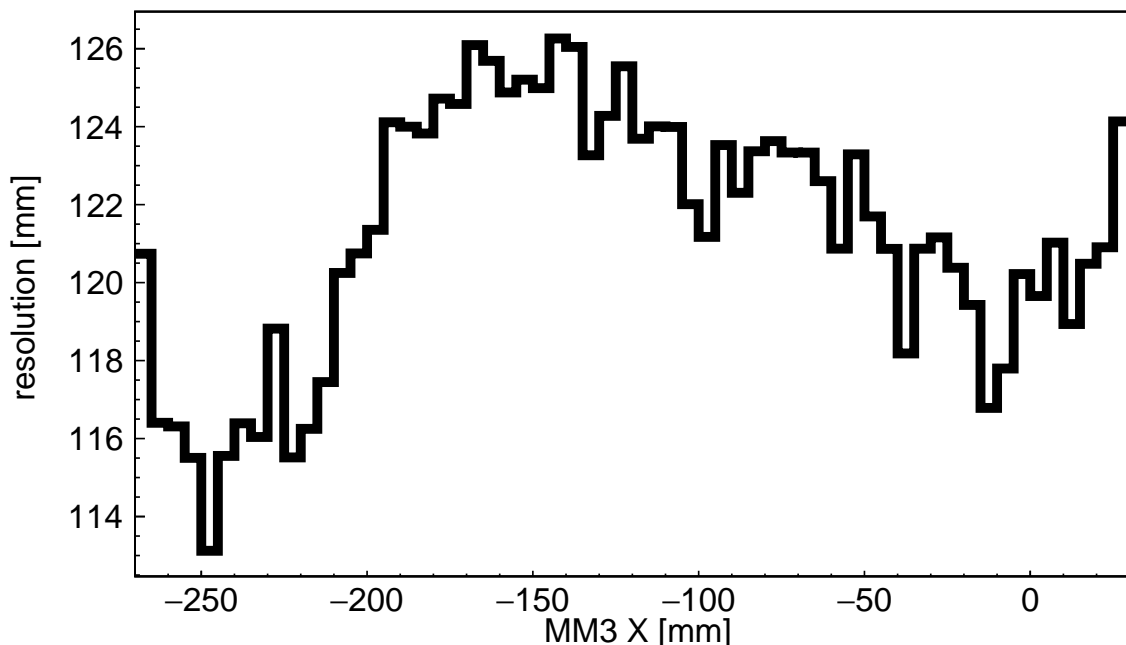


Figure 101: Distribution of spatial resolution in X direction for the 300 *mm* long 30° geometry wrapped in Tyvek for fiber 1-5.

The measured resolution varies in the range from 113 *mm* to 126 *mm*. This variation may have different origins. One is photon statistics. The more photons a SiPM detects in an event the higher is the fraction of photons taking a more direct way to the readout than others. At positions with a more efficient coupling from scintillator to fiber more photons can be detected possibly resulting in a lower width of propagation time differences. Another reason comes from geometrical effects, where regions of the scintillator are more effective with respect to propagation time differences. Such effects are close to the edge, since the angular acceptance of the fiber for the scintillation light is higher, reducing the time spread of at least one SiPM. This can be seen in Figure 101, but since the first mentioned effect influences such general geometrical considerations the resulting distribution is not symmetric. A last issue to discuss is the validity of the linear fit. Figure 100 shows minor deviations from

<sup>39</sup>The actual distribution is not a perfect Gaussian, but since this direction is going to deliver only a coarse spatial resolution this fit is sufficient and the mean and width parameter are used to characterize the detector.

a straight line originating again from geometrical properties of the trapezoidal rod. This error propagates when rescaling the distribution into the spatial coordinate system. But since the deviation from a linear fit is small and the width of this resolution with more than one third of the entire detector length is rather large, a straight line fit is considered to be sufficient. A more detailed discussion about the achieved resolutions follows in chapter 7.5.3. Another quantity describing the quality of a detector is given by the residual. It is defined to be the difference of the position recorded by the reference system and the reconstructed position of the device under test. In case of PoSSuMuS the propagation time difference of the SiPMs is taken, rescaled with the effective speed of light, and subtracted from the position of the Micromegas detector event by event. The result is shown in Figure 102.

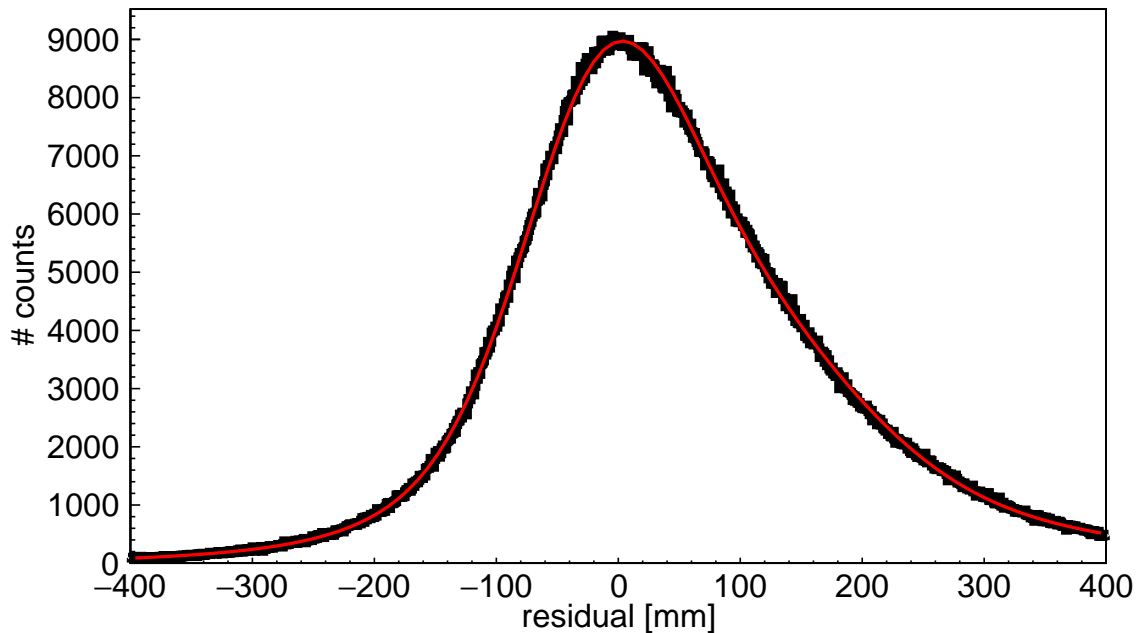


Figure 102: Residual distribution for the 300 *mm* long 30° geometry wrapped in Tyvek for fiber 1-5. The residual is defined as difference between reference track position and reconstructed track position. It is fitted with a triple Gaussian function providing a weighted mean of 103 *mm*.

What can be seen is an asymmetric function which can be fitted by the sum of three Gaussian distributions. Weighting the width of each Gaussian with its integral a total width of this distribution of 103 *mm* can be calculated. Reasons for the use of the triple Gaussian function originate from the use of two independent readout channels, which can both have an own Gaussian distribution<sup>40</sup>. Additionally the entire system has its own statistical fluctuations. The asymmetry itself is also reasonable. As mentioned the calculation is done by  $X_{\text{Micromegas}} - X_{\text{PoSSuMuS}}$ . Events with this difference providing a large positive value

<sup>40</sup>The light for each readout channel comes from different scintillation photons as well as from different wavelength shifted photons.

means that the value for the position reconstructed by PoSSuMuS is too small, hence a propagation time difference close to zero. Values close to zero, even in case of a mis-measurement, are located inside the detector. A too large runtime difference would mean a reconstructed position outside the detector, which is a kind of mis-measurement which is unphysical and therefore suppressed. Hence the calculation for this difference should more often give a low runtime difference, rather than a large one.

Fiber 1-5 was chosen to explain the procedure since it provides the best results of all four fibers. The occurred problems using the other fibers have again a statistical nature. A histogram like in Figure 99 is made for all four fibers, each having the requirement that both connected SiPMs produced a signal in the TDC. As mentioned in chapter 7.3 a LTD in front of the TDC requests a certain pulse height<sup>41</sup> in order to send a start signal to the TDC. Since more light is produced for a muon transition close to the thick base, this threshold is reached more frequently in such events, see Table 7. The other effect playing an important role in this case is the beam spot, which is located closer to the upper side of PoSSuMuS, sketched in Figure 103.

This asymmetric beam profile within PoSSuMuS is the reason why all four fibers show a different behavior when producing histograms like 99:

- Fiber 0-4: It is located at the thick base of the second trapezoid in beam direction. For low Y values of the muon impact position a large amount of events is expected in which the threshold of the LTD in front of the TDC is reached due to the thick base of the trapezoid located here, see Figure 103. This means that a large amount of statistics are collected to analyze the detector. On the other side, medium statistics for high Y values should be observed, due to the thin base of the trapezoid and large distance to muon impact but high muon count due to beam center.
- Fiber 1-5: Since it is glued to the thin side of the second trapezoid, the statistics are expected to be lower compared to fiber 0-4 for low Y values. Still it is rather high because enough photons are produced there per event to pass the threshold of the LTD. For high Y values, since the fiber is close to those impact positions and the center of the beam causes lots of muon triggers, high statistics is expected.
- Fiber 2 – 6: This fiber is located at the thick base and close to the center of the beam spot, just like fiber 1-5. This combination of a high light yield and high beam intensity results in very good statistics for high Y values, but a very poor one for low Y values.

---

<sup>41</sup>This threshold is chosen such that during time intervals of no beam, no signal passes the discriminator in order to suppress dark current events starting the TDC time measurement in advance of a muon event, which would disturb the time measurement. But this means that the trigger was set to an extremely high value of  $\approx 200$  mV. This adjustment was done once for the entire beam time and for each channel individually.

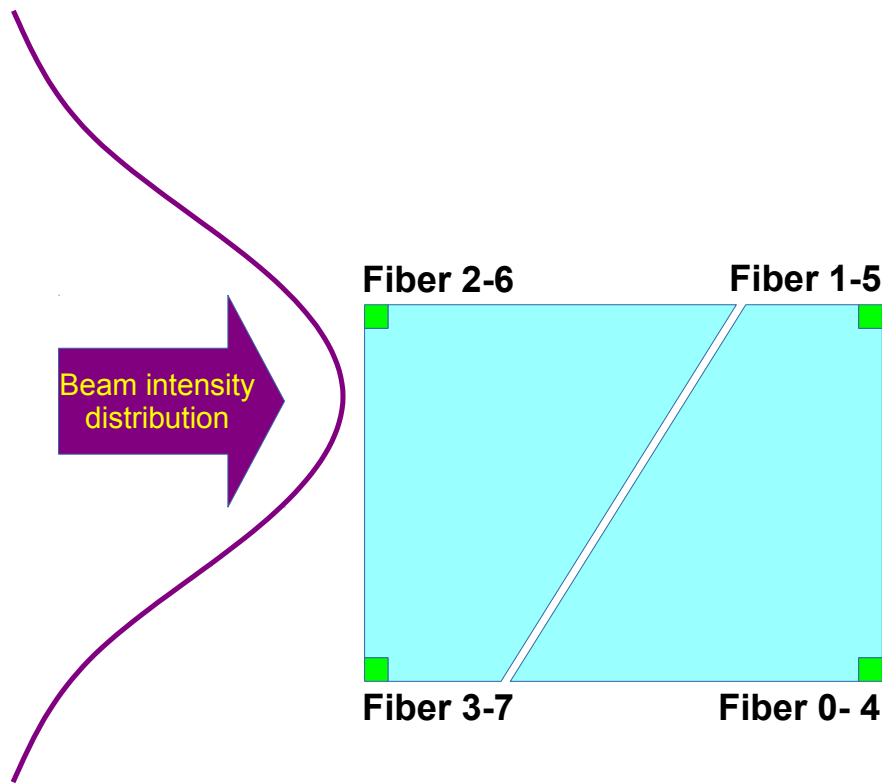


Figure 103: Scheme of the beam intensity distribution. As already mentioned the center of the beam beam is located in the upper part of PoSSuMuS.

- Fiber 3 – 7: It collects the light at the thin side of the first detector half. A larger distance to the beam center and less scintillation material cause low statistics for muon impacts close to this readout. The low distance between impact and readout still slightly compensates those negative effects. For high Y values a reasonable amount of statistics are expected which is enough to analyze the timing there.

All expectations gathered above are observed. The only fiber with the best efficiency over the whole detector is fiber 1-5 with 61 %, see Table 9. As a comparison data taken with fiber 0-4 is presented. First of all Figure 104 shows the hit distribution for events in which the TDC recorded a timing signal for channel zero and four.

Compared to the hit distribution shown in Figure 94 more slices in X direction are visible and the maximum is shifted to lower Y values. The higher number of slices is again a result from the shift of PoSSuMuS through the reference system in order to illuminate the total detector. In total six positions of PoSSuMuS were necessary to investigate the full detector length. In contrast to Figure 103 the maximum of the event count of the histogram in Figure 104 is measured for low Y values despite the fact that the beam profile is still shifted to high Y values. Even if the beam provides more statistics for higher Y values the LTD gives more triggers for a higher light yield. This effect becomes so dominant, that for several bins in

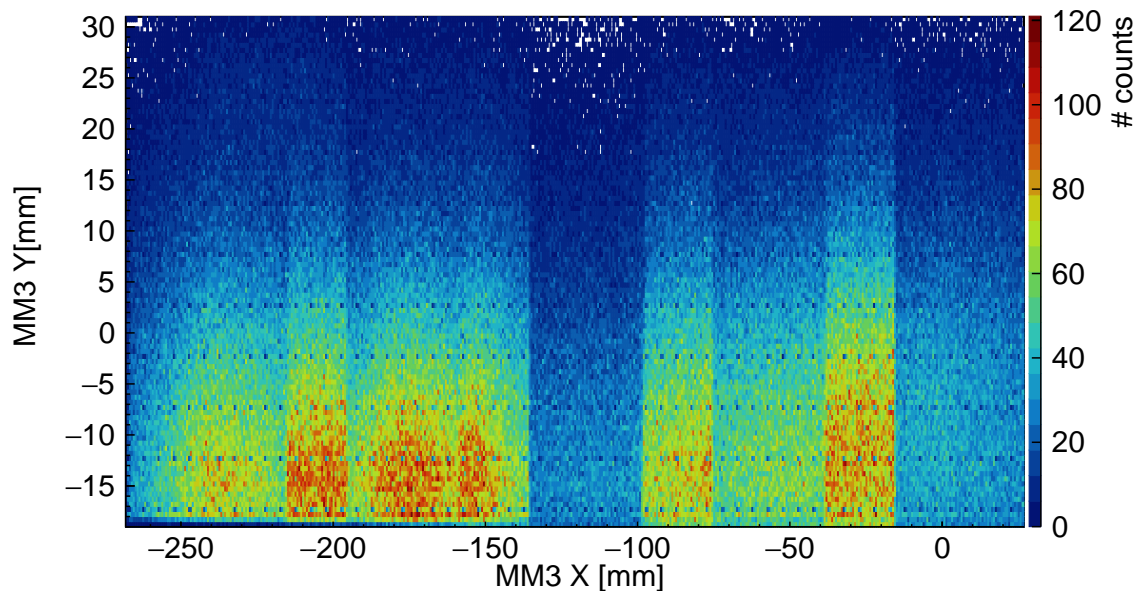


Figure 104: Hit distribution for the 300 *mm* long  $30^\circ$  geometry wrapped in Tyvek for fiber 0-4. Despite the fact that the beam provides more muons triggering the readout in the upper part of the picture, the requirement of having a signal in the TDC for channel zero and four highly favors events producing more photons, i.e. those at the bottom of the detector. The slices in X direction result from the need of several runs with shifted PoSSuMuS positions with respect to the reference system in order to study the full detector length. In total six positions are used for this.

the upper part of the histogram just very few counts are registered. For the analysis this means that the bin size in X direction needs to be enlarged to achieve statistically relevant results. Additionally sticking to a comparison taking into account only SiPMs connected to the same fiber results in a Y dependent behavior of the X resolution discussed in chapter 7.5.2. Chapter 7.5.3 will deal with this problem introducing other methods to combine SiPMs of different fibers in order to get a timing value.

The Y dependency becomes even more clear, looking at Figure 105.

Like for fiber 1-5 discussed at the beginning, a decrease of timing values is observed not only in X direction but also in Y direction. Additionally also the slope of the timing value (Figure 105) decreasing from left to right is flatter for higher Y values. Looking at impacts further away from the readout fiber, the time distribution of photons arriving at the readout fiber flattens out, hence the difference in time the light needs to travel to both ends of the fiber becomes more and more negligible with increasing Y, which results in a worse spatial resolution. A more detailed look at this was done by [Kulosik, 2017], which is summarized in the next chapter. Another point which becomes clear due to this plot is that the method described above, projecting those timing values to the X axis, does not work for this fiber due to the high dependence on the Y coordinate of the impact. Therefore quoting a spatial

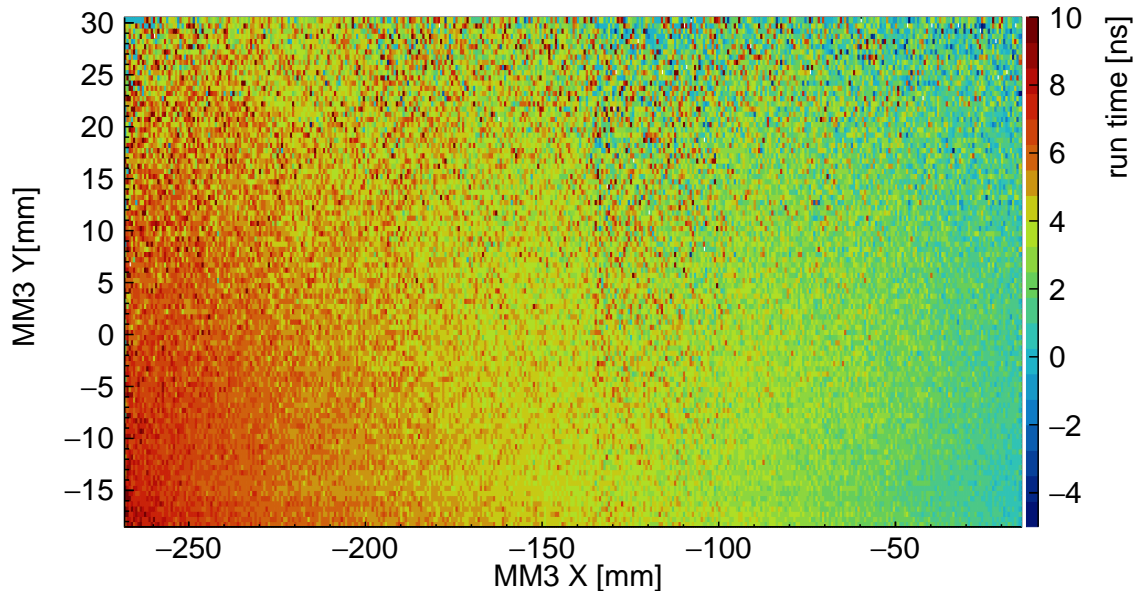


Figure 105: Timing distribution of the 300 *mm* long 30° geometry wrapped in Tyvek for fiber 0-4. In the lower regions of this histogram a clear decrease of the timing signal is observed from left to right. But additionally a decrease in the timing values from bottom to top is observed.

resolution for this fiber, which is *Y* independent, is just the average of a good resolution for low *Y* values and a bad resolution for larger *Y* values. Combining the timing information of all connected SiPMs can result in a better spatial resolution, otherwise it would be necessary to take the second coordinate of PoSSuMuS into account, which is problematic, since a wrongly reconstructed coordinate in *Y* direction would also influence the determination of the *X* coordinate in a negative way.

### 7.5.2 Estimates about Achievable Spatial Resolution based on Light Propagation Time and Statistics Effects

Due to the complexity of the system having, e.g., a trapezoidal structure and a wavelength shifting process a detailed simulation of the system is required for a statement on the resolution. As already mentioned the resolution in this coordinate is in the order of 100 *mm*, which is much higher than the resolution in *Y* direction expected to be less than 10 *mm*. An estimate of effects contributing to this rather high resolution can be done as a back-of-the-envelope calculation.

A first idea, already mentioned in the previous chapter, concerns the *Y* dependence of the *X* resolution, where [Kulosik, 2017] started with some basic thoughts using a simplified model to describe the photon propagation inside the scintillator. It is assumed that the photon being responsible for triggering the TDC travels its entire way towards the readout along a straight line just inside the scintillator without hitting the wavelength shifting fiber, see

Figure 106.

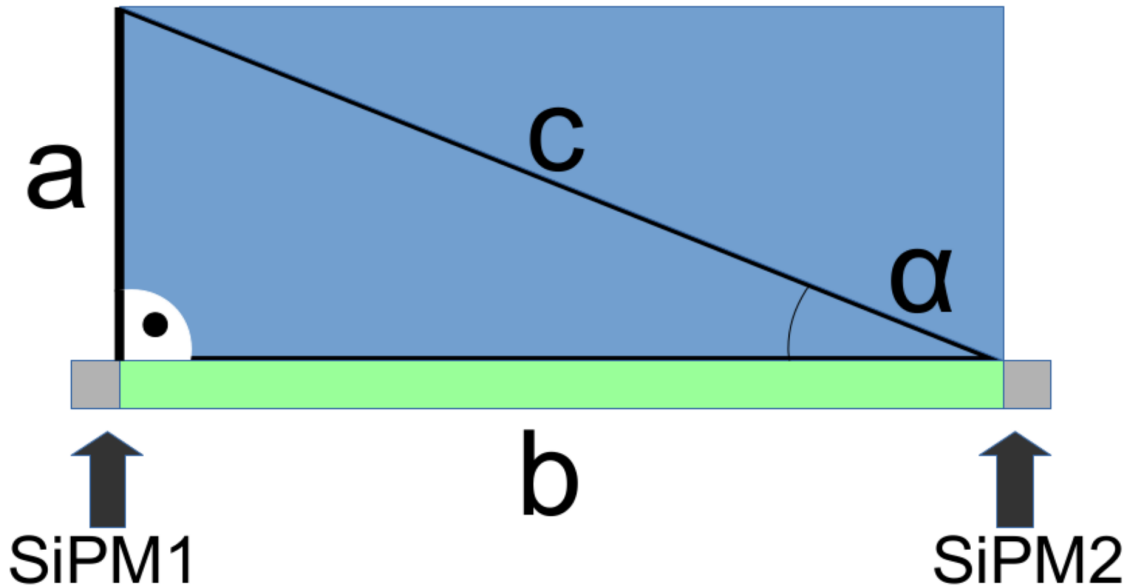


Figure 106: Scheme of a simplified model to describe the timing distribution. Here it is assumed that a photon travels inside the scintillator its entire way towards the readout. Image taken from [Kulosik, 2017].

Goal of this model is to determine the slope of the timing values as a function of the distance between impact and fiber, which is represented by  $a$  in the scheme of Figure 106. In general the slope can be written as

$$m = \frac{(t_L - t_R)(left) - (t_L - t_R)(right)}{b} \quad (7.5.1)$$

with  $t_L$  and  $t_R$  being the time values obtained from the left and right readout. The timing is then calculated on the left and on the right side of PoSSuMuS. In this model the timing evaluated on the left side of PoSSuMuS is proportional to the path difference of  $a$  and  $c$ . Due to symmetry reasons the timing on the left side is just the negative of the timing on the right side. Hence equation 7.5.1 can be re-written as

$$m \propto \frac{(a - c) - (c - a)}{b} = 2 \cdot \frac{(a - c)}{b} \quad (7.5.2)$$

Finally plugging in Pythagorean theorem for  $c$  into equation 7.5.2 leads to

$$m \propto \frac{a - \sqrt{a^2 + b^2}}{b} \quad (7.5.3)$$

The qualitative dependence on  $a$  is similar to the data in Figure 105: For small values of  $a$  the slope has a maximum, while it decreases monotonously for increasing  $a$ . The pro-

portionality factor in this equation is given by the inverse of the speed of light inside the scintillation material, which is  $\frac{n}{c} = \frac{1.58}{300 \frac{mm}{ns}} = 0.0053 \frac{ns}{mm}$ , [Saint Gobain, 2011a]. Table 8 shows the theoretical values for the slope obtained from plugging in the geometrical dimensions of the scintillator<sup>42</sup> into equation 7.5.3. Also the measured values for the inclination are given, which, even without taking error-bands into account, are far off the values of the model.

	$a = 0 \text{ mm}$	$a = 50 \text{ mm}$
theory	$-0.0053 \frac{ns}{mm}$	$-0.0045 \frac{ns}{mm}$
measurement	$-0.023 \frac{ns}{mm}$	$-0.0092 \frac{ns}{mm}$

Table 8: Theoretical and observed conversion factors from a timing value to a spatial position. Those factors can be interpreted as the inverse of the effective speed of light for the photons traveling towards the readout.

This shows on the one hand, that just the direct path to the readout is not what is detected in reality due to neglected influence of reflection processes. On the other hand this model is still sufficient to explain the fact that the X resolution is Y dependent.

Important for the time resolution is not the absolute value of the speed of light inside the medium but rather its component in direction towards the readout, labeled as effective speed of light in chapter 7.5.1, which is of course smaller than its absolute value. This means that the measured resolution should be much better than predicted by this model.

With a digitization step given by the TDC of  $35 \text{ ps}$  and the inverse of the effective speed of propagation speed of  $0.023 \frac{ns}{mm}$  the limitation of the spatial resolution determined by the electronics is given by  $\frac{35 \text{ ps}}{0.023 \frac{ns}{mm}} = 1.5 \text{ mm}$ . Even for the case of a large distance between impact and fiber the limit of the spatial resolution is  $\frac{35 \text{ ps}}{0.0092 \frac{ns}{mm}} = 3.8 \text{ mm}$ . Both limits are far away from the values plotted in Figure 101, which are in the order of  $115 \text{ mm}$ .

Up to now only velocities have been taken into account, but the statistical nature of the scintillation and the wavelength shifting process are neglected. The decay time of the scintillation and wavelength shifting process are  $2.4 \text{ ns}$  and  $2.7 \text{ ns}$ , respectively, [Saint Gobain, 2011a], [Saint Gobain, 2011b]. Close to fiber 0-4 a photon would propagate with an effective speed of light of  $\approx 45 \frac{mm}{ns}$ <sup>43</sup>. A convolution of those two statistical processes results in a width of  $3.6 \text{ ns}$ . Multiplying this time spread with the effective speed of light gives a spatial spread of  $163 \text{ mm}$ , which is close to the observed spatial resolution but a bit too large<sup>44</sup>. Taking into account that a single muon produces  $\approx 20000$  photons per cm of traversed scin-

<sup>42</sup> $a = 50 \text{ mm}$  and  $b = 300 \text{ mm}$

<sup>43</sup>This value is much smaller than the speed of light in the scintillator, which is  $\approx 190 \frac{mm}{ns}$ . What is observed here are effects like reflections, elongating the path of the photon as well as excitation inside the wavelength shifting fiber prolonging the time between trigger and readout signal.

<sup>44</sup>No faster products are available from the supplier Saint Gobain [Saint Gobain, 2011b].

tillator<sup>45</sup>, while only  $\approx 100$  of them are counted in an event, means that enough light is produced to assume that only the fast produced photons are considered in this time spread. This would reduce the time spread given by the convolution of both timing constants, hence reduce the spatial resolution. It gives also a motivation to further develop the detector concept to improve the light yield in order to enhance the fraction of fast produced photons in the total detected light yield. The results for the spatial resolution obtained with the current detector are presented in the next chapter.

### 7.5.3 Achieved Timing Resolution with Different Techniques

The following chapter deals with the search for a method to pick those two SiPMs in each event providing overall a low spread of the measured timing values. Since the contribution of the wavelength shifting process is larger than the 100 *mm* long geometries, for the following only the 300 *mm* long PoSSuMuS detectors are investigated concerning their resolution in X direction. Results obtained with the shorter geometries are summarized in appendix C. There are three criteria according to which the choice of the SiPMs needs to be evaluated. These criteria are:

1. low Y dependence on the timing signal
2. high efficiency
3. good resolution

To investigate the first two criteria the detector is divided in Y direction into five 10 *mm* wide slices labeled from one to five, see Table 9. Slice one is the lowest one in Y direction and slice five the highest. The resolution in each slice should be as identical as possible to each other and to the resolution of the entire detector. No drop in efficiency should be observed. The following five methods to pick a readout channel from each side are investigated:

- A: The SiPMs of each side of the fiber are taken. This method is used to have a very well defined reference, meaning that in contrast to all following methods here the used readout channels are predefined. As examples only the results for the fibers 0-4 and 1-5 are presented.
- B: In addition to the SiPM signals also the time of the trigger is recorded by the TDC. Taking the difference between this time and the time of all four SiPMs of each side of PoSSuMuS eight time values are calculated. For each side the channel is chosen, which provides the lowest difference to the trigger signal, i.e. using the signal from the earliest scintillation photon.

---

<sup>45</sup>The mean energy loss of a muon is  $\approx 2 \frac{\text{MeV}}{\text{cm}}$ , [PDG, 2012] and it takes  $\approx 100 \text{ eV}$  to create one scintillation photon, [Leo, 1994].

- C: The average time over all SiPMs of each side is calculated and used for timing calculation.
- D: A large pulse height detected by a SiPM also means a significant quantity of photons arriving very quickly at the readout. The channel which collected the most photons on each side is used.
- E: The timing is calculated for all 16 combinations of SiPMs from the left and the right side. The smallest time difference is further investigated.

For method B to E it is important to first calibrate the channels of the TDC. The goal here is that the four SiPMs of each side provide the same time distribution for the same hit position of a muon. For this two  $5 \times 5 \text{ mm}^2$  large irradiation areas are chosen, as sketched by the red areas in Figure 107.

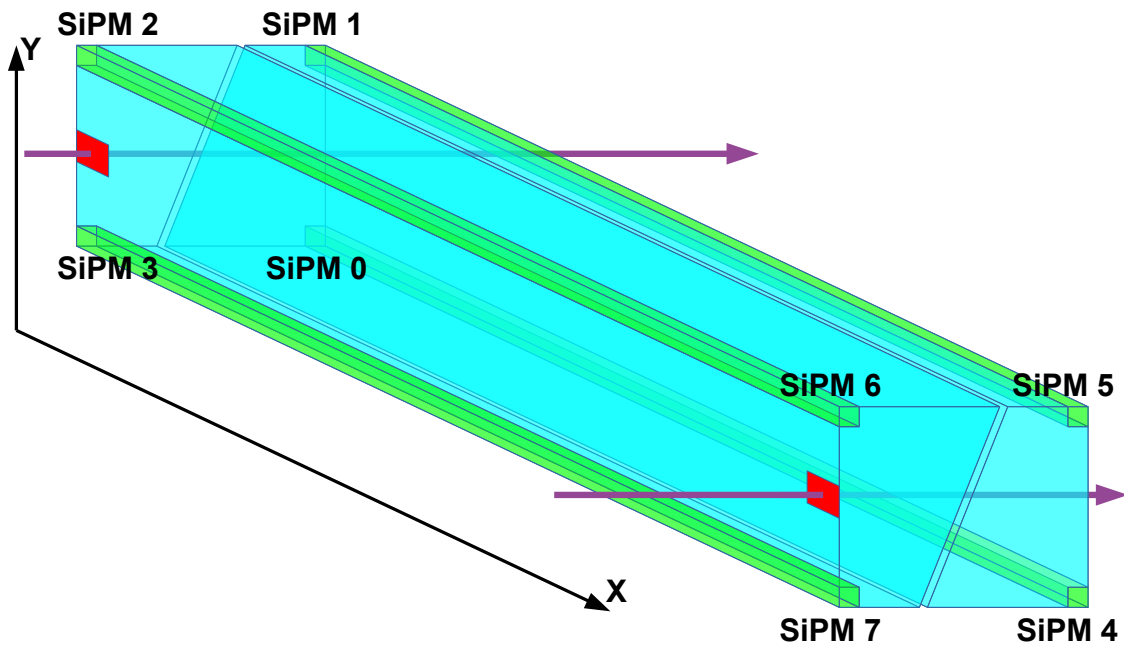


Figure 107: Scheme for the calibration of the TDC channels. Two  $5 \times 5 \text{ mm}^2$  large areas, shown in red, are localized in the center of PoSSuMuS in Y direction with one being on the left and one on the right side of the rod. SiPMs 1 to 3 are calibrated using muon passing the red area on the left side and vice versa for SiPMs 4 to 7. The timing values the different TDC channels provides have to be identical to each other for SiPMs on the same side of the rod. In order to suppress disturbing side effects a calibration position as close to the readout channels as possible is chosen.

In Y direction both positions are centered with respect to PoSSuMuS, while in X direction one area is close to the left and one close to the right side. The left irradiation area is used to calibrate SiPM channels zero to three and the right area is used for channel four to seven. In Table 9 the achieved efficiencies of all methods are shown for each Y slice and for the whole detector.

slice	one	two	three	four	five	whole detector
# events	679030	780090	903292	930381	946496	4239289
A: Fiber 0-4	78 %	52 %	26 %	12 %	5 %	34 %
A: Fiber 1-5	80 %	75 %	60 %	49 %	42 %	61 %
B: Fastest left/right	97 %	98 %	95 %	99 %	99 %	98 %
C: mean	97 %	95 %	98 %	99 %	99 %	98 %
D: most photons	97 %	98 %	95 %	99 %	99 %	98 %
E: fastest timing	97 %	98 %	95 %	99 %	99 %	98 %

Table 9: Efficiencies of X coordinate measurements. Shown are the number of events in which the reference Micromegas reconstructed a muon within the active area of PoSSuMuS. The efficiencies are given by the number of events in which the methods could be applied with respect to the overall number of events PoSSuMuS detected. For this study the detector is subdivided into five 10 *mm* wide slices in Y direction

As reference for the efficiency calculations the number of events, in which the reference Micromegas reconstructed a muon within the active area of PoSSuMuS, is chosen. A reconstruction of the X coordinate is possible only if the required channels showed a signal. This results in a drastic drop of efficiency for method "Fiber 0-4" and "Fiber 1-5". For all other methods it is enough if at least one TDC channel at each side recorded a signal and therefore the efficiency is always above 95 % meaning that all presented methods are applicable for the reconstruction of the X coordinate.

In the following plots showing the achieved resolution of the discussed methods only results for slice one, three, five and the whole detector are drawn in order to keep the histogram sufficiently clear. First the resolution of the two mentioned fibers is presented with fiber 0-4 serving as an example of the achievable resolution of a fiber located at the thick base of a trapezoid, plotted in Figure 108.

The black curve in this histogram shows the resolution including all events inside the PoSSuMuS area which is between 110 *mm* and 122 *mm*, which is slightly better than the results from the first prototype detector. The efficiency is only 34 % for this method. The variation is due to edge effects of reflections of scintillation photons produced close to a side of PoSSuMuS, described in chapter 7.5.1. Looking at the slice close to this readout fiber (red line) the obtained resolution ranges from 78 *mm* to 100 *mm*, which is much better than the average result of the whole detector. In principle one could think of selecting a fiber according to the reconstructed Y position. But as the efficiency is still just 78 % this idea is not investigated. The other two slices have a worse resolution and a worse efficiency. All in all this fiber alone should not be used for a reconstruction of the X coordinate.

The second presented fiber 1-5 has a more stable efficiency as a function of the slice number. Resolutions for this fiber are plotted in Figure 109.

As mentioned the resolution for the whole detector is measured to be between 113 *mm* and

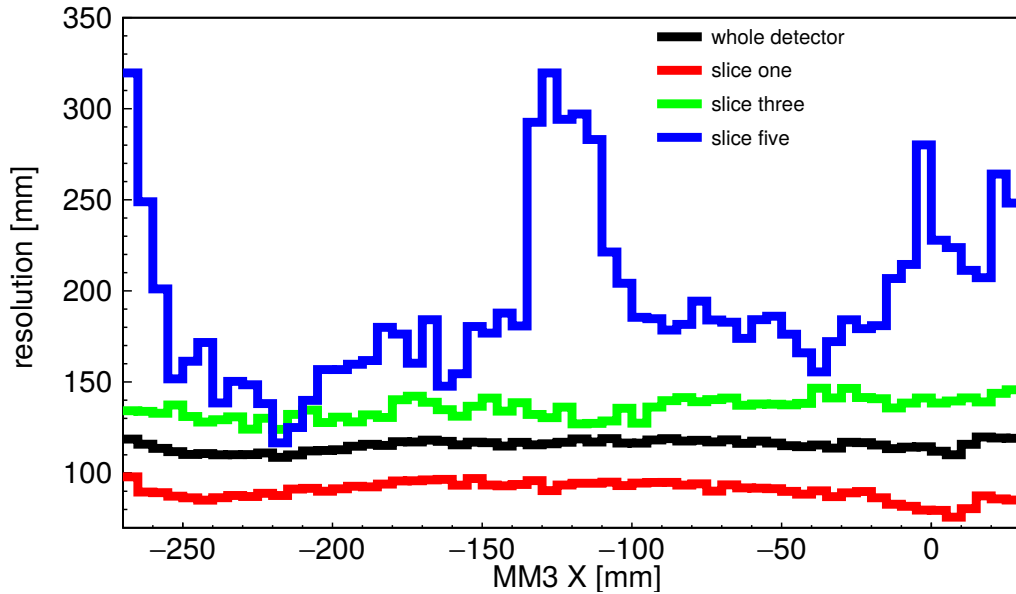


Figure 108: X resolution for the 300 *mm* long 30° geometry wrapped in Tyvek obtained with fiber 0-4. Shown are the resolutions for four different spatial selections of muon events. In this case slice one is close while slice five is far from the analyzed fiber. Note that the statistics for slice five is very low, see Table 9. The black curve representing the whole detector yields an average resolution of  $\approx 120$  *mm*.

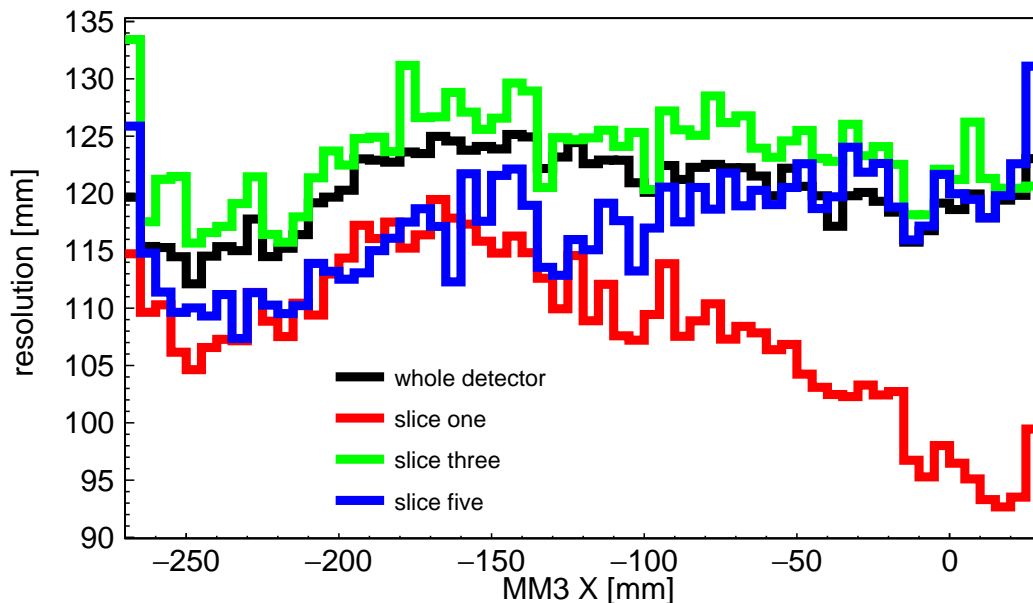


Figure 109: X resolution for the 300 *mm* long 30° geometry wrapped in Tyvek obtained with fiber 1-5. Shown are the resolutions for four different spatial selections of muon events. In this case slice five is close to the analyzed fiber while slice one is far away from it. The curve representing the whole detector yields an average resolution of  $\approx 120$  *mm*.

126 *mm*, which is basically the same as for fiber 0-4. For this fiber both slices close to the bases of the trapezoid perform better than the detector average while the central region

is slightly worse. While for slice one in average more photons are generated per incident muon, slice five provides the smallest distance to the actual readout fiber. Both situations are obviously supporting a good spatial resolution. The other fiber of a thin base, i.e. fiber 3-7, suffers from the adjustment of the setup with respect to the beam. Like for slice five and fiber 0-4 too few events are recorded in order to derive a value for the resolution. A comparison of both is therefore not possible.

As an intermediate conclusion it can be stated that the improvement in light yield did not lead to an improvement of the spatial resolution in light propagation direction, when investigating only pairs of SiPMs as an entangled system. Despite this result the analysis methods to combine SiPMs from different fibers drastically improve the efficiency to reconstruct an X coordinate and also improve the spatial resolution. The much better efficiency is explained by the fact that now a reconstruction can be performed, if at least one SiPM on each side gives a signal in the TDC.

Starting here with the approach B to pick on each side the one SiPM providing the quickest time signal in the TDC a resolution below  $100\text{ mm}$  is achieved, see Figure 110.

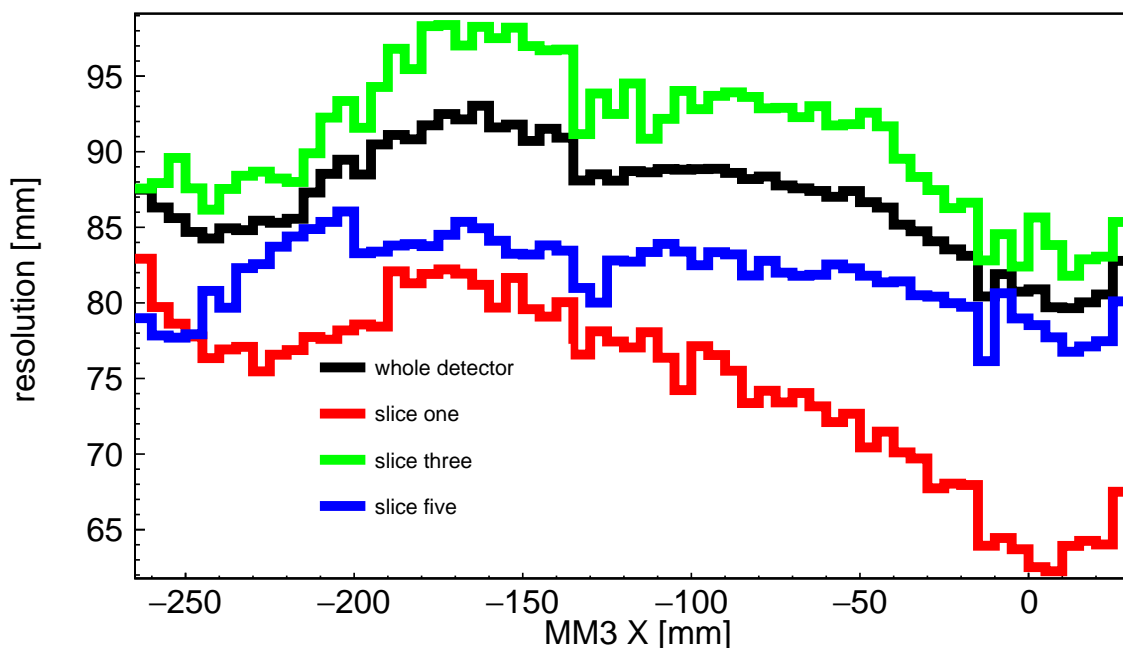


Figure 110: X resolution for the  $300\text{ mm}$  long  $30^\circ$  geometry wrapped in Tyvek obtained with fastest responding SiPMs. Shown are the resolutions for four different spatial selections of muon events. The resolution is better for slices close to the readout fiber compared to the central slice or the detector average which is  $\approx 85\text{ mm}$ .

In average over the whole detector a resolution between  $80\text{ mm}$  and  $93\text{ mm}$  is measured. In case of slice one values even below  $65\text{ mm}$  are observed. Since the behavior of both slices close to the readout fibers show better resolutions than the central one, similar to the case shown in Figure 109 for the readout of fiber 1-5, it can be concluded that dominantly the

SiPMs closer to the impact will be the one with a better resolution and this method picks the best one.

Since fluctuations can occur either to higher or to lower time values, another rather stable value should be the mean of all four readout channels per side of PoSSuMuS (method C), which is shown in Figure 111.

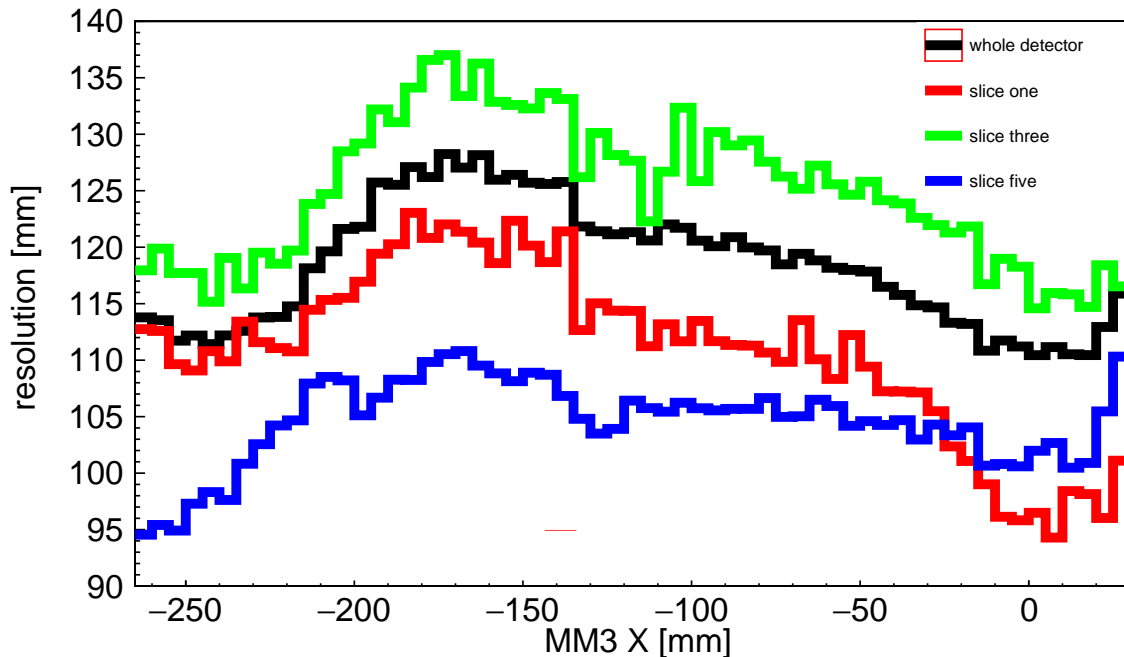


Figure 111: X resolution for the 300 *mm* long 30° geometry wrapped in Tyvek obtained with the mean of all SiPMs on each side. Shown are the resolutions for four different spatial selections of muon events. The resolution is better for slices close to the readout fiber compared to the central slice or the detector average which is  $\approx 120$  *mm*.

It turned out that with a resolution around 120 *mm* the mean is not as stable as the quickest value (method B). The problem is that the scintillation light has time limits to propagate to the readout. The lower limit is reached for photons taking the shortest path to the readout. Towards large times there is also such a limit, given by the absorption length of the material, but the distribution is highly asymmetric with the steeper tail for faster events. In the calculation of the mean, events with a larger time will pull the result towards higher values, and since the range for this is rather large, the width of the mean values increases.

Another way to sort for a specific SiPM is to pick the one with the highest light yield (method D), shown in Figure 112.

Despite the assumption that more photons also means an increased fraction of fast photons, the resolution of 120 *mm* to 130 *mm* achieves the worst result. A noteworthy fact is that slice one is considerably better than the other two presented slices and the detector average. For this slice the chance of picking channel zero and four as the one with the most photons

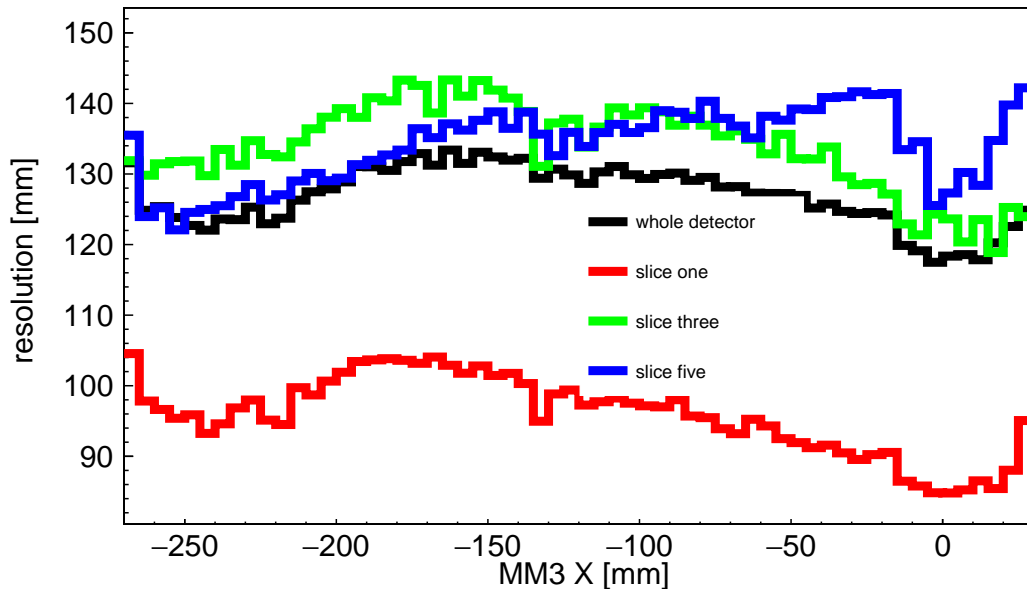


Figure 112: X resolution for the 300 *mm* long 30° geometry wrapped in Tyvek obtained with method D - the SiPMs detecting the most light. Shown are the resolutions for four different spatial selections of muon events. Muon events with a low Y value, being counted in slice one, show by far the best resolution using this method. Since this method prefers fiber 0-4 for muons in slice one and fiber 2-6 for slice five due to the geometrical shape of PoSSuMuS, this result shows that fiber 0-4 performs much better than fiber 2-6. An overall resolution of  $\approx 125$  *mm* is achieved.

is high since they are located close to slice one as well as to the thick base of the trapezoid. The resolution for this combination and this slice is already shown to perform well (see red curve in Figure 108). Fiber 2-6, the counterpart to the just described case has a resolution of  $\approx 140$  *mm*. The answer to the question, why this method does not perform as expected, is therefore explained by the asymmetry of the resolutions of the fibers at the thick base. Another impact comes from the discriminator sending a pulse just after the threshold is reached. An effect called time walk arises, since a different pulse height causes a difference in time, when the LTD threshold is reached [Leo, 1994]. The efficiency in this fiber is with 87 % rather high, hence a lack in statistics can not be a reason for this behavior. The final answer to this problem are high fluctuations in readout channel two, compared to the other channels to be investigated.

The last presented method E is similar to the first one. It searches for each event the lowest timing value of all possible combinations with SiPMs from the left and right side, see Figure 113.

Also in this case, slices close to the fibers give a better result than the central slice and are also better than the average. A reason for this is, also like before, a faster coupling to the fiber suppressing events with many photon reflections that widen the width of the distribu-

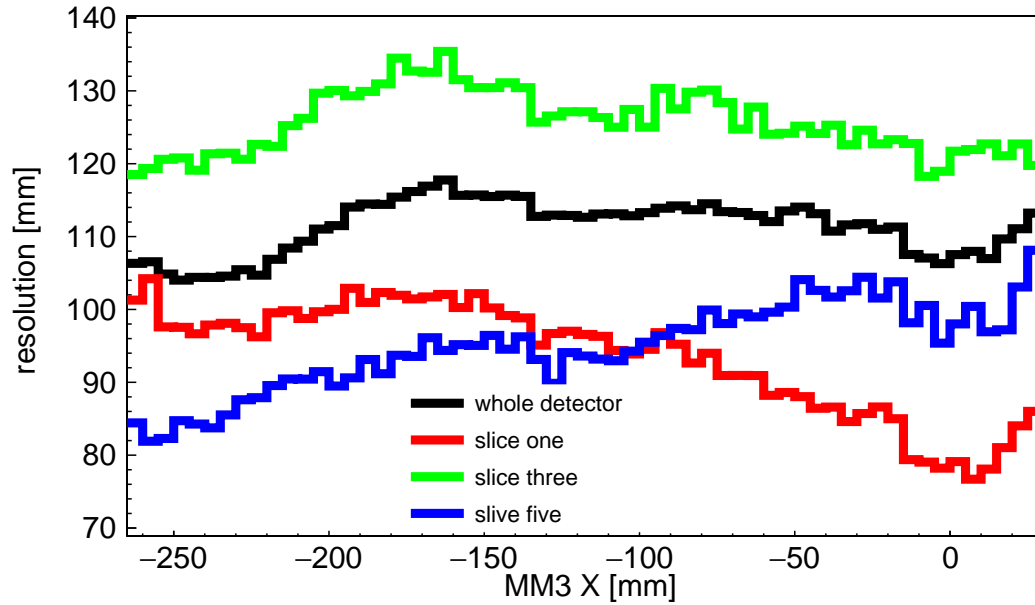


Figure 113: X resolution for the 300 *mm* long 30° geometry wrapped in Tyvek obtained with lowest time difference between left and right. Shown are the resolutions for four different spatial selections of muon events. The resolution is better for slices close to the readout fiber compared to the central slice or the detector average which is  $\approx 110$  *mm*.

tion.

To summarize methods A to E, the resolution distributions of the whole detector for all methods are plotted together in one histogram shown in Figure 114.

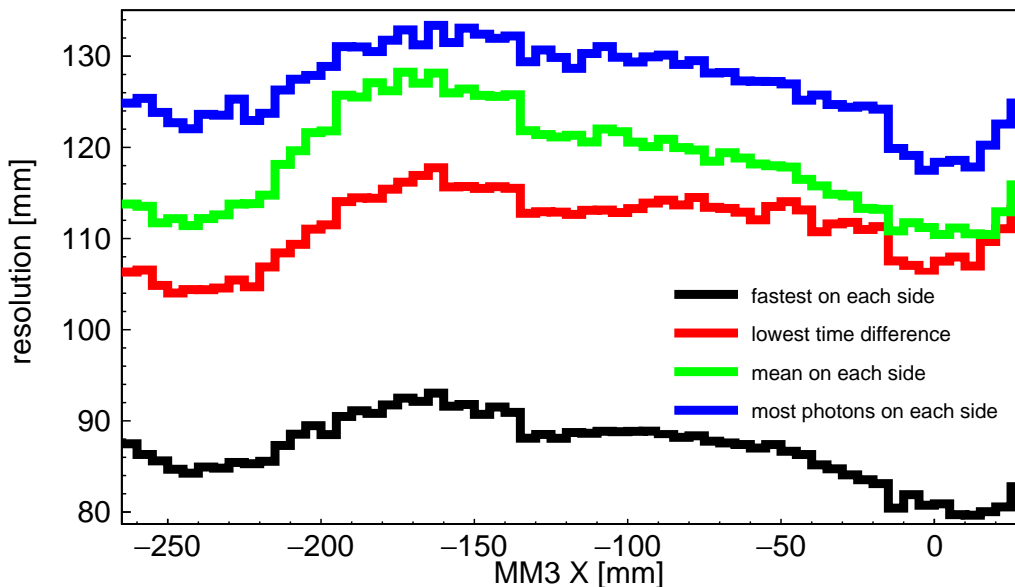


Figure 114: Comparison of methods two to five with respect to their achieved spatial resolution for the whole detector. With a resolution of  $\approx 85$  *mm*, the method searching for the fastest responding readout channel on each side provides the best result by far.

The by far best result is given by method B (black curve) picking the channel with the fastest response on each side. Compared to the first prototype an improvement from a range of  $(117 - 127)$   $mm$  to  $(80 - 93)$   $mm$  is observed. The setup to investigate the first prototype allowed only for the use of one specific pair of SiPMs, see [Müller, 2013]. A re-analysis of the old data in order to perform the same method on these data is therefore not possible. It is shown that it is possible to reconstruct a track with PoSSuMuS in X direction with a resolution of  $\approx 86$   $mm$ , which is clearly an improvement due to the new geometry and a more clever choice in readout electronics and readout channel selection. According to the calculations in chapter 7.5.2 it can be assumed that the major part on this resolution comes from the decay time of the wavelength shifting process, which means that the large improvement comes from the choice out of four SiPMs per side. Still another important issue to improve is the use of a constant fraction discriminator (CFD)<sup>46</sup> instead of a LTD in front of the TDC. A CFD gives out its pulse after a certain percentage of the maximum pulse height is reached and therefore showing no or little time walk [Leo, 1994]. In chapter 7.5.1 a residual histogram was shown. This can now also be done for the choice of the fastest responding channel on each side (method B), see Figure 115.

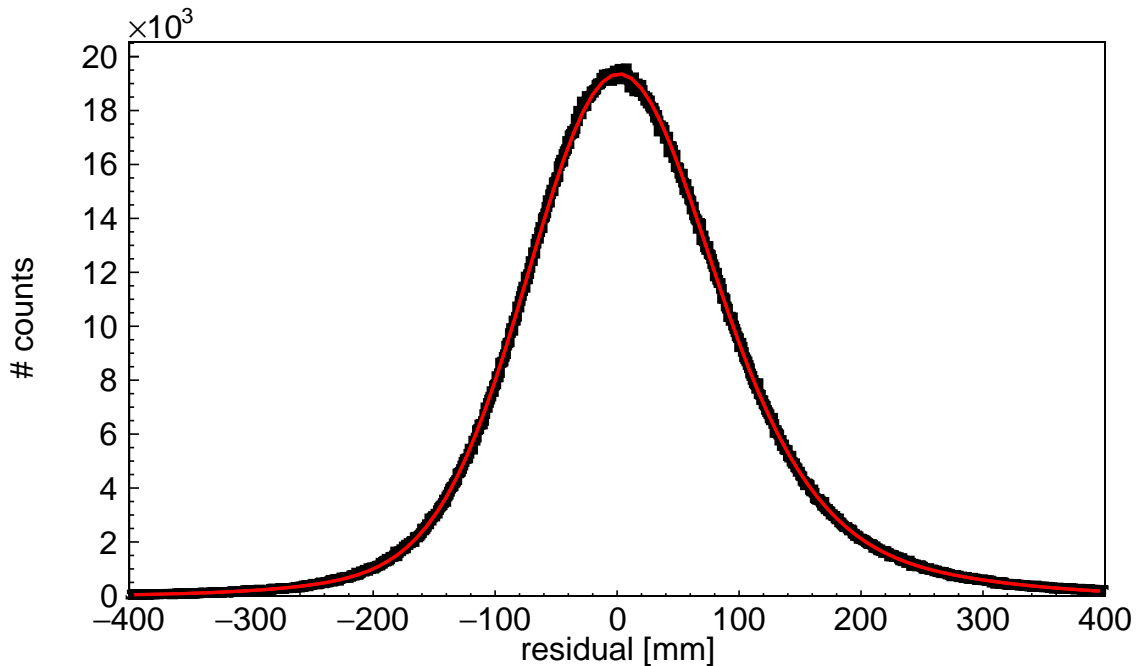


Figure 115: Residual distribution for the 300  $mm$  long  $30^\circ$  geometry wrapped in Tyvek obtained with method B choosing fastest responding SiPMs. Again the sum of three Gaussian functions is used to fit the signal resulting in a weighted width of  $\approx 80$   $mm$ .

Using the same arguments as for Figure 102, a sum of three Gaussian distributions is fitted to the graph resulting in a weighted mean of 80  $mm$ . This way of characterizing the de-

<sup>46</sup>Also the threshold has to be lowered for further investigations.

tector seems to better deal with the different values for the resolution depending on the Y coordinate of the incident muon. In Figure 110, slice one and five show resolutions of around or even below  $80\text{ mm}$ . Comparing reference and PoSSuMuS event by event takes those varying resolutions better into account than first averaging over PoSSuMuS and afterwards comparing it to the reference.

Up to now the fine granularity of the micro pattern based reference system was used to present results on the resolution. To compare these results with the results from the CERN test beam in 2012, see also Figure 72, where the position measurement was based on a  $5 \times 5\text{ mm}^2$  pair of trigger scintillators, see Figure 73, only muons passing PoSSuMuS through three  $5 \times 5\text{ mm}^2$  large areas are taken into account. Setting  $X = 0$  in the center of PoS-SuMuS the three locations are around  $X_1 = -148\text{ mm}$ ,  $X_2 = 0\text{ mm}$  and  $X_3 = 148\text{ mm}$ . As timing again the method B of the fastest responding channels on the left and right side is chosen. The result for the timing is scaled so that the peaks are located at the just mentioned positions in X. The histogram showing the distributions for the three cases is given in Figure 116.

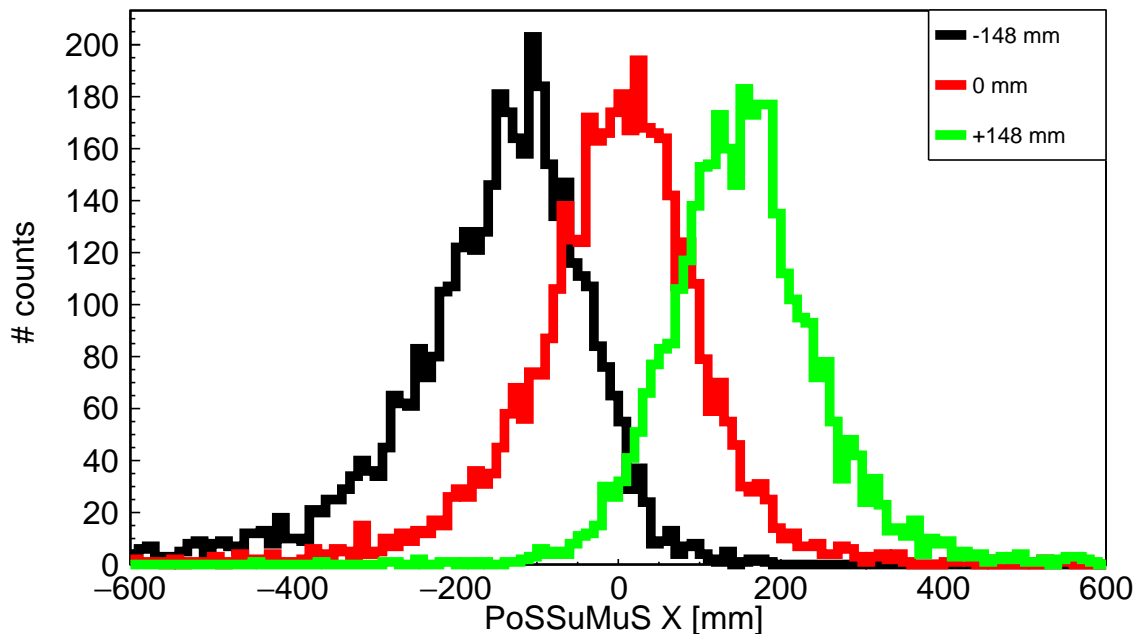


Figure 116: Reconstructed spatial coordinates for three  $5 \times 5\text{ mm}^2$  large areas using the method which searched for the fastest SiPMs. Those areas are located centrally in Y direction and on the most left, central and most right position in X direction, according to the positions investigated for the first prototype. Compared to this first prototype the distributions for left and right impact are much better separated using the new geometry.

Compared to Figure 73 the improvement is obvious. The distributions of the left and right position cross well below their half maximum. Also comparing both peaks to the central one shows a better separation of the distributions. The widths of the three distributions are

$\sigma_1 = 92 \text{ mm}$ ,  $\sigma_2 = 94 \text{ mm}$  and  $\sigma_3 = 84 \text{ mm}$ . The values for the widths agree with the green curve in Figure 110 at the positions  $X = -265 \text{ mm}$ ,  $X = -120 \text{ mm}$  and  $X = 25 \text{ mm}$ .

A last point in this chapter is the comparison between a diffuse and a direct reflective cover material. The results presented so far are obtained using Tyvek as diffuse reflective cover. The measurements at CERN started with this choice due to its good performance in the first prototype. As already mentioned the aluminum based wrapping of the  $300 \text{ mm}$  long PoSSuMuS happened at the end of the beam time and it was not possible to investigate the entire detector and the investigated parts have a factor of two lower statistics. As detector material the identical trapezoidal rods have been used. The result here is therefore more a first look into the aluminum wrapping rather than a complete analysis. Still there are expectations, like a lower light yield and a better timing resolution compared to Tyvek. The results should be able to judge whether those expectations are fulfilled.

As Table 7 shows, this cover really provides a lower light yield, but having a look at Figure 117, it can be seen that time resolution is not as good as for Tyvek. All four methods to

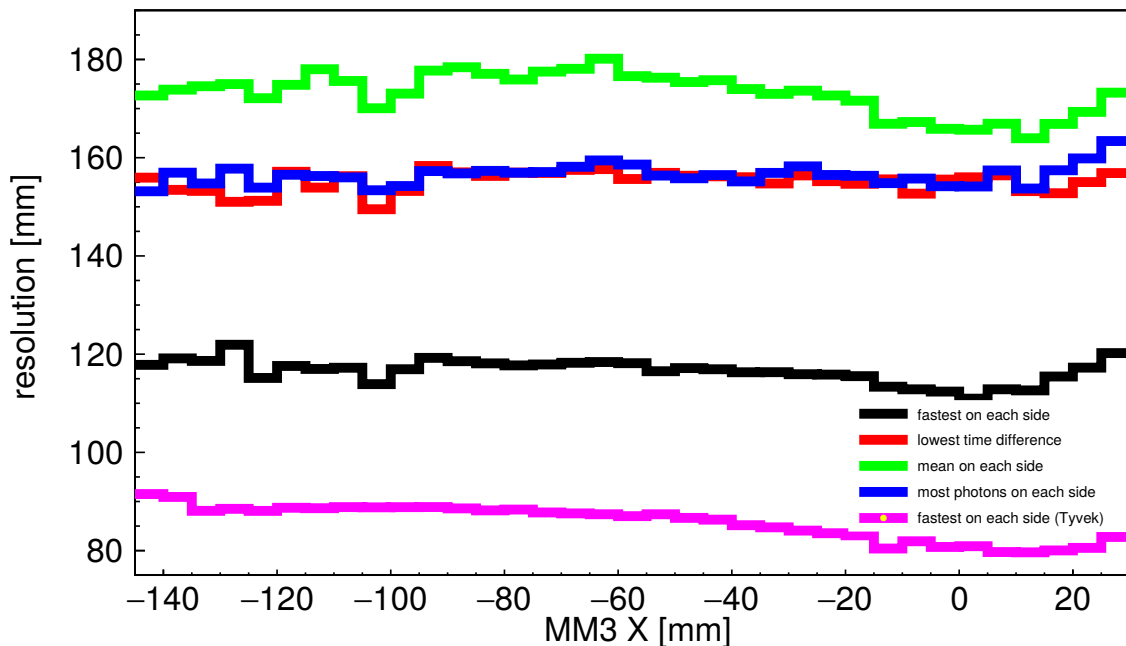


Figure 117: Comparison of method B to E with respect to the achieved spatial resolution for the whole detector. With a resolution of  $\approx 115 \text{ mm}$ , the method searching for the fastest responding readout channel on each side provides the by far best result, but it is also shown that in this case the Tyvek wrapping still gives better results.

choose a time information on each side are plotted for a wrapping of PoSSuMuS in aluminum. The color coding is identical to the same plot for a Tyvek wrapping, see Figure 114. Additionally Figure 117 shows the best observed resolution with a diffuse cover as the pink curve. On a first look aluminum shows a resolution worse than Tyvek, which was not expected. The expectations base on experiments done with the  $100 \text{ mm}$  long old geometry.

The data taken should be sufficient to judge this result as correct. Nevertheless it is advisable to repeat those measurements with more statistics. Having a closer look to the aluminum curves shows that again picking the fastest readout channels on each side gives the best result. But in contrast to the diffuse wrapping the method D of choosing the channel with highest light yield has the same resolution as searching for the combination with the lowest difference (method E). In this case the time distribution of SiPM two is not as broad as for the Tyvek case. It is therefore assumed that method D would also give suitable results for Tyvek. An explanation why SiPM two performs better now could not be found analyzing the available data, giving another reason to repeat the measurement.

## 7.6 Position Resolution in the Light Yield Coordinate

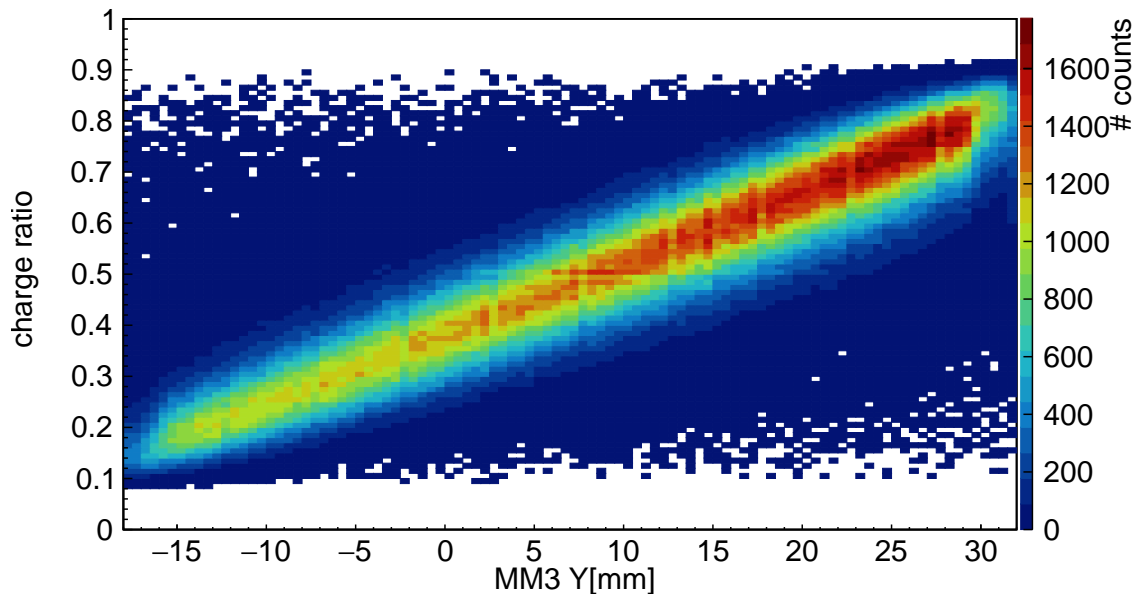
Since the light output characteristics of the new geometries have been discussed already in chapter 7.4, this section focuses on the spatial resolution achieved by comparing the light yields in both trapezoidal scintillators of PoSSuMuS. The procedure to reconstruct the spatial coordinate is based on the ratio:

$$\frac{Q_{1^{st} \text{ Scintillator}}}{Q_{1^{st} \text{ Scintillator}} + Q_{2^{nd} \text{ Scintillator}}} \quad (7.6.1)$$

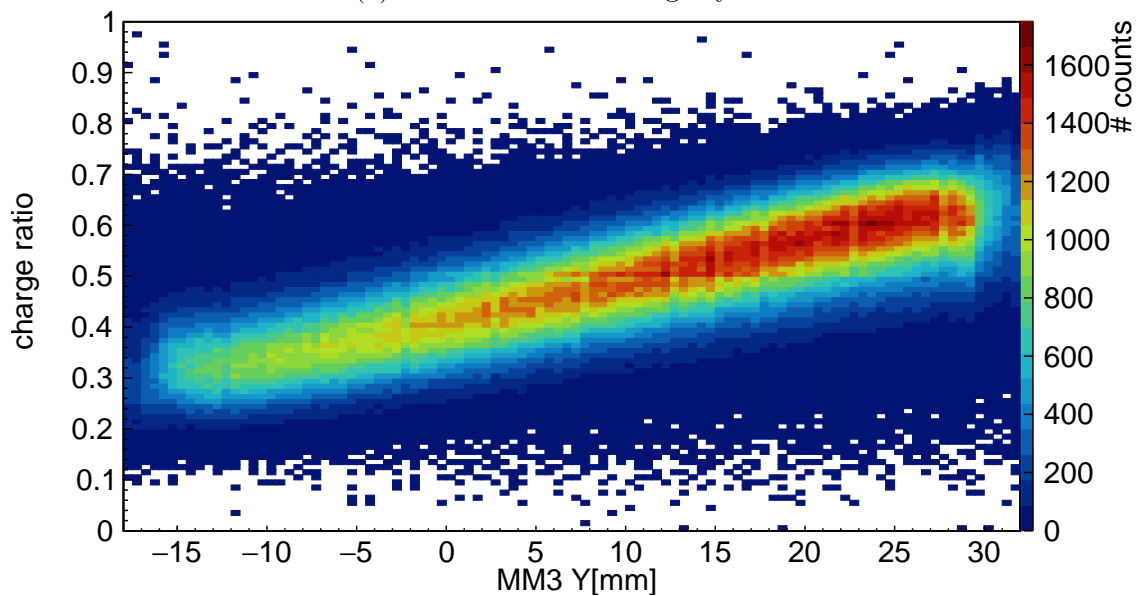
with  $Q_i$  being the amount of light detected in trapezoid one or two. To determine a value for  $Q_i$  we consider the four readout channels, see Figure 91, two at the thick base and two at the thin base. It was already discussed that the light yield curves are different for the read out at both bases. As an example, only measured values from the same base enter into the light yield ratio, hence there are two possibilities, one taking into account only the thick base readout channels and one with the thin base only. The value of the ratio can now be plotted against the Y coordinate of the reference system, as shown in Figure 118 for the  $35^\circ$  geometry.

To determine values of the spatial resolution the distribution is sliced in vertical direction for each bin on the X axis and each of the slices is fitted with a Gaussian function. The graph for the means of all Gaussians shows a linear function. Like for the X reconstruction a function with a steep inclination and a small width of the Gaussian fits is required for good spatial resolution. The width of the distribution is transformed into units of  $mm$  by dividing it with the slope of the linear function derived from the means of the Gaussians.

The fact that in both histograms of Figure 118 the ratio does not range from 0 to 1 is caused by the use of a trapezoidal geometry rather than a triangular one. Here even in the most extreme case of perpendicular muons traversing the detector at one edge both scintillators will detect light, hence neither  $Q_{1^{st} \text{ scintillator}}$  nor  $Q_{2^{nd} \text{ scintillator}}$  can be zero, which gives a



(a) Ratio of thick base light yields



(b) Ratio of thin base light yields

Figure 118: Light yield ratios for the 100 *mm* long 35° geometry. In Figure 118a only the SiPMs of the thick bases are used, while for the histogram in 118b only the thin base readout channels are considered. Figure 118a shows a dynamic range of  $0.6 = 0.75 - 0.15$ , Figure 118b a considerably smaller range of  $0.3 = 0.6 - 0.3$ .

limitation to the slope of the curves<sup>47</sup>. The excess in statistics for a higher value of the ratio is again beam related. It was already shown that the setup is placed relative to the beam such that the detector counts more hits with higher *Y* values, see Figure 103. A high *Y* value also means a high ratio since the first scintillator has its thick base at around  $Y = 30$  *mm*

<sup>47</sup>A summary of the slopes is given Table 10.

and therefore  $Q_{1^{st} \text{ scintillator}}$  and with this also the charge ratio is large for most of the hits the setup recorded.

As expected the slope for the thick base is steeper compared to the one of the thin base due to the effect of increased photon production in the thicker scintillation material. The large difference of the slopes already shows that similar to the older prototypes a readout including all channels and treating them identically will not be sufficient to reconstruct a spatial coordinate.

What is also visible in this plot is a spread of the values along the function coming from the Landau like energy loss, described in chapter 6.1. Ideas to compensate for the Landau energy loss are presented in appendix D, because it will turn out that the uncorrected results are better and fulfill the desired resolution to be better than 10 *mm*, see chapter 5.5.

### 7.6.1 Technique to Combine all Readout Channels

For reconstruction of the Y coordinate from the light yields  $Q$  in both scintillators equation 7.6.1 is used. Since the investigated scintillators have two readout fibers each, a combination of these light yields is considered. To shorten the following equations the labeling of a fiber is done by referring to just one of the connected SiPMs. For this always one of the first four SiPMs is chosen, for example  $Q_{0-4}$  is shortened to  $Q_0$ . As shown before the Y dependence for a fiber at the thick and the thin base is different and their signals can not simply be added like

$$\frac{Q_{1^{st} \text{ Scintillator}}}{Q_{1^{st} \text{ Scintillator}} + Q_{2^{nd} \text{ Scintillator}}} = \frac{Q_2 + Q_3}{Q_2 + Q_3 + Q_0 + Q_1} \quad (7.6.2)$$

A better approach uses the light ratio curves as shown in Figure 118. To explain the following calculation those light ratio curves are schematically shown in Figure 119.

The curves are represented by a linear function. On the horizontal axis, given by the Y coordinates of the reference system, the range of PoSSuMuS in Y is shown by the distance from A to B. In this range the light yield ratio goes from  $R_0$  to  $R_1$  and  $r_0$  to  $r_1$  for the thick and thin base, respectively. The function describing the thick base ratio is given by

$$\frac{Q_2}{Q_2 + Q_0} = R_0 + (R_1 - R_0) \frac{Y - A}{B - A} \quad (7.6.3)$$

and the function for the thin base is given by

$$\frac{Q_3}{Q_3 + Q_1} = r_0 + (r_1 - r_0) \frac{Y - A}{B - A} \quad (7.6.4)$$

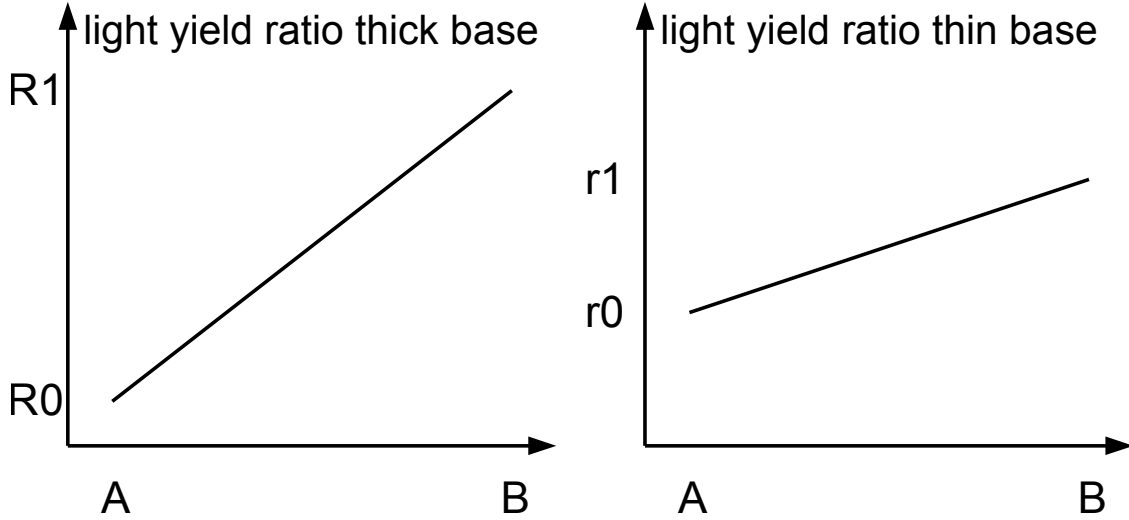


Figure 119: Schematic light ratio curves for thick and thin base. On the horizontal axis of both graphs the Y values of the reference system is given with A and B indicating the range of PoSSuMuS in Y. On the vertical axis the charge ratios are drawn according to  $R = \frac{Q2}{Q2+Q0}$  for the thick base and  $r = \frac{Q3}{Q3+Q1}$  for the thin base. The values R0, R1, r0 and r1 are the respective minimum and maximum values measured for the ratios.

By adding both equations and solving them for Y the correct method to combine both sides of the trapezoid is given by

$$Y = \left( \frac{Q2}{Q2+Q0} + \frac{Q3}{Q3+Q1} - (R0 + r0) \right) \frac{B - A}{R1 - R0 + r1 - r0} + A \quad (7.6.5)$$

The values for R0, R1, r0 and r1 are taken from the respective light ratio curves for each geometry as calibration constants. In theory they are directly related to the geometry used but since the light collection efficiency is not perfectly homogeneous, as shown in the discussion of Table 7, the calibration is needed.

### 7.6.2 Achieved Resolution in Light Yield Direction

In this section the results of the previously described methods to reconstruct the Y coordinate from the light yield detected in both trapezoids of PoSSuMuS are presented. At first just the slopes  $m$  for the light yield ratios against the Micromegas reference system are shown in Table 10.

Also reported in this table are the theoretical slopes which are given by the shape of the trapezoid as

$$m_{theory} = \frac{\frac{a}{a+b} - \frac{b}{a+b}}{c} \quad (7.6.6)$$

	$m_{thick} \cdot 10^{-4} \frac{1}{mm}$	$m_{thin} \cdot 10^{-4} \frac{1}{mm}$	$m_{theory} \cdot 10^{-4} \frac{1}{mm}$
100 mm; 35° Tyvek	131	69	128
100 mm; 30° Tyvek	101	47	94
100 mm; 20° Tyvek	67	13	51
100 mm; 10° Tyvek	41	-10	22
300 mm; 30° Tyvek	101	47	94
300 mm; 30° Aluminum	89	38	94

Table 10: Slopes of light ratio curves, as shown in Figure 118. The slopes decrease for a decreasing trapezoidal angle as expected. For both 30° lengths the inclinations are identical. Also shown are the theoretical inclinations given by the shape of the trapezoid.

with  $a$ ,  $b$  and  $c$  being the length of the thick base, the length of the thin base and the height of the trapezoid, respectively, as defined in Figure 91. All given inclinations show a decreasing tendency for a decreasing angle of the trapezoid. While the values for the thin base are much smaller than the theoretical ones, the inclinations of the thick base tend to be larger. Again this result shows the impact of the second effect entering the light yield ratios, the distance of the muon impact to the fibers. The negative inclination for the 100 mm; 10° geometry using the thin-base fibers is expected given the result presented in Table 7. This geometry is the only one where the maximum light yield is reached experimentally at the thin base and the minimal light yield at the thick base.

Table 10 shows also that to increase the slope further other geometries are needed, because the current ones already exceed the theoretical value. Here the only recommended change is to elongate  $a$  while having  $b$  as small as possible but still being fully efficient. A length of  $b = 9.81 \text{ mm}$  as for the 35° geometry seems to be close to ideal, because on the one hand it is small and on the other hand it provides with an average of  $\approx 80$  photons a good statistical value. A shortening of  $c$  would increase the amount of readout channels required for a certain area to be covered by PoSSuMuS.

In Figure 120 the distributions for the spatial resolution for the Y coordinate are shown.

It can be seen that the readout using only the fibers of the thick base in the 35° geometry provides an excellent behavior of the resolution along Y. It ranges from 3 mm to 5 mm, which is better than the requirement for a use in the CRF, where a resolution of  $\approx 10 \text{ mm}$  would be already enough. Even the case of the 20° geometry, which is very close to the inclination of the older prototype with 22°, would be sufficient. The result for the first prototype, presented in [Ruschke, 2014], ranged from 7.5 mm to 12.5 mm. With a shorter trapezoidal height, the lowest value for the resolution could not be reached, but with a range from 8 mm to 9.5 mm the variation of the resolution could be decreased and the maximum value is now also smaller than 10 mm, see green curve in Figure 120a. The reason for the decreasing range of the resolution and with this also the general fact that the resolution is

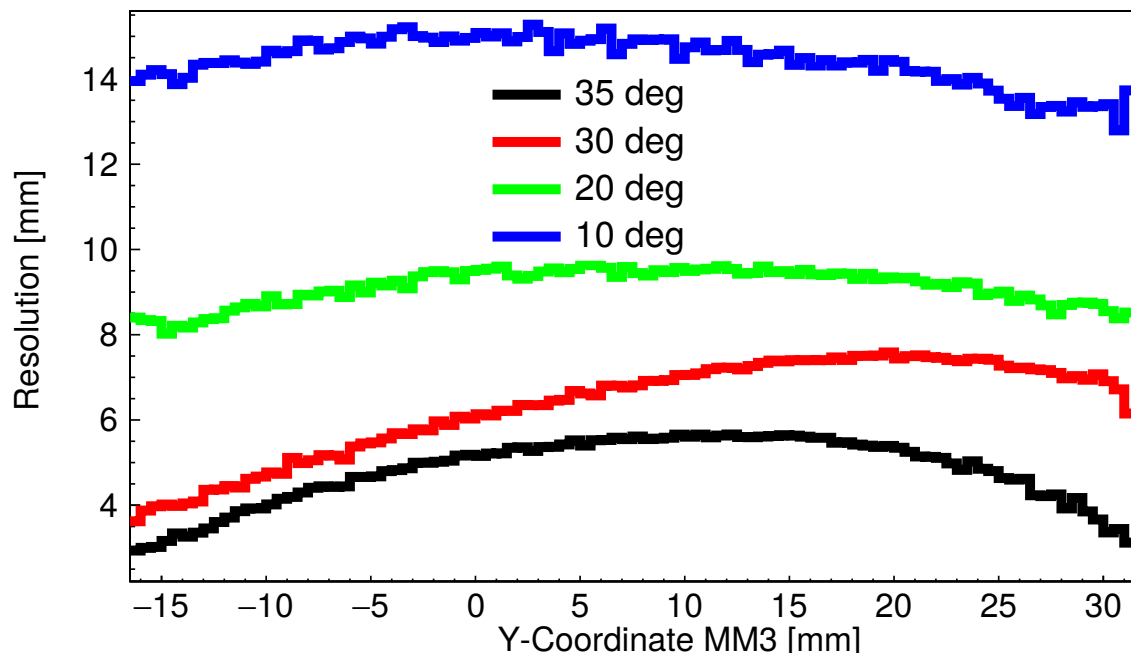
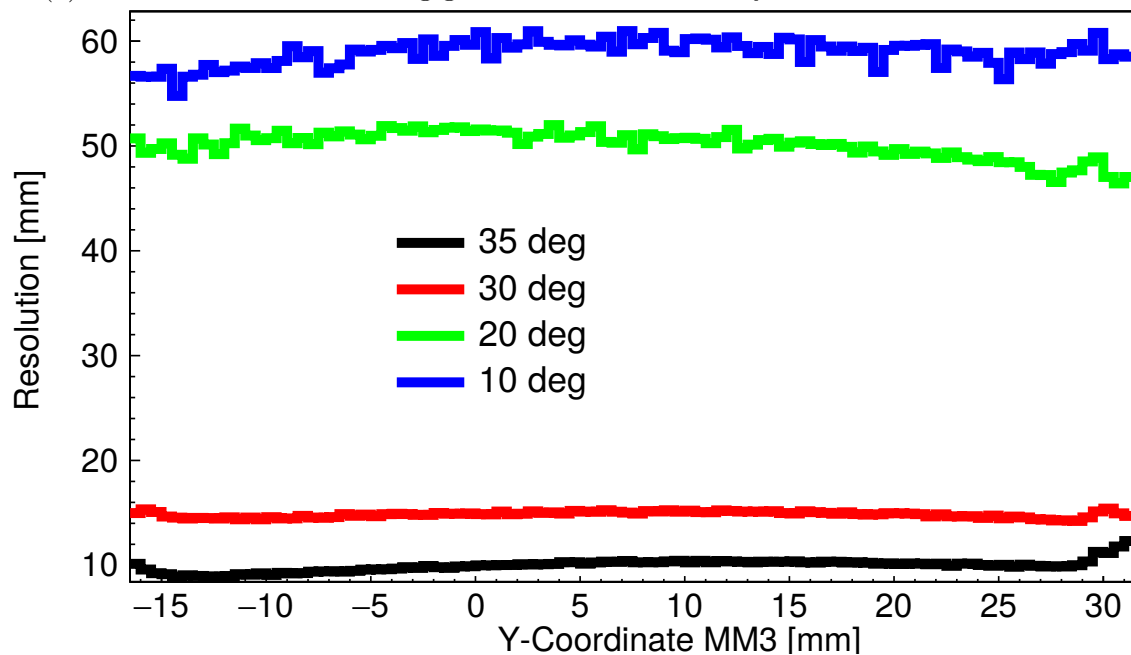
(a) Resolution of 100 *mm* long geometries evaluated only with the thick-base fibers.(b) Resolution of 100 *mm* long geometries evaluated only with the thin-base fibers.

Figure 120: Resolutions for the 100 *mm* long geometries. In 120a the results for the ratios of the thick-base fibers are shown and in 120b the ones for the thin base equivalent.

larger for a central muon impact is given by the light yield of one fiber as already shown by the simulation of the shortening of trapezoidal height, see figures 80 and 81. Here the light yields flatten out for an increasing distance of the muon impact to the readout fiber. While in the regions close to the fiber always one half of PoSSuMuS provides high dependency of

the light yield from the spatial coordinate of the muon, in the central regions the flat part of both light yield curves overlap resulting in a worse resolution. For a geometry with a shorter height those central regions get smaller and with this also the resolution gets better. In the edge regions still the behavior of one half dominates the behavior of the whole PoSSuMuS, which gives the reason why the resolution there stayed rather constant.

While the curves for the width scaled to units of  $mm$  in Figure 120 show a clear dependence on the angle of the trapezoid, the non scaled widths are all very similar to each other. This means that the impact of the geometric angle only affects the slope of the light yield ratio curves and not their spread, hence a smaller angle is not favored.

The results for thin-base fibers are as expected worse compared to the other results. Here only the  $35^\circ$  geometry is sufficient for a use in the CRF. In the histogram for this geometry, see the black curve in Figure 120b, the resolution goes up close to the edges because of the relative high cut out for the groove of the wavelength shifting fiber.

Because the  $35^\circ$  geometry shows the best resolution it is used to further study the possibility of combining the readout channels, as described in chapter 7.6.1. A plot showing the resolution for a thick base ratio, a thin base ratio and a combined ratio is given in Figure 121.

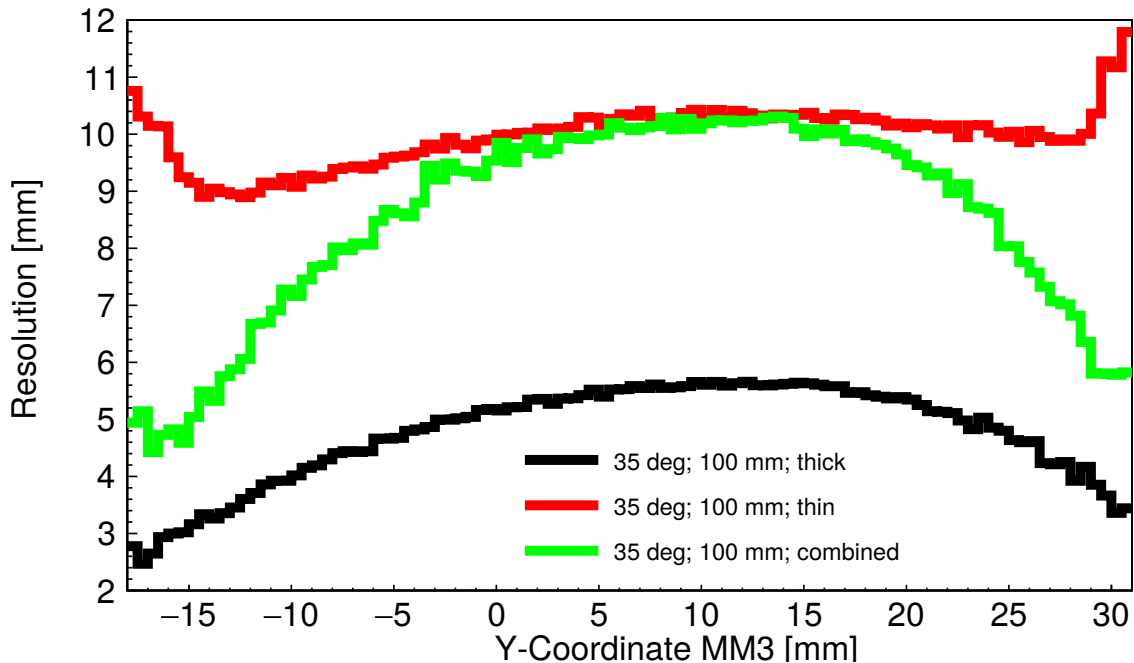


Figure 121: Resolutions for the  $100\text{ mm}$  long  $35^\circ$  geometries. Shown are the resolutions for an evaluation of the fibers at the thick and, respectively, at the thin base only and a combination of all fibers as described in chapter 7.6.1.

On a first view the combination provides a resolution in between both evaluation methods concerning only similar fibers. A reason, why this combination does not give a better result is given by a different reconstructed position. The  $Y$  in equation 7.6.3 and 7.6.4 can differ

slightly due to statistical effects like the energy loss of the muons. Therefore the combination of both equations will get slightly wrong. Depending on which light yield ratio provides the larger spread the resolution using all fibers is either closer to the thick base ratio or to the thin base ratio. In the central region the ratio of fibers at the thin base clearly worsens the resolution.

Finally it can be stated that the  $35^\circ$  geometry provides the best spatial resolution of all investigated geometries, when read out only at the fibers of the thick base. Any method concerning the other fibers results in a worse resolution, see also appendix D.

In the following the best geometry is used to perform similar studies as also done for the X direction. First again a comparison to the older analysis is done. For this three  $5 \times 5 \text{ mm}^2$  areas are selected. In X direction those areas are located in the middle of the detector and in Y one is in the center and the other two are  $\pm 22 \text{ mm}$  off the central position. The result is shown in Figure 122.

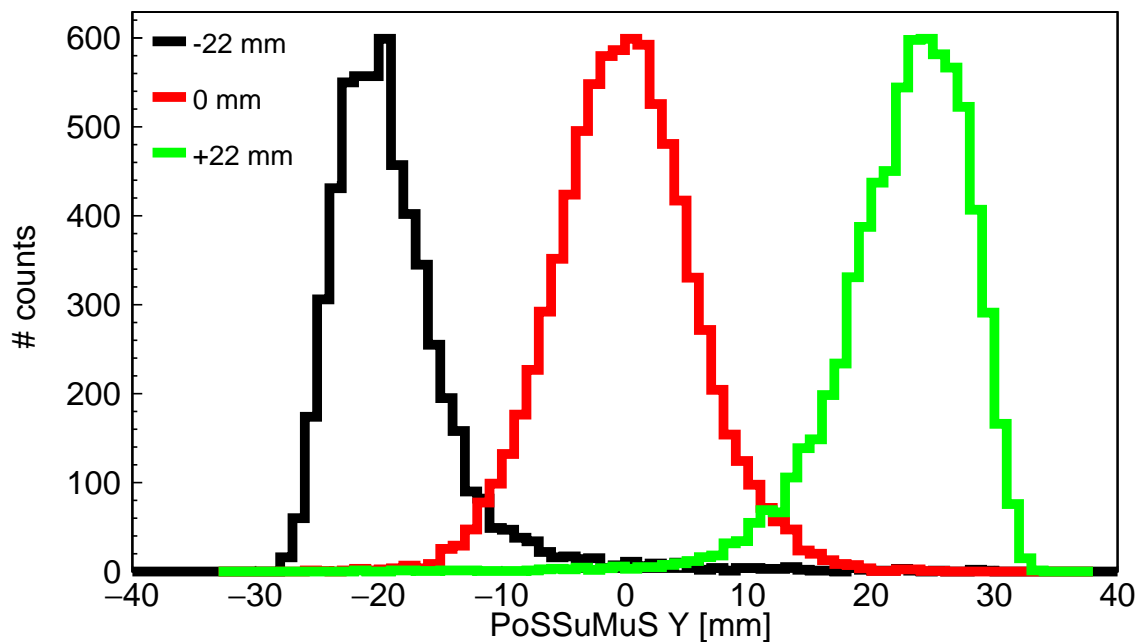


Figure 122: Distribution of three reconstructed positions in Y direction for the 100 mm long  $35^\circ$  geometry wrapped in Tyvek obtained using the fibers at the thick base. The positions for the central (red) and lower (black) area are reconstructed well, while the top (green) position is reconstructed by  $\approx 4 \text{ mm}$  too high.

While the central (red) and lower (black) area are reconstructed well, the green curve representing the area in the upper region of PoSSuMuS is reconstructed slightly too high. Using another factor to adjust the light yield ratio to a spatial position would allow the red and green curve to fit the actual coordinates, while the black one gets too close to the center. This asymmetry seems to be an effect of slightly different light collection efficiencies of both scintillator halves. For a final operation this would mean that a more sophisticated calibra-

tion is needed, than just using a linear function. For this proof of concept study the use of a linear function is sufficient, because it can be shown that a reconstruction of the positions is possible with a resolution of  $\approx 4 \text{ mm}$ . This is demonstrated in the very low overlap of the three curves. The three positions are closer together compared to the old prototype, but the overlap could be reduced considerably compared to Figure 76.

For this configuration also the residual was calculated by the difference of the Y position of the Micromegas and PoSSuMuS, shown in Figure 123.

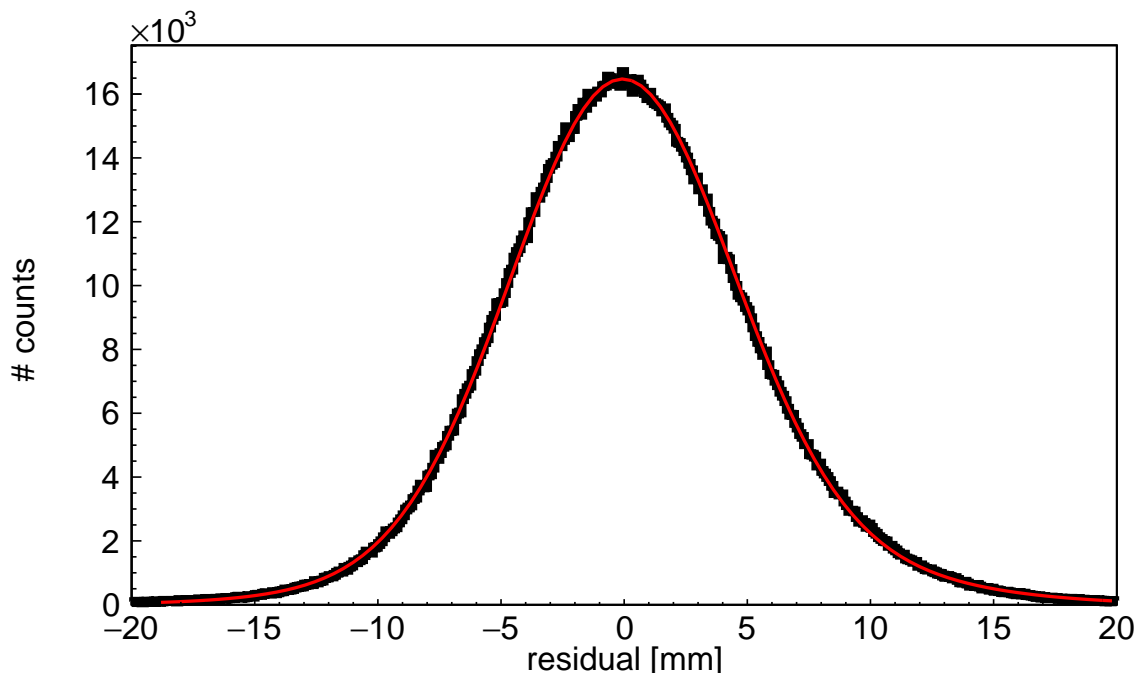


Figure 123: Residual for the Y direction investigated with  $100 \text{ mm}$  long  $35^\circ$  geometry using only the fibers of the thick base in the light yield ratio. A double Gaussian function is fitted to this distribution resulting in a weighted average width of  $4.9 \text{ mm}$ .

A double Gaussian is used to fit this distribution. Weighting the standard deviations of both functions with their integral gives a total standard deviation of  $4.9 \text{ mm}$ . The two effects playing a role in this measurement and hence causing the need of two Gaussian functions are on the one hand statistical fluctuations and on the other hand the production of low energetic secondary particles which lead to an additional scintillation inside one half of PoS-SuMuS. The value of the width has to be interpreted as mean of the resolution which is position dependent.

Since in a large area approach of PoSSuMuS the individual rod will get longer, also a comparison to the resolution using the  $300 \text{ mm}$  long geometry is of high interest. For this the  $30^\circ$  geometries are compared, since they are the only ones investigated in  $100 \text{ mm}$  and  $300 \text{ mm}$  length. The result for those geometries and also for the use of aluminum as wrapping material for the  $300 \text{ mm}$  long PoSSuMuS is shown in Figure 124.

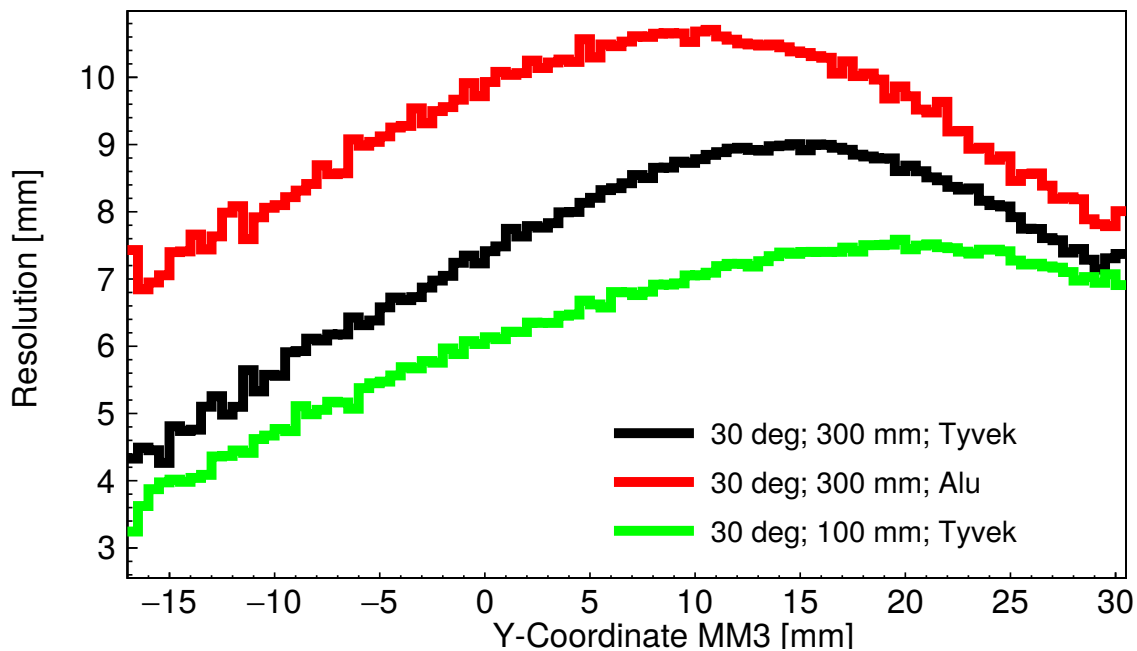


Figure 124: Resolution for the Y direction investigated with 300 *mm* long 30° geometry using only the fibers of the thick base in the light yield ratio. The 300 *mm* long PoSSuMuS show a slightly worse resolution compared to the shorter design. A wrapping in Tyvek gives as for the first prototypes a better resolution compared to an aluminum wrapping.

Since the longer detector shows a lower light yield, see Table 7, a slightly worse resolution is expected. With  $\approx 1$  *mm* worse resolution this is exactly what is observed. Also the better performance of Tyvek as cover is reproduced similar to the older prototypes.

The last issue to discuss is the efficiency to reconstruct a muon track. To calculate the efficiency, the same idea is used as for the X coordinate. First the number of events is counted, in which the reference Micromegas reconstruct a track inside the active area of PoSSuMuS. If in such an event all four SiPMs from either the thick-base fibers or the thin-base fibers provide a signal, PoSSuMuS is able to reconstruct a coordinate of the muon impact. Such an event is called efficient either for a thick base reconstruction or a thin base reconstruction, respectively, and the number of efficient events is divided by the total number of events to obtain the efficiency. Those values are shown in Table 11 for all investigated geometries.

An efficiency of 94 % taking only the Y direction into account for the 100 *mm* long 35° geometry is a very good value. Improving the scintillator quality by, e.g., using new material and improving the method to couple the wavelength shifting fiber to the scintillator can further increase this efficiency. Despite this going to even longer rods might lower it again, hence further studies need to be done for this. The observed very good efficiency for the 300 *mm* long 30° geometry wrapped in Tyvek with 98 % gives hope that the elongation of the rod has a minor impact on the efficiency. One obvious explanation for this high efficiency is a very clean surface of the used scintillators for this PoSSuMuS. The observed higher efficiencies

	reconstr. tracks	thick	thin	timing and thick
100 mm; 35° Tyvek	2323084	94 %	97 %	64 %
100 mm; 30° Tyvek	2264180	93 %	95 %	91 %
100 mm; 20° Tyvek	1516416	93 %	94 %	93 %
100 mm; 10° Tyvek	1063179	94 %	95 %	93 %
300 mm; 30° Tyvek	4239289	98 %	99 %	96 %
300 mm; 30° Aluminum	1685101	92 %	97 %	88 %

Table 11: Efficiency of PoSSuMuS of reconstructing a Y coordinate either by evaluating fibers of the thick base or of the thin base. Also shown is the combined efficiency for a reconstruction of an X coordinate out of the fastest responding SiPMs on each side and an X coordinate using fibers of the thick base.

of possible reconstruction using the thin-base fibers comes again from the asymmetry in the positioning of the setup within the beam line as discussed several times above. Also shown in the last column of Table 11 is the ratio of events in which a reconstruction in both directions is possible. Outstanding here is the extremely low efficiency for the geometry claimed to be the best in this chapter. Due to the fact that the efficiencies are fine taking only the Y reconstruction into account, the low efficiency of only 64 % is a result of the X reconstruction. This is understandable because during the investigation of this geometry it was realized that the TDC was not properly adjusted and therefore many events are recorded without any TDC response.

The very good result of the Y coordinate shows that the use of a smaller height of the trapezoidal geometry provides a structure well suited for the use as a spatially resolving trigger in the CRF. The use of a fiber at the thin base is for this geometry not necessary to reconstruct the Y coordinate of traversing muon, but as presented in chapter 7.5.3, it is helpful for the X coordinate.

## 8 Conclusion and Outlook

This thesis, which can be divided into two parts, in general deals with issues concerning the quality control of large area Micromegas detectors. The first part focuses on the quality control of such detectors for the upgrade of the inner endcap region of the ATLAS muon spectrometer called New Small Wheel (NSW). In the second part a possible upgrade of the Cosmic Ray Facility (CRF) is studied, which will improve the spatial resolution of the facility by enabling it to select muons with a high energy. A higher spatial resolution of the reference tracks has a positive impact on the calibration of the Micromegas using the CRF. In order to cope with the upgrade of the LHC at CERN to higher luminosities, hence to a higher occupancy of the detector components, the current detectors of the inner endcap region of the ATLAS muon spectrometer will be replaced by Micromegas and sTGC detectors. In Munich one module of the Micromegas part of this upgrade will be built. Using two extremely planar surfaces, one given by a granite table and one by a lightweight aluminum structure called stiffback, in a two-step gluing process planar and parallel sandwich panels can be built. Such a panel has a core of aluminum honeycomb and aluminum profiles and PCB material as outer shells. Five of these panels stacked enclose the active volume of four Micromegas in between them, hence this assembly is called quadruplet. For the NSW upgrade four geometries of quadruplets are constructed with the SM2 modules are partially built in Munich.

Following the detailed description of the construction procedure for SM2 sandwich panels a setup including a laser distance sensor to scan the topology of the panels is presented. The concept of this sensor is based on laser triangulation. The device emits a laser beam which is reflected back to the device by the surface to measure. Available are two devices, one with a red laser and the other with a blue sensor, both being able to measure the distance either via diffuse or specular reflection. Due to semitransparent surfaces to measure during SM2 quality control, the blue sensor in an inclined mode showed the best results. After calibration using the mentioned granite table this system has a height resolution better than  $10 \mu\text{m}$ . It is used to scan all surfaces of the panels built in Munich. The products glued so far show a planarity with an RMS of  $14 \mu\text{m}$ , which is a factor of two better than the desired limit of  $30 \mu\text{m}$ . Such mechanical tolerances are imposed because the planarity of the panels influences the later resolution of the detector which should be better than  $100 \mu\text{m}$  for each Micromegas of a quadruplet. Therefore it is shown that the described procedure of building SM2 is sufficient to produce panels of the required planarity. Another crucial tolerance is given by the alignment of the readout strips. For all strips within a quadruplet their non parallelism must not exceed  $20 \frac{\mu\text{m}}{\text{m}}$ . In order to measure this value the Cosmic Ray Facility (CRF) is introduced as one possibility. Here the tracks of cosmic muons are reconstructed by two Monitored Drift Tube (MDT) chambers sandwiching the SM2 quadruplet under test.

---

Since such a quadruplet does not exist up to now, a study using a  $1\text{ m}^2$  prototype is quoted to show the feasibility of this concept.

A current limitation of the resolution of the reference tracks in the CRF is due to low energetic muons. They are easily deflected by multiple Coulomb interaction along their way through the CRF and reference tracks will no longer match to the track of the device under test. In a proof of concept study it was shown that PoSSuMuS, a position sensitive scintillating muon detector with silicon photomultiplier (SiPM) readout, is a good candidate for an upgrade of the facility enabling it to enhance the fraction of high energetic muons ( $E_\mu > 4\text{ GeV}$ ) in the analysis. The idea of such an enhancement is a comparison of the reference track to the position of the muon below a  $300\text{ mm}$  thick iron layer. For this a fast spatial resolving detector is desired, which was found using PoSSuMuS. The second part of the thesis deals with a study searching for a new geometry in order to increase the spatial resolution of PoSSuMuS to be better than  $10\text{ mm}$ .

PoSSuMuS is a two dimensional spatially resolving scintillation detector with SiPM readout on a modular basis. Each module consists of two optically isolated scintillation rods with a trapezoidal shape stacked on top of each other. The light in each half of the module is collected and guided by a wavelength shifting fiber to the readout of both sides. The X position of the impact of a muon along the rod is given by the propagation time the scintillation light needs to reach both ends of PoSSuMuS. Comparing the light yield produced by a traversing particle in each half module gives a measure of the Y position perpendicular to the rod.

In an early proof of concept study a light yield of maximum  $\approx 30$  photons has been reached, resulting in a spatial resolution for X and Y of  $125\text{ mm}$  and  $13\text{ mm}$ , respectively. A simulation of the detector concept suggested that reducing the height of the trapezoid from  $90\text{ mm}$  to  $50\text{ mm}$ , placing the readout fibers at the thick and thin base and increasing their cross sections from a diameter of  $1.5\text{ mm}$  to the size of the SiPM's active area, being  $3 \times 3\text{ mm}$ , will result in an improved light yield and a better spatial resolution.

In a test beam time at CERN four PoSSuMuS geometries are investigated with  $120\text{ GeV}$  muons. All trapezoids have a height of  $50\text{ mm}$  and thick base of  $45\text{ mm}$ , while differing in the size of the thin base. The length of the rods available for the test beam are  $100\text{ mm}$  and  $300\text{ mm}$ . The module halves are wrapped in three layers of diffuse reflecting Tyvek and one final layer of aluminum foil for optical isolation. While all four geometries with the  $100\text{ mm}$  length have been studied with Tyvek wrapping, for the  $300\text{ mm}$  long geometries the one with the  $16\text{ mm}$  long thin base was measured in the beam for comparison of both the diffuse reflective cover Tyvek and a single aluminum wrapping. Due to limitations of beam availability at the end of the test beam time, the measurement of the aluminum wrapped rod could not be completed.

The former prototypes had a remote controlled online gain stabilization for the highly temperature sensitive SiPMs. For the beam time this gain stabilization is slightly improved by

new electronics, but the main idea to adjust the voltage applied to the SiPM according to the environmental temperature by a remote controllable voltage divider stayed the same. In addition to this the readout chain is designed such that a finer offline gain correction can be applied to the data. The new design has an increased light yield of  $\approx 40$  photons for a muon impact close to the thin side and up to  $\approx 120$  on the other side. Those values are taken from the best performing geometry. The light yield varies with different size of the thin base. This means that the new geometry provides a factor of four more light compared to the previous prototypes.

For the X direction a TDC is measuring the time between SiPM pulse and trigger pulse with a sampling of  $35\text{ ps}$ . There are several methods to select the timing signal for each side of PoSSuMuS. Out of five presented in this thesis the one searching the readout channel on each side of the rod with the shortest time difference between trigger and data pulse provided the best resolution in X direction. For this measurement the  $300\text{ mm}$  long geometry is used because results from the first prototype suggested a resolution in the order of  $100\text{ mm}$  making an investigation of this with the  $100\text{ mm}$  long geometries not meaningful. The resolution is depending on the impact position of the muon along the X direction. Close to the readout a resolution of  $80\text{ mm}$  is measured going up to  $90\text{ mm}$  for a muon in the central region of PoSSuMuS. The resolution is improved but still rather broad. The main limiting factor to this are the statistical processes of scintillation and wavelength shifting. With a decay time constant of  $2.4\text{ ns}$  and  $2.7\text{ ns}$ , respectively, the spread of the creation time of the photons is large.

For the Y coordinate a resolution of  $3\text{ mm}$  to  $5\text{ mm}$  is achieved, again measuring the lower value close to the readout fiber and the larger one in the center. It turns out that the smaller the size of the thin base is, the better is the resolution. Here only the  $100\text{ mm}$  long detectors are compared, because all four trapezoidal geometries have been investigated in this beam time. For an implementation of PoSSuMuS into the CRF the rods will have a length of  $4\text{ m}$ . The  $300\text{ mm}$  device has a resolution of  $4\text{ mm}$  to  $8\text{ mm}$ , hence the resolution degrades for longer trapezoidal rods.

Further investigations with longer rods and new scintillation material are mandatory as a next step. The currently used scintillating material comes from the OPAL experiment at the former LEP accelerator at CERN, showing after about 30 years aging effects like a drastically decreased mean free path of the scintillation light being one reason for the decrease of the Y resolution. Another field of optimization is the fiber. Currently a bundle of four  $1.5\text{ mm}$  thick round wavelength shifting fibers fill a rectangular cross section fitting to the active area of the SiPM. During the gluing of those bundles air bubbles are trapped between the fibers. Using rectangular fibers should solve this problem and make it easier to connect the fiber to the scintillator.

In the test beam only perpendicular muon tracks traversing PoSSuMuS are investigated, but

---

in the CRF incident angles of up to  $30^\circ$  are of high interest because such tracks can occur. Despite those measurements, which are beyond the scope of this thesis, it has been shown that the new geometry perfectly fulfills the requirement of a resolution better than  $10\text{ mm}$  on the precision coordinate perpendicular to the trapezoidal rod and  $\approx 90\text{ mm}$  resolution along the rod.

## Appendix A Investigation of Steel Tube and Hard Disk with Laser Distance Sensor

In the bachelor thesis of Christian Kolberg, [Kolberg, 2016], among others, two objects of potential interest for the quality control described in this thesis have been investigated, a steel pipe and a hard disk using the micro Epsilon sensor optoNCDT2300.

For the scan of the steel pipe the sensor was moved perpendicular to the pipe, hence measuring a part of a circle. It was shown, that it is possible to measure the radius of the pipe quite well. For this the data points have been fitted with a circular function and the parameter representing the radius was fitted to  $5.2\text{ cm}$ , which is the same result as for a caliper.

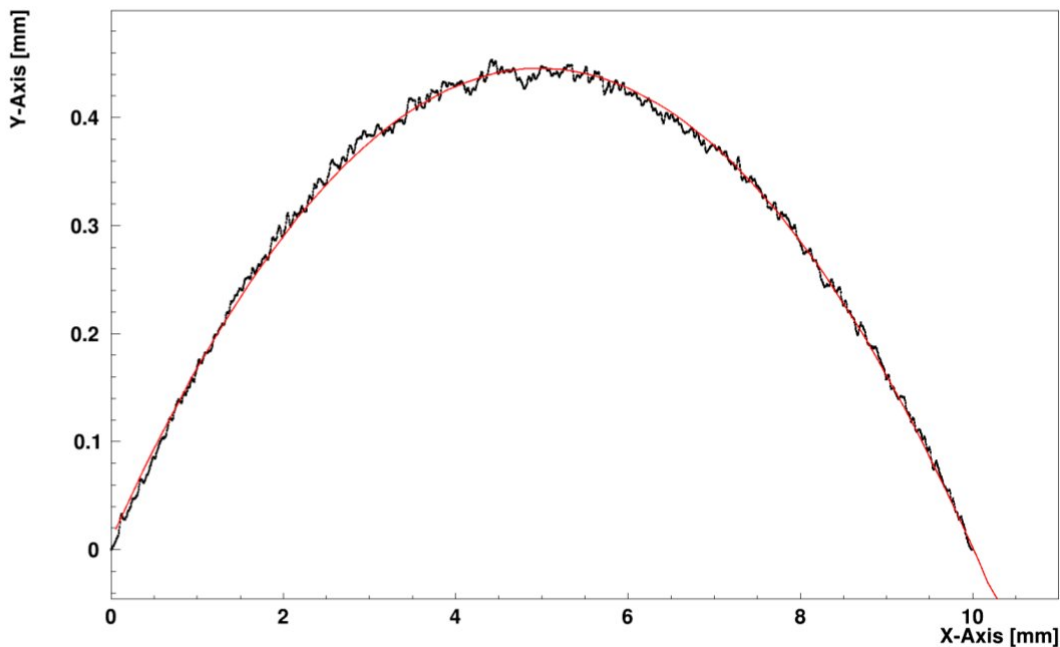


Figure 125: Measurement of a steel pipe using the red distance sensor. Fitting a circular function to the points gives the same outer radius of the pipe of  $5.2\text{ mm}$  as a caliper.

For a plot zoomed into the highest peak of the circle, i.e. the flattest path in this setup, no major deviations from a circle are visible, see Figure 125. Here  $\Delta_{\min-\max} \approx 0.45\text{ mm}$ , which is in the same order as the worst sandwich objects. Farer away from the peak the deviations increase due the fact that the beam is reflected by the large inclination of the pipe such, that Equation 4.3.4 does not apply anymore. Therefore the quality control is not affected by this effect.

The other interesting object scanned was a hard disk. On the one hand it is extremely flat and on the other hand it is highly reflective. Supporting it on one side gives a precise straight and inclined track to measure, shown in Figure 126.

Despite of measuring a straight line a step function with  $\approx 50\text{ }\mu\text{m}$  high step size was mea-

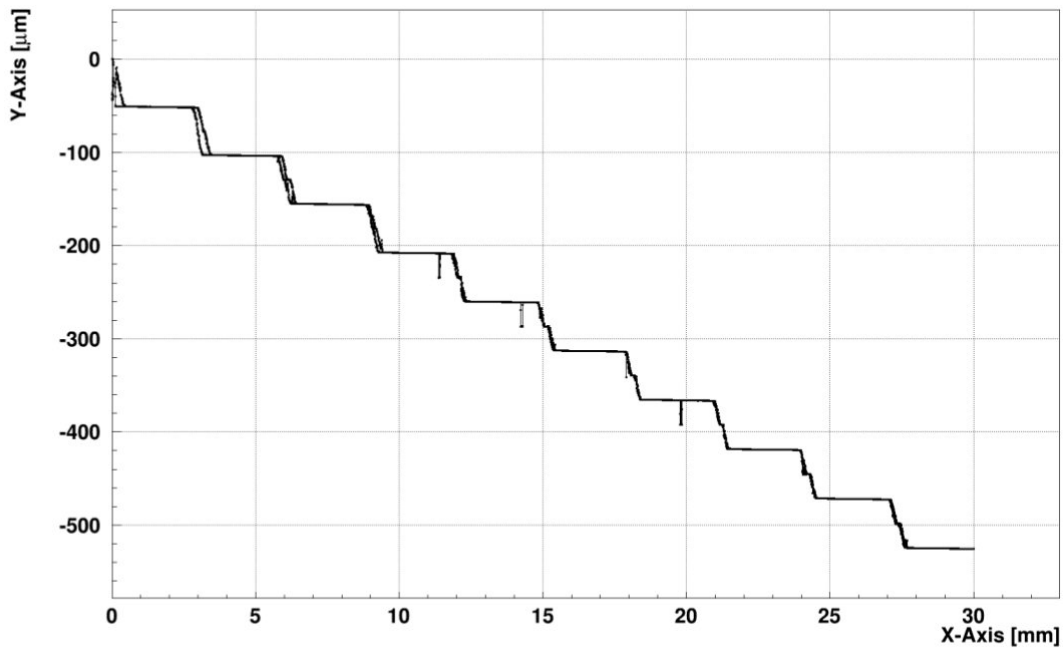


Figure 126: Measurement of a hard disk. The disk was supported on one edge to provide an inclined surface.

sured. It turned out to be necessary to dim the beam if highly reflective surfaces are scanned. By doing so, this effect could be eliminated, see Figure 127.

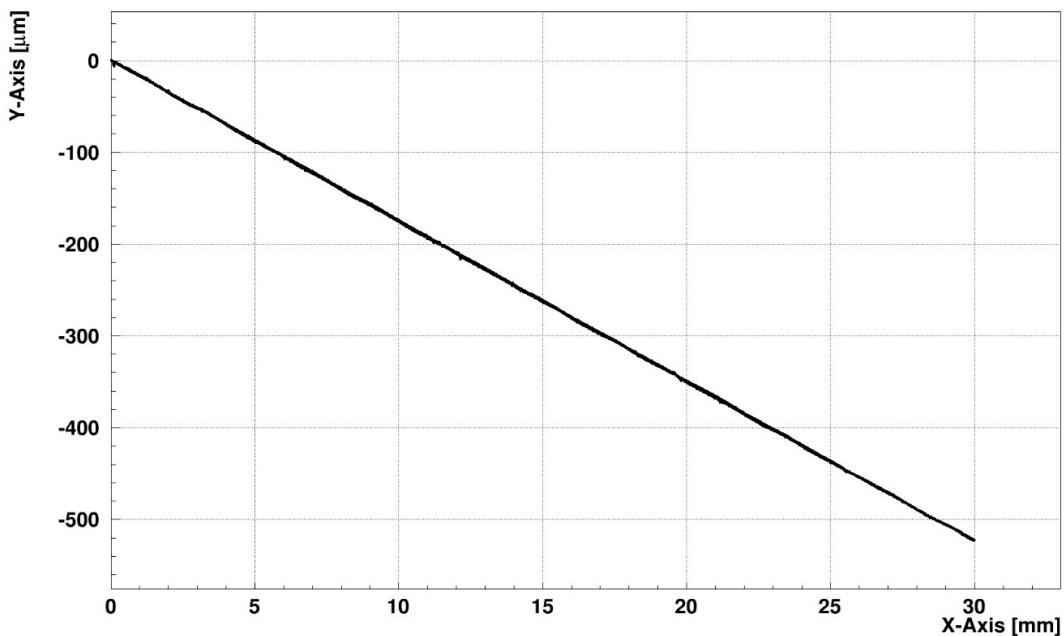


Figure 127: Measurement of a hard disk after dimming the laser beam. The expected straight line is observed.

## Appendix B Photos and Circuit Diagrams of SiPM Power Supply

In this appendix photographs and circuit diagrams of the components for the voltage supply for the SiPMs are shown. This includes:

- the card hosting the arduino and the voltage connectors to the power supplies
- the card for the voltage divider, pre-amplifier and the connection to the SiPMs and to the data acquisition
- the crate for the mentioned cards

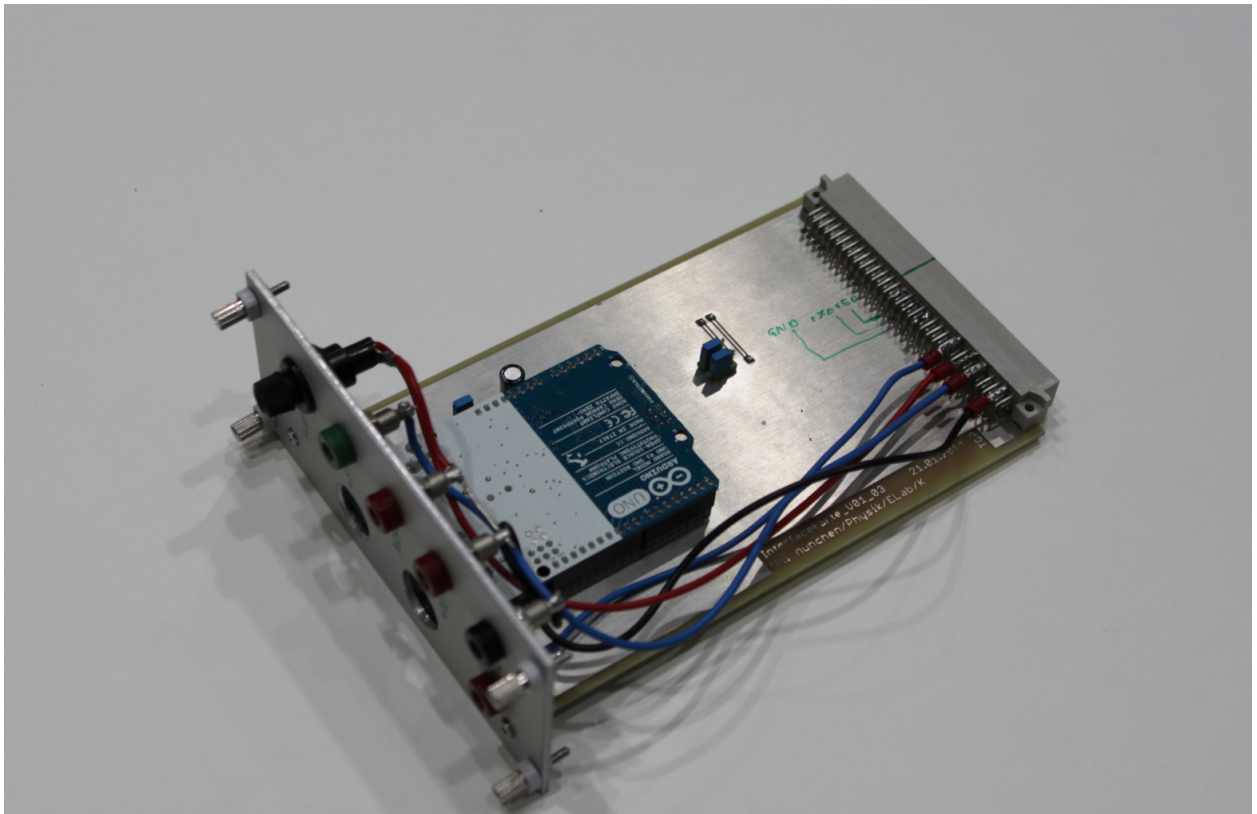


Figure 128: Card housing the arduino. It is the same card already used by [Grossmann, 2014]. Since the new design has a central voltage supply, cables had to be applied for this. A circuit diagram is shown in Figure 129.



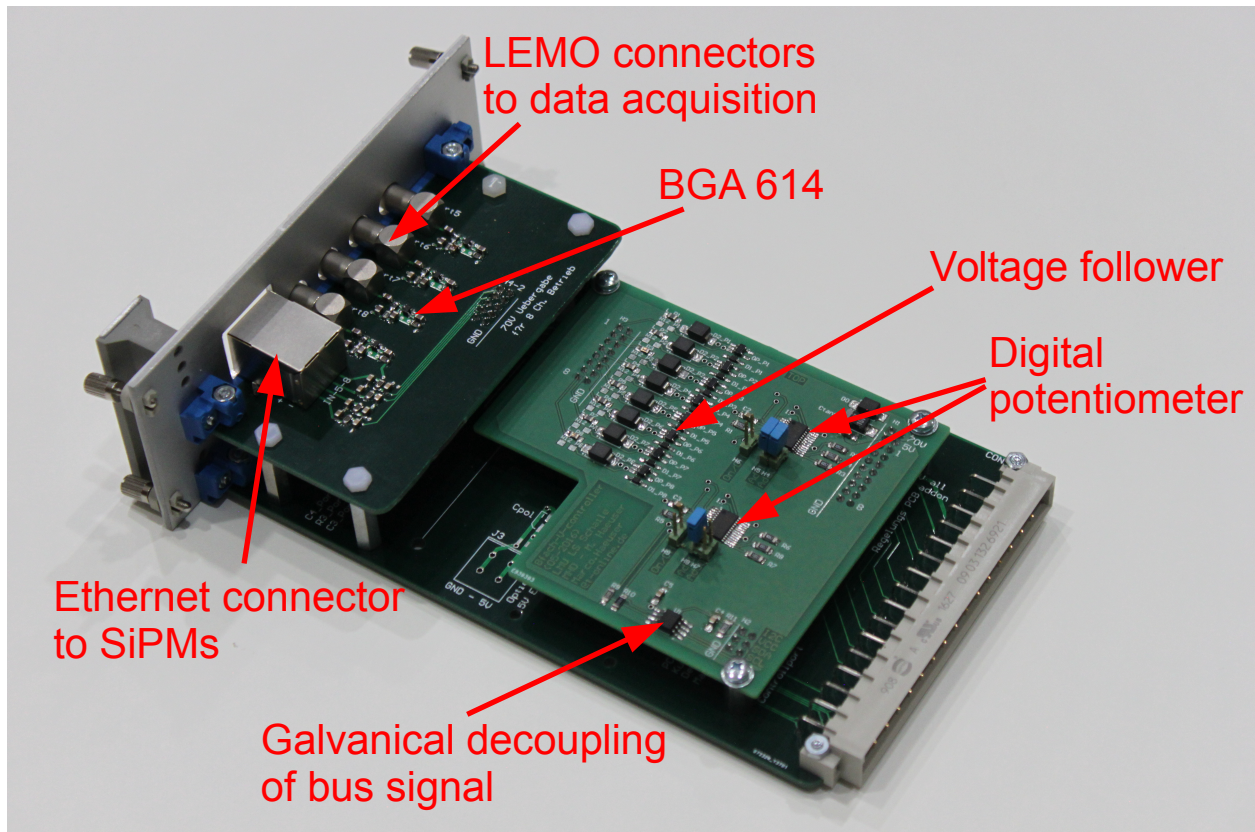


Figure 130: Voltage supply card. Actually there are two parts shown here. The dark green PCBs is one unit which can be operated with and without the pale green PCB, housing the voltage divider. It is foreseen that the setup can be supplied with an external voltage source for the SiPMs, then just the dark green PCB is needed. On this PCB the external voltage is given to the Ethernet connectors, where the SiPMs can be plugged in. The signals from the SiPMs are pre-amplified and passed via LEMO connectors to the data acquisition. In this case eight voltages for the eight SiPMs to be connected need to be applied to the card. A more comfortable method uses the pale green extension. This card now houses the voltage dividing components. Here the  $I^2C$  bus controls two voltage dividers capable of adjusting in total eight voltage. Now only two voltages need to be applied,  $V_{high}$  and  $V_{add}$ , see chapter 7.2. Circuit diagrams for the dark green pre-amplification PCB are shown in figures 131 and 132. For the voltage divider extension card the diagrams are shown in figures 133 and 134.



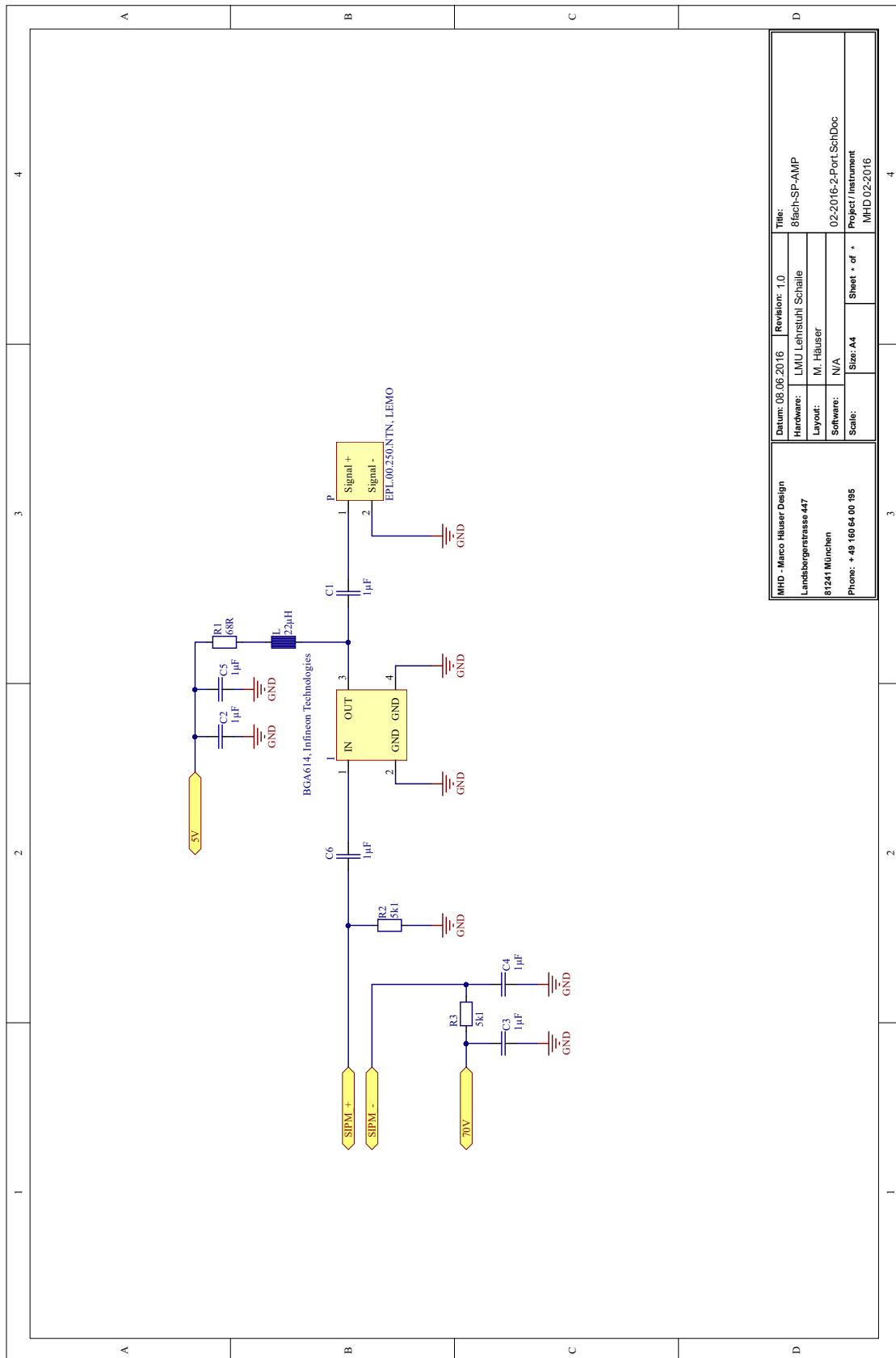


Figure 132: Detailed circuit diagram for the pre-amplifier.



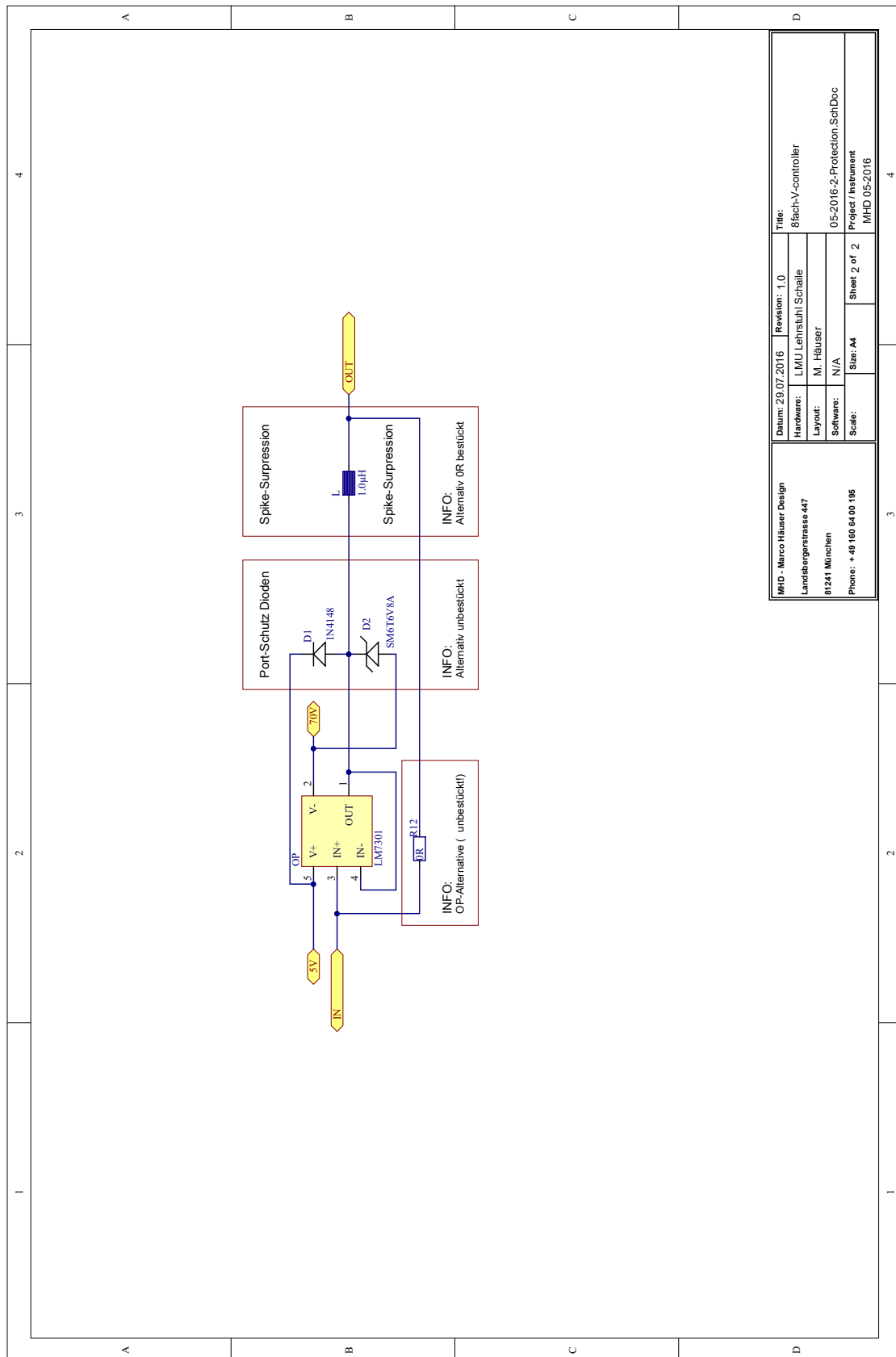


Figure 134: Circuit diagram for the voltage follower protecting the digital potentiometers from overload.

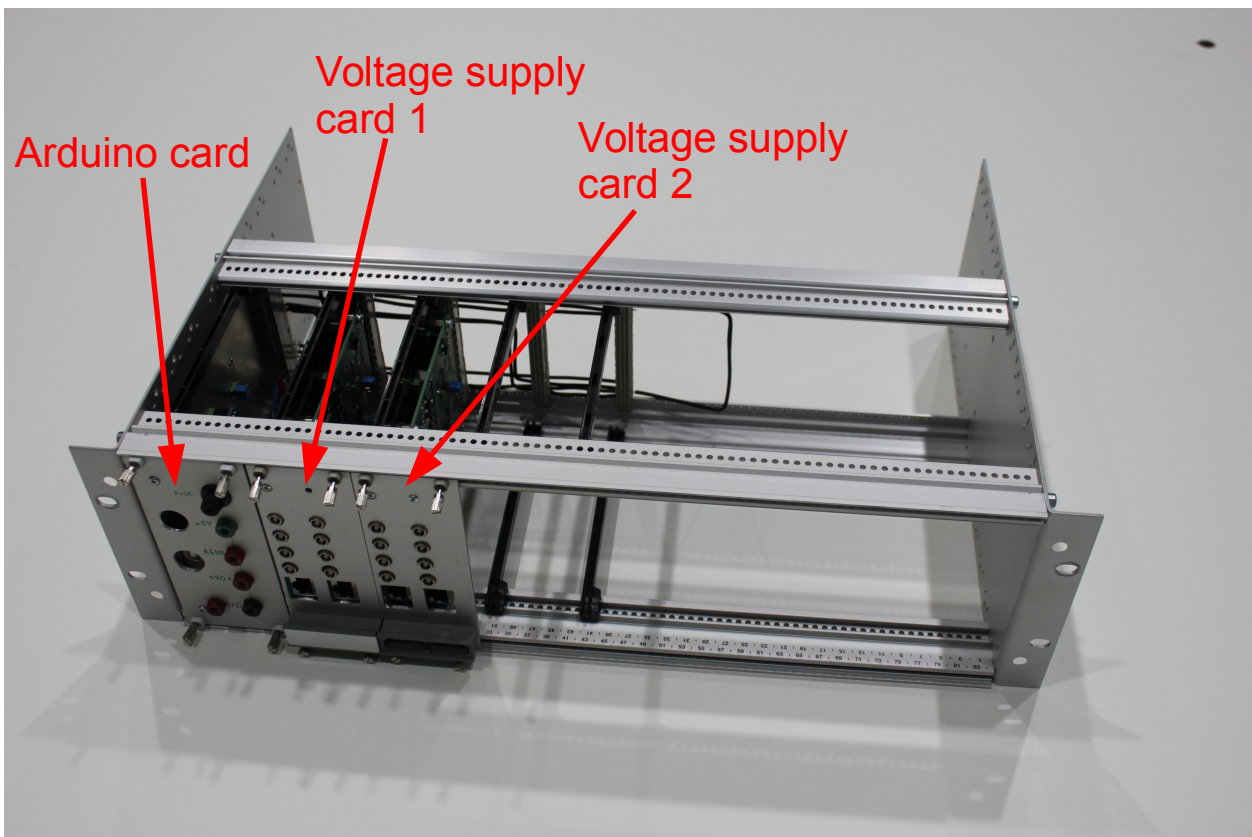


Figure 135: Crate housing the arduino card and two voltage supply cards. In total 16 channels can be operated with this configuration.

## Appendix C Spatial Resolution of the Time of Flight Coordinate for 100 mm long Geometries

The final result for the resolution along the time of flight coordinate gave (80 – 90) mm, which is in the same order as the shorter geometry with its 100 mm length. A detailed investigation of this length is therefore not meaningful, additionally to the fact that in the CRF even longer rods will be used. Still the result should be presented in this thesis. As for the longer geometry also the method of the fastest responding channel on each side is used to define the timing values for the left and right side, because again this method provides the best results. It is shown in Figure 136 for the 30° geometry to compare it to the longer geometry.

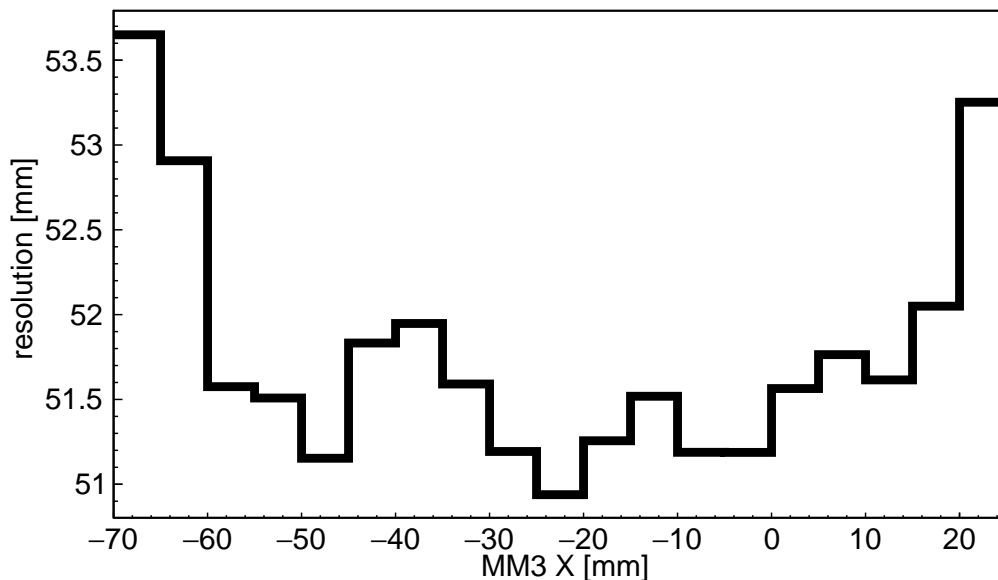


Figure 136: X Resolution for the 100 mm long 30° geometry wrapped in Tyvek obtained with the method searching for the fastest responding channel on each side. With  $\approx 51.5$  mm the resolution is much better than the (80 – 90) mm of the longer geometry.

The effective speed of light inside this geometry is measured to be  $\approx 77 \frac{mm}{ns}$ , which is faster than the  $\approx 45 \frac{mm}{ns}$ . This means that here less reflections are performed before the light is detected by the SiPM, reducing the path of the light from the position of the scintillation to the readout, which again effectively increases the propagation speed. Since a higher propagation speed means a lower inclination of the timing curve, see Figure 100, a worse resolution is expected. In contrast to this expectation the result is with  $\approx 51.5$  mm much better, which means that the width of the timing curve is much narrower for shorter geometries. Again this can be explained by a lower number of reflections.

The resolution for a shorter rod is obviously better, but for a prototype of a large area application the result of the 300 mm long geometry has more relevance.

---

## Appendix D Methods to Determine the Impact of the Landau Energy Loss

In this part two ideas to account for the Landau distributed energy loss are presented. The first method searches for a relation of the light detected in both halves. Figure 137 shows the correlation of both light yields.

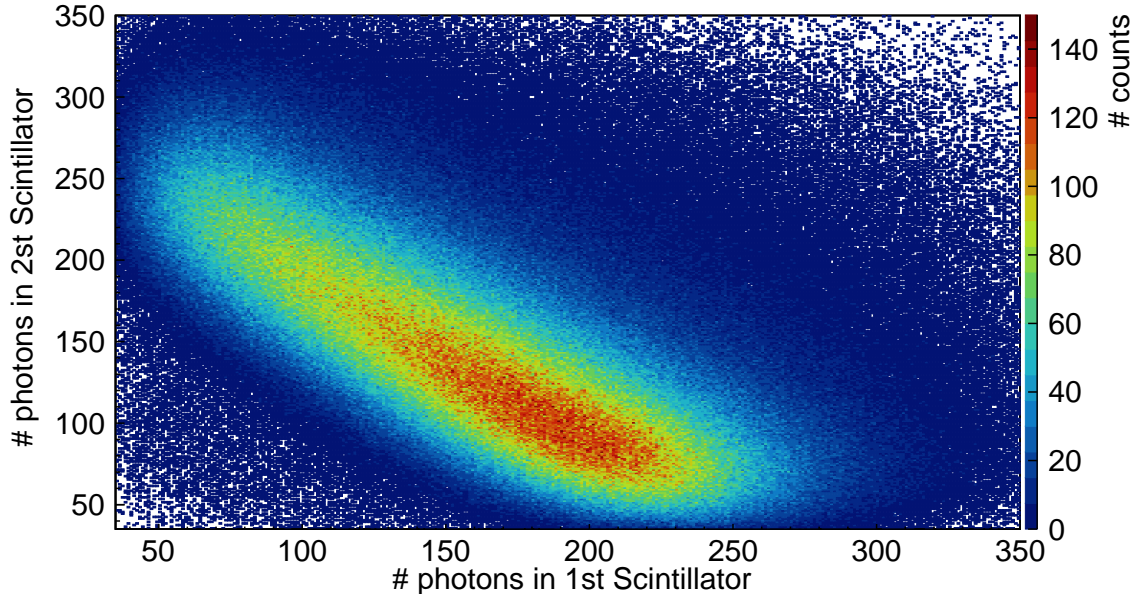


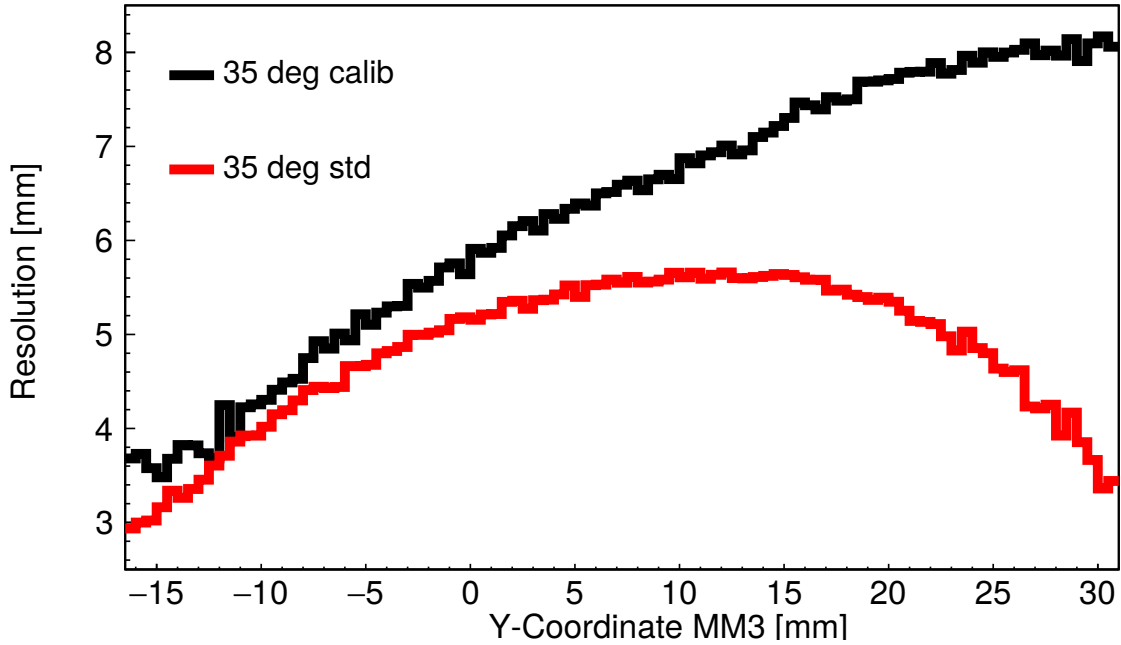
Figure 137: Light yield correlation of both scintillator halves for the 100 mm long 35° geometry when evaluating only the fibers at the thick base. The increased amount of entries showing more photons in the first than in the second scintillator are coming from the positioning of the setup with respect to the beam.

An increased amount of entries showing a higher light yield in the first scintillator, while the second one sees less light can be understood taking into account that the setup is located a bit too deep with respect to the center of the muon beam, hence more events are counted for a muon traversing in the upper part of PoSSuMuS, where the first scintillator has its thick base. Also observed is a rather wide spread of the entries along a linear function being the correlation of the light yields of both scintillator halves. This spread is caused by the independently Landau distributed energy losses in both trapezoids. The idea is to fit a straight line  $f(Q_1)$  to this distribution. Instead of using equation 7.6.1 to obtain the light yield ratio out of both measured quantities  $Q_0$  and  $Q_2$ , the following relation can be used

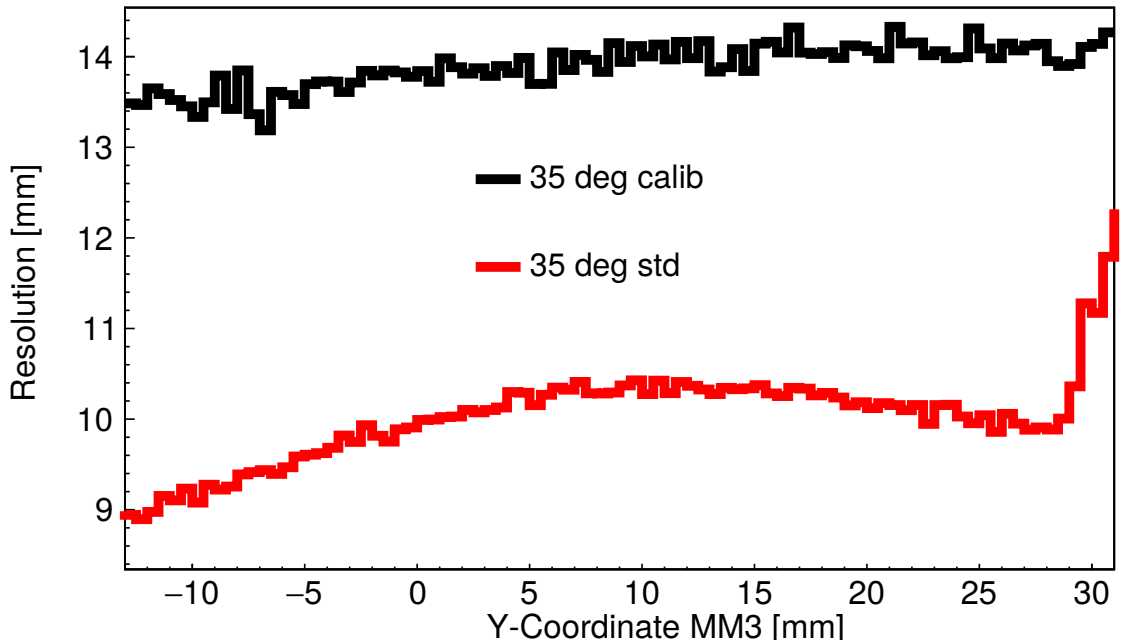
$$\frac{Q_{1^{st} \text{ Scintillator}}}{Q_{1^{st} \text{ Scintillator}} + f(Q_{1^{st} \text{ Scintillator}})} \quad (4.0.1)$$

involving now only one scintillator. The hope is that by calibrating the detector to obtain  $f(Q_1)$  and using this function to get the light yield of the second scintillator, the resolution

can be improved because now only one value shows this Landau distributed energy loss. In Figure 138 the resolution obtained with the calibration method is compared to the standard way to obtain a resolution discussed in chapter 7.6.2.



(a) Resolution of 100 mm long geometries evaluated only with the thick base fibers.



(b) Resolution of 100 mm long geometries evaluated only with the thin base fibers.

Figure 138: Resolutions for the 100 mm long 35° geometry with and without calibration. In Figure 120a the results using only the thick base fibers are shown and in 120b the ones for the thin base equivalent are shown.

It can be seen that the resolution of the standard method is still better meaning that the

calibration does not work well. Especially this time the resolution is highly asymmetric towards the center of the muon beam. A hint that such an effect will occur is already given by Figure 137. Here the distribution is much wider in the direction of the photon count in the first scintillator (X axis) for less photons in the second trapezoid. This effect might be related to the positioning of the setup within the beam, but a more re-measurement would be needed to prove this assumption. Since the resolution does not improve using this method such a measurement seems not very meaningful.

A second approach assumes that the measured light yields can be factorized in a spatial component and a Landau component like

$$Q_i = Q_i(Y) \cdot L_i \quad (4.0.2)$$

with the measured light yield  $Q$  and the current energy loss caused by the Landau distribution  $L$ . With this equation 7.6.3 and 7.6.4 can be rewritten as

$$\frac{Q_2(Y) \cdot L_{23}}{Q_2(Y) \cdot L_{23} + Q_0(Y) \cdot L_{01}} = \frac{Q_2(Y)}{Q_2(Y) + Q_0(Y) \cdot L} = R_0 + (R_1 - R_0) \frac{Y - A}{B - A} \quad (4.0.3)$$

and

$$\frac{Q_3(Y) \cdot L_{23}}{Q_3(Y) \cdot L_{23} + Q_1(Y) \cdot L_{01}} = \frac{Q_3(Y)}{Q_3(Y) + Q_1(Y) \cdot L} = r_0 + (r_1 - r_0) \frac{Y - A}{B - A} \quad (4.0.4)$$

with  $L = \frac{L_{01}}{L_{23}}$ . Eliminating the factor  $L$  out of both equations results in a quadratic function for  $Y$ . One of the final solutions for  $Y$  can be interpreted as the Landau corrected spatial coordinate. The problem here is that the measured quantity of equation 4.0.2 is  $Q$  and not  $Q(Y)$ . To account for this first the values of  $R_0$ ,  $R_1$ ,  $r_0$  and  $r_1$  are calibrated for only special choice of muon events. This choice is an application of the 70 % truncated mean method, [PDG, 2012].  $Y$  dependent only the events which produced up to 70 % of the maximum light yield are considered in the light yield ratio curve. This should cut away the tail given by the Landau fluctuations. This would mean that one took  $Q_i(Y)$  to perform this calibration. Hence one also could solve equation 4.0.2 for  $Q_i(Y)$  and perform the same calculations as before for  $Q_i$  now for  $Q_i(Y)$ . The light yields inserted in the formula for  $Y$  have to be the measured values  $Q_i$ . The result is shown in Figure 139.

It can be seen that again the attempt to improve the resolution failed. Which can be explained by the failure of the 70 % truncated mean method, because the scintillator reaches a thickness where the energy loss can no longer be described by a Landau function alone. The method was not considered further because the result here is much worse compared to the simple calculation of the light yield according to the measured values of the fibers at the thick base.

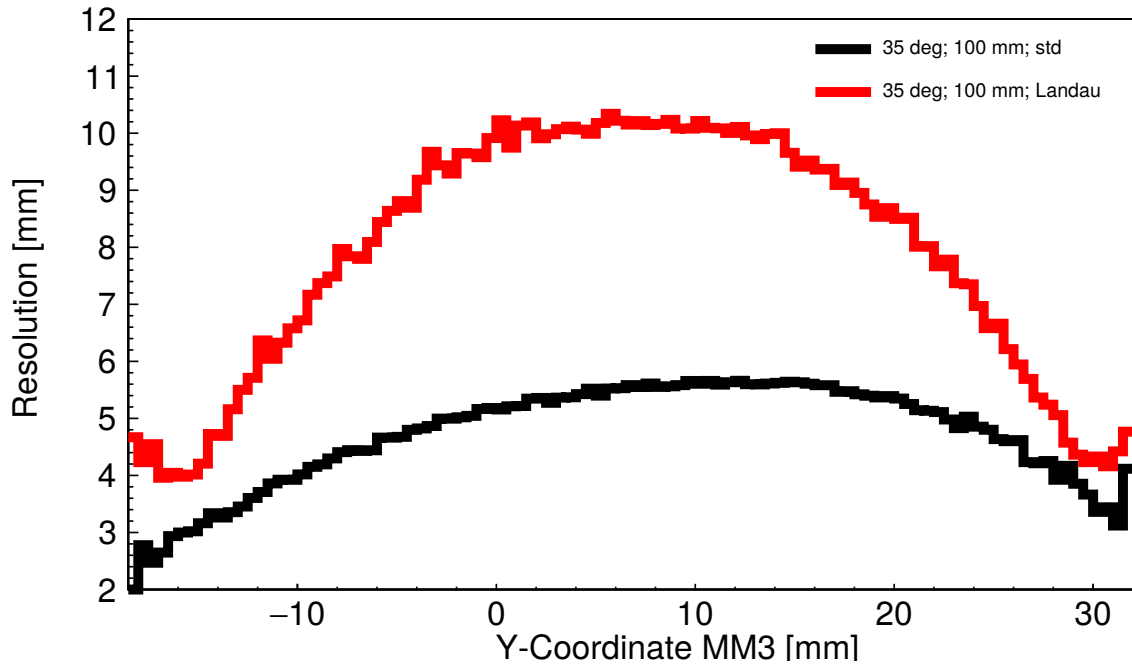


Figure 139: Resolutions for 100 *mm* long 35° geometry with and without a correction to the Landau distributed energy loss. The non corrected curve is always below the corrected one, hence the correction does not work well.

It can be concluded that the statistical process of the energy loss can not be calibrated out of the result. Still the resolution of the detector is well below the requirement.

## List of Abbreviations

---

<b>sTGC</b>	small-strip Thin Gap Chambers
<b>Micromegas</b>	Micro Mesh Gaseous Structure Detectors
<b>NSW</b>	New Small Wheel
<b>MDT</b>	Monitored Drift Tube
<b>CSC</b>	Cathode Strip Chambers
<b>CMM</b>	Coordinate Measurement Machine
<b>PCB</b>	Printed Circuit Board
<b>LHC</b>	Large Hadron Collider
<b>CRF</b>	Cosmic Ray Facility
<b>SiPM</b>	silicon photomultiplier
<b>QDC</b>	charge-to-digital converter
<b>TDC</b>	time-to-digital converter
<b>FiFo</b>	Fan in - Fan out
<b>LTD</b>	low threshold discriminator
<b>CFD</b>	constant fraction discriminator
<b>P-LTD</b>	programmable low threshold discriminator
<b>FEC</b>	front end concentrator cards
<b>SRU</b>	scalable readout unit
<b>SRS</b>	scalable readout system
<b>FADC</b>	flash analog-to-digital converter
<b>MIP</b>	minimum ionizing particle
$V_{BD}$	breakdown voltage
$V_{bias}$	bias voltage
$V_{over}$	over voltage
<b>WLSF</b>	wavelength shifting fiber



- [Alexopoulos et al., 2011] Alexopoulos, T., Burnens, J., de Oliveira, R., Glonti, G., Pizzirusso, O., Polychronakos, V., Sekhniaidze, G., Tsipolitis, G., and Wotschack, J. (2011). A spark-resistant bulk-micromegas chamber for high-rate applications. *Nuclear Instruments and Methods in Physics Research Section A: Accelerators, Spectrometers, Detectors and Associated Equipment*, 640(1):110–118.
- [Amelung et al., 2014] Amelung, C., C. Bini, Giraud, P.-F., Iakovidis, G., Iengo, P., Iodice, M., Lelouch, D., Mikenberg, G., Pontecorvo, L., Schune, P., and Vlachos, S. (2014). NSW Requirements. Technical report. [https://edms.cern.ch/ui/file/1350308/1/NSW\\_Requirements.pdf](https://edms.cern.ch/ui/file/1350308/1/NSW_Requirements.pdf).
- [ANALOG DEVICES, 2012] ANALOG DEVICES (2012). AD5263, <http://www.analog.com/media/en/technical-documentation/data-sheets/AD5263.pdf>, 2017-03-08.
- [ATLAS Collaboration, 2008] ATLAS Collaboration (2008). The ATLAS Experiment at the CERN Large Hadron Collider. *Journal of Instrumentation*, 3(08):S08003.
- [ATLAS MUON Collaboration, 2013] ATLAS MUON Collaboration (2013). New Small Wheel Technical Design Report, <http://cds.cern.ch/record/1552862/files/ATLAS-TDR-020.pdf?version=4>.
- [Bengtson and Moszyński, 1974] Bengtson, B. and Moszyński, M. (1974). Energy-transfer and light-collection characteristics for different types of plastic scintillators. *Nuclear Instruments and Methods*, 117(1):227–232.
- [Bini et al., 2014] Bini, C., Giraud, J., Giraud, P.-F., Hertenberger, R., Iengo, P., Iodice, M., Jeanneau, F., Lacava, F., Ponsot, P., Schune, P., and Vlachos, S. (2014). Micromegas Mechanical Tolerances. Technical report. [https://edms.cern.ch/ui/file/1400235/1/MM\\_Panel\\_Module\\_Mechanical\\_Requirements\\_v4\\_20140725.pdf](https://edms.cern.ch/ui/file/1400235/1/MM_Panel_Module_Mechanical_Requirements_v4_20140725.pdf).
- [CAEN, 1991] CAEN (1991). N 113 - DUAL 12 INPUTS OR, <http://www.caen.it/servlet/checkCaenManualFile?Id=9324>, 2017-02-27.
- [CAEN, 1993] CAEN (1993). N 405 - 3 FOLD LOGIC UNIT/MAJORITY WITH VETO, <http://www.caen.it/servlet/checkCaenManualFile?Id=9759>, 2017-02-27.
- [CAEN, 2003] CAEN (2003). N 108A - DUAL DELAY, <http://www.caen.it/servlet/checkCaenManualFile?Id=5130>, 2017-02-27.
- [CAEN, 2004] CAEN (2004). V 977 -16 CHANNEL I/O Register, <http://www.caen.it/servlet/checkCaenManualFile?Id=5172>, 2017-02-27.

- 
- [CAEN, 2006a] CAEN (2006a). N 625 - QUAD LINEAR FAN IN / FAN OUT, <http://www.caen.it/servlet/checkCaenManualFile?Id=5257>, 2017-02-27.
- [CAEN, 2006b] CAEN (2006b). N 93B - DUAL TIMER, <http://www.caen.it/servlet/checkCaenManualFile?Id=5239>, 2017-02-27.
- [CAEN, 2010a] CAEN (2010a). V 792 (N) - 32/16 CH QDC, <http://www.caen.it/servlet/checkCaenManualFile?Id=6992>, 2017-02-27.
- [CAEN, 2010b] CAEN (2010b). V 814 - LOW THRESHOLD DISCRIMINATOR, <http://www.caen.it/servlet/checkCaenManualFile?Id=6978>, 2017-02-27.
- [CAEN, 2011] CAEN (2011). N 845 - 8-16 CHANNEL LOW THRESHOLD DISCRIMINATOR, <http://www.caen.it/servlet/checkCaenManualFile?Id=7685>, 2017-02-27.
- [CAEN, 2012] CAEN (2012). V 775 (N) - 32/16 CHANNEL MULTIEVENT TDC, <http://www.caen.it/servlet/checkCaenManualFile?Id=8891>, 2017-02-27.
- [DuPont, 2012] DuPont (2012). Tyvek, [http://www2.dupont.com/Tyvek/en\\_US/index.html](http://www2.dupont.com/Tyvek/en_US/index.html).
- [Farthouat and Gällnö, 2000] Farthouat, P. and Gällnö, P. (2000). TTC-VMEbus INTERFACE TTCvi - MkII, <http://ttc.web.cern.ch/TTC/TTCviSpec.pdf>, 2017-03-31.
- [Flierl, 2018] Flierl, B. (2018). *Studies on two dimensional GEM Detectors*. Phd thesis, LMU Munich, [http://www.etp.physik.uni-muenchen.de/publications/theses/download/phd\\_bflierl.pdf](http://www.etp.physik.uni-muenchen.de/publications/theses/download/phd_bflierl.pdf).
- [GEANT4-Collaboration, 2017] GEANT4-Collaboration (2017). Geant4: A toolkit for the simulation of the passage of particles through matter, <http://geant4.web.cern.ch/geant4/>, 2017-03-16.
- [Giomataris et al., 1996] Giomataris, Y., Rebourgeard, P., Robert, J. P., and Charpak, G. (1996). MICROMEGAS: a high-granularity position-sensitive gaseous detector for high particle-flux environments. *Nuclear Instruments and Methods in Physics Research Section A: Accelerators, Spectrometers, Detectors and Associated Equipment*, 376(1):29–35.
- [Grossmann, 2014] Grossmann, J. (2014). *Optimization of a scintillation detector with wave length shifting fiber and SiPM readout*. Master thesis, LMU Munich, [http://www.etp.physik.uni-muenchen.de/publications/theses/download/master\\_jgrossmann.pdf](http://www.etp.physik.uni-muenchen.de/publications/theses/download/master_jgrossmann.pdf).
- [Hamamatsu, 2015] Hamamatsu (2015). Datasheet Hamamatsu S12572-025, -050, -100C/P, [http://www.hamamatsu.com/resources/pdf/ssd/s12572-025\\_etc\\_kapd1043e.pdf](http://www.hamamatsu.com/resources/pdf/ssd/s12572-025_etc_kapd1043e.pdf), 2017-03-14.

- [Hamamatsu Electronics, 2008] Hamamatsu Electronics (2008). MPPC Techinfo, [http://www.hamamatsu.com/resources/pdf/ssd/mppc\\_techinfo\\_e.pdf](http://www.hamamatsu.com/resources/pdf/ssd/mppc_techinfo_e.pdf).
- [Infineon, 2011] Infineon (2011). BGA 614, [http://www.infineon.com/dgdl/Infineon-BGA614-DS-v02\\_01-en.pdf?fileId=db3a304314dca3890115418ffd35163a](http://www.infineon.com/dgdl/Infineon-BGA614-DS-v02_01-en.pdf?fileId=db3a304314dca3890115418ffd35163a), 2017-03-08.
- [Jeanneau and Iodice, 2015] Jeanneau, F. and Iodice, M. (2015). MicroMegas Construction Manual. Technical report. <https://edms.cern.ch/ui/#!master/navigator/document?P:1357908794:1827003523:subDocs>.
- [Jones et al., 1999] Jones, L. L., French, M. J., Morrissey, Q. R., Neviani, A., Raymond, M., Hall, G., Moreira, P., and Cervelli, G. (1999). The APV25 deep submicron readout chip for CMS detectors.
- [Keithley, 2016a] Keithley (2016a). 6517B Electrometer/High Resistance Meter, [http://de.tek.com/sites/tek.com/files/media/media/resources/6517B-Datasheet\\_1KW-60280-1.pdf](http://de.tek.com/sites/tek.com/files/media/media/resources/6517B-Datasheet_1KW-60280-1.pdf), 02.05.17.
- [Keithley, 2016b] Keithley (2016b). Series 2400 Source Meter, [http://de.tek.com/sites/tek.com/files/media/media/resources/Series\\_2400\\_DS\\_041216.pdf](http://de.tek.com/sites/tek.com/files/media/media/resources/Series_2400_DS_041216.pdf), 02.05.2017.
- [Kolberg, 2016] Kolberg, C. (2016). *Untersuchung der Eigenschaften eines Laserabstandssensors bei Vermessung verschiedener Oberflächen*. Bachelor thesis, LMU Munich, [https://www.etp.physik.uni-muenchen.de/publications/bachelor/download\\_auth\\_etp/bac16\\_ckolberg.pdf](https://www.etp.physik.uni-muenchen.de/publications/bachelor/download_auth_etp/bac16_ckolberg.pdf).
- [Kröger, 2014] Kröger, F. (2014). *Simulationsstudien zu einem ortsauflösenden Szintillations-Detektors mit Geant4*. Bachelor thesis, LMU Munich, [https://www.etp.physik.uni-muenchen.de/publications/bachelor/download\\_auth\\_etp/bac14\\_fkroeger.pdf](https://www.etp.physik.uni-muenchen.de/publications/bachelor/download_auth_etp/bac14_fkroeger.pdf).
- [Kulosik, 2017] Kulosik, P. (2017). *Temporal Studies of Trapezoidal Scintillators*. Bachelor thesis, LMU Munich, [https://www.etp.physik.uni-muenchen.de/publications/bachelor/download\\_auth\\_etp/bac17\\_pkulosik.pdf](https://www.etp.physik.uni-muenchen.de/publications/bachelor/download_auth_etp/bac17_pkulosik.pdf).
- [Landau, 1944] Landau, L. D. (1944). On the energy loss of fast particles by ionization. *Journal of Experimental and Theoretical Physics (USSR)*, 8(201).
- [Leo, 1994] Leo, W. R. (1994). *Techniques for Nuclear and Particle Physics Experiments*. Springer-Verlag, second edition.

- 
- [Lösel, 2017] Lösel, P. (2017). *Construction, Commissioning and Calibration of Large Area Micromegas Detectors*. Phd thesis, LMU Munich, [http://www.etp.physik.uni-muenchen.de/publications/theses/download/phd\\_ploesel.pdf](http://www.etp.physik.uni-muenchen.de/publications/theses/download/phd_ploesel.pdf).
- [Meschede, 2015] Meschede, D. (2015). *Gerthsen Physik*. Springer Spektrum, Berlin Heidelberg, 25 edition.
- [MicroEpsilon, 2016] MicroEpsilon (2016). Instruction Manual optoNCDT 2300, <http://www.micro-epsilon.de/download/manuals/man--optoNCDT-2300--en.pdf>.
- [Müller, 2013] Müller, R. (2013). *Development of a Position Sensitive Scintillating Muon Detector with Silicon Photo-Multiplier Readout*. Master thesis, LMU Munich, [http://www.etp.physik.uni-muenchen.de/publications/theses/download/master\\_rmueeller.pdf](http://www.etp.physik.uni-muenchen.de/publications/theses/download/master_rmueeller.pdf).
- [Müller, 2015] Müller, R. (2015). Design and construction of precision tooling for the construction of resistive strip micromegas detectors for the ATLAS Small Wheel upgrade project. In *2015 IEEE Nuclear Science Symposium and Medical Imaging Conference (NSS/MIC)*, pages 1–6.
- [Müller et al., 2016] Müller, R., Biebel, O., Hertenberger, R., Lösel, P., and Schaile, O. (2016). Fast and precise large area metrology of micropattern detectors using laser distance sensors. *Nuclear Instruments and Methods in Physics Research Section A: Accelerators, Spectrometers, Detectors and Associated Equipment*, 824:215–217.
- [Müller and Lösel, 2014] Müller, R. and Lösel, P. (2014). Design and Construction of Large Size Micromegas Chambers for the Upgrade of the ATLAS Muon Spectrometer.
- [PDG, 2012] PDG (2012). Particle Data Group, <http://pdg.lbl.gov/>.
- [Pequenao, 2008] Pequenao, J. (2008). Computer generated image of the whole ATLAS detector.
- [Pree, 2014] Pree, E. (2014). *Construction of Large Area Micromegas Detectors*. Master thesis, LMU Munich, [http://www.etp.physik.uni-muenchen.de/publications/theses/download/master\\_epree.pdf](http://www.etp.physik.uni-muenchen.de/publications/theses/download/master_epree.pdf).
- [Ruschke, 2014] Ruschke, A. (2014). *POSSuMUS - A Position Sensitive Scintillating Muon SiPM Detector*. Phd thesis, LMU Munich, [http://www.etp.physik.uni-muenchen.de/publications/theses/download/phd\\_aruschke.pdf](http://www.etp.physik.uni-muenchen.de/publications/theses/download/phd_aruschke.pdf).

- [Saint Gobain, 2011a] Saint Gobain (2011a). Organic Scintillation Materials, <http://www.detectors.saint-gobain.com/uploadedFiles/SGdetectors/Documents/Brochures/Organics-Brochure.pdf>.
- [Saint Gobain, 2011b] Saint Gobain (2011b). Scintillating Optical Fibers and Plastic Scintillating Fibers, <http://www.detectors.saint-gobain.com/uploadedFiles/SGdetectors/Documents/Brochures/Scintillating-Optical-Fibers-Brochure.pdf>.
- [Saint Gobain, 2012] Saint Gobain (2012). Detector Assembly Materials, [http://www.detectors.saint-gobain.com/uploadedFiles/SGdetectors/Documents/Product\\_Data\\_Sheets/SGC\\_Detector\\_Assembly\\_Materials\\_Data\\_Sheet.pdf](http://www.detectors.saint-gobain.com/uploadedFiles/SGdetectors/Documents/Product_Data_Sheets/SGC_Detector_Assembly_Materials_Data_Sheet.pdf).
- [Sigma-Aldrich, 2013] Sigma-Aldrich (2013). Polyvinyltoluene, <http://www.sigmaaldrich.com/catalog/product/fluka/464945?lang=de&region=DE>.
- [Sylvac, 2016] Sylvac (2016). Digital indicators S \_ Dial WORK Digital indicators S \_ Dial WORK, [http://www.sylvac.ch/products/digital-indicators/digital-indicator-s\\_dial-work-advanced-detail](http://www.sylvac.ch/products/digital-indicators/digital-indicator-s_dial-work-advanced-detail), 2016-07-13.
- [White, 1988] White, T. O. (1988). Scintillating fibres. *Nuclear Instruments and Methods in Physics Research*, 273:820–825.
- [Wikimedia Commons, 2007] Wikimedia Commons (2007). Franck Condon Principle.
- [Zibell, 2014] Zibell, A. (2014). *High-Rate Irradiation of 15mm Muon Drift Tubes and Development of an ATLAS Compatible Readout Driver for Micromegas Detectors*. Phd thesis, LMU Munich, [http://www.etp.physik.uni-muenchen.de/publications/theses/download/phd\\_azibell.pdf](http://www.etp.physik.uni-muenchen.de/publications/theses/download/phd_azibell.pdf).



# Acknowledgement

At this point, I would like to give thanks to all those persons who supported me during my work on this thesis.

- I would like to thank Prof. Dr. Dorothee Schaile for giving me the opportunity to write this thesis at her chair and Prof. Dr. Otmar Biebel for supervising the work. His advices are always helpful and profound, and his door is always open for questions.
- My thanks go also to Dr. Ralf Hertenberger for his extraordinary engagement even in times where the NSW project has the highest priority. His permanent good mood is a key feature of the fruitful working atmosphere in this group.
- Another key aspect why I enjoyed almost every day at work are my colleagues of the hardware group: Philipp, Andre, Bernhard, Maximilian, Felix. A friendship during but also after work evolved over the years.
- In addition to the hardware also a lot of help and interesting discussions come from my software colleagues: Thomas, Michael B., Michael A. and Friedrich; our secretary Elke Grimm-Zeidler; our technician Atila Varga and our HistPresent inventor Dr. Otto Schaile. Thanks for everything.
- Also I have to thank my bachelor students Felix, Christian, Maximilian, Benjamin and Peter supporting me and this thesis with their work.
- Since it is a hardware topic without the mechanical workshop in Garching and their outstanding work and advises live would be much harder, special thanks to Rolf Oehm and Sigfried Huber.
- Special thanks go also to Dr. Jona Bordtfeld for his efforts to make the beam time happening smooth.
- Thanks a lot to all my friends supporting this thesis in any way, especially to Alexander Arth for his advices after reading this thesis and Marco Häuser for the design of the revised readout electronics.
- Thanks to my girlfriend Annabel Säurig for enduring me writing a scientific thesis a third time and all the inconveniences accompanying this process.
- Last but not least I want to thank my entire family, especially my parents Karin and Ewald, for making the study at the LMU possible although this means that I had just very little time for them.